Scuola di Dottorato in Ingegneria Industriale
Università degli Studi di Firenze

DOTTORATO DI RICERCA IN

INGEGNERIA INDUSTRIALE E DELL'AFFIDABILITÀ

XXIV CICLO

Settore scientifico disciplinare di afferenza: ING-IND/13

TESI DI DOTTORATO

Development of innovative models for the wear analysis and wheel profile optimisation in railway vehicles

Tutor universitario:

DOTT. ING. ANDREA RINDI

Coordinatore della Scuola di Dottorato:

PROF. ING. MARIO TUCCI

Candidato: MIRKO IGNESTI

Anno 2011

Alla mia famiglia

Ringraziamenti

Desidero innanzitutto ringraziare in modo particolare l'Ing. Andrea Rindi e il Prof. Paolo Toni per avermi consentito di affrontare anche questo percorso formativo, per il loro supporto e per tutte le opportunità che mi hanno concesso in questi anni di collaborazione.

Ringrazio tutte le persone che hanno contribuito in qualche misura allo svolgimento di questo lavoro: mi riferisco agli Ingg. Cheli, Grande e Desideri di Trenitalia S.p.A. e agli Ingg. Mele e Finocchi di Italcertifer S.c.p.A, sia per il loro diretto contributo che per aver messo a disposizione tutta la documentazione tecnica necessaria per portare a termine l'attività. Ringrazio in particolare le persone con le quali ho lavorato a stretto contatto: in primo luogo l'Ing. Enrico Meli, per avermi seguito assiduamente in qualità di relatore e per le competenze dimostrate, determinanti per la riuscita dell'attività; in secondo luogo vorrei citare l'Ing. Jury Auciello, per il suo importante apporto nella prima parte del lavoro.

Vorrei ringraziare in modo speciale tutte le persone della Sezione di Meccanica Applicata, soprattutto coloro con i quali ho trascorso e trascorro tuttora molto tempo, in un ambiente lavorativo — e non solo — che ritengo piacevole e stimolante. Non posso fare a meno di elencarli tutti: Susanna, Andrea, Francesco, Stefano, Enrico, Jury, Fabio, Luca, i Proff. Toni e Allotta, Monica, Alessandro, Roberto, Gregorio, Lorenzo, Alice e Riccardo. La loro splendida compagnia ha reso tutto molto più facile.

Desidero infine rivolgere il ringraziamento più importante alla mia famiglia. L'instancabile supporto, la pazienza inesauribile e il continuo incoraggiamento che hanno saputo dimostrarmi in questi anni sono stati per me davvero fondamentali.

Firenze, 29 gennaio 2012

Mirko

Contents

Introduction

The wheel-rail contact is surely one of the most important and interesting aspect in rail transportation. This interaction plays a fundamental role as regards the safety, the maintenance costs and the logistic of the rolling stock and the railway infrastructure. Due to these important reasons, several authors have been treating this topic in literature for many years, from different points of view. A few aspects of great importance, still now analysed with increasing interest, are the wheel-rail contact modelling for dynamic simulation purposes, the estimation of wheel and rail wear and the general optimisation of the wheel and rail profiles, in order to improve the running dynamics and the resistance to wear of the contact surfaces.

The wear in the wheel-rail interaction tends to modify the geometry of wheels (Fig. 1) and rails with important safety and economic consequences. For instance, wheel profiles modified by wear can make the vehicle unstable in straight tracks over a certain travelling speed and lead to a serious damage of the railway infrastructure, not to mention the risk of a derailment; a derailment can even occur at low speed in curves if the wheel and rail because of the wear, no longer have the proper original geometry.

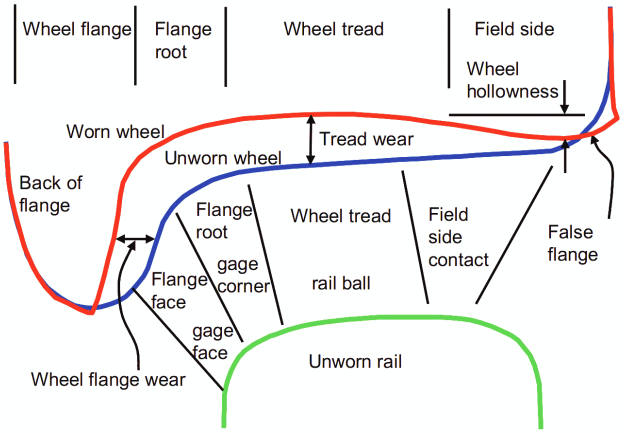

Figure 1. Sections of unworn and worn wheel with a section of an unworn rail [1].

In order to avoid these consequences, maintenance interventions on both the vehicles and the tracks are periodically carried out on the altered geometries. In regard to the

wheels, as the wear proceeds, the shape of a wheel profile changes leading to variations in the characteristics of the wheelset-rail coupling, with consequences on the vehicle performance which may not be acceptable. For this reason, after covering a certain mileage, the wheels of a vehicle have to be checked to decide whether the original profile must be re-established on the worn wheel by means of turning or not. Since the re-turning can be carried out only a few times before the end of life of wheels and taking into consideration that the operation is onerous both in economic sense and in terms of vehicle availability, it is clearly advantageous to reduce its frequency.

In light of what has shown up to this point, the correct prediction of the wear rate in a particular railway context by using reliable software tools may be very important, first of all, in planning the wheelset maintenance interventions and in reducing the overall costs. As a further and obvious application, a reliable wear model can also be used to choose an optimal wheel profile from a wear point of view. In fact, a proper wheel profile can guarantee a more uniform and slower wear, allowing the wheel-rail contact to maintain stable and acceptable geometric characteristics. In this way, not only the wear rate may be reduced leading to higher mean times between two consecutive maintenance interventions, but the performance of the wheel-rail contact may also be kept nearly constant over time.

However, in the development of an accurate wear model [2, 3, 4], one of the most critical aspect is the availability of experimental results, since the collection of data usually requires at least a few months with relevant economic costs. In fact, besides the general organisational and technical costs, the experimental measurements have to be done on trains which are in service and periodically their service must be interrupted for data acquisition, with remarkable induced costs. Moreover, the collected data must be opportunely organised to correlate all the main influential factors (vehicle characteristics, tracks, rail conditions, etc.) to the wear evolution. In other words, the route of the vehicle must be exactly known and obviously the measured data should be expressed as a function of the travelled kilometrage. If on line experimental measurements cannot be carried out, the problem can be overcome by carrying out experimental tests on a scaled test rig, as described in [2, 3].

Among the several works available in literature on the wear and its consequences in the railway field, a work of Kalousek [5] can also be cited; he proposed a solution to ease the wear by reducing the spread between the worn and unworn profiles based on the reduction of the hollow in the tread of the wheel profile; in addition, the work of [6] can also be of interest: he describes the effect of the hollow in the performance of the wheel-rail interaction by means of multibody simulations. Conversely, with regard to the wheel profile optimisation from different points of view, in the works of I.Y. Shevtsov [7, 8, 9, 10], numerical procedure based on the rolling radius difference function are used in combination with optimisation criteria such as the stability of wheelset, the minimal wear, the contact forces magnitude. The arising wheel shape is then tested by multibody simulation of running dynamics.

An approach based on penalty indexes is provided Persson and Iwnicki [11] in which the performance of optimised wheel profile is evaluated taken into consideration the lateral

force, the safety against derailment and the comfort. Optimisation algorithms based on penalty indexes are also used by Novales [12] which also introduces the evaluation of wear in different running conditions.

The present thesis deals with the wear evaluation and the formulation of optimal wheel profiles, within a research project issued by Trenitalia S.p.A. (the main manager of the rolling stock in the Italian railways) mainly focused on wear assessment and wheel profile optimisation. The project, titled 'Ottimizzazione dei profili delle ruote su binario con posa 1/20" was aimed at finding alternative wheel profiles to be employed in vehicles which are operated on the Italian railways, to the standard nonlinear wheel geometry widely used both in Italy and in Europe: the ORE S1002. This wheel profile was developed tens of years ago to increase the mean life of the wheels. The ORE S1002 profile, as it will explained in detail, is not suitable to be applied on vehicle circulating on the Italian railways, because it was developed for track having a lying inclination (the inclination angle of the symmetry axis of the rail section to vertical) different from that used in Italy.

The research work has been executed by the Section of Applied Mechanics of the University of Florence in collaboration with Trenitalia S.p.A and Rete Ferroviaria Italiana (the manager of the railway infrastructure). The research activity had to be performed via numerical simulations of vehicle dynamics taking into consideration a few real contexts of practical interest and by exploiting experimental data provided by the project partners.

With regard to the adopted methodology, which will be described in great detail in the thesis, a general architecture made up of a group of mutually interacting software tools has been specifically developed for this work. This general model basically encloses a multibody model of the railway vehicle under investigation, a detailed contact model to be used in dynamic simulations in combination with the multibody part and finally a mathematical model capable of evaluating the wheel wear. The whole developed architecture, before being used to perform the wear evaluations has been validated thanks to the experimental data relative to the Aosta-Pre Saint Didier line and the ALn 501 Minuetto vehicle circulating on this track.

The main part of the work have been focused on the wear assessment of wheels regarding to two real train compositions: the Aln 501 Minuetto and the E464-Vivalto train, both widely used for the regional passenger transport in Italy. Numerical simulations have been carried out on "virtual tracks", that is statistical representations of the whole railway nets on which the vehicles are in service. This statistical method have been introduced in order to simplify the approach to a complex railway line with several vehicles operated. The aim of these numerical simulations was to perform a comparison between the performance, in terms of wear, via analysis of the changes in shape of the different wheel profiles. The study has involved the S1002 profile and alternative proposed solutions; the results of the wear assessment have been compared extensively and a successive estimation of the stability, considering the vehicles equipped with the new profiles and the worn profiles have been carried out.

For what concerns the structure of the present thesis, it is arranged in the following

manner: Chapter 1 presents the fundamental aspects of the wheel-rail interface with a particular attention focused on the geometric aspects and on the kinematic movement of a wheelset; Chapter 2 is a detailed description of the general architecture of the model. Chapter 3 consists of two parts: in the first one the multibody models of the vehicle taken into consideration in this study are described without going into modelling details; the second part is a detailed description of the contact model used in multibody simulations. Chapter 4 explains the wear model and its three sub-parts, while Chapter 5 described the method adopted in building the innovative wheel profiles. Finally, Chapter 6 and 7 show the results of the wear analysis and the stability assessment respectively.

CHAPTER 1

Wheelset and Track Interaction

In this chapter a brief introduction to the basic notions of the wheel-rail interaction will be presented. Focus will turn especially on the geometric aspects of the contact and on the kinematic motion of the wheelset, while the main aspects of the contact forces will be treated in detail in the next chapters.

1.1 Wheelset and track geometry

The fundamental unit of a railway vehicle, either it is a bogie vehicle or a two-axle vehicle, is the wheelset, which basically consists of two wheels fixed to a common axle. The guidance of the wheelset on the track is obtained through the following basic arrangements:

- the wheels are not cylindrical (Fig. 1.1), but the rolling radii increases toward the centre of the wheelset, so that in curves, as the wheelset moves laterally, the external wheel can raise its rolling radius as the internal wheel reduces its own. Since the angular speed of the wheels is the same, this solution provides a differential effect which reduces the slip between wheels and rails in curves;
- the wheels have a flange on the internal side, in order to avoid the derailment. In fact, the mechanism previously described is often insufficient to ensure the guidance in all the possible running conditions because the required lateral clearance can be greater than the available amount; this usually happens in sharp curves and on the switches, but it can even occur in other situations, depending on the contact geometry characteristics. In these cases an additional restoring force is provided by the contact between the flange and the rail. Nevertheless, in normal running conditions, the phenomenon should be avoided, since it can induce high lateral forces and remarkable effects on wear, both for the wheel and the rail.

The current geometry of the wheelset is a result of a long development and nowadays meets the requirements of guidance and moreover it is particularly favourable for the method of switching in use. In fact, being the wheels fixed on the axle, if the tread profile

were cylindrical large displacement would be caused by minimal errors in parallelism and the wheelset would run in flange contact continuously, since the flange would be the only guidance system. In regard to the position of the flanges, they must be located on the inside mainly for two reasons. If the flanges were on the outside, the conicity would have the opposite sign with respect to the standard arrangement in use and the wheelset would run into the flange anyway, remaining in contact. Furthermore, in sharp curves, if the flange is on the inside, the lateral force exerted by the rail to the leading wheelset of a bogie is applied on the external wheel, on which the vertical load is enhanced by the centrifugal acceleration. Conversely, if the flanges were on the outside, the lateral force would be applied on the inner wheel, with a consequent higher derailment risk [13], as it will be clarified in the next sections.

The main dimensions of a wheelset-track matching are indicated in Fig. 1.1 [1]:

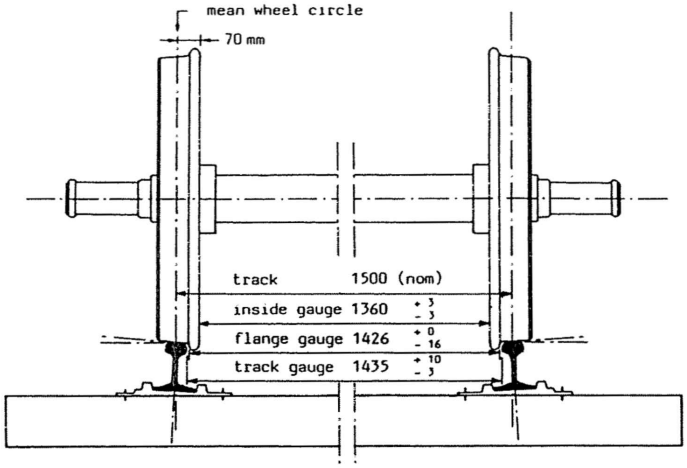

Figure 1.1. Wheelset and track main dimensions.

- *track gauge*: distance between the inside of the rail heads measured 14 mm below the rail surface. The gauge is 1435^{+10}_{-3} mm on normal tracks. By measuring 14 mm below the top, the result is less influenced by lipping and lateral wear as well as by the rail radius of 13 mm in the rail head face;
- *track*: distance between the contact points of the mean wheel circles when the wheelset is centered on the track; the standard value is 1500 mm;
- *inside gauge*: distance between the internal sides of the two wheels, whose standard value is equal to 1360^{+3}_{-3} mm;
- *flangeway clearance*: the distance the wheelset can be displaced laterally until the flange contact occurs.

Since many years ago the wheel profile were conical with an inclination of $1/20$ rad, the rails were being lain with the same angle with respect to the vertical, so that the load was applied centrally on the rail head (Fig. 1.2). Nowadays the conical profiles for wheels

are not being used, but for the same reason the rail must be lain with a cant angle anyway, which is commonly 1/40, 1/30 or 1/20 rad.

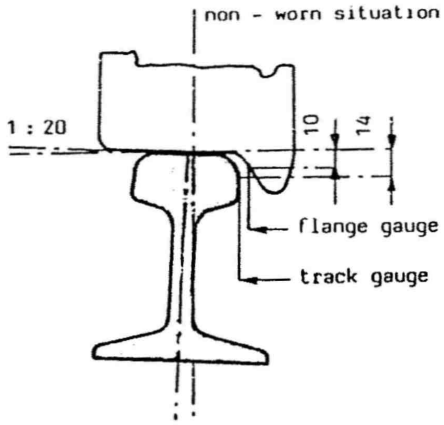

Figure 1.2. Matching between a conical wheel profile and a rail profile with a cant of 1/20 rad.

1.2 The Klingel's model

Besides the differential effect in negotiating curves, the presence of the conicity in the wheel-rail contact introduces a kinematic oscillation of the wheelset in straight tracks, as stated by the Klingel's model ([13, 14]) which gave the first mathematical description of the phenomenon in 1883. In the Klingel's kinematic linear model (Fig. 1.3) the wheelset is modelled as a bicone and the rails as two blades without thickness, so that the contact points on the ground have a fixed lateral position.

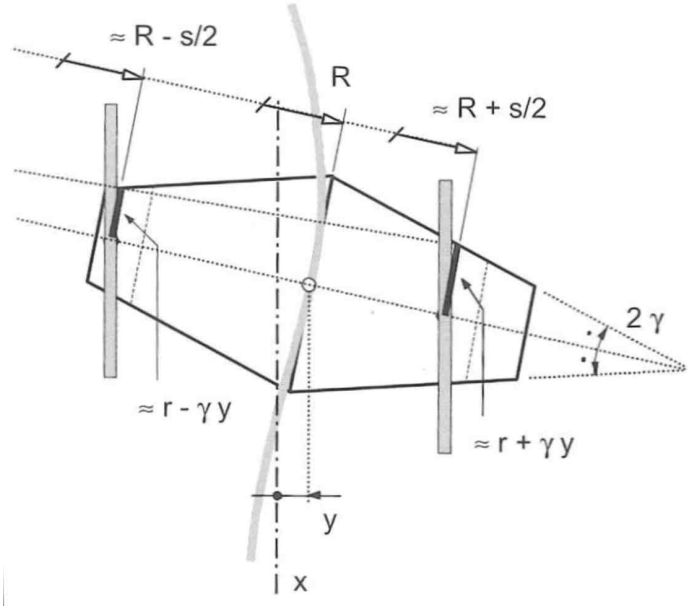

Figure 1.3. Klingel's linear model for the kinematic motion of wheelset.

Assuming that the travelling speed is kept constant, the wheelset plane motion have two

degrees of freedom: the lateral position y and the yaw angle ψ. Assuming that the wheelset maintains pure rolling during the motion and hence no slips in the contact points occur while the longitudinal speed is kept constant, the lateral motion can be described by a second order differential equation:

$$y''(x) + \frac{2\gamma}{rs} y(x) = 0\,, \tag{1.1}$$

where r is the nominal wheel rolling radius (with the wheelset centered in the track) and s is the track gauge. If either the initial conditions $y(0)$ and $y'(0)$ are non-zero, the resultant motion is sinusoidal with a wavelength equal to

$$L = 2\pi\sqrt{\frac{rs}{2\gamma}}\,, \tag{1.2}$$

which means that the spatial frequency of the kinematic oscillation is proportional to $\gamma^{-1/2}$ and inversely proportional to r^2; the temporal frequency can be easily deduced by introducing the constant vehicle speed ($f = V/L$). It is clear that with an high value of γ, the frequency of the oscillation will become quite high quickly as the travelling speed increases. The wheelset oscillation induces lateral accelerations and could contribute to make the vehicle unstable if the frequency of the oscillation coincides with a natural frequency of the vehicle.

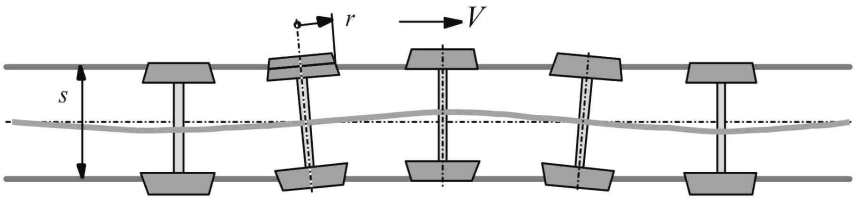

Figure 1.4. The kinematic oscillation of a wheelset.

1.3 Considerations on guidance and stability

In a kinematic context the forces and the inertial properties do not play any role, while as regards the dynamic behaviour the situation becomes more complicated. The hypothesis of pure rolling in the contact points is no longer true because tangential forces in the contact patches are necessary to balance the inertial forces of the wheelset due to the lateral and yaw accelerations; these tangential forces can arise only if a certain amount of creepage comes off in the contact points. The slip in a contact patch can be conveniently expressed by the *creepage vector*, defined as the deviation in relative velocity divided by forward speed. The longitudinal component of this vector is responsible of the longitudinal force exchanged in tangent plane of the contact point, while the other component leads to a lateral force. On first approximation, for the sake of brevity, both the forces are proportional to the respective creepage for small value of the creepage modulus and their effects

can also be superimposed in the linear approximation [15].

As a result, when the wheelset is displaced laterally by an amount y and a yaw angle ψ equal to zero, the two wheels have different tangential speed because the two rolling radii are not equal and the longitudinal creepages that appear provide a yaw couple which tends to steer the wheelset toward the centre of the track. If instead the wheelset is rotated by an yaw angle but it is not displaced laterally, lateral creepage and consequently lateral forces arise on both the wheels. This coupling between the two degrees of freedom constitutes a sort of feedback and hence dynamic instability could occur.

Basically, the amplitude of the oscillation, which is simply an initial condition in the kinematic motion, in a dynamic context depends mainly on the characteristics of the vehicle (inertial properties, stiffness and damping properties, geometries etc.), on the speed as well as on the wheel-rail interface conditions (wheel and rail profiles, gauge, friction coefficient). As a result, as the speed increases, the amplitude of the oscillation becomes more and more higher until the flange contact occurs and the wheelset is rebound. In these conditions the frequency tends to rises quickly if the speed is being increased further and then it can assume a critical value for the rolling stock from a resonance point of view. The motion is no longer harmonic due to presence of flange contact, but it has a zig-zag shape: the phenomenon is known as *hunting*.

Although many parameters come into play in the dynamic context, the influence of the wheel contact geometry is remarkable anyway. The choices in selecting the proper contact geometry for each application have to be made considering the stability requirements; nevertheless, the aspect of guidance must be carefully taken into account. The guidance of a bogie or a vehicle can be defined as the performance to follow the track, especially in negotiating curves; an enhancement of the performance in terms of guidance generally leads to an overall lower travelling resistance and lower wheel-rail contact forces. The real problem is that the choices in bogie design which generally improve the guidance performance usually make the stability conditions worse, and vice versa.

An exhaustive discussion of the stability of the restrained wheelset and the restrained bogie carried out mostly by means of linear models can be found in [13]; the influence of the most important parameters, such as the inertial characteristics, the stiffness and damping properties of primary suspensions as well as the linearised wheel-rail interaction are discussed in detail, highlighting the presence of a strong conflict between the guidance and the stability of the vehicle.

1.4 Rolling Radius Difference function (RRD)

The conical profiles were substituted for the better performing “worn profiles”, because the wear modifies quickly the shape of a conical wheel, with remarkable consequences on the overall performance of the wheel-rail matching. The worn profiles are instead conceived with a shape which is similar to the average shape caused by wear after a significant kilometrage has been covered; the ORE S1002 is surely the most used example of worn

profile adopted in Europe. The S1002 profile indeed, was created by taking the average of a relevant number of worn wheel profiles.

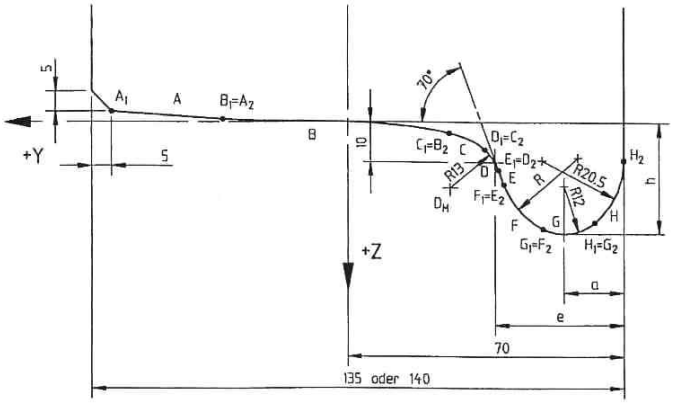

Figure 1.5. Detail of the ORE S1002 "worn" wheel profile.

Being a worn profile characterized by a hollow form, the radius rolling difference $r_1 - r_2$ between the left and the right side of the track (which in the following will sometimes be referred to as RRD) is a nonlinear function of the wheelset lateral displacement y, as it is shown in Fig. 1.6.

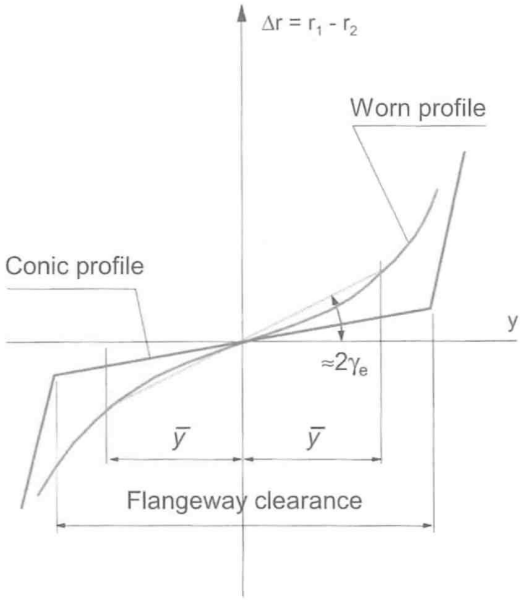

Figure 1.6. Radius rolling difference function for a conical and a worn profile; linearised slope of the latter for a given displacement $\bar{y}$.

The $r_1 - r_2 = \Delta r = f(y)$ function has a fundamental importance in railway dynamics. In fact, the derivative $\Delta r'$ with respect to y is a nonlinear function which expresses the actual conicity of the wheel-rail coupling for a given lateral displacement $\bar{y}$; for a conical profile the conicity is constant as long as the wheelset moves within the flangeway clearance without any flange contact. For nonlinear profiles, the definition of an *equivalent conicity* is

of practical utility:

$$\gamma_{eq} = \frac{r_1 - r_2}{2y}\,; \tag{1.3}$$

therefore it is defined as the linearised slope of the rolling radius difference for a displacement amplitude equal to $\bar{y}$ with respect to the centered position. Nevertheless, according to the relative European Standard [16], the equivalent conicity can be calculated by means of a few techniques, which can give slight different results. The equivalent conicity is often referred to as the value of the expression (1.3) for $\bar{y} = \pm 3\,\text{mm}$ [17], although this definition may be totally inappropriate, such as when the derivative of γ_{eq} is decreasing, as in the case a) of Fig. 1.7. The two conicity functions have the same value for a displacement amplitude of 3 mm, but the influence on the dynamic behaviour will be entirely different.

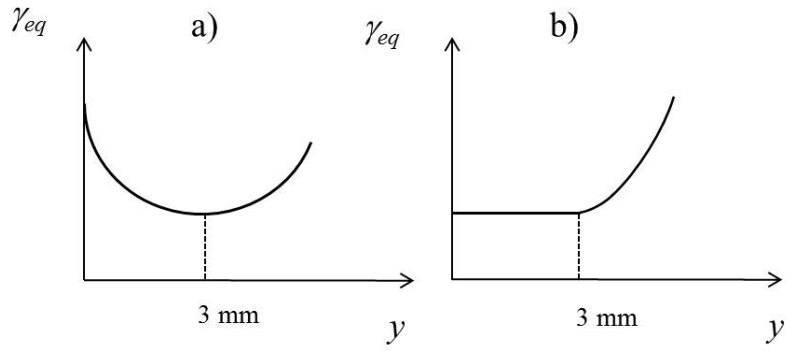

Figure 1.7. Two different equivalent conicity functions, having the same value for a displacement of 3 mm.

Another way widely used to define the equivalent conicity function is via numerical integration of the so-called harmonic linearisation:

$$\gamma(A) = \frac{1}{2\pi A}\int_0^{2\pi} \Delta r(A\sin\phi)\sin\phi\, d\phi\,, \tag{1.4}$$

where $\epsilon < A < y_{max}$ is the amplitude of the harmonic displacement being used in the linearisation [18].

In the comparison between a conical and a worn profile, besides the problem of the remarkable variation in the shape due to wear, the first one has the disadvantage that a considerable lateral movement of the wheelset causes two points of contact, with a consequent impact. As shown in Fig. 1.8, if the wheel and rail profiles are assumed to be circular in the contact location, a lateral displacement Δy of the wheelset with respect to the track will cause a translation of the contact point on the rail equal to:

$$\Delta s = \frac{\rho_{rail}}{\rho_{wheel} - \rho_{rail}}\Delta y\,, \tag{1.5}$$

while the change in rolling radius will be:

$$\Delta r = \gamma_0 \frac{\rho_{rail}}{\rho_{wheel} - \rho_{rail}} 2\Delta y = 2\gamma_{eq}\Delta y\,, \tag{1.6}$$

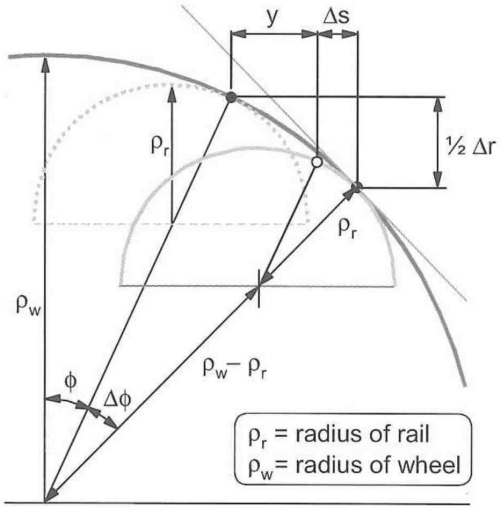

Figure 1.8. Displacement of the contact point on the rail caused by a wheelset displacement.

therefore, being the radius of the conical profile ρ_{wheel} infinitive, the displacement of the contact point on the rail is zero; as a consequence, the wear will be extremely concentrated on one point. If instead the radii of the wheel and rail are almost equal to each other, the contact points jumps for small lateral displacements of the axle, to the detriment of the ride comfort. The analysis of the Δr function can highlight the presence of jumps, as shown in the example of Fig. 1.9, concerning the S1002 profile matched with the UIC54 rail.

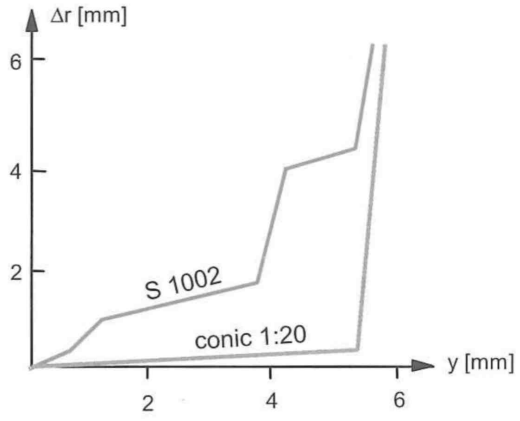

Figure 1.9. Theoretical Δr function for the S1002 wheel profile and the UIC54 rail (rail cant 1:40, gauge 1434 mm).

The nonlinear profiles also introduce an additional force between the wheelset and the track. When the wheelset is centered on the track and the wheel are rolling on equal radii, the contact planes are inclined to the horizontal at a small angle, as visible qualitatively in Fig. 1.10a. If the wheelset is displaced laterally, the contact occurs in new points and the

inclination of the contact plane changes; as shown in Fig. 1.10b, on one wheel the angle is increased while on the other one it is reduced. Since the normal forces between the wheelset and the rail are inclined to the vertical at the same angle, they cause a resultant lateral force which is proportional to lateral displacement. This restoring force is usually referred to as *gravitational stiffness* and its effect can be deduced by observing the first derivative $\Delta r'$ of the RRD function.

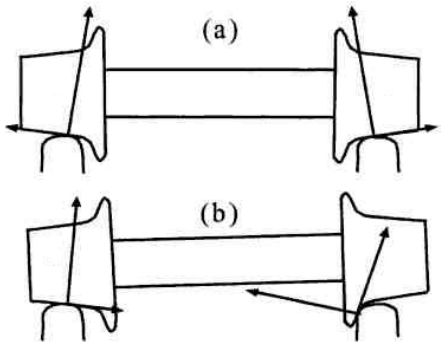

Figure 1.10. Gravitational stiffness effect: normal and lateral tangential forces acting on wheelset a) in central position, b) in laterally displaced position.

1.5 Contact angle on the flange

With respect to what has been presented up to this point, the RRD function and its first derivative synthesize effectively much information about the contact geometry in terms of difference of functions (relative to the right and the left side of the track). Nevertheless, in regarding to the flange of the profile, it is useful focus the attention on the effective inclination of the profile in this zone. As suggested by Fig. 1.5, the slope of the profile have a maximum due to the presence of a point of inflection, to which corresponds an angle of inclination to the horizontal of $70°$.

Generally, the value of the contact angle on the flange of a new profile must be chosen as a compromise between the safety against derailment and ride quality. The safety against derailment can be evaluated by Nadal's criterion [14, 19] and assuming that a wheel is in contact with the rail only on one point of the flange (Fig. 1.11):

$$\frac{Y}{Q} \leq \frac{\tan\alpha - \mu}{1 + \mu\tan\alpha} = \frac{Y}{Q}\text{lim}\,; \tag{1.7}$$

therefore, the flange angle α, the coefficient of friction μ and the vertical Q and lateral forces Y are involved in the wheel climb phenomenon. For this to happen, the Y/Q ratio of a wheel must be greater than the $Y/Q\,\text{lim}$, otherwise the wheel cannot remain lifted. Nevertheless, the condition (1.7) is necessary but not sufficient for having a derailment. Anyway, the Nadal's criterion shows that, the forces being equal, low flange angle and high friction coefficient tends to enhance the derailment risk since the $Y/Q\,\text{lim}$ becomes

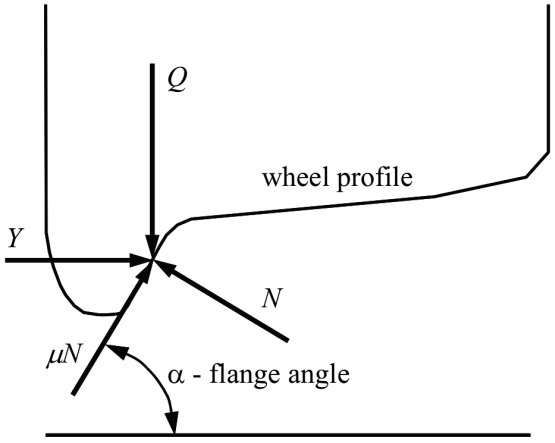

Figure 1.11. Equilibrium of forces in the flange contact.

lower.

In contrast, the flange angle cannot be too high to avoid a wheel-rail geometry with remarkable jumps in the RRD function for large wheelset displacements, which would also lead to bad performance from a ride quality point of view due to the presence of impact in curve entry. For this reason, the optimal value for the flange inclination fall in the range $65 - 75°$.

1.6 Worn wheel profiles

Considering what has been seen up to this point, the conicity of the wheel-rail contact should always fall in an optimal range, in order to satisfy both the steering and stability requirements. The equivalent conicity value depends on the wheel and rail profiles, the rail inclination and the gauge; in regards to this point, the Fig. 1.12 is useful to report the situation for the S1002 profile matched with the UIC60 rail. For all the considered rail inclinations, the equivalent conicity generally decreases as the gauge increases, whereas, for a given gauge, γ_{eq} becomes higher as the rail inclination decreases from 1:20 to 1:∞. The 0.1–0.4 is the optimal range for conicity: the stability limit is conventionally set equal to 0.4 while 0.1 is considered a steering limit. In fact, below the steering limit the conicity is insufficient to guarantee enough differential effect even in curve of large radius.

With regard to this point, to make a wheelset take a radial position with no slip in curve, the following condition has to satisfied (see Fig. 1.3):

$$\frac{r + \delta r}{r - \delta r} = \frac{R + s/2}{R - s/2}, \tag{1.8}$$

where $\delta r = \gamma y$ is the variation in rolling radius for each wheel due to the lateral displacement and not the RRD. The required δr for negotiating the curve without slip is therefore equal to:

$$\delta r = \frac{sr}{R}\,. \tag{1.9}$$

The required lateral displacement so that the pure rolling occurs is hence given by

$$y = \frac{rs}{2\gamma R}\,; \tag{1.10}$$

therefore the slip can be avoided if either the flangeway clearance or the radius curve are enough large. It also useful to note that, while the Δr function does not depend on the wheel radius, the required difference in rolling radius δr for pure rolling is instead proportional to the latter, thus, small diameter wheels are better for sharp curves from a steering point of view. On the contrary, large diameter wheels turn out to be better as regards the stability, as suggested by the Klingel's model, since the frequency of the kinematic oscillation tends to be lower as the wheel diameter increases.

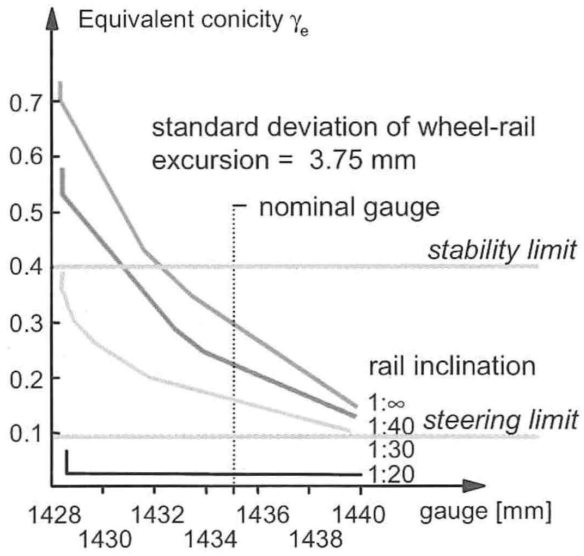

Figure 1.12. Equivalent conicity of the S1002 coupled with a UIC60 rail for different values of the track gauge and the rail cant.

It is interesting to observe that, while the performance of the matching between the S1002 profile and the UIC60 rail with an inclination of $1/40$ rad are good, the coupling of the same profiles with a $1/20$ rail cant (widely used in Italian railways) entails a very poor conicity that moreover does not depend on the gauge value.

With regard to wear, past researches reported have shown that in the matching S1002-UIC60 with a rail cant of $1/40$ rad over a period of time, the wheel profile tends to remain stable, with an equivalent conicity of 0.2–0.3, below the stability limit; at the same time, the rails tends to wear uniformly for gauge values between 1432 and 1436 mm. This behaviour is also intuitively confirmed by Fig. 1.13, in which the excursion of the contact point on the rail is reported as a function of the gauge and the rail inclination. On the contrary, as the Figs. 1.12 and 1.13 suggest, the principle of the worn profile does not work if the rail cant is equal to $1/20$ rad.

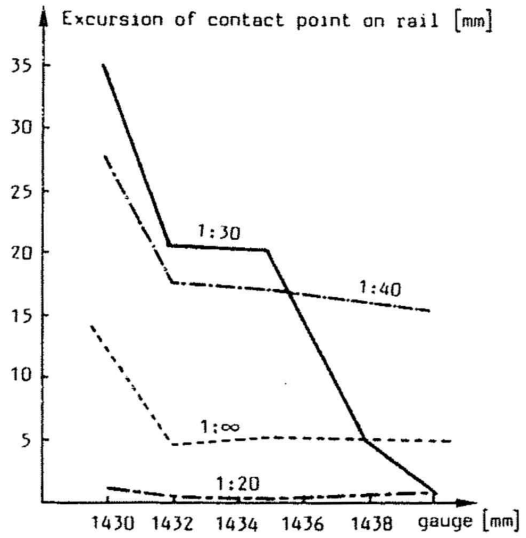

Figure 1.13. Contact point excursion on the rail for a S1002 matched with the UIC60.

The poor performance of this arrangement in terms of steering can also be highlighted by the contact geometry comparison peformed by means of SIMPACK [18] and summarized by Figs. 1.14 and 1.15. In both the figures the following quantities are reported as a function of the lateral displacement of the wheelset:

- the radius difference function;
- the equivalent conicity;
- the contact angle difference function, that is the difference between the inclination of the two tangent planes in the contact points;
- the distribution of the contact points between each wheel-rail pair;

the result have been obtained by setting the 1435 mm track gauge, an amplitude of the displacement equal to 10 mm and a wheelset yaw angle equal to zero. For the $1/20$ inclination the functions are almost zero as long as the lateral displacement is lower than the flangeway clearance and the contact point locations are greatly concentrated, especially on the rails. Conversely, the standard arrangement with a rail cant of $1/40$ rad is characterized by an almost constant equivalent conicity for displacement up to 6 mm and moreover, the contact points move more both on the wheel and the rail.

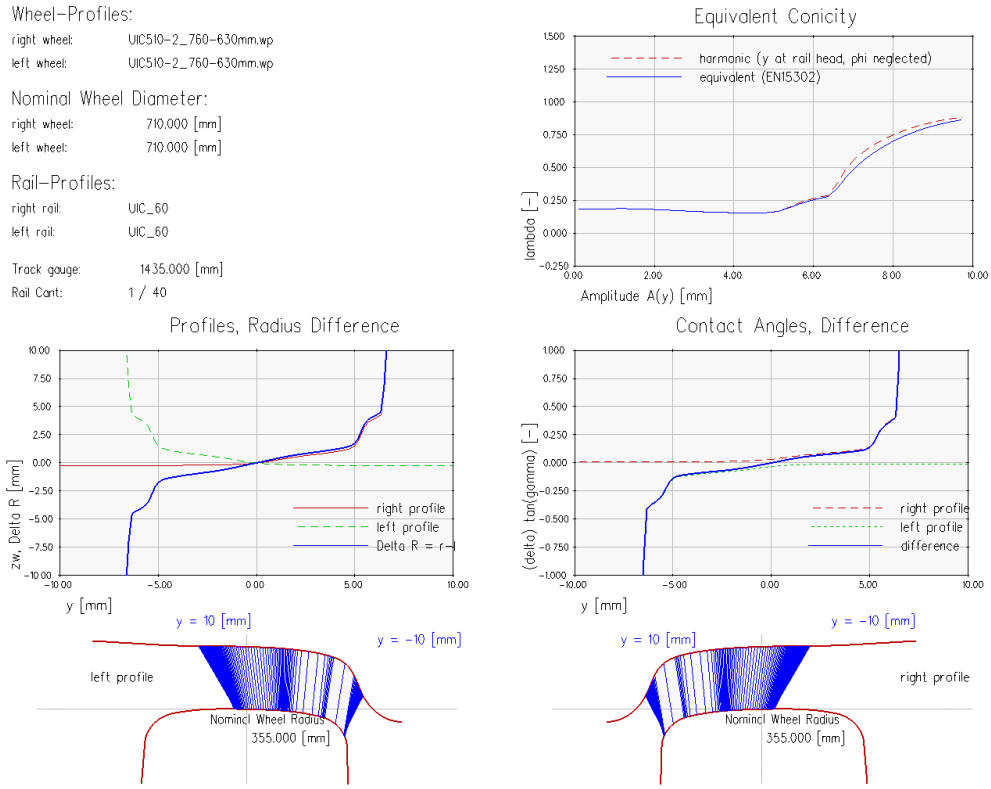

Figure 1.14. Contact geometry of the S1002 profile matched with the 1/40 UIC60 rail.

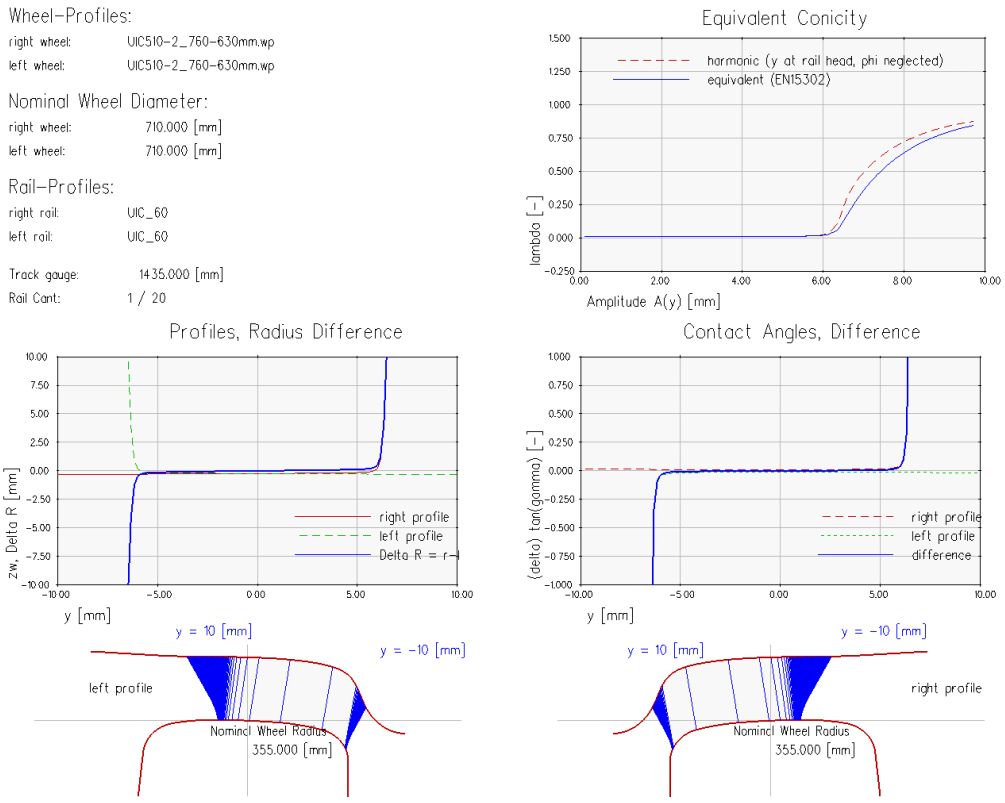

Figure 1.15. Contact geometry of the S1002 profile matched with the 1/20 UIC60 rail.

CHAPTER 2

General Architecture of the Model

The approach to deal with the wear analysis via numerical simulations which have been chosen in this research activity envisages the use of different software and subprograms which mutually interact during the whole procedure. The general layout of the working architecture was arranged in agreement with the project partners Trenitalia S.p.A and Rete Ferroviaria Italiana, according to the following main working hypotheses:

- the wear evolution is treated with a discrete approach, by dividing the mileage to be simulated in spatial steps and by updating the wheel profile only after each step has been completed. Thus the change in wheel profile takes place only when a certain distance has been covered and not during the simulations.
- the track is not subjected to wear and the rails have time-independent profiles, which can be either new or worn. Although the model used in this work is capable to reproduce even the variation in shape of rails, this ability has not been exploited since the research project aimed at evaluating the evolution of wheel profiles only. However, since the wheel wear and the rail wear have two different temporal scales, the two phenomena should be analyzed separately, by allowing the wheel shape varies and letting the rail remain constant, or vice versa;
- the amount and the distribution of wear is evaluated by means of an experimental law [2, 20], mainly based on the adhesion wear;
- in the dynamic simulations each vehicle wheel has always the same profile; the output of the wear model is a mean wheel profile to be used in the next step, obtained by including the effects of wear on all the vehicle wheels during the simulation.
- the wheel-rail contact is supposed to be under dry conditions.

The first important aspect is hence the discretisation of the numerical procedure. The whole kilometrage to be investigated is divided in a few spatial steps within which the wheel profile is maintained constant. After completing the simulation of the current step, a wear analysis is performed to allow the update of the wheel profile for the next step

of the procedure. Obviously the presence of a loop to be repeated several times is surely one of the most important aspect of the procedure because it introduces a discretisation error dependent of the step length, which directly affects the results. Concerning this, the choice of the step length, which depends on the total simulation distance and the required precision, has to be done as a compromise between accuracy and computational time: the shorter the step length, the higher the precision and the elapsed real time.

As can be discussed in Sec. 4.2, the step length can also be chosen constant throughout the entire mileage or variable according to a certain criterion, such as a threshold on the amount of the local removed material. When the kilometrage to be simulated is short, the constant step length is an optimal choice, providing comparable results in terms of accuracy and better performance in terms of numerical efficiency. Differently, the variable step is suitable for longer analysis, with a considerable amount of wear, to speed up the procedure.

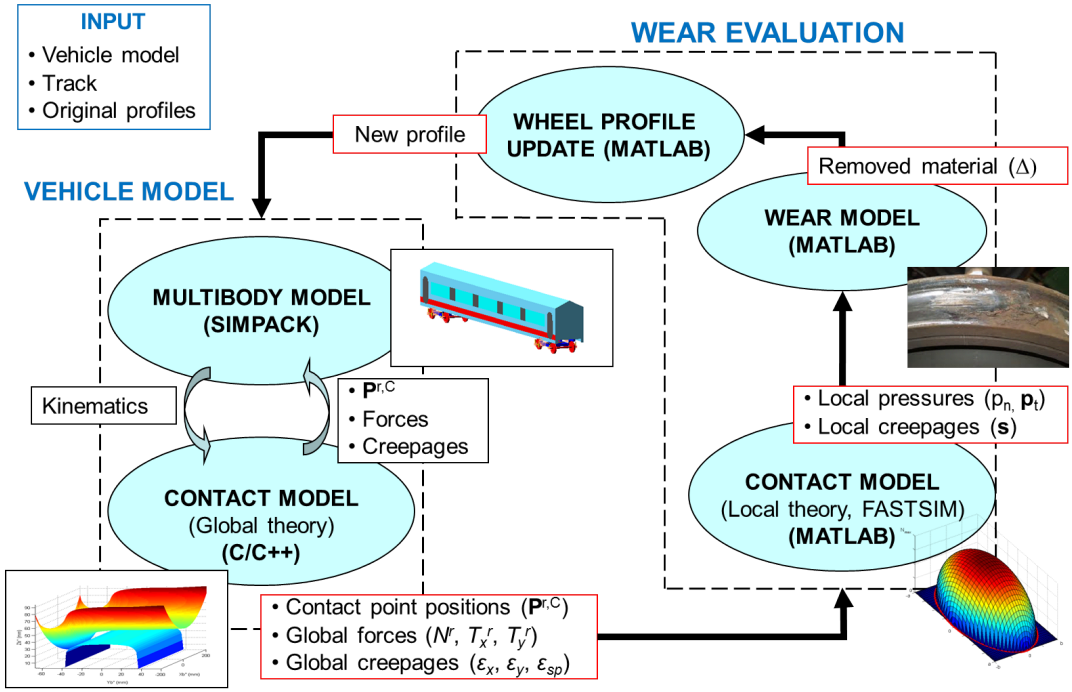

Figure 2.1. General architecture of the model.

However, the most important issue which involves the computation time is the intrinsic timescale of the physical problem. In fact, the wheel wear in railway applications is a phenomenon which requires at least tens of thousand kilometers (but even hundreds of thousands in the most cases) to express its effects and consequently the simulated distances cannot be as long as the real ones to be investigated, because they would require unacceptable computational times, even if the whole track has been divided into discrete steps.

That is generally true even adopting a simpler dynamic model for the vehicle, which would also not guarantee the same accuracy. This issue can be overcome by hypothesizing a proportionality between the wear relative to a single discrete step and the amount of wear

relative to the distance really simulated by means of the numerical multibody model (that is the two wear rates are the same); this hypothesis is reasonable only if the numerically simulated track is a significant representation, in statistical terms, of the track associated to the discrete spatial step.

In regarding to the general architecture of the whole model, a block representation is visible in Fig. 2.1. It can be seen that it consists of two main parts that work alternatively during each procedure step: on the left there is the *vehicle model* block, the part responsible for the dynamic simulations; on the right there is the *wear evaluation* block. The first one comprises the multibody model and the *global contact model*, which interact online to each other during the simulations to reproduce the whole vehicle dynamics on the track. The second part comprises three sub-parts instead: the *local contact model*, the *wear model* and the *wheel profile update*.

Going into detail, the simulations represents the first task of each procedure step in which the multibody model implemented in the SIMPACK™ environment exchanges data continuously at each integration time step with the global contact model [21, 22, 23]. The latter implements in details the whole wheel-rail interaction (the track and the contact forces) while the SIMPACK model is an accurate description of the vehicle dynamics except for the wheel-rail contact.

During the multibody simulation, SIMPACK passes continuously the wheelset kinematic variables (wheelset position and orientation and their derivatives) and receives the positions of the contact points, the wheel-rail contact forces and the global kinematic creepages from the global contact. The global contact model is hence a user subroutine written in C/C++ language which acts in place of the standard SIMPACK's routines developed for the wheel-rail contact.

Once the multibody simulations are completed, the output results relative to the global contact variables (that is the variable relative to each contact patch: contact point positions $\mathbf{P}_c^r$, normal, longitudinal and transversal forces N, T_x, T_y, global creepages ϵ_x, ϵ_y, ϵ_{sp}) are passed to the local contact model. This sub-program is an external routine written in the MATLAB™ environment and based on the FASTSIM algorithm [15] which calculates the distribution of the local contact variable within each contact patch: contact pressures, local creepages and consequently the total frictional work ($\mathbf{p}_t$, p_n, $\mathbf{s}$, L_F respectively).

The wear model exploits these data in order to calculate the amount of the removed material and its distribution along the wheel profile by means of the experimentally proven law [2, 3, 20]. After completing these operations, the wheel profile is updated through suitable numerical procedures and the whole model is generated in order to perform the multibody simulations of the next procedure step.

With regard to the evolution of the wheel wear, the problem can be approached in different manners, depending on the goals of the study. If the aim is the analysis of the phenomenon on a single track of reasonable length, the methodology can be applied as described above, while if the track is too long to carry out accurate simulations within reasonable time, or if the study must be conduct on a complex railway line with many vehicles

in service, a statistical approach turns out to be necessary to achieve general significant results. If applied, the statistical approach entails more than one multibody simulation for each procedure step: as it will be discussed successively in Sec. 4.2, the considered railway track, or the complex railway net can be substituted with an equivalent set of different curved tracks having opportune characteristics, such as radius, superelevation and travelling speed. Such kind of approach has been exploited a few times during this work, during both the model validation on the Aosta-Pre Saint Didier track (Sec. 5.3) and the subsequent wear simulations on the Italian mean lines (Sec. 5.2). Therefore, simulations have not been performed on the real railway lines, but they have been carried out on a equivalent representation of this railway net, derived by consulting detailed track database provided by Rete Ferroviaria Italia.

CHAPTER 3

Vehicle Models

The following chapter deals with the building of the vehicle models to be used in the multibody simulations. As hinted in the description of the general architecture (Sec. 2), the vehicle model in this work can be usefully considered made up of the multibody part which includes all the significant elements of the real railway vehicle and of the global contact model, through which the track and the wheel-rail interaction are implemented. In the first part of the chapter, the most significant characteristics of the SIMPACK multibody models will be described briefly without getting down to the modelling details; in the second part, the analytic description of global contact model will be accurately presented.

3.1 The multibody models

In the present research the multibody approach [24] have been chosen in order to simplify the handling of complex mechanical systems such as the railway vehicles without introducing significant simplifications. In fact, in the multibody approach a generic mechanical system is being implemented as a lumped parameter model, mainly made up of rigid or elastic bodies interconnected via force elements and constraints which can reproduce the dynamics behaviour for large displacements, taking into account all the relevant nonlinearities as well.

In the present research three different vehicles have been modelled in the SIMPACK environment to perform dynamic simulations aimed at wear assessment with different wheel profiles. The three considered vehicles are the following:

- ALn 501 Minuetto;
- Vivalto coach;
- E464 locomotive.

The analyses have been carried out with the ALn 501 and with a composition of the Vivalto coach pulled by a E464 locomotive. All the three multibody models have been built by consulting the technical documentation provided by Trenitalia [25], hence the models are

a close representation of the real vehicles. Since structural analysis and response at high frequency were not of interest in this work, all the bodies have been introduced in the models as rigid.

The E464-Vivalto composition have been assembled taking into account the geometrical and stiffness properties of buffers and drawgear. Further detail about the multibody modelling and simulation through SIMPACK can be found in [18].

3.1.1 Minuetto multibody model

The first railway vehicle on which this study has been performed is the ALn 501 "Minuetto" (Fig. 3.1), a blocked composition train produced by Alstom S. A. widely used on the Italian Railways for passenger transport. It is a diesel multiple unit (DMU) made up of three coaches and four bogies with two wheelsets each; the external bogies are motorized (Fig. 3.2) whereas the two intermediate trailer bogies are of Jacobs type, shared between two coaches (Fig. 3.3a). The main characteristics of the Aln 501 are summarized in Tab. 3.1.

Figure 3.1. Aln 501 Minuetto.

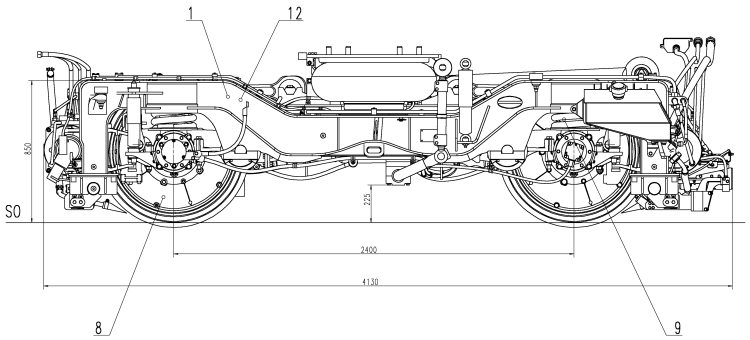

Figure 3.2. Motor bogie of the Minuetto.

Like the most part of passenger trains, the bogies are equipped with two stages of suspensions to fulfill the different requirements of dynamic behaviour and passenger comfort. The primary suspensions, which link the axleboxes to the bogie frame, are constituted by Flexicoil springs (Fig. 3.4), made up of two coaxial springs, which mainly provide the vertical stiffness. The Flexicoil element have also a significant stiffness in the radial direction,

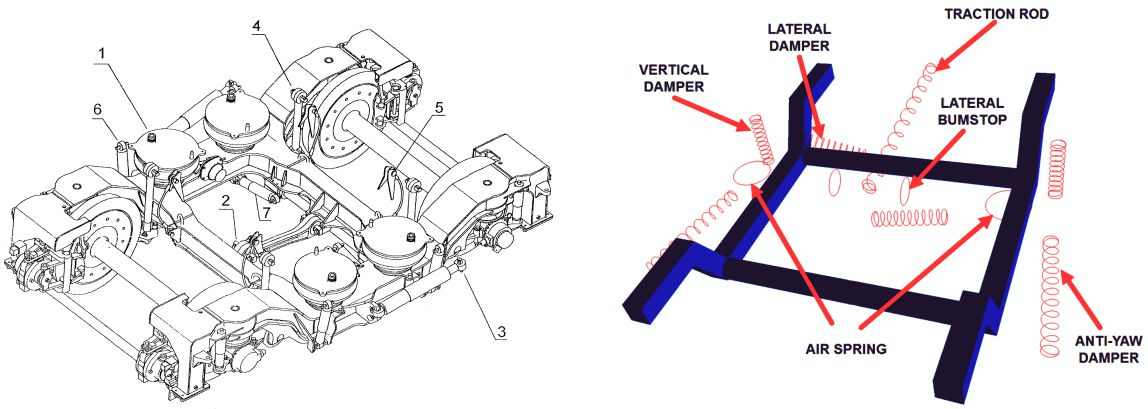

(a) (b)

Figure 3.3. Jacobs bogie: isometric view a); the multibody model b).

Table 3.1. Main characteristics of the Aln 501 Minuetto DMU.

Length	51.9 m
Width	2.95 m
Height	3.82 m
Bogie pivot distances	14.8-13.8-14.8 m
Bogie wheelbase	2.80 m
Unladen weight	100 t
Wheel arrangement	Bo-2-2-Bo
Wheel diameter	850 mm
Max speed	130 km/h

thanks to the rubber edge which encloses the external coils of the two springs. Nevertheless, since the stability against hunting at high speed in straight tracks requires higher longitudinal and lateral stiffnesses than those provided by these springs, the most part of the longitudinal stiffness is entrusted to a linking arm which connects the axlebox with the frame, while a suitable lateral stiffness is provided by a bushing element (Sutuco). A nonlinear damper is responsible for the damping of the vertical relative displacements while there are no dedicated damping elements for the lateral and longitudinal directions.

The secondary suspension stage comprises the following elements:

- two airsprings (four in the Jacobs bogie);
- a nonlinear longitudinal rod;
- a torsion bar;
- nonlinear lateral bumpstops;
- nonlinear lateral dampers;
- nonlinear vertical dampers;

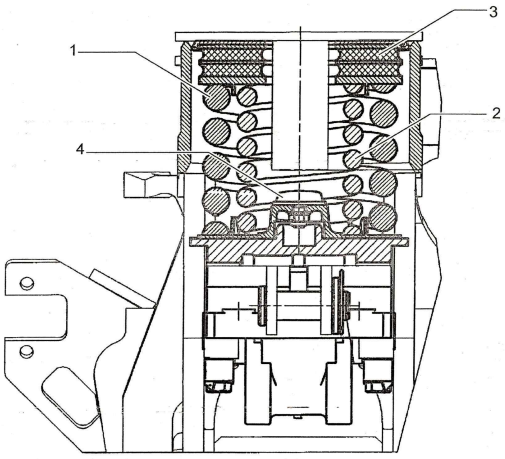

Figure 3.4. Flexicoil primary suspension: (1) external spring, (2) internal spring, (3) rubber wedge, (4) bumpstop.

- nonlinear anti-yaw dampers.

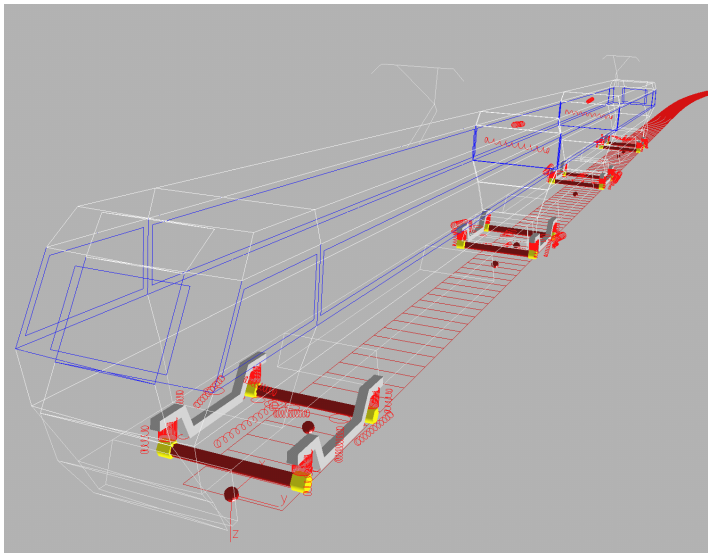

Figure 3.5. Aln 501 Minuetto multibody model.

Airsprings are widely used in the secondary suspensions of low-floor trains because besides the passengers' comfort, they also provide a simple automatic regulation of the coaches height which allow the coach floor to remain at the curb height whatever the vertical load in the spring is. However, since the airsprings provide a correct stiffness in the vertical direction but a too low stiffness for the longitudinal and lateral forces to be balanced, other force elements have to be included in this stage. The longitudinal rods provide the longitudinal stiffness, whereas the lateral relative displacements are bounded by lateral bumpstops; the correct rolling stiffness is achieved with the torsion bar. All the dampers are viscous.

The connection between two coaches consists of a stiffness element and a nonlin-

ear damper that attenuates the relative lateral and roll motions. The resultant SIMPACK multibody model, shown in Fig. 3.5, includes 31 rigid bodies: 3 coaches, 4 bogie frames, 8 wheelsets and 16 axleboxes. The most significant inertial properties of the model bodies and the vertical position of the centres of mass with respect to the top of rail are summarized in Tab. 3.2.

Table 3.2. Aln 501 Minuetto main inertial properties.

	Mass kg	I_{xx} kg m^2	I_{yy} kg m^2	I_{zz} kg m^2	z_{CoG} m
External coach	31568	66700	764000	743000	-1.91
Internal coach	14496	30600	245000	236000	-1.98
Motor bogie frame	3306	1578	2772	4200	-0.5
Trailer bogie frame	3122	1647	3453	5011	-0.5
Wheelset	2091	1073	120	1073	-0.425

All the kinematic constraints and the force elements (Fig. 3.3b) have been modeled as viscoelastic force elements, taking into account all the mechanical non linearities (clearance of bumpstops, dampers characteristics and variable stiffnesses of traction rods) [19, 26]. In this regard, the main linear characteristics of the suspensions are summarized in Tab. 3.3; in addition, two examples of nonlinear behavior of dampers of both stages of suspensions are shown in Fig. 3.6.

Table 3.3. Main linear stiffness properties of the ALn 501 "Minuetto".

Primary suspension	Flexicoil k_z	$9.01 \cdot 10^5$ N/m
	Flexicoil k_x, k_y	$1.26 \cdot 10^6$ N/m
	Sutuco bushing k_x	$2.0 \cdot 10^7$ N/m
	Sutuco bushing k_y	$1.5 \cdot 10^7$ N/m
Secondary suspension	Airspring k_z	$3.98 \cdot 10^5$ N/m
	Airspring k_x, k_y	$1.2 \cdot 10^5$ N/m
	Anti-roll bar k_α	$2.6 \cdot 10^6$ Nm/rad
Coach connection	Bushing k_x, k_z	$7.24 \cdot 10^7$ N/m
	Bushing k_y	$5.2 \cdot 10^6$ N/m

In conclusion, the whole ALn 501 model, including the wheelsets with their inertia properties, has been implemented in the SIMPACK environment except for the wheel-rail forces, which are entrusted to the global contact model.

3.1.2 The Vivalto coach multibody model

The Vivalto is a two-floor coach widely used in Italy for the regional passenger transport, produced by the Corifer consortium. "Vivalto" is also the name of the typical train composition (Fig. 3.7) in which this coach is employed, made up of five coaches hauled by

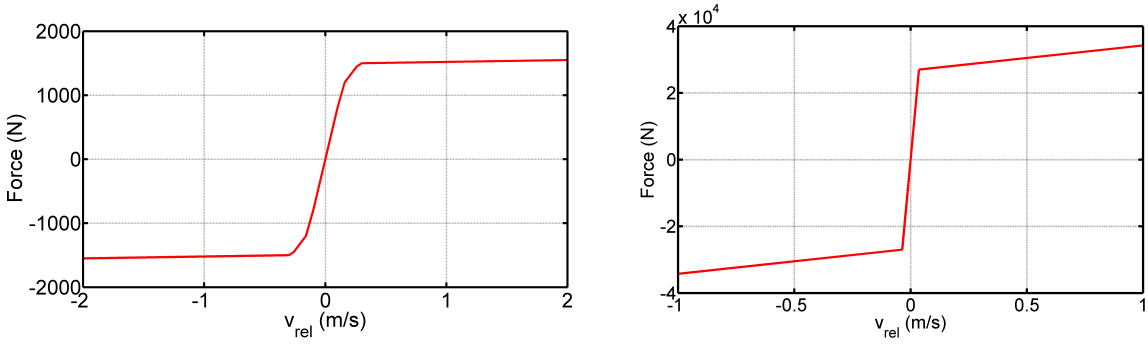

(a) Vertical damper of the primary suspension.

(b) Anti-yaw damper of the secondary suspension.

Figure 3.6. Examples of nonlinear characteristic of dampers.

a electrical E464 locomotive. The main general characteristics of the coach are summarized in Tab. 3.4.

Figure 3.7. Vivalto train composition.

The coach is equipped with two SF400 bogies produced by Siemens; a isometric view of the resultant multibody model of this bogie is shown in Fig. 3.8. The most significant properties of the whole SIMPACK multibody model are sum up in Tab.3.5.

As regards the primary suspensions, each axlebox have two slots which house a pair of coil springs and two sheaths where the device responsible for the transmission of longitudinal and lateral forces is inserted. This device has two pins attached to the bogie frame; each of these two pins is coaxial with respect to the coil spring and transmits the forces by means of rubber cylindrical element conveniently patterned. The vertical relative displacements are allowed through an adapter sleeve which can slide with respect to the internal surface, while it is fixed to the external cylindrical surface of the rubber elements. The solution allows the vertical forces to be exchanged between the coil springs and the bogie frame without the involvement of the adapter sleeves; the tractive, braking and lateral forces are instead transmitted by means of the rubber elements. These rubber elements are not axisymmetrical in order to provide different stiffness values in the lateral and longitudinal direction.

Table 3.4. Main characteristics of the Vivalto coach.

Length	26.1 m
Width	2.72 m
Height	4.30 m
Bogie pivot distances	20.0 m
Bogie wheelbase	2.50 m
Wheel diameter	920 mm
Unladen weight	50 t
Max speed	160 km/h

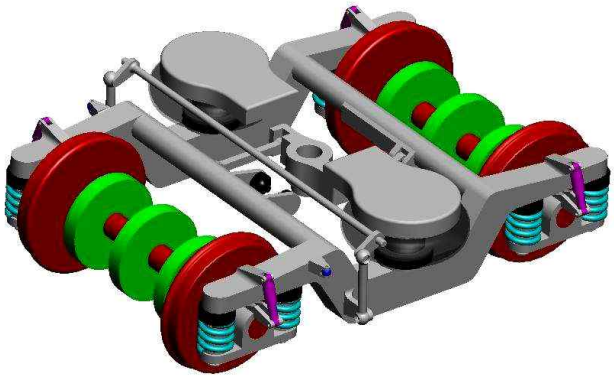

Figure 3.8. Multibody model of the SF400 bogie.

The equivalent vertical stiffness of the primary suspension is given by the serial combination of the coil spring and a rubber element, while the vertical damping is provided by a damper, whose characteristics is almost linear. The stiffness and damping properties of the primary suspension stage are summarized in Tab. 3.6.

Like the Minuetto, the vertical stiffness of the secondary suspension is provided with airsprings in order to guarantee a constant height of the coach floor with respect to the top of rail, since in the full load condition the mass of coach is increased of 16 t. Given the unsatisfactory stiffness in the lateral and longitudinal directions, other elements are required to complete the arrangement of the secondary suspension. The longitudinal tractive and braking forces between the bogies and the coach are transmitted through a system made up of a central pin for each bogie fixed to the coach; two rods and a rocker arm constitute a common "zeta" connection which constrain the pin to the bogie. In regard to the lateral displacements, they are limited by lateral bumpstops after a stroke of 20 mm and are damped by the two viscous dampers which are fixed on one side to the rocker arm and on the other side to the internal flanges of the bogie. A sufficient amount of roll stiffness is provided by the torsion bar, while in this version of the bogie the anti-yaw dampers are not present. The most interesting stiffness and damping characteristics of the secondary suspension stage are again reported in Tab. 3.6.

Even for the Vivalto, all the kinematic constraints and the force elements have been

Table 3.5. Inertial properties of the Vivalto coach.

	Mass kg	I_{xx} kg m^2	I_{yy} kg m^2	I_{zz} kg m^2	z_{CoG} m
Car body	50935	128120	2911000	2811000	-1.6
Bogie frame	2470	1890	2014	3737	-0.57
Wheelset	1410	866	101	866	-0.46

Table 3.6. Main stiffness and damping properties of the SF400 bogie.

Primary suspension	k_x	$5.50 \cdot 10^6$ N/m
	k_y	$2.43 \cdot 10^7$ N/m
	k_z	$5.0 \cdot 10^6$ N/m
	c_x	$1.2 \cdot 10^4$ Ns/m
	c_y	$9.0 \cdot 10^3$ Ns/m
	c_z	$2.0 \cdot 10^3$ Ns/m
Secondary suspension	k_x	$1.40 \cdot 10^5$ N/m
	k_y	$1.40 \cdot 10^5$ N/m
	k_z	$2.80 \cdot 10^5$ N/m
	c_x	$8.40 \cdot 10^2$ Ns/m
	c_y	$8.40 \cdot 10^2$ Ns/m
	c_z	$2.50 \cdot 10^4$ Ns/m
	Anti-roll bar k_α	$9.74 \cdot 10^5$ Nm/rad
	Anti-roll bar c_α	$1.0 \cdot 10^2$ Nm/rad

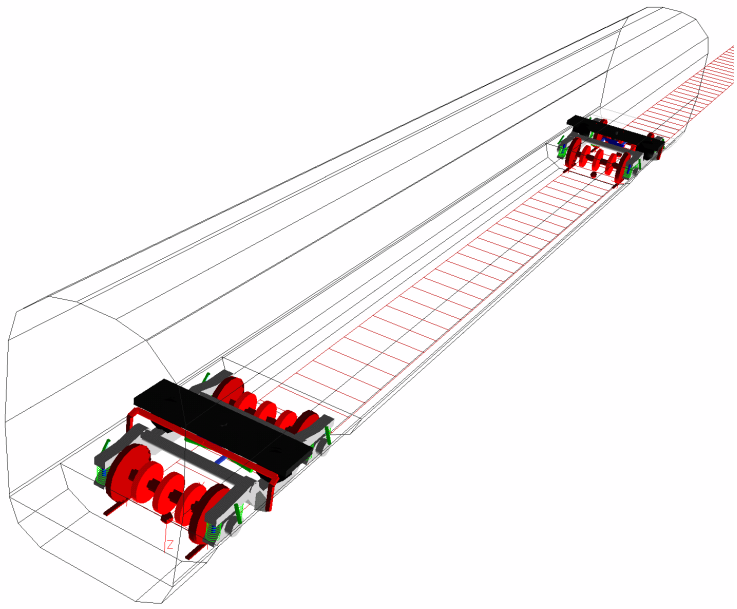

Figure 3.9. Multibody model of the Vivalto coach.

modelled as viscoelastic force elements, taking into account all the possible non linearities.

3.1.3 The E464 multibody model

The E464 is a light locomotive typically used as a traction unit in trains which operate for logistic reasons as blocked composition convoys without being such. An image of the whole multibody model is shown in Fig. 3.10.

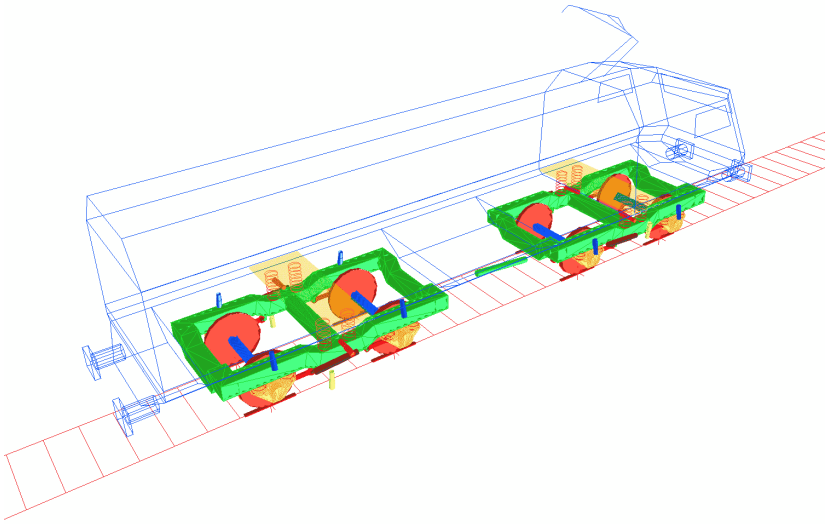

Figure 3.10. Multibody model of the E464 locomotive.

The principal characteristics of this vehicle are presented in Tab. 3.7.

Table 3.7. Main characteristics of the E464 locomotive.

Length	15.75 m
Width	3.106 m
Height	4.279 m
Bogie pivot distances	7.54 m
Bogie wheelbase	2.65 m
Unladen weight	72 t
Wheel arrangement	Bo'Bo'
Wheel diameter	1100 mm
Max tractive effort	200 kN
Max speed	160 km/h

As regards the vehicle structure, the E464 have two bogies characterized by standard technical arrangements such as two independent motorized axles, hollow-shaft elastic transmission and traction bars in low position (Fig. 3.11).

In the primary suspension arrangement, a SKF rocking axlebox is constrained to the bogie by means of two coil springs housed in two seats of the axlebox itself and through a linking arm, which is attached to the frame and the axlebox by means of two bushings.

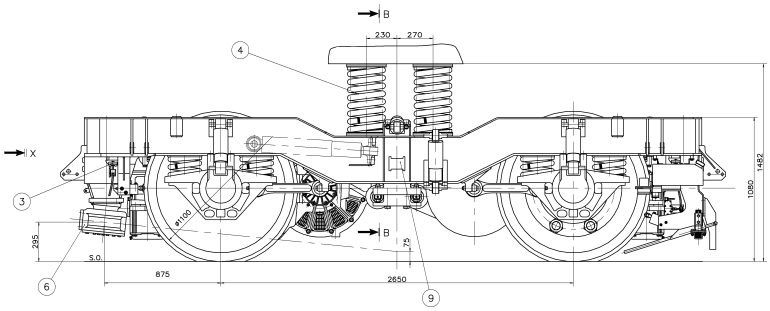

Figure 3.11. Lateral view of the E464 bogie.

The stiffness in the relative vertical displacements is provided by the coil springs, while the higher longitudinal and lateral stiffnesses are due to the linking arm and the rubber elements.

Table 3.8. Main stiffness properties of the E464 bogie.

Primary suspension	Axlebox-frame link	k_{ax}	$1.2 \cdot 10^7$ N/m
		k_{rad}	$8.5 \cdot 10^7$ N/m
		k_{tors}	$1.80 \cdot 10^3$ Nm/rad
	Coil spring	k_x	$1.73 \cdot 10^6$ N/m
		k_y	$1.73 \cdot 10^6$ N/m
		k_z	$8.52 \cdot 10^5$ N/m
		k_α	$2.0 \cdot 10^6$ Nm/rad
		k_β	$2.0 \cdot 10^6$ Nm/rad
		k_γ	$2.0 \cdot 10^6$ Nm/rad
Secondary suspension	Coil spring	k_x	$8.43 \cdot 10^4$ N/m
		k_y	$8.43 \cdot 10^4$ N/m
		k_z	$2.84 \cdot 10^5$ N/m
		c_x	$2.0 \cdot 10^6$ Nm/rad
		c_y	$2.0 \cdot 10^6$ Nm/rad
		c_z	$2.0 \cdot 10^6$ Nm/rad
	Traction rod	k_x	$1.0 \cdot 10^7$ N/m

The secondary suspension stage is first of all made up of four coil springs for each bogie and three nonlinear dampers, which provide the damping for vertical and the lateral displacement as well as for the yaw rotation. The coach is leaned on the four springs of the bogie without any intermediate beam. The longitudinal forces, as previously mentioned, are transmitted through the traction bars in low position to reduce the vertical load transfers between the axles of a bogie; the bars are attached to the bogie and the coach by means of rubber elements.

The principal inertia properties of the vehicle included in the model are reported in Tab. 3.9.

Table 3.9. Main inertial properties of the E464.

	Mass kg	I_{xx} kg m^2	I_{yy} kg m^2	I_{zz} kg m^2	z_{CoG} m
Coach	43000	61000	524700	524300	-2.1
Bogie frame	10605	1735	6670	8224	-0.29
Wheelset	1599	954	220	954	-0.55

3.2 The global contact model

The wheel-rail contact interaction is surely of the most important and interesting aspects in the numerical simulation of railways vehicle dynamics. Depending on the aims of the study and the required accuracy, the problem can be approached in different manners; in any case an efficient numerical procedure to handle the problem is of fundamental importance to avoid unacceptable computational times. In fact, usually the wheel-rail contact model is the most time-consuming part of the multibody model of a railway vehicle and an optimised algorithm could speed-up the simulations significantly.

First of all, the formulation of a solving procedure can be developed considering two distinct aspects of the problem: the research of contact points and the calculation of forces. The localization and the number of contact points has a great influence on the intensities and the directions of forces and moments, so it is as important as the second task. With regard to the research of contact point, several authors have dealt with the wheel-rail contact modelling, thus many procedures for the detection are available in literature. Typically, two different approaches can be used:

- The *constraint or rigid approach*, based on nonlinear kinematic contact constraint equations. The contact surfaces are represented in a parametric form using the differential geometry methods and the contact points are detected during the dynamic simulation by solving the nonlinear algebraic-differential equations associated to the constrained multibody system. Each wheel has only five degrees of freedom with respect to the rail, and no penetration and lift between the two bodies are allowed [27, 28, 29, 30].

- The *elastic approach* in which the wheelset is a rigid body with six degrees of freedom with respect to the rails. The local deformation of the contact surface at the contact point is taken into account. This type of approach allows the separation between the wheel and the rail and to manage multiple contact points as well. The idea is to minimize the distance between the wheel and rail surfaces, often by introducing further hypotheses on the position of the contact points in order to simplify the geometry of the problem [31, 32, 33, 19].

Both the approaches are widely used in commercial multibody software which include a railway vehicle environment, such as SIMPACK. In the constraint method, the normal forces to the surfaces are calculated as the Lagrange multipliers that, together with the

system generalized coordinates and the surface parameter time derivatives, constitute the unknown vector of the differential algebraic equation system which describes the vehicle dynamics. Differently, in the elastic approach, the normal component of the contact force is evaluated as a function of the penetration between the surfaces according to the Hertz's theory or alternatively by means of stiffness and damping coefficients. The calculation of the tangential components of the contact force (the creep forces) can be done making reference to different theories available in literature [15, 14].

In this work the contact point positions are evaluated by means of a innovative semi-analytical procedure [21, 22, 23]. The normal contact forces calculation is based on the Hertz's theory, while for the creep forces the Kalker's global theory is adopted [15].

The global contact model permits to perform an *online* calculation of the contact forces at the wheel-rail interface during the multibody simulations. Online means that the contact points are detected analytically during the simulations without any pre-calculated kinematic contact table [34]. The latter is a useful tool widely used in commercial multibody program [18, 33] to speed-up the simulations by avoiding an analytic research of the contact point at each integration step, which is substituted by a simpler look-up table interpolation. This strategy is advantageous especially when high accuracy in the resolution of the contact problem is not required, though detailed contact table can be easily calculated; nevertheless, due to the need to analyse the behaviour of vehicle in sharp curves, in this activity an online calculation has been reckoned better than the pre-calculated table.

By exploiting the new global contact model, at each time step, SIMPACK passes the kinematic data (wheelset position and orientation and their derivatives) to the global contact model, which evaluates the interaction forces to be applied to the wheels in the simulations. In the following sections the contact model will be described in detail.

3.2.1 Analytical formulation of the problem

This section is to explain the mathematical notations and the reference systems adopted in the formulation of problem. First of all, a right-handed *fixed reference system* $O_f x_f y_f z_f$ is introduced with the x_f axis tangent to the track centerline in the point O_f and the positive z_f axis normal to the plane of the rails and pointing up. The railway track can be expressed as a three-dimensional curve $\boldsymbol{\gamma}(s)$ in the fixed global system (Fig. 3.12):

$$\boldsymbol{\gamma}(s) : I \subset \mathbb{R} \rightarrow \mathbb{R}^3 \,, \tag{3.1}$$

where s is the curvilinear abscissa of $\boldsymbol{\gamma}$. As visible in the same figure, the curve $\tilde{\gamma}(s')$ is also defined as the projection of $\boldsymbol{\gamma}$ in the $x_f y_f$ plane. In fact, the track description is usually given in terms of curvature $K(s')$ and slope $p(s')$. The curve $\tilde{\boldsymbol{\gamma}}(s')$ can be determined by integrating the Frenet's equations:

$$\frac{\mathrm{d}\mathbf{t}}{\mathrm{d}s'} = K(s')\mathbf{n}(s') \,, \quad \frac{\mathrm{d}\mathbf{n}}{\mathrm{d}s'} = -K(s')\mathbf{t}(s') \,, \tag{3.2}$$

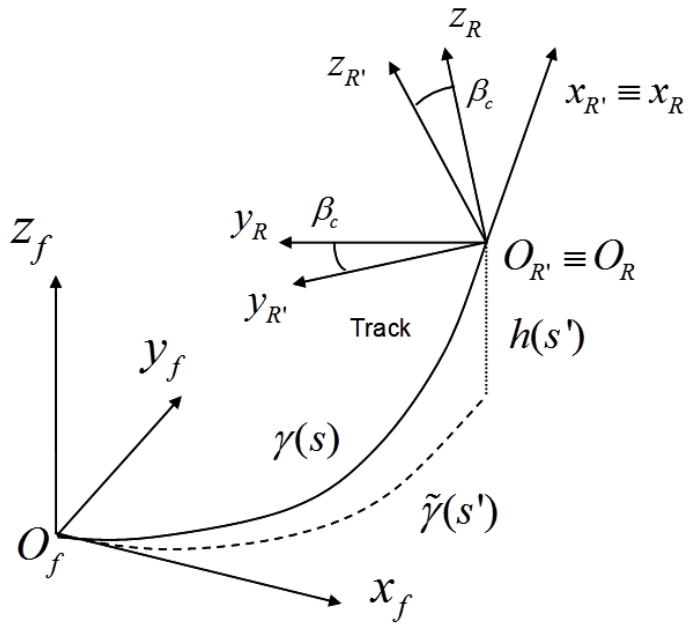

Figure 3.12. Fixed and auxiliary reference systems.

considering that $\mathbf{t}(s') = \tilde{\gamma}(s')/\mathrm{d}s'$ where $\mathbf{t}$ and $\mathbf{n}$ are respectively the tangent and the normal unitary vectors whose initial conditions are respectively $\mathbf{t}(0) = [1,0]^T$, $\mathbf{n}(0) = [0,1]^T$, since $\mathbf{t}$ is tangent to the x_f axis. The third component γ_z of $\boldsymbol{\gamma}$ is instead given by integrating the track slope.

Finally, the expression of $\gamma(s)$ can be established through a relation between s and s':

$$s(s') = \int_0^{s'} \left\| \frac{\mathrm{d}\tilde{\gamma}(t)}{\mathrm{d}t} \right\| \mathrm{d}t = \int_0^{s'} \left\| \begin{pmatrix} \mathbf{t} \\ p(t) \end{pmatrix} \right\| \mathrm{d}t = \int_0^{s'} \sqrt{1 + p(t)^2}\, \mathrm{d}t\,, \tag{3.3}$$

which can be numerically inverted.

A second reference system, the *auxiliary refence system* $O_b x_b y_b z_b$ is defined as shown in Figs. 3.12 and 3.13. The origin of this system, which is not fixed to any body, moves along the track just below the rail surfaces rolling plane, following the wheelset, with the x_b axis tangent to the centreline in the point O_b and the z_b axis normal to the plane of the rails. The position of the origin O_b (whose coordinates in the fixed reference system are indicated by $\mathbf{o}_b^f$) can be deduced from the wheelset centre of mass position G (whose coordinates in the fixed reference system are indicated by $\mathbf{o}_r^f$) by imposing a condition that is equivalent to state that the plane yz contains the point G (Eq. 3.4):

$$(\mathbf{o}_w^f - \mathbf{o}_r^f) \cdot \mathbf{i}_b = (\mathbf{o}_w^f - \boldsymbol{\gamma}(s)) \cdot \frac{\mathrm{d}\boldsymbol{\gamma}(s)}{\mathrm{d}s} = 0\,, \tag{3.4}$$

and solving it with respect to the variable s. The definition of the y_b and z_b axis can be performed referring to an another reference system, the *secondary reference system* characterized

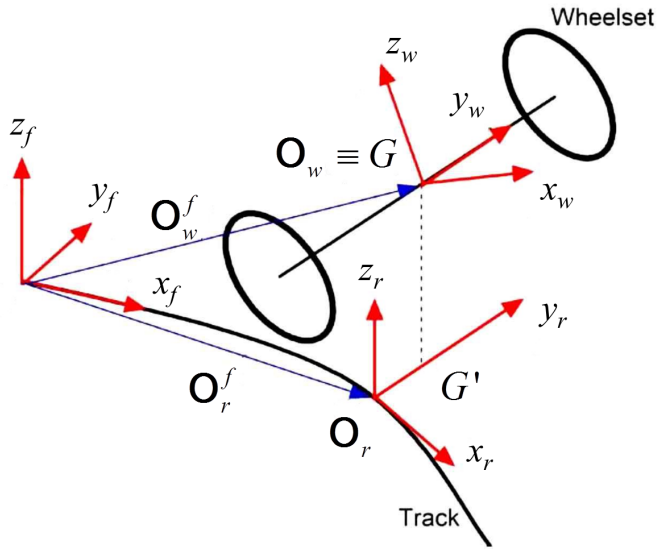

Figure 3.13. Fixed, auxiliary and local reference systems.

by the unitary vectors $\mathbf{i}'_r$, $\mathbf{j}'_r$ and $\mathbf{k}'_r$, relative to the axes x'_r, y'_r and z'_r, defined as follows:

$$\mathbf{i}_{r'} = \mathbf{i}_r = \frac{\mathrm{d}\gamma}{\mathrm{d}s} \Big/ \left\| \frac{\gamma}{\mathrm{d}s} \right\| , \tag{3.5a}$$

$$\mathbf{j}_{r'} = \mathbf{k}_f \times \mathbf{i}_{r'} , \tag{3.5b}$$

$$\mathbf{k}_{r'} = \mathbf{i}_{r'} \times \mathbf{j}_{r'} . \tag{3.5c}$$

Thus, the unitary vectors of the auxiliary system can be calculated in the following manner:

$$[\mathbf{i}_r \quad \mathbf{j}_r \quad \mathbf{k}_r] = [\mathbf{R}_{cant}][\mathbf{i}_{r'} \quad \mathbf{j}_{r'} \quad \mathbf{k}_{r'}] = [\mathbf{R}_1] , \tag{3.6}$$

where $[\mathbf{R}_1]$ is the rotation matrix which links the auxiliary system with the fixed one and $[\mathbf{R}_{cant}]$ is the rotation matrix related to the cant angle β_c.

The last reference system to be introduced is the *local reference system* $O_w x_w y_w z_w$ whose origin is in the wheelset centre of mass. This is a system rigidly connected to the wheelset except for the rotation around the axis. The y_w axis coincides with the rotation axis while the x_w axis, whatever the position of the wheelset is, is parallel to the $x_r y_r$ plane.

According to the kinematics relations, the position of a generic point in the three reference systems (fixed, auxiliary and local) are:

$$\mathbf{p}^f = \mathbf{o}_r^f + [\mathbf{R}_1]\mathbf{p}^r , \tag{3.7a}$$

$$\mathbf{p}^r = \mathbf{o}_w^r + [\mathbf{R}_2]\mathbf{p}^w , \tag{3.7b}$$

$$\mathbf{p}^f = \mathbf{o}_w^f + [\tilde{\mathbf{R}}]\mathbf{p}^w , \tag{3.7c}$$

where the $\mathbf{o}_w^f$ and $\mathbf{o}_w^r$ are respectively the position of the wheelset centre of mass (hence

the position of O_w) in the fixed and in the auxiliary system, whereas $[\tilde{\mathbf{R}}]$ is the rotation matrix which expresses the orientation of the local system with respect to the fixed one. The matrix $[\mathbf{R}_2] = [\mathbf{R}_{z,\alpha}][\mathbf{R}_{x,\beta}]$ which links the local system with the auxiliary one, depends on the roll angle β and the yaw angle α of the wheelset respect to the track.

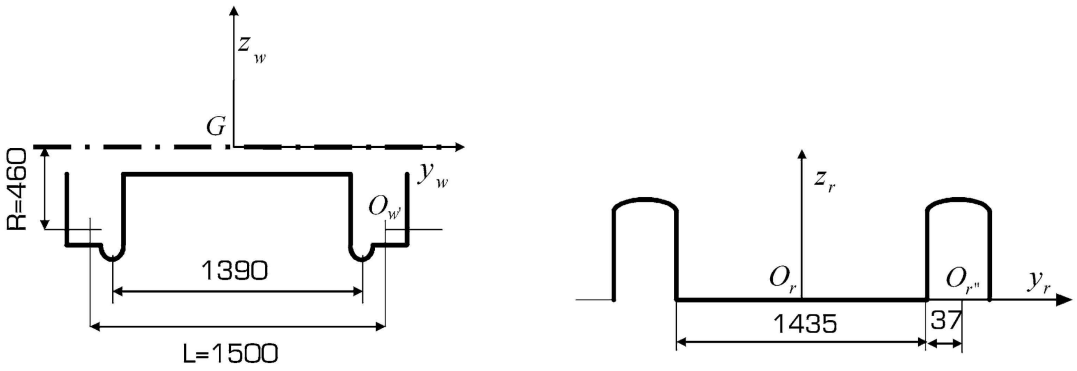

(a) Wheelset (b) Rails

Figure 3.14. Generative functions of wheelset and rails.

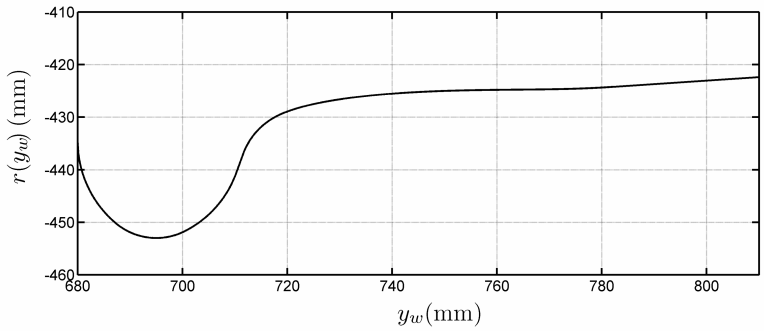

Figure 3.15. The ORE S1002 wheel profile.

The wheelset surface can be simply generated as a revolution surface, by using a generative function $r(y_w)$, made up of circular and polynomial parts; the rails are instead generated by extrusion of the rail profile generative function $b(y_r)$, which is supposed to be constant along the track. Both the generative functions are schematically shown in Fig. 3.14. Conversely, examples of real wheel and rail profiles are respectively presented in Figs. 3.16 and 3.15.

The coordinates of a point on the wheel (Fig. 3.17) in the local reference system are:

$$\mathbf{p}_w^w(x_w, y_w) = \begin{bmatrix} x_w \\ y_w \\ \sqrt{r(y_w)^2 - x_w^2} \end{bmatrix}, \tag{3.8}$$

while the coordinates of a generic point in the auxiliary system are:

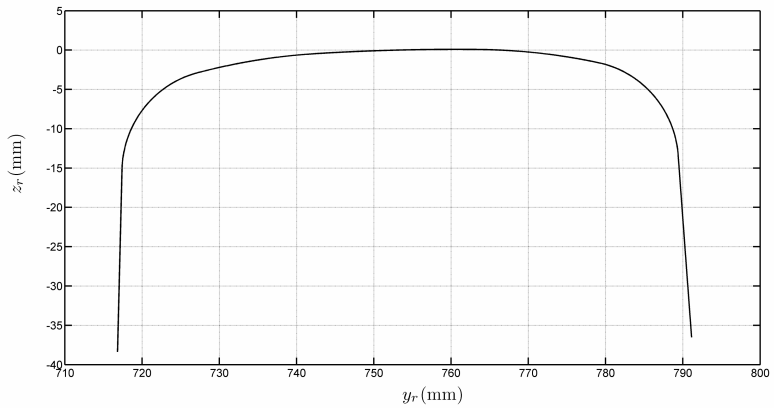

Figure 3.16. UIC60 rail profile with a cant angle of 1/40 rad.

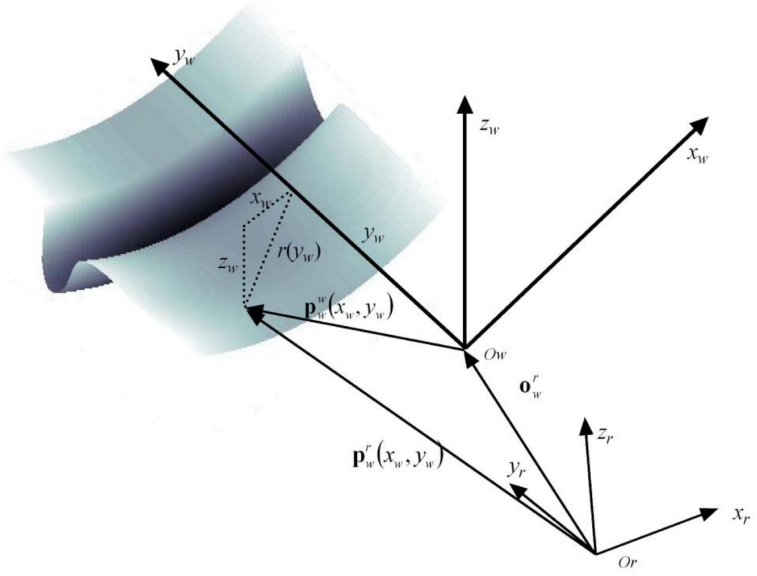

Figure 3.17. Coordinates of a point on the wheel surface.

$$\mathbf{p}_r^r(x_r, y_r) = \begin{bmatrix} x_r \\ y_r \\ b(y_r) \end{bmatrix}. \tag{3.9}$$

As a last step, the normal unitary vectors for both the surfaces have to defined; by convention, the normal vectors point outward from the surface (Fig. 3.18). The normal unit vector in a point of the wheelset surface has, in the local system, the following expression

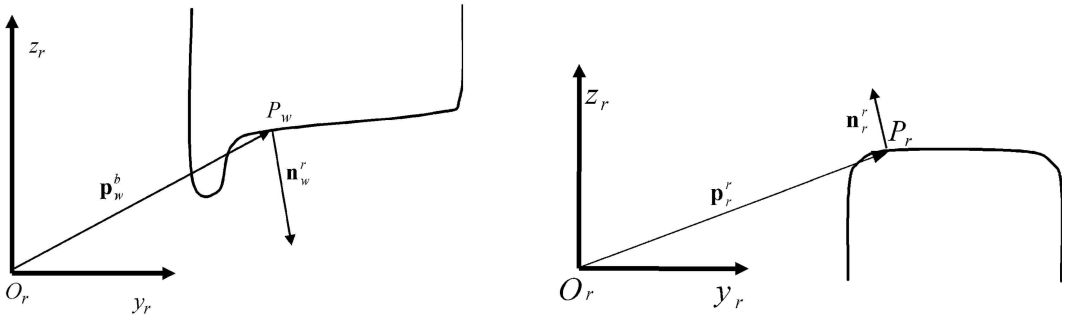

(a) Wheelset (b) Rails

Figure 3.18. Normal unitary vectors on wheelset and rails.

(Eq. 3.10):

$$\mathbf{n}_w^w(\mathbf{p}_w^w) = -\left(\frac{\partial \mathbf{p}_w^w}{\partial x_w} \times \frac{\partial \mathbf{p}_w^w}{\partial y_w}\right) \Bigg/ \left\| \frac{\partial \mathbf{p}_w^w}{\partial x_w} \times \frac{\partial \mathbf{p}_w^w}{\partial y_w} \right\| = \\ = \left(\sqrt{\frac{r(y_w)^2(r'(y_w)^2+1)}{r(y_w)^2 - x_w^2}}\right)^{-1} \begin{bmatrix} x_w / \sqrt{r(y_w)^2 - x_w^2} \\ r(y_w) r'(y_w) / \sqrt{r(y_w)^2 - x_w^2} \\ -1 \end{bmatrix}, \quad (3.10)$$

where $r'(y_w)$ is the wheel profile derivative with respect to the y_w coordinate. It is useful to note that the argument of the radical $\sqrt{r(y_w)^2 - x_w^2}$ cannot be equal or less than zero because $r(y_w)^2 >> x_w^2$.

The expression of the normal unit vector in the auxiliary system is simply obtained pre-multiplying it by the rotation matrix $\mathbf{R}_2$:

$$\mathbf{n}_w^r(\mathbf{p}_w^r) = [\mathbf{R}_2]\mathbf{n}_w^w(\mathbf{p}_w^w). \quad (3.11)$$

As regards the rail normal vector, the analytic expression in the auxiliary system is given by Eq. 3.12:

$$\mathbf{n}_r^r(\mathbf{p}_r^r) = -\left(\frac{\partial \mathbf{p}_r^r}{\partial x_r} \times \frac{\partial \mathbf{p}_r^r}{\partial y_r}\right) \Bigg/ \left\| \frac{\partial \mathbf{p}_r^r}{\partial x_r} \times \frac{\partial \mathbf{p}_r^r}{\partial y_r} \right\| = \left(\sqrt{1 + b'(y_r)^2}\right)^{-1} \begin{bmatrix} 0 \\ -b'(y_r) \\ 1 \end{bmatrix}, \quad (3.12)$$

where $b'(y_r)$ is the rail profile derivative with respect to y_r.

3.2.2 Research of the contact points: the DIST method

This first step in the resolution of the contact problem, the detection of the contact locations between the wheelset and the rails, is entrusted to an algorithm (the DIST method [21, 22]) the development of which, within the Section of Applied Mechanics, started in previous works. The algorithm is based on the standard idea that the distance between the surfaces of wheelset and rails is stationary in the contact points [35, 24], but the innovative

implementation allows the original multi-dimensional contact problem to be reduced to a simpler scalar problem, which can be easily resolved by means of numerical methods. In reducing the dimension of the numerical problem there are also remarkable advantages listed below:

- a wide range of algorithms can efficiently resolve the algebraic problem, even the elementary non-iterative ones;
- the multiple solution handling is simpler;
- the convergence can be easily achieved and the algorithm converges to the solutions with fewer iterations.

The research requires to solve an algebraic system, the formulation of which arises by imposing a few geometrical conditions, which can be stated as follows:

- the normal unitary vector relative to the rail surface $\mathbf{n}_r^r(\mathbf{p}_r^r)$ and the wheel surface unitary vector $\mathbf{n}_w^r(\mathbf{p}_w^r)$ have to be parallel:

$$\mathbf{n}_r^r \times \mathbf{n}_w^r(\mathbf{p}_w^r) = \mathbf{n}_r^r(\mathbf{p}_r^r) \times \mathbf{R}_2 \mathbf{n}_w^w(\mathbf{p}_w^w) = \mathbf{0}\,; \tag{3.13}$$

- the rail surface normal unitary vector $\mathbf{n}_r^r(\mathbf{p}_r^r)$ has to be parallel to the distance vector $\mathbf{d}^r = \mathbf{p}_w^r - \mathbf{p}_r^r$ between the generic point of the wheel and of the rail:

$$\mathbf{n}_r^r(\mathbf{p}_r^r) \times \mathbf{d}^r = \mathbf{0}\,. \tag{3.14}$$

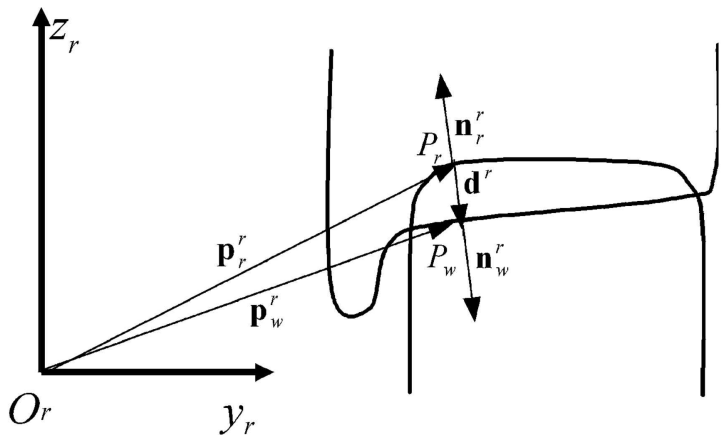

Figure 3.19. Distance method: vectors involved in the algorithm formulation.

The problem can also be formulated in a different way by imposing that the distance vector $\mathbf{d}^r$ is perpendicular both to the wheel and to the rail tangent plane. Nevertheless it would imply a different arrangement of the algebraic equations and both the resolution algorithm and the calculation would be more complicated than the one arising from Eqs. 3.13 and 3.14.

The distance vector between the generic points on the wheel and on the rail can be written as

$$\mathbf{d}^r(x_w, y_w, x_r, y_r) = \mathbf{p}_w^r(x_w, y_w) - \mathbf{p}_r^r(x_r, y_r) = \mathbf{o}_w^r + \mathbf{R}_2 \mathbf{p}_w^w(x_w, y_w) - \mathbf{p}_r^r(x_r, y_r)\,, \tag{3.15}$$

which shows that it depends on four parameters (x_w, y_w, x_r, y_r) that identify a point on both the surfaces. The Eqs. 3.13 and 3.14 constitute a system with six scalar equations and four unknowns (x_w, y_w, x_r, y_r), since only four of the six equations are independent. The reducing of the original problem to a scalar equation in the unknown y_w is carried out expressing x_w, x_r, and y_r as functions of y_w. As a first step, the second component of (3.13) gives

$$r_{13}\sqrt{r(y_w)^2 - x_w^2} = r_{11}x_w - r_{12}r(y_w)r'(y_w)\,; \tag{3.16}$$

where r_{13}, r_{11} and r_{12} are elements of the $\mathbf{R}_2$ matrix. Assuming that for simplicity $A = r_{13}$, $B = r(y_w)$, $C = r_{11}$ and $D = r_{12}r(y_w)r'(y_w)$, the previous equation becomes

$$A\sqrt{B^2 - x_w^2} = Cx_w - D\,. \tag{3.17}$$

By removing the radical in the previous equation and solving for x_w, the following expression arises:

$$x_{w1,2}(y_w) = \frac{CD \pm \sqrt{C^2D^2 - (C^2 + A^2)(D^2 - A^2B^2)}}{C^2 + A^2}\,; \tag{3.18}$$

therefore, there are two possible values of x_w for each y_w. At this point, an expression for the rail derivative can be written by substituting $x_{w1,2}(y_w)$ in the first component of (3.13):

$$b'(y_r)_{1,2} = \frac{r_{21}x_{w1,2}(y_w) - r_{22}r(y_w)r'(y_w) - r_{23}\sqrt{r(y_w)^2 - x_{w1,2}(y_w)^2}}{r_{32}r(y_w)r'(y_w) + r_{33}\sqrt{r(y_w)^2 - x_{w1,2}(y_w)^2}} \tag{3.19}$$

Considering separately both the track sides, if $b'(y_r)_{1,2}$ is decreasing monotonous, the (3.19) is numerically invertible and it gives $y_{r1,2}$. On the contrary, the numerical inversion would be possible anyway, but it would produce a further multiplication of the solution number.

As regards the second scalar component of (3.14), it can be rearranged as

$$x_{r1,2}(y_w) = r_{11}x_{w1,2}(y_w) + r_{12}y_w - r_{13}\sqrt{r(y_w)^2 - x_{r1,2}(y_w)^2}\,. \tag{3.20}$$

Finally, the values of the three variables x_w, x_r and y_r can now be inserted in the first component of the (3.14), to write the Eq. 3.21:

$$\begin{aligned} F_{1,2}(y_w) = -b'(y_{r1,2}(y_w))\Big(G_z + r_{32}y_w - r_{33}\sqrt{r(y_w)^2 - x_{w1,2}(y_w)^2} - b\big(y_{r1,2}(y_w)\big)\Big) \\ - \Big(G_y + r_{21}x_{w1,2}(y_w) + r_{22}y_w - r_{23}\sqrt{r(y_w)^2 - x_{w1,2}(y_w)^2} - y_{r1,2}(y_w)\Big) = 0\,; \end{aligned} \tag{3.21}$$

these are two simple scalar equations in the y_w variable, easy to resolve numerically with the advantages previously mentioned. The dimension of the initial problem has been reduced from four to one.

In the following, y^C_{w1j} and y^C_{w2k} with $1 \leq j \leq n_1$ and $1 \leq k \leq n_2$, will be the generic solutions of $F_1(y_w) = 0$ and $F_2(y_w) = 0$ respectively. For each y^C_w, the values of the unknowns x^C_w, x^C_r, y^C_r and consequently the contact point positions on the wheel and the rail $\mathbf{p}^{r,C}_w = p^r_w(x^C_w, y^C_w)$ and $\mathbf{p}^{r,C}_r = p^r_r(x^C_r, y^C_r)$ can be simply determined by substitution.

Nevertheless, since the Eq. 3.21 includes irrational terms, a root can be accepted only if it satisfies all the following analytical conditions:

- x^C_{w1j} and x^C_{w2k} (calculated by (3.18) for y^C_{w1j}, y^C_{w2k}) have to be real numbers;
- the terms $\sqrt{r(y^C_{w1j})^2 - x(y^C_{w1j})^2}$ and $\sqrt{r(y^C_{w2k})^2 - x(y^C_{w2k})^2}$ of (3.21) have to be real too;
- (x^C_{w1j}, y^C_{w1j}) and (x^C_{w2k}, y^C_{w2k}) have to be actual solutions of (3.16), the radical having been removed;

in addition, a few conditions have also to be respected so that the contact is physically possible:

- the penetration between the wheel and rail surfaces ($p_n = \mathbf{d}^r \cdot \mathbf{n}^r_r$) have to be less or equal to zero, according to the adopted nomenclature;
- multiple solutions have to be rejected;
- the normal curvatures of the wheel and rail surfaces in the longitudinal and lateral direction ($k^C_{1,wi}$, $k^C_{1,ri}$, $k^C_{2,ri}$, $k^C_{2,ri}$), evaluated in the contact points, have to satisfy the convexity condition in order to make the contact physically possible ($k^C_{1,wi} + k^C_{1,ri} > 0$; $k^C_{2,wi} + k^C_{2,ri} > 0$).

In regard to the last point, the normal curvatures in the contact point of the wheel and rail surfaces Fig. 3.20 can be calculated starting from the expressions of the principal curvatures in a generic point [35] (Eq. 3.22 for the wheel and Eq. 3.23 for the rail). By covention, the normal curvature in a point is greater than zero if the surface is locally convex.

$$\begin{aligned} K_{1w}(y_w) &= \frac{1}{|r(y_w)|\sqrt{1 + r'(y_w)^2}}, \\ K_{2w}(y_w) &= \frac{r''(y_w)}{(1 + r'(y_w)^2)^{3/2}}, \end{aligned} \tag{3.22}$$

$$\begin{aligned} K_{1r}(y_r) &= 0, \\ K_{2r}(y_r) &= \frac{-b''(y_r)}{(1 + b'(y_r)^2)^{3/2}}. \end{aligned} \tag{3.23}$$

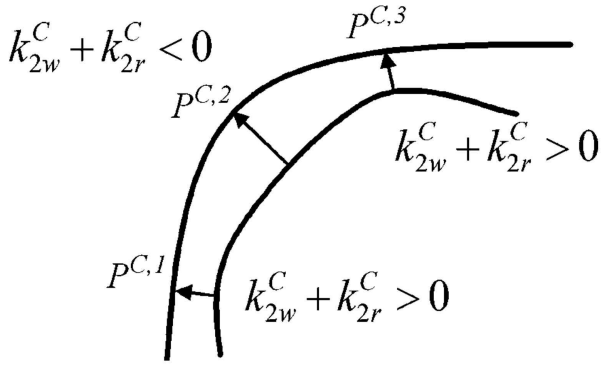

Figure 3.20. Normal curvatures in the contact points.

3.2.2.1 The DIFF method

An alternative formulation for the detection of the contact points (the DIFF method) has been developed to simplify the method described in the previous section and to improve the overall computational efficiency (Fig. 3.21). Unlike the DIST method, this one is based on the idea that in the contact points the difference between the wheel and rail surface is minimised in the direction of the k_r unitary vector:

$$D(x_w, y_w) = (\mathbf{p}_w^r(x_w, y_w) - \mathbf{p}_r^r(x_w, y_w)) \cdot \mathbf{k}_r \,, \tag{3.24}$$

where the difference $D(x_w, y_w)$ is a two-dimensional surface.

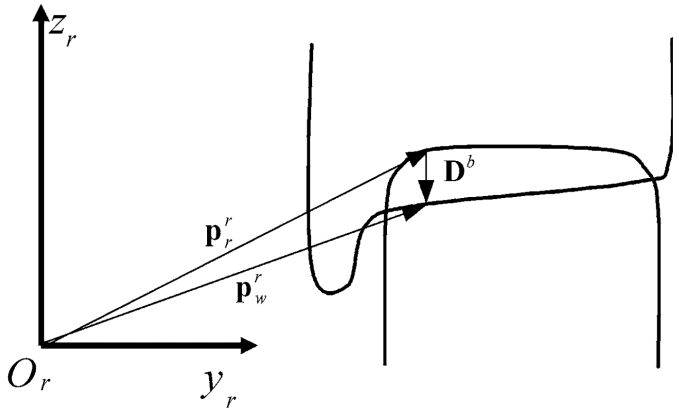

Figure 3.21. The DIFF method in researching the contact points.

The detection problem can be resolved by imposing that the partial derivatives are equal to zero:

$$\frac{\partial D(x_w, y_w)}{\partial x_w} = 0 \,, \quad \frac{\partial D(x_w, y_w)}{\partial y_w} = 0 \,. \tag{3.25}$$

In order that the contact points can be accepted, the solution of system (3.25) must be a minimum of the surface (3.24), hence the Hessian matrix $H_D(x_w, y_w)$ of $D(x_w, y_w)$ have to be positive defined in the points (x_{wi}^C, y_{wi}^C) with $i = 1, 2, ..., n$:

$$H_D(x_w, y_w) = \begin{pmatrix} \frac{\partial^2 D}{\partial x_w^2} & \frac{\partial^2 D}{\partial x_w \partial y_w} \\ \frac{\partial^2 D}{\partial x_w \partial y_w} & \frac{\partial^2 D}{\partial y_w^2} \end{pmatrix} . \tag{3.26}$$

Since $D(x_w, y_w) : \mathbb{R}^2 \rightarrow \mathbb{R}^2$, this leads to

$$\frac{\partial^2 D}{\partial x_w^2}(x_{wi}^C, y_w^C i) > 0, \quad det\, H_D(x_{wi}^C, y_w^C i) > 0\,, \tag{3.27}$$

with $i = 1, 2, ..., n$. As has been seen for the DIST method, the dimension of the problem can be analytically reduced by following a similar strategy. The DIFF formulation is a valid, though less general, alternative to the DIST method to carry out the research of contact points.

3.2.3 Evaluation of the contact forces

Once the contact points are detected, the calculation of the contact forces can be carried out starting from the wheelset kinematic variables, considering that the problem comprises two different aspects: the evaluation of the force in the normal direction to the tangent plane and the calculation of the tangential components in that plane. A semi-elastic approach based on both Hertz and Kalker's global theories [15] is used in this work.

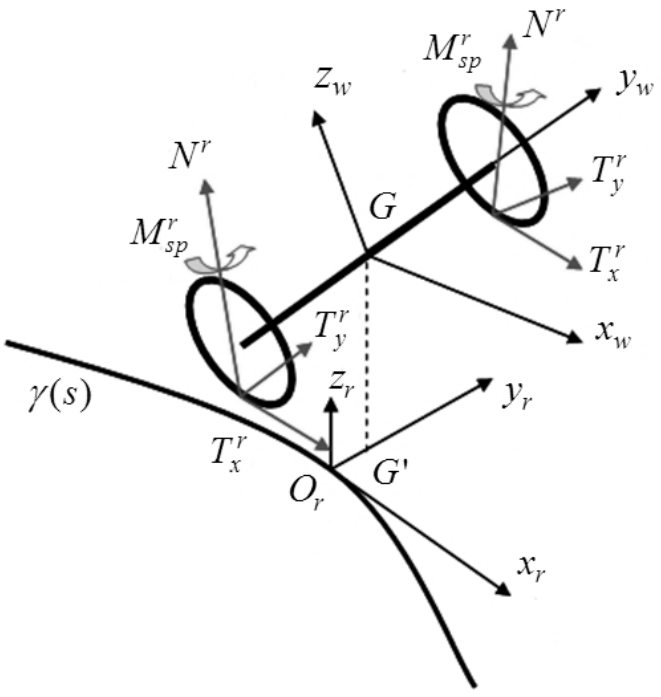

Figure 3.22. Nomenclature of the contact forces.

The normal contact force, according to Hertz's theory, depends on both the penetration p_n between the surface of wheel and rail and the penetration velocity $v_n = \mathbf{v} \cdot \mathbf{n}_r^r(\mathbf{p}_r^{r,C})$,

where $\mathbf{v}$ is the contact point velocity, assuming that it is rigidly connected to the wheel:

$$N^r(\mathbf{p}_r^{r,C}) = \left[-k_h|p_n|^\gamma + k_v|v_n|\frac{\mathrm{sgn}(v_n)-1}{2}\right]\frac{\mathrm{sgn}(p_n)-1}{2}\,, \tag{3.28}$$

where γ is equal to $3/2$, k_h is a Kalker's stiffness constant depending on the surface geometries and the material properties, k_v is a damping contact constant [15]. The same theory also provides the contact patch semiaxes a, b and the ellipse eccentricity. The linear Kalker's theory is then applied to calculate the tangential forces and the spin moment (Fig. 3.22) in each contact patch:

$$T_x^r(\mathbf{p}_r^{r,C}) = -f_{11}\xi_x\,; \tag{3.29a}$$

$$T_y^r(\mathbf{p}_r^{r,C}) = -f_{22}\xi_y - f_{23}\xi_{sp}\,; \tag{3.29b}$$

$$M_{sp}^r(\mathbf{p}_r^{r,C}) = -f_{23}\xi_y - f_{33}\xi_{sp}\,, \tag{3.29c}$$

where the value of the f_{ij} coefficients, which are function of the material properties and the ellipse semiaxes, can be found in literature [15].

ξ_x, ξ_y and ξ_{sp} are the longitudinal, lateral and the spin creepages, as defined below:

$$\xi_x = \mathbf{v}\cdot\mathbf{i}_r \Big/ \left\|\dot{G}_{w,f}^r\right\|\,;$$

$$\xi_y = \mathbf{v}\cdot\mathbf{t}_r^r \Big/ \left\|\dot{G}_{w,f}^r\right\|\,; \tag{3.30a}$$

$$\xi_{sp} = \boldsymbol{\omega}^r\cdot\mathbf{n}_r^r \Big/ \left\|\dot{G}_{w,f}^r\right\|\,, \tag{3.30b}$$

where $\dot{G}_{w,f}^r$ is the absolute velocity of the wheelset centre of mass, $\mathbf{i}_r$ is the unit vector of the x_r axis, $\boldsymbol{\omega}^r$ the wheelset angular velocity expressed in the auxiliary reference system and $\mathbf{t}_r^r = \mathbf{n}_r^r \times \mathbf{i}_r$.

Since the Kalker's theory is linear, to include the effect of the adhesion limit due to friction, a saturation criterion has to be introduced in the model to limit the magnitude of the tangential contact force $\tilde{T}^r = \sqrt{\tilde{T}_x^{r2} + \tilde{T}_y^{r2}}$ which cannot exceed the slip value $T_s^r = \mu N^r$. Therefore, a saturation coefficient ϵ (3.31) widely common in literature, is defined as

$$\epsilon = \begin{cases} \dfrac{\mu N^r}{\tilde{T}^r}\left[\left(\dfrac{\tilde{T}^r}{\mu N^r}\right) - \dfrac{1}{3}\left(\dfrac{\tilde{T}^r}{\mu N^r}\right)^2 + \dfrac{1}{27}\left(\dfrac{\tilde{T}^r}{\mu N^r}\right)^3\right] & \text{if } \tilde{T}^r \le 3\mu N^r \\ \dfrac{\mu N^r}{\tilde{T}^r} & \text{if } \tilde{T}^r > 3\mu N^r \end{cases}; \tag{3.31}$$

in this way the saturated tangential force will be $\mathbf{T}^r = \epsilon\tilde{\mathbf{T}}^r$.

CHAPTER 4

Wear Evaluation

The wear evaluation block, previously discussed in the explanation of the general architecture will be treated in detail in the following chapter. Because of the way the model is arranged, the wear assessment requires three fundamental steps which are the evaluation of the contact variables, the wear calculation and the profile update.

4.1 Local contact model

After completing the multibody simulations, the results are exploited to carry out the wear evaluation, the aim of which is to provide the wheel profile to be used in the next step of procedure. The *local contact model* performs the calculation of the local contact variables (normal pressures, tangential stresses and creepages) within each detected contact patch, starting from the global contact variables (contact point positions, contact forces and spin moments, creepages and patch semiaxes), which are the outputs of the dynamic simulations, as summarized in Tab. 4.1. Even though the global contact model can handle whatever number of contact points, the general layout is arranged so that each wheelset can have up to six contact points contemporaneously.

Table 4.1. Output quantities of the multibody simulation for each contact patch.

Symbol	Quantity	Unit
V	Axle speed	m/s
y_w^C	Contact point lateral position in $O_r x_x y_r z_r$	m
s_x	Longitudinal creepage	m/s
s_y	Lateral creepage	m/s
ϕ_z	Spin creepage	rad/s
N	Normal force	N
T_x	Longitudinal tangential force	N
T_y	Lateral tangential force	N
a	Longitudinal ellipse semiaxis	m
b	Transversal ellipse semiaxis	m

The local contact model is based on an approximate but very efficient version of the Kalker's local theory implemented in his FASTSIM algorithm [15], extensively used in railway multibody simulations to resolve the tangential contact problem at each integration step. Conversely, in this activity the above-mentioned algorithm is utilised *offline* to process the results, hence only after completing the dynamic analyses.

With regard to the implementation, the FASTSIM algorithm works in a local reference system, whose origin is located in the centre of the elliptical contact patch, with the x, y axes defined in the tangent plane to the contact surfaces, as visible in Fig. 4.1; generally, these axes are not parallel to neither the local reference system of the wheelset nor the auxiliary system, because the tangent plane is inclined to horizontal at the contact angle. In addition, as shown in the same figure, the method needs a meshing of the contact patch.

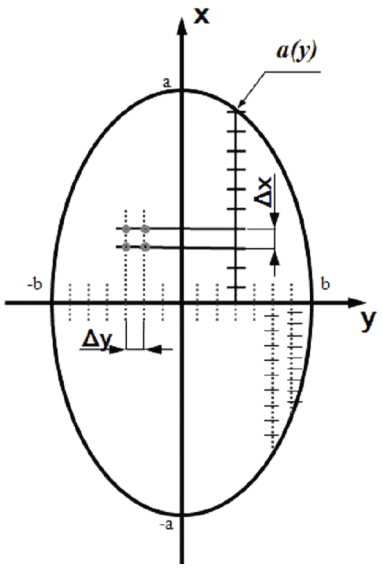

Figure 4.1. Contact patch discretization in the FASTSIM algorithm.

The fundamental hypothesis of the algorithm is the proportionality between the tangential pressure $\mathbf{p}_t$ and the elastic displacement $\mathbf{u}$ in a generic point of the contact patch:

$$\mathbf{u}(x,y) = L\mathbf{p}_t(x,y)\,; \qquad L = L(\boldsymbol{\xi}, a, b, G, \nu)\,, \tag{4.1}$$

where the flexibility L is a function of the global creepage vector $\boldsymbol{\xi}$, the ellipse semiaxes a and b, the combined shear modulus G and the combined Poisson's coefficient ν, as expressed below:

$$L = \frac{|\xi_x|L_1 + |\xi_y|L_2 + c|\xi_{sp}|L_3}{\sqrt{\xi_x^2 + \xi_y^2 + c^2\xi_{sp}^2}}\,, \tag{4.2}$$

in which $L_1 = 8a/(3Gc_{11})$, $L_2 = 8a/(3Gc_{22})$, $L_3 = \pi a^2/(4Gcc_{23})$ and $c = \sqrt{ab}$. The Kalker's coefficients c_{ij}, that are functions of a/b and ν can be found in tabular form in literature, whereas the combined parameter G and ν are evaluated as an opportune average between

the properties of the wheel and the rail:

$$G = 2\frac{G_w G_r}{G_w + G_r}\,; \quad \nu = \frac{\nu_w G_w + \nu_r G_r}{G_w + G_r}\,. \tag{4.3}$$

The first local variable to be found is the local creepages in a generic point which can be obtained by deriving the elastic displacements and taking into account both the rigid global creepages and the vehicle speed V, or directly the absolute creepages s_x, s_y:

$$\sigma(x,y) = \dot{\mathbf{u}}(x,y) + \begin{bmatrix} s_x \\ s_y \end{bmatrix}\,. \tag{4.4}$$

The evaluation of σ and the other local variables p_n, $\mathbf{p}_t$ is performed in each point of the grid adopted to mesh the contact patch (Fig. 4.1), discretised with a variable resolution. In fact, the transversal axis of the contact ellipse, with respect to the travelling direction, is divided into $n_y - 1$ parts with a length of $\Delta y = 2b/(n_y - 1)$ by means of n_y equidistant nodes. Similarly, the longitudinal sections of the patch, which are $2a(y) = 2a\sqrt{1-(y/b)^2}$ long, are divided into $n_x - 1$ equal parts of $\Delta x(y) = 2a(y)/(n_x - 1)$ length by using n_x equidistant nodes. This choice implies a not constant longitudinal resolution which increases in the nearby of the lateral edges of the ellipse, where the length $a(y)$ are shorter. Thus, the accuracy near the edges is appreciably higher than that obtainable with a constant resolution grid, which would produce more errors of discretisation. The n_x and n_y parameters must be chosen as a compromise between numerical efficiency and precision; to this end, the range $15 \div 25$ has proven to work fine.

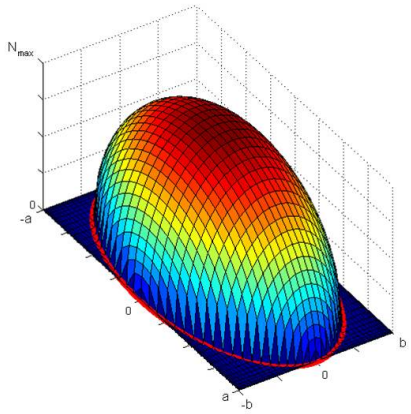

Figure 4.2. Elliptical distribution of the normal pressures.

As regards the procedure of the algorithm, the expression of the normal pressure (Fig. 4.2) and the adhesion limit pressure in a generic point (x_h, y_l) of the grid, with $1 \le h \le n_x$, $1 \le l \le n_y$ are the following:

$$p_n(x_h, y_l) = \frac{3}{2}\frac{N^r}{\pi a b}\sqrt{1 - \frac{x_h^2}{a^2} - \frac{y_l^2}{b^2}}\,, \tag{4.5}$$

$$\mathbf{p}_A(x_h, y_l) = \mathbf{p}_t(x_h - \Delta x(y_l), y_l) - \begin{bmatrix} \xi_x \\ \xi_y \end{bmatrix} \frac{\Delta x(y_l)}{L} = \mathbf{p}_t(x_{h-1}, y_l) - \begin{bmatrix} \xi_x \\ \xi_y \end{bmatrix} \frac{\Delta x(y_l)}{L} \tag{4.6}$$

where N^r is the normal contact force. Starting from the values of the local variables in (x_{h-1}, y_l), the algorithm works iteratively to find the exact distribution of the local variables in (x_h, y_l):

$$\|\mathbf{p}_A(x_h, y_l)\| \leq \mu p_n(x_h, y_l) \Rightarrow \mathbf{p}t(x_h, y_l) = \mathbf{p}_A(x_h, y_l); \quad \sigma(x_h, y_l) = \mathbf{0} \tag{4.7}$$

$$\|\mathbf{p}_A(x_h, y_l)\| > \mu p_n(x_h, y_l) \Rightarrow \begin{cases} \mathbf{p}_t(x_h, y_l) = \mu p_n(x_h, y_l) \mathbf{p}_A(x_h, y_l) / \|\mathbf{p}_A(x_h, y_l)\| \\ \sigma(x_h, y_l) = \frac{LV}{\Delta x(y_l)} \left(\mathbf{p}_t(x_h, y_l) - \mathbf{p}_A(x_h, y_l)\right) \end{cases} \tag{4.8}$$

where the boundary conditions are $\mathbf{p}_t(x_1, y_l) = \mathbf{0}$, $\sigma(x_1, y_l) = \mathbf{0}$, $1 \leq l \leq n_y$, since creepages and pressures have to be zero outside the contact patch. Finally, the distributions of the pressures $p_n(x_h, y_l)$, $\mathbf{p}_t(x_h, y_l)$ and the creepages $\sigma(x_h, y_l)$ are found by iterating the procedure for $2 \leq h \leq n_x$ and $1 \leq l \leq n_y$. The contact patch is hence divided into an adhesion zone, which does not contribute to wear and a slipping zone characterised by tangential actions, as shown qualitatively in Fig. 4.3. As the tangential force rises, the magnitude of the global creepage becomes higher and consequently the slipping zone increases.

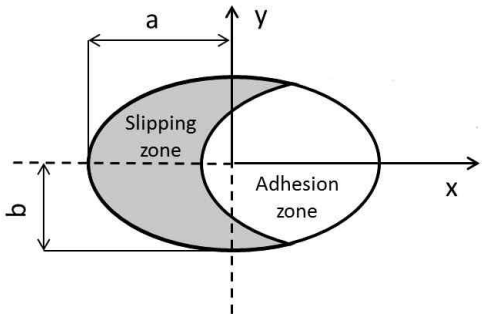

Figure 4.3. Adhesion and slipping zone in the contact patch.

4.2 Wear model

Once the local analysis has been carried out, the results can be exploited for the wear evaluation by means of the wear model written in MATLAB. As discussed in the sections relative to the general architecture, a fews working hypotheses have been introduced in agreement with the partners of the project in order to find a reasonable approach to the problem and to meet the main requirements of the research activity. The main points are listed again for the sake of convenience:

- the wear affects only the wheels, while the rails keep their original (worn or unworn) profile during the whole process;
- the output of the wear model is a single mean wheel profile to be used in the next step, which includes the effect of the wear on all the vehicle wheels;

- the wear is evaluated according to a experimental law [2, 20];
- dry conditions of friction are assumed in the wheel-rail interface.

In regard to the first point, the logical approach to the problem and its modeling can be easily extended, involving the case the simulation of the rail profile evolution as well. As hinted in the discussion about the general architecture, since the evolution of the rail profile is significantly slower than the variation in the wheel profiles of the vehicles, the two phenomena cannot be analysed contemporaneously for the presence of different time scales. It is more convenient to introduce some hypotheses and keep one profile constant during the analysis of the other one's evolution.

The second hypothesis has been introduced in this work to meet the requirements of the project issued by Trenitalia S.p.A which aims, as said in the Introduction, at a wheel profile optimisation. It is certainly true that the mean profile as a single output of the wear model tends to hide some important information about the actual wear conditions on the different wheels of the vehicle, but it is of great importance to sum up the results in the comparison of performance provided by different wheel profiles. If more than one wheel profile were taken into account, the comparison would be surely more complicated.

The third point concerns the strategy adopted in calculating the amount and the distribution of wear on wheels. The evaluation is based on an experimentally proven law which gives a non linear relation between the volume of removed material and the total frictional work developed in a point of the contact patch. The computation of wear is carried out by applying an averaging procedure in which the contribution of each detected patch during the simulation (up to six patches for each wheelset are allowed by default, but global the contact model can handle whatever number of contact points) is taken into account and whose effect on the final result obviously depends on both the time of existence and the wear rate developed.

The main output of the wear model is the specific volume $\delta_{P_i^{jk}(t)}(x, y)$, expressed in $\mathrm{mm}^3/(\mathrm{mm}^2\mathrm{m})$, a function of the time which describes the specific volume (the volume per unit of area and per unit of travelled distance) of material to be removed in the generic grid position (x, y) of the contact patch $P_i^{jk}(t)$.

The integral respect to x and y over the grid gives the specific volume of removed material relative to the contact patch $P_i^{jk}(t)$. More precisely, the subscript $P_i^{jk}(t)$ indicates the contact patch relative *i-th*, relative to the wheelset *j-th* in the *k-th* multibody simulation of the statistical analysis of the track, if more than analyses have to performed; otherwise this index can be neglected. Regarding to the statistical approach to the track and its features, they will be explained in detail in the Sec. 5.1. At this moment, it is sufficient to assert that the three indexes just introduced are variable in the following intervals:

- $1 \leq j \leq N_W$ where N_W is the number of the vehicle's wheels;
- $1 \leq i \leq N_P$ where N_P is the maximum allowed number of the contact points for each wheelset;

- $1 \leq k \leq N_C$ with N_C equal to one if only a single track is analysed, on the contrary it is equal to the number of the multibody simulations in the statistical description of the real track or railway net.

The quantity $\delta_{P_i^{jk}(t)}(x,y)$ has to be evaluated in each point (x_h, y_l) of the contact patch grid. To this aim, the local frictional power in these points can be estimated by means of the *wear index* I_W (N/mm^2):

$$I_W = \frac{\mathbf{p_t} \cdot \boldsymbol{\sigma}}{V}, \tag{4.9}$$

which is experimentally related to the *wear rate* K (µg/(m mm)) as visible in Fig. 4.4: the wear rate gives a measure of the amount of material removed per meter of travelled distance (m) covered by the train and per mm of surface. The analytic expression for $K(I_W)$ is given by Eq. 4.10. Typically the wear rate in normal conditions falls in the two first zone K_1 and K_2. These data, arising from experimental tests on roller rig and concerning the case of a steel-steel contact under dry conditions are available in literature in [2, 20].

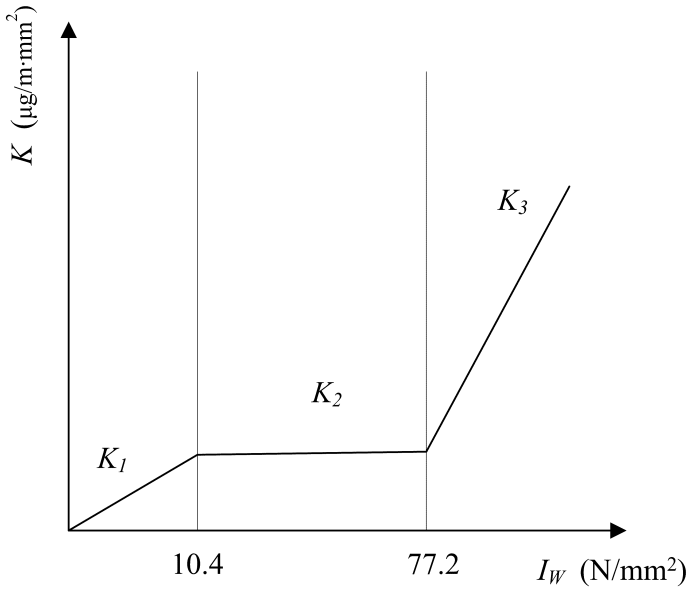

Figure 4.4. Wear rate as a function of the wear index.

$$K_W(I_W) = \begin{cases} 5.3 \cdot I_W & I_W < 10.4 \quad \text{N/mm}^2 \\ 55.0 & 10.4 \leq I_W \leq 77.2 \quad \text{N/mm}^2 \\ 61.9 \cdot I_W - 4723 & I_W > 77.2 \quad \text{N/mm}^2 \end{cases}. \tag{4.10}$$

After evaluating the wear rate, the specific volume $\delta_{P_i^{jk}(t)}(x,y)$ can be calculated as follows:

$$\delta_{P_i^{jk}(t)}(x,y) = \frac{K(I_W)}{\rho} \qquad \left(\text{mm}^3/(\text{m mm}^2)\right), \tag{4.11}$$

in which ρ is the material density (expressed in kg/m^3). The numerical wear rate arising from the model could be different than the real overall rate if the effects of plastic or fatigue

wear were remarkable. A further tuning of the model, acting on the filter used in each step of the procedure to smooth the wheel profiles, could compensate possible differences in the comparison with experimental data. Therefore, as will be clarified below, the filter has two purposes: first of all, it cuts the noise in the distribution of removed material, erasing the physically meaningless short spatial wavelengths in the profile that would cause problems to the resolution of contact problem during the simulations; moreover, it could allow the reduction of the errors related to the presence of other wear mechanisms which are not taken into account in the model (i.e the plastic and fatigue wear).

4.3 Profile update

The profile update is the part of the whole architecture which provides, by means of numerical procedures, the wheel profile for the next step $r_n(y_w)$ starting from the profile used at the current step $r_p(y_w)$ and by exploiting the outputs of the wear model. The calculation of the new profile is surely a key point of the whole procedure since the choices which are being made usually affects the results appreciably. The importance of this task lies in the following issues:

- the wear model, according to the working hypotheses, has to generate as output a single wheel profile taking into account the information relative to all the vehicle's wheels. A single function of material to be removed must be obtained from the analysis of all the detected contact patches during the dynamic simulation;
- due to the discrete approach to the wheel update, the distribution $\delta_{P_i^{jk}(t)}(x, y)$ presents a considerable numerical noise and needs to be treated to avoid, as stated previously, a non-physical profile with short spatial wavelengths, which, apart from having poor physical meaning, they may not be handled by the global contact model.

In regarding to the second point, a certain numerical noise is usually present first of all because the expression of frictional power in each grid point depends on both the local creepage and the tangential pressure which, in turn, depend above all on the temporal derivative of the kinematic state and the normal force. The strong dependency of the wear rate from the temporal derivatives of other quantities which can vary quickly in simulation, may introduce numerical noise and spikes in the resultant time progress of I_w and consequently, in $\delta_{P_i^{jk}(t)}(x, y)$. In addition, if irregularities (arising from experimental measurement or of stochastic sort) are added to the track model in multibody simulations, in order to reproduce a more realistic condition, an higher amount of numerical noise will overlap with the results.

The numerical procedure that generates the new profile starting from the current wheel geometry consists of a series of steps described below:

1) Longitudinal integration:

$$\frac{1}{2\pi r(y_i^{jk})}\int_{-a(y)}^{a(y)} \delta_{P_i^{jk}}(x,y)\,dx = \delta^{tot}_{P_i^{jk}(t)}(y) \qquad \left(\mathrm{mm}^3/(\mathrm{m\,mm}^2)\right). \tag{4.12}$$

With this integration, all the wear contributions in the longitudinal direction are summed and spread along the circumference of radius $r(y_i^{jk})$, so that the effect on the final wheel geometry of the wear due to the generic contact patch in the considered simulation have a rotational symmetry. This hypothesis is reasonable since the wheel shapes adopted in simulation have no flats and there is no reason to formulate a different working hypothesis. Insofar as superfluous it may sound to be highlighted, it is of primary importance an accurate calculation of the number and the position of contact points, both in the lateral and in the longitudinal direction, especially on the external wheel in curves. Clearly algorithms which allow a single contact patch for each wheel are to be avoided because they usually provide a correct solution only in large radius curves or in particular situations and they are hence inappropriate in most cases, where the contemporary presence of contact both on the tread and the flange must be carefully taken into consideration. Besides these simplified approaches, even those algorithms which allow two contact points for each wheel can be inadequate if the evaluation of the longitudinal position of the contact point on the flange is excessively approximate. A correct detection of patch position on the flange, indeed, is important not only to evaluate the exact direction and magnitude of the normal contact force, but also to estimate the vertical position of the point itself. The importance of an accurate localization of points is hence fundamental either if the attention is focused on the safety against derailment or if the the analysis concerns the wear assessment. Nevertheless, if the rail or the wheel is badly worn the contact on the external wheel may occur in more than two points, hence a generic and not approximate, though slower, algorithm is preferable in this kind of study.

2) Time integration:

$$\int_{T_i}^{T_f} \delta^{tot}_{P_i^{jk}(t)}\left(s_w - s_{wi}^{jk,C}(t)\right) V(t)\,dt \cong \Delta_{P_i^{jk}}(s_w) \qquad (\mathrm{mm})\,; \tag{4.13}$$

where $y \cong s_w - s_{wi}^{jk,C}$ (see Fig. 4.5); s_w is the generic curvilinear abscissa, $s_{wi}^{jk,C}(t)$ is the curvilinear abscissa of the contact point on the wheel at the time t and $V(t)$ is the vehicle speed. The integration sums all the contributions during the considered dynamic simulation: the result is a 2D function, that is the depth of material to be removed due to the generic contact point.

3) Sum on the contact points:

$$\sum_{i=1}^{N_P} \Delta_{P_i^{jk}}(s_w) = \Delta_{jk}(s_w)\,; \tag{4.14}$$

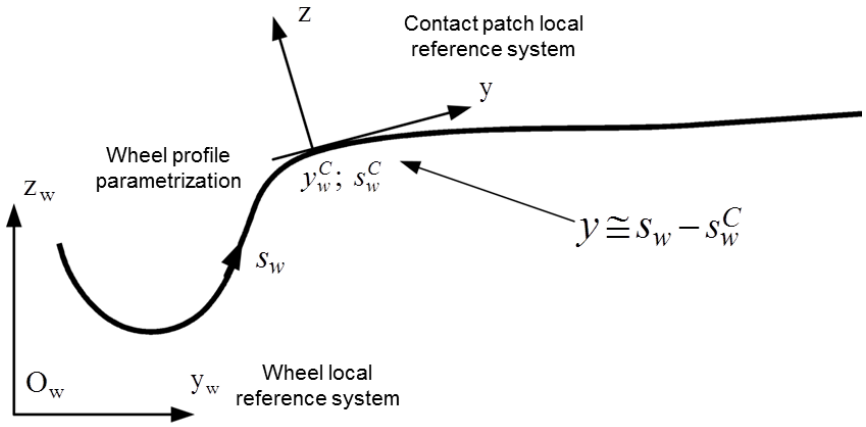

Figure 4.5. Wheel profile parametrisation.

where N_P is the above-mentioned maximum number of contact points on a single wheel and $\Delta_{jk}(y_w)$ is the removed material of the *j-th* wheel during the *k-th* dynamic simulation. Considering what has been seen up to this point, the contact patches are usually less than N_P and their number can vary during the simulation; hence, since the summation is extended to N_P, the contribution of the missing points is being automatically set equal to zero.

4) Average on the wheels and the simulations:

$$\sum_{i=1}^{N_C} p_k \frac{1}{N_W} \sum_{j=1}^{N_W} \Delta_{jk}(s_w) = \bar{\Delta}(s_w)\,. \tag{4.15}$$

This task involves the average on the N_W wheels if the output of the wear model has to be a single wheel profile and the weighted average on the N_C simulations if the considered context consists in more than one single track. The p_k, $1 \leq k \leq N_C$, $\sum_{i=1}^{N_C} p_k = 1$ are the normalized weights related to each track and introduced to differentiate the relative impact on the overall wear due to each analysed track. These relative weights are necessary when the set of tracks represent a statistical description of a long track which would be too long for accurate simulations or of a complex railway net: in this case the importance of each sub-track depends on the frequency with which it appears in the real situation, thus the weighting factors have to be defined to meet this requirement.

5) Smoothing of the amount of removed material:

$$\Im\left[\bar{\Delta}^{sc}(s_w)\right] = \bar{\Delta}^{sc}_{sm}(s_w)\,. \tag{4.16}$$

This procedure aims at the following targets:

- model tuning;
- compensation to include other wear mechanisms;

- numerical noise filtering;
- removal of physically meaningless short spatial wavelengths.

In fact, depending on the choice of the parameters, the filter could contribute to the agreement with experimental data, but it has not been used in this sense as a tuning tool. On the contrary, it has been exploited mainly to cut the numerical noise as highlighted by the difference between numerical results and experimental data (slightly underestimated) due to the presence of other wear mechanisms (see Sec. 5.3). The numerical noise and the short wavelength contributions are treated with a first order discrete filter [36]: a moving mean with a window width equal to the $1\% \div 5\%$ of the total points that discretises the wheel profile. This solution is simple and at the same time the filter does not change the total mass of removed material, as obviously required. Conversely, a significant change in the mass to be taken away would be obtained by exploiting low pass filters of whatever order to cut the high frequencies in the function $\bar{\Delta}^{sc}(s_w)$.

6) Scaling of the covered distance:

Since an appreciable evolution of the wheel profile requires thousands of kilometres to manifest itself, the scaling of the distance becomes critically important to get results in a reasonable time. Although the real chosen mileage km_{tot} that the vehicle has to run is divided in discrete steps of length km_{step} (Fig. 4.6), the step length is excessive anyway for the multibody approach and thus the scaling of Eq. 4.17 is adopted:

Figure 4.6. Partitioning of the total distance to be run in discrete steps.

$$\bar{\Delta}(s_w)\frac{km_{step}}{km_{runs}} = \bar{\Delta}^{sc}(s_w). \tag{4.17}$$

In fact, the amount of removed material $\bar{\Delta}(s_w)$ depends on the overall mileage travelled by the vehicle during the N_C simulations and the number of wheelsets, that is $km_{runs} = N_W L_C$, where L_C is the length of curved tracks on which the results of the vehicle dynamics are extrapolated. An example of removed material function after taking the average on wheels and simulations and before applying the scaling of the mileage is depicted in Fig. 4.7, in which it is also visible a typical effect of the filter.

As stated previously, if the numerically simulated track is a significant statistical representation of the track associated to the discrete spatial step or simply a sub-multiple of the real distance, the adopted working hypothesis is reasonable. The proportionality is exploited only within a distance equal to *kmstep* and the non-linearity of the physical problem is preserved.

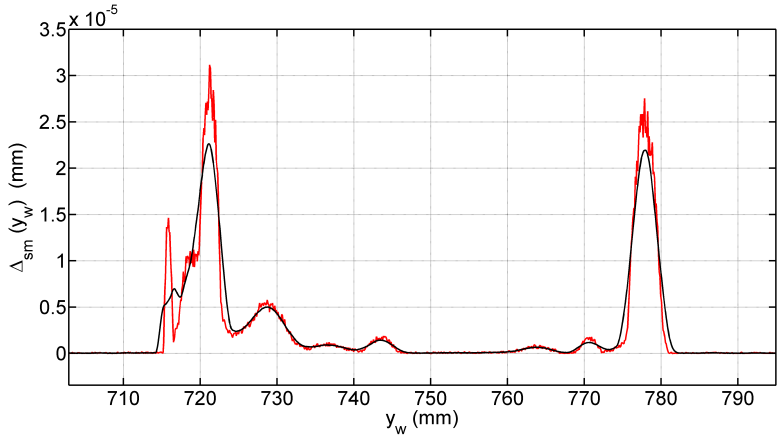

Figure 4.7. Comparison between the distributions of removed material due to wear as a function of the wheel lateral coordinate of wheel after taking the average on wheels and simulations and before scaling the mileage: unfiltered function (in red) and filtered function (in black).

After the scaling, the quantity $\bar{\Delta}^{sc}(s_w)$ is related to a spatial step with a length equal to km_{step}, instead of km_{runs}. However, even though the scaling reduces conveniently the total computational time, the choice of the km_{step}, (and hence the number of the steps, once the km_{tot} is fixed), affects strongly the results and has to be done properly as a compromise between numerical efficiency and accuracy. A high number of steps, indeed, leads to an accurate description of the phenomenon, requiring at the same time relevant computational efforts, while a large km_{step} increases the effect owing to the discrete approach and moreover amplifies the relative importance of the filter action and the numerical profile treatment on the final result.

For this reason, if km_{step} is chosen constant, it must be set sufficiently shorter than km_{tot}, otherwise it can be set variable according to adaptive procedures: the criterion adopted in the most part of this work is based on the maximum value d_{max} of the removed mass function $\bar{\Delta}^{sc}(s_w)$). For each step of the procedure, the height of material to be removed in normal direction along the wheel profile is set equal to a value $\hat{d}$, defined before the beginning of the procedure, which can be considered acceptable as a discretisation error. From experience, values of $\hat{d}$ on the order of 10^{-1} mm have proven to work fine.

At each step, the distribution of worn material evaluated after filtering the distribution itself, is scaled by a factor $\hat{d} > d_{max}$ in order that d_{max} becomes equal to $\hat{d}$: if this factor is greater than 1, it means that the wear progress in that step has been slower than the acceptable rate, hence the correspondent real mileage can be magnified by this factor to speed up the procedure. On the contrary, a ratio less than 1 means that the wear progress is faster than the acceptable rate for the required accuracy and thus the equivalent real covered distance is reduced by the same factor. As a conclusion, while with the constant step arrangement the changes in the wear rate are detectable by observing the difference in two consecutive wheel profile, with the variable step procedure the variations are indicated by the progress of the km_{step}.

7) Profile update:

$$\begin{pmatrix} y_w(s_w) \\ r_p(y_w(s_w)) \end{pmatrix} - \bar{\Delta}^s_{sm}(s_w)\mathbf{n}^r_r \xrightarrow{re-parametrization} \begin{pmatrix} y_w(s^*_w) \\ r_n(y_w(s^*_w)) \end{pmatrix} \tag{4.18}$$

Finally, the profile for the next step is obtained removing the material in the normal direction from the current profile $r_p(s_w)$ (according to the function $\bar{\Delta}^s_{sm}(s_w)$) and then performing a new parametrisation, to get again a curve parametrised by means of the curvilinear abscissa. The choice of the normal direction to the profile to remove the material seems to be the most reasonable hypothesis.

CHAPTER 5

Statistical Approach to Tracks and Model Validation

This first part of this chapter is focused on the procedure used to derive a significant statistical description of the railway tracks, an essential task to make possible and rationalize the approach and the simulation work on a complex railway line, such as a railway net made up of more than one route covered by a certain number of vehicles in service. In the second part of the chapter, the validation of the whole model via numerical simulations on the statistical representation of the Aosta-Pre Saint Didier track will be shown and discussed.

5.1 The statistical approach

When the wear analyses have to be carried out on a set of tracks of considerable length by using at the same time accurate models for the vehicle and the wheel-rail contact, the utilisation of "railway line statistical model" may be a indispensable way to overcome a series of problems due to the computational times and the organisation of the simulations themselves. The basic idea is to substitute a complex railway net or the too long tracks to be simulated with a set of simpler tracks which can produce an equivalent amount and distribution of wear on the wheels. The need of a similar approach to the whole scenery is even higher if the wear analyses must be performed from a wheel profile optimisation point of view; a complete study, considering in detail the characteristics of the hundred of kilometers covered by the vehicle (curve radius, superelevation, speed) would imply a relevant number of simulations, where the contribution of each of them might be not much significant. In such cases it is of fundamental importance to sum up in a statistical model of the whole line the most relevant information about the real scenery on which the involved vehicles operate, in order to get results in terms of average behaviour of the vehicle-wheel profile coupling considered. In the following, the resultant statistical arrangement of the real tracks (or of the railway net) will be indicated, for the sake of brevity, with expressions such as "virtual track" or "mean line".

In the present work the statistical approach has been exploited to draw up the mean line of the Minuetto and the Vivalto-E464 composition, where the latter will sometimes be referred to as "the mean line of Vivalto" for the sake of brevity. These two mean lines had to be a significant and equivalent synthesis of the whole set of tracks in Italian railways on which the two train compositions are operated every day. Moreover, the same strategy has been used also in drawing up a virtual track of the Aosta-Pre Saint Didier line for the model validation by comparison with available experimental results, as it will explained in Sec. 5.3.

The methodology is hence based on the knowledge and the exhaustive analysis of the tracks on which the vehicles operate as well as the relative number of weekly shifts. The shifts are arranged by the single districts of administrative competence of the overall covered railway net, which, in the present activity are the following:

- Minuetto Diesel: Firenze, Torino, Verona and Napoli;
- Vivalto-E464: Milano, Roma, Firenze, Genova, Bologna and Bari.

The extent of the analysed data for each district area is summarized respectively in Tab. 5.1 for the Minuetto and in Tab. 5.2 for the Vivalto, where the distances are in reality the sum of the products between the length of the sections and the relative number of weekly shifts, to taken into account the frequency of the service in each track. The whole data which permitted to build each virtual line were made available by Trenitalia S.p.A. and Rete Ferroviaria Italiana as electronic databases, paper plans and paper charts of the single tracks, with a consequent heterogeneous accuracy of the useful information.

Table 5.1. Percentage of analysed data for the Minuetto vehicle.

District area	**Analysed distance** (km)	**Total distance** (km)	%
Firenze	15576	37043	42.0
Torino	52220	78358	66.6
Napoli	16740	32939	50.8
Verona	15182	22715	66.8
Total	85719	171055	50.1

Table 5.2. Percentage of analysed data for the Vivalto vehicle.

District area	**Analysed distance** (km)	**Total distance** (km)	%
Firenze	17934	21588	83.1
Milano	5261	8206	64.1
Bologna	11235	14547	77.2
Genova	1636	1712	95.5
Bari	4667	4668	99.9
Roma	33195	103257	32.1
Total	73929	153978	48.0

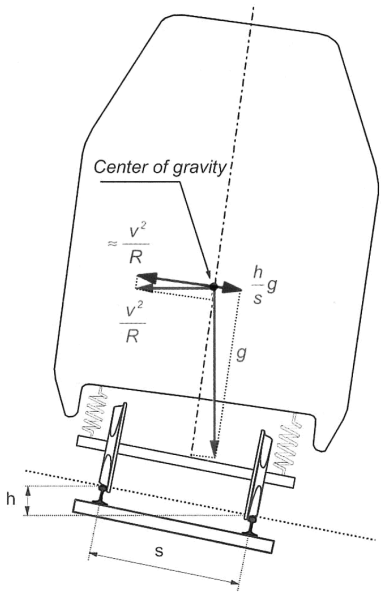

Figure 5.1. Accelerations in curve.

Before proceeding, a brief review of the concept of *non-compensated acceleration* or the equivalent *cant deficiency* can be useful in the following. The term "cant deficiency" is defined for a rail vehicle running at constant speed on a constant radius curve. In this context the term "cant", that should not be confused with the cant of a single rail previously discussed in detail, refers to the superelevation of the curve, that is, the elevation of the outside rail minus the elevation of the inside rail (see Fig. 5.1). The cant reduces or eliminates the influence of centrifugal acceleration, improving the passenger comfort and the horizontal loading of the track and allowing the vehicle to run at higher speed being the curve radius the same. The remaining part of the centrifugal acceleration which is not balanced by the component of the gravity acceleration tangent to the track is the non-compensated acceleration a_{nc}:

$$a_{nc} = \frac{V^2}{R} - g\frac{h}{s_t}\,, \tag{5.1}$$

where s_t is the nominal distance (1.500 m) between the two contact points on the wheelset when it is centred on the track and V the train speed. For a given speed V, the ideal cant for which the non-compensated acceleration vanishes is then:

$$a_{nc} = 0 \Rightarrow \hat{h} = \frac{s_t V^2}{gR}\,. \tag{5.2}$$

Since the ideal cant $\hat{h}$ is a function of the speed, if on the same curve run both passenger and freight trains, the effective cant has to be chosen as compromise to avoid an excess of cant for the slow-running traffic. As a result, for high speed train the cant is often lower than the ideal cant and a cant deficiency can be defined as:

$$h_d = \frac{s_t V^2}{gR} - h = \hat{h} - h\,. \tag{5.3}$$

Carrying on the main topic, since the idea is to obtain a set of simple right curved tracks, each of them characterized by curve radius, superelevation height and a travelling speed, as a first step the whole data for each vehicle have been grouped in radius classes, according to the classification shown in Tab. 5.3. The criterion on which the table have been generated is the rigid angle of attack of wheelsets, that is, the difference in yaw angle between the effective position of the wheelset in the track and the radial position by assuming zero equivalent yaw flexibility in the primary suspensions. Consequently, the rigid attack angle is a theoretical borderline case which represents the worst possible condition of guidance because the bogie (or the vehicle, if it is a two-axle vehicle) follows the track maximising the travelling resistance and the wear in negotiating curves. Conversely, the radial position is usually the condition through which the resistance and the consequent wear are minimised, not to mention the significant benefits in safety against derailment, since even the longitudinal position of the contact patch on the flange of the external wheel is reduced to almost zero.

Table 5.3. Classification intervals based on the rigid angle of attack.

Max rigid angle (mrad)	**Min rigid angle** (mrad)	**Min radius** R_m (m)	**Max radius** R_M (m)	**Mean radius** R_r (m)
6.0	5.5	227	208	217
5.5	5.0	250	227	238
5.0	4.5	250	278	263
4.5	4.0	278	313	294
4.0	3.5	313	357	333
3.5	3.0	357	417	385
3.0	2.5	417	500	455
2.5	2.0	500	625	556
2.0	1.5	625	833	714
1.5	1.0	833	1250	1000
1.0	0.5	1250	2500	1667
0.5	0.0	2500	10000	5000
0.0	0.0	1000	∞	∞

The rigid attack angle depends only on the bogie wheelbase and the radius of the curve and for this reason it is only an index to classify qualitatively the hypothetical wear severity of curved tracks. The rigid angle attack should not be confused with the effective steady angle of attack of wheelsets in curve (real or in simulation), which is strongly affected by other several parameters of the bogie (yaw stiffness, geometric quantities) as well as the wheel-rail contact condition (friction coefficient); moreover, each wheelset has its own angle of attack depending on the position in the bogie (trailing or leading wheelset) as well as on the bogie. The rigid angle represents a superior limit of the angle of attack when

the yaw stiffness provided by the primary suspensions (due to a couple of longitudinal stiffness elements which link each axlebox to the bogie frame) tends to infinitive. Bogies designed for high speed trains, having a remarkable stiffness in the primary suspensions tends to generate angle of attacks similar to the correspondent rigid angle in negotiating sharp curves. On the contrary, the opposite situation, that is an angle of attack equal to zero, is rarely verified notably for the leading wheelset of a bogie, because it would require a zero yaw stiffness, and this, for reasons due to requirement of stability of the vehicle in straight track, cannot be accepted.

Table 5.4. Distribution of the curve radius for the Vivalto.

Mean Radius (m)	**Frequency** (%)
217	0.01
238	0.01
263	0.01
294	0.07
333	0.15
385	0.34
455	1.99
556	1.82
714	3.34
1000	5.80
1667	5.42
5000	6.59
∞	74.45

Tab. 5.3 have been drawn up considering a bogie wheelbase equal to 2.5 m and a step of 0.5 mrad between each class. The reference radius of each class R_r has been calculated as a weighted average among the radii included in the class interval. For instance, the application of the criterion just introduced, in the case of the Vivalto, leads to the distribution of frequency summarized in Tab. 5.4, where the frequency of each radius class is calculated as the ratio between the overall length of each track included in the class itself and the total distance taken into account in the analysis.

In the statistical approach it is assumed that the wear evolution can be reproduced with a series of simulations on steady curves and straight tracks, neglecting the contribution of the transition lengths (parabolic curves and clothoids [1]) used to connect sections having different superelevation and curve radius. In fact, it would be conceptually difficult to classify and take into consideration these sections; for this reason, these transition lengths have been introduced only in the calculation of the length of curves, by assigning half length to the curve part and half length to the straight part or to the other adjacent section in case of consecutive curves. For all the missing transition lengths, the information of which were not available, a reasonable length has been introduced on the basis of the maximum allowable roll speed $\Omega \leq 0.038\,\mathrm{rad/s}$ and the maximum allowable derivative of the non-compensated acceleration $\Psi \leq 0.35\,\mathrm{m/s^3}$ for the rank to which the vehicle belongs.

The expressions of these two quantities are the following:

$$\Omega \cong \frac{\Delta h \cdot V}{s_t l}\,; \tag{5.4a}$$

$$\Psi \cong \frac{V \cdot \Delta a_{nc}}{l}\,; \tag{5.4b}$$

where the variation in superelevation Δh and s_t are expressed in mm, V is the constant vehicle speed in transition sections (in m/s), Δa_{nc} (m/s^2) is the variation in non-compensated acceleration and l (in m) the length of the transition section. The two above mentioned criteria can be satisfied at the same time by choosing an opportune value for the superelevation gradients dh/ds with respect to the curvilinear abscissa s of the track in the range 1–1.5‰ (mm/m), considering that $dh/ds \cdot l = \Delta h$.

The further division of each radius class in superelevation classes has been arranged as listed below, by grouping the class of superelevation in five groups and choosing a few height values in each of them:

- 0;
- 10–40: 10, 20, 30, 40;
- 50–80: 50, 60, 70, 80;
- 90–120: 90, 100, 110, 120;
- 130–160: 130, 140, 150, 160;

since in reality the superelevation heights are usually rounded to the nearest centimetre. For the purpose of the dynamic simulations, each superelevation class is represented by the reference value h_r to which corresponds the highest sum of products between section lengths and number of weekly shifts.

5.1.1 Determination of the speed in each class

In regarding to the speed V_r to be assigned to each track in the mean line, the choice has been made according to the table in Fig. 5.2, which summarizes the speeds in km/h to be observed by B-rank vehicles. In fact, there are four different rank classes in Italy (P, C, B, and A, in descending order of quality) which generally have to observe different speed limits in the same track.

The for each combination of curve radius and superelevation, the speed is chosen sufficiently high, according to a certain criterion: as depicted in the speed table, three criteria (corresponding to different sectors of the table) are taken into account. In order to explain the procedure, first of all the non-compensated acceleration can be generally thought as

$$a_{nc} = \frac{V^2}{R} - \frac{\hat{V}^2}{R}\,, \tag{5.5}$$

	Superelevation (mm)															
	0	10-40				50-80				90-120				130-160			
Mean radius (m)	0	10	20	30	40	50	60	70	80	90	100	110	120	130	140	150	160
217	45	45	50	50	50	55	55	55	60	60	60	65	65	65	65	70	70
238	45	50	50	55	55	55	60	60	60	65	65	65	65	70	70	70	75
263	50	50	55	55	60	60	60	65	65	65	70	70	70	70	70	75	75
294	55	55	55	60	60	65	65	65	70	70	70	70	70	75	75	80	80
333	55	60	60	65	65	65	70	70	70	70	70	70	75	80	80	85	85
385	60	65	65	70	70	70	70	70	70	70	75	75	80	85	85	90	95
455	65	70	70	70	70	70	70	70	70	75	80	85	90	90	95	100	100
556	70	70	70	70	70	70	70	75	80	85	90	95	95	100	105	110	115
714	70	70	70	70	70	70	80	85	90	95	100	105	110	115	120	125	130
1000	70	70	70	70	75	85	90	100	105	115	120	125	130	135	140	145	150
1667	70	70	70	85	95	110	120	130	140	145	155	160	160	160			
5000	70	85	120	145	160												

Figure 5.2. Speed table suitable for B-rank vehicles having a maximum service speed of 160 km/h.

in which V is a generic speed in the track and $\hat{V}$ is the speed for which the non-compensated acceleration is zero because the centrifugal force is exactly balanced by the component of the gravitational force along the tangent plane to the track. In particular, let V_{max} be the maximum speed on the considered track, so that $\hat{V} = cV_{max}$ the (5.5) becomes

$$a_{nc} = \frac{V_{max}^2}{R} - \frac{\hat{V}^2}{R} = \frac{V_{max}^2}{R}(1 - c^2)\,. \tag{5.6}$$

In addition, the Eq. 5.2 can be resolved in terms of balancing speed for a given superelevation, by expressing the balancing speed as a fraction of the maximum speed:

$$\hat{V} = \frac{V_{max}}{c^2} = \sqrt{\frac{gRh}{s_t}}\,. \tag{5.7}$$

After changing the units to have the speed in km/h, the (5.6) and the (5.7) provide a system of two equations in the unknowns V_r and a_{nc}, where the first one is the reference speed to be used in each subclass of the mean line, chosen equal to V_{max}:

$$V_r^2 = \frac{(Rh_r}{11.8c^2}\,; \tag{5.8a}$$

$$a_{nc} = \frac{V_r^2}{12.96}(1 - c^2)\,, \tag{5.8b}$$

For each sector of the speed table depicted in Fig. 5.2, the speed is chosen by means of the system (5.8) according to different criteria listed below.

Dark sky blue sector

In this sector the reference speed V_r is chosen so that the height of superelevation is proportional to the non-compensated lateral acceleration, after assuming $c = 0.8$. More precisely, the speed for each combination of superelevation and radius is given by $V_r =$

$\min(\tilde{V}_r, 130)$ for the Minuetto and $V_r = \min(\tilde{V}_r, 160)$ for the Vivalto, where $\tilde{V}_r$ is defined as

$$\tilde{V}_r = 1.06\sqrt{\frac{Rh_r}{7.55}}\,, \tag{5.9}$$

where the radius curve is in m, and the height of superelevation is in mm; the factor 1.06 means that the speed can be increased by 6% with respect to the value included in the radical, because the vehicle belongs to the B-rank class (both the Minuetto and the Vivalto are B-rank vehicles). In a few words the a_{nc} is slightly variable being the coefficient c constant for the combination of this group. The speed of the other subtracks belonging to the same dark sky blue group can be derived in the same way: the final speeds are rounded down to the nearest multiple of 5 km/h.

Yellow sector

In the yellow part the speed of each subtrack is chosen lower or equal to 70 km/h in order to avoid a non-compensated acceleration greater than $0.8\,\mathrm{m/s^2}$, as prescribed by the regulations in force for the B-rank vehicles. In detail, $V_r = \min(\tilde{V}_r, 70)$ where the $\tilde{V}_r$ in this case is equal to

$$\tilde{V}_r = 3.6\sqrt{R(g\frac{h}{s_t} + 0.8)} \quad (\mathrm{km/h})\,. \tag{5.10}$$

Clearly, with this choice the coefficient c would be variable within the combinations of this sector.

Dark sky blue sector

$$V_r = 70\,\mathrm{km/h}\,; \tag{5.11}$$

this group comprises all the remaining combinations for which the superelevation is lower than the value corresponding to the one arising from the proportionality criterion mentioned in the first case. The speed is set to 70 km/h everywhere after being evaluated for the lowest mean curve radius (217 m) with a superelevation of 160 mm.

There also cases which are only exceptions to the rules just presented and they will not be discussed further.

5.2 The virtual tracks of the Minuetto and the Vivalto

The application of the criteria explained in the previous section have provided the two mean lines reported in Tab. 5.5(a) for the Minuetto and in Tab. 5.5(b) for the Vivalto: the mean radius, the speed, the superelevation and the statistical weight of each class have also been specified. The virtual track of the Minuetto is made up of 34 classes while the Vivalto

mean line consists of 31 classes and a considerable amount of straight track with respect to the Minuetto (74 % instead of 52 %).

The division in classes is also convenient, from an organizational point of view, when the same are divided in groups so that the overall computational time in completing the multibody simulations of each group is much the same: the number of the groups depends on the maximum number of processes allowed by the CPU.

Table 5.5. Virtual tracks.

(a) Minuetto

R_m (m)	R_M (m)	R_r (m)	h_{range} (mm)	h_r (mm)	V_r (km/h)	p_k %
250	278	**263**	90–120	90	65	1.90
			130–160	160	75	4.21
278	313	**294**	90–120	90	70	1.11
			130–160	160	80	1.62
313	357	**333**	90–120	90	70	0.44
			130–160	140	80	1.24
357	417	**385**	50–80	50	70	0.80
			90–120	120	80	1.33
			130–160	150	90	4.17
417	500	**455**	50–80	80	70	1.44
			90–120	100	80	4.72
			130–160	130	90	1.29
500	625	**556**	10–40	10	70	0.14
			50–80	80	80	1.52
			90–120	90	85	2.01
			130–160	150	110	1.46
625	833	**714**	10–40	10	70	0.09
			50–80	70	85	1.56
			90–120	90	95	1.77
			130–160	130	115	0.78
833	1250	**1000**	10–40	10	70	1.10
			50–80	50	85	2.41
			90–120	120	130	2.16
			130–160	140	130	0.93
1250	2500	**1667**	0	0	70	0.17
			10–40	30	85	1.91
			50–80	80	130	1.68
			90–120	90	130	0.99
			130–160	150	130	0.17
2500	10000	**5000**	0	0	70	1.08
			10–40	20	120	1.21
			50–80	50	130	0.25
			90–120	100	130	0.004
		∞				52.3

(b) Vivalto-E464

R_m (m)	R_M (m)	R_r (m)	h_{range} (mm)	h_r (mm)	V_r (km/h)	p_k %
278	313	**294**	90–120	100	70	0.04
			130–160	140	75	0.03
313	357	**333**	90–120	120	75	0.74
			130–160	160	85	0.74
357	417	**385**	50–80	60	70	0.82
			90–120	90	70	0.07
			130–160	160	85	0.19
417	500	**455**	50–80	50	70	0.03
			90–120	120	90	0.20
			130–160	150	100	1.76
500	625	**556**	10–40	30	70	0.02
			50–80	60	70	0.15
			90–120	120	95	0.36
			130–160	140	105	1.29
625	833	**714**	10–40	20	70	0.03
			50–80	80	90	0.25
			90–120	90	95	1.14
			130–160	160	130	1.93
833	1250	**1000**	10–40	40	70	0.07
			50–80	80	105	1.87
			90–120	120	130	1.80
			130–160	160	150	2.05
1250	2500	**1667**	0	0	70	0.09
			10–40	40	95	0.56
			50–80	80	140	2.27
			90–120	110	160	1.78
			130–160	160	160	0.73
2500	10000	**5000**	0	0	70	0.51
			10–40	30	145	3.96
			50–80	50	160	2.12
			90–120	90	160	0.003
		∞				74.4

Notwithstanding the needs to generate a single profile for the whole vehicle, the model can easily handle different wheel profiles to distinguish the wear evolution of each wheel, axle or bogie. Nevertheless, among these four strategies to generate the output profiles, the mean on the axle or on the vehicle are surely the most interesting. In fact, the mean on the bogie does not add much information because the difference between bogies consists above all in the vertical load and in the position along the vehicle which has an certain influence on the dynamic behaviour (and hence on the wear) but the overall effect is usually not so considerable. Instead, the mean on the single wheel, being the result "side-dependent" cannot be used in the statistical approach with only right curve but only on a single track, because the two side of the vehicle would be subjected to progress and distribution of wear completely different and unreal.

5.2.1 The worn rail profiles

With respect to what has been presented thus far in building the virtual tracks, detailed information about the track geometry have not been introduced yet. In particular, nothing has been said about the rail profile to be used in simulation. The simple hypothesis of a constant rail profile (a UIC60 rail profile for example, the standard for the Italian Railways) for all the tracks could be useful to overcome any conceptual difficulty in building a significant model of a railway net, but at the same time it can greatly reduce the validity of the results. In fact, the shape of the rails affects the position of the contact points both on rails and on wheels, the contact forces and, as a consequence, the amount of wear and its distribution.

In this work, the available data on the rail profiles, provided by Trenitalia and RFI, have been exploited to select a series of rail profiles to be used as constant profiles in the multibody simulations. According to the working hypothesis, based on the whole collected data, that in small radius curves it is easier to find a deeply worn rail profile than in straight tracks or large radius curves, a pair of representative rail profiles, in a statistical sense, has been selected for each radius curve interval.

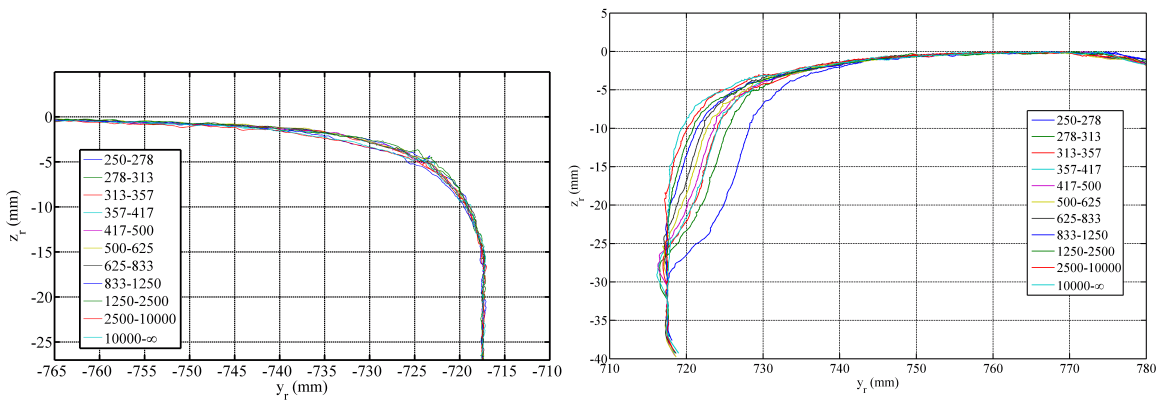

(a) Internal (b) External

Figure 5.3. Unfiltered profiles of internal and external rails (cant of 1/20 rad).

In detail, the population of the curve radius comprises the same 11 classes of the mean line and for each class a left and right rail profile have been assigned. The choice of these profiles has been made by analysing the data concerning rails in different regions of Italy (Tuscany, Latium, Veneto, Trentino-Alto Adige and Sicily) and by calculating the average wear at 45 degrees. The rail profile having the minor deviation with respect to this average wear have been selected as the representative external rail profile of the class, where the associated profile on the other side of the track has been selected as the internal one.

The internal and external rail profiles which have been chosen are shown in Fig. 5.3; the second ones are also compared in detail with the unworn UIC60 in Fig. 5.4. The worn rail geometry, acquired through an optical tools (the GF2 system) included a certain amount of numerical noise and they had to be treated in order to smooth the profiles and their

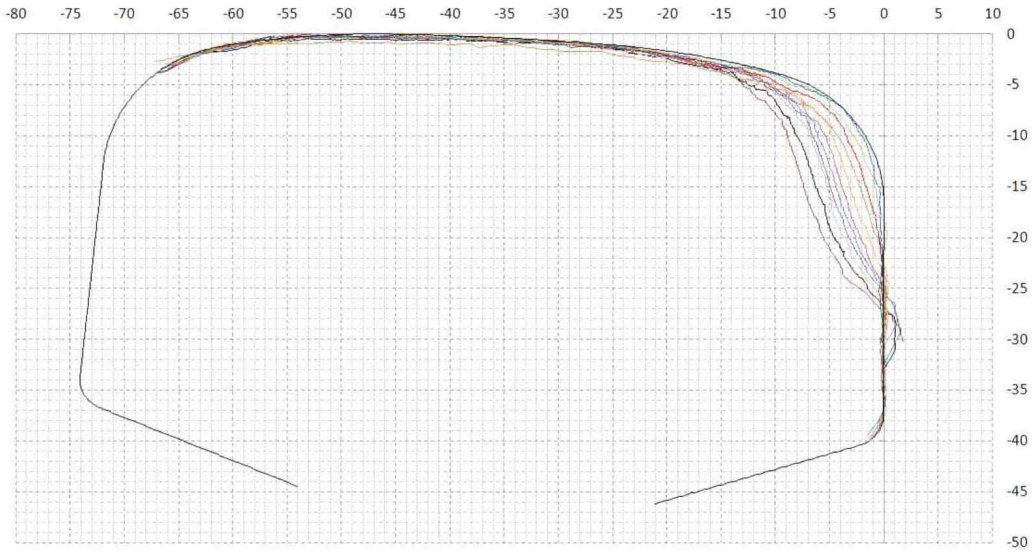

Figure 5.4. External rail worn profiles compared with the unworn UIC60 rail profile (cant of 1/20 rad).

derivatives. To this end, the data were filtered with a sliding mean filter and then the rail profile have been rebuilt through several sections of cubic splines. Finally, these pairs of rail profile have been associated to each class of the two virtual tracks depending on the radius curve.

5.3 The Aosta-Pre Saint Didier line: model validation

Besides the determination of the Italian virtual tracks for the Minuetto and the Vivalto, the statistical approach have also been used for the validation of the whole model. In particular, the method has been applied in order to build a mean line starting from a real context of which experimental data were available. The scenery in question is the Aosta-Pre Saint Didier line, a track of about 26 km of length with sharp curves where the Minuetto exhibited serious problems of precocious wear.

The distribution of the curve radii is shown in Tab. 5.6: about the 57 % of the total length corresponds to small radius curve, with curve radii between 150 m and 250 m. In light of these high and frequent curvatures, the first class in Tab. 5.6 have been further split.

Finally, the statistical approach to the Aosta-Pre Saint Didier railway line has provided the classification shown in Tab. 5.7, made up of 18 different classes (17 curves and the straight track). The results are summarized in the last four columns: the mean curve radius R_m, the representative superelevation h, the travelling speed V and the percentage weight p_k, $1 \leq k \leq N_C$. The speed of each track has been chosen according to the usual criterion; the max speed value in the track is equal to $V_{max} = 70$ km/h.

The validation of the model on the Aosta-Pre Saint Didier line has been performed by means of a constant new rail profile (UIC60), since the data about the worn rails were not available during this step of the work.

Table 5.6. Distribution of curvature in the Aosta-Pre Saint Didier track.

Max Angle (mrad)	**Min Angle** (mrad)	**Lower Radius** (m)	**Upper Radius** (m)	**Total Length** (m)	**Percentage** (%)
8.0	6.0	155	208	12439	40.0
6.0	5.5	208	250	5284	17.0
5.5	4.5	250	278	2103	6.77
4.5	4.0	278	313	897	2.89
4.0	3.5	313	357	676	2.17
3.5	3.0	357	417	454	1.46
3.0	2.5	417	500	71	0.23
2.5	2.0	500	625	189	0.61
2.0	1.5	625	833	348	1.12
1.5	1.0	833	1250	734	2.36
1.0	0.5	1250	2500	405	1.31
0.5	0.0	2500	10000	565	1.82
-	-	1000	∞	6918	22.2

Table 5.7. Mean line of the Aosta-Pre Saint Didier track.

R_m (m)	R_M (m)	R_r (m)	h_{range} (mm)	h_r (mm)	V_r (km/h)	p_k (%)
147.1	156.3	**150**	90–120	120	55	0.77
156.3	166.7	**160**	90–120	110	55	0.48
		165	130–160	140	55	0.56
166.7	178.6	**170**	90–120	110	55	0.82
		175	130–160	130	55	1.55
178.6	192.3	**190**	90–120	100	55	8.37
		180	130–160	130	55	0.45
192.3	208.3	**200**	90–120	90	55	20.64
			130–160	130	60	4.00
208.3	227.3	**220**	50–80	80	55	0.70
			90–120	100	55	3.76
227.3	250.0	**240**	50–80	80	55	7.26
			90–120	110	60	5.28
250.0	312.5	**270**	50–80	70	55	3.91
			90–120	90	60	5.29
312.5	416.7	**370**	50–80	60	55	2.26
		345	90–120	100	70	1.63
416.7	∞	∞	0	0	70	32.27

5.4 Reference dimensions of wheel profiles

Before continuing with the validation of the model, it is useful to give a brief description of the wheel profile quotas which are of interest in this context. According to the regulations in force [37], the state of wear in a wheel can be easily represented through three reference dimensions, without a complete detection of the whole 2D profile. The three dimensions and the adopted nomenclature are the following (Fig. 5.5):

- the *flange thickness* fT;
- the *flange height* fH;
- the qR dimension.

With reference to the figure, these quantities are defined as follows:

- the point P0 on the profile is 70 mm distant from the internal side of the wheel;
- the point P1 is 2 mm above the lowest point V of the flange on the wheel profile;
- the point P2 is 10 mm below P0 on the profile;
- the flange thickness fT is defined as the distance between P2 and the internal vertical side of the wheel; the qR is the horizontal distance between P1 and P0; the flange height fH is the vertical distance between P0 and V. P0 is also the point where the conventional rolling radius of a wheel is taken.

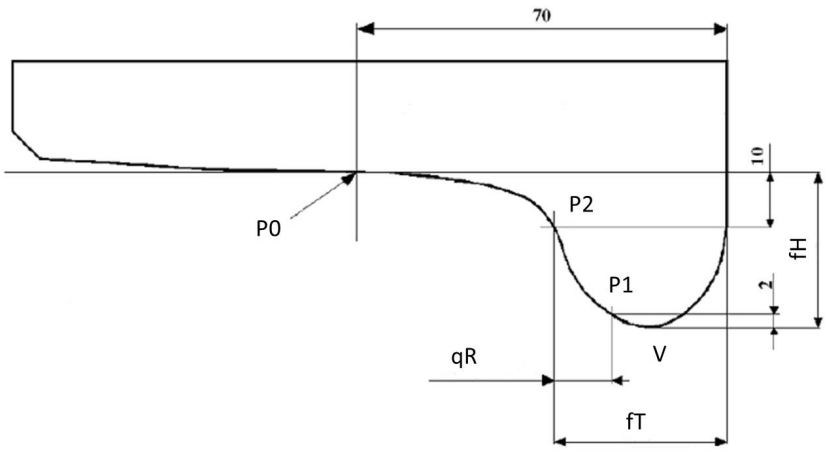

Figure 5.5. Reference dimensions of the wheel profile.

Because of the way the quotas are defined, they are positive and do not depend on the wheel rolling radius. The values of these parameters are measured periodically in order to decide whether the profile has to be re-turned or not (if it is still possible), considering the maximum or minimum values suggested by the regulations [37]. These limit values are reported in Tab. 5.8.

Table 5.8. Limit values (mm) of the flange height, the flange thickness and the qR quota for a wheel with an actual diameter equal to d (mm).

		$d \leq 630$	$630 < d \leq 760$	$760 < d$
fH	min	31.5	29.5	27.5
	max		36	
		$d \leq 760$	$760 < d \leq 840$	$840 < d$
fT	min	27.5	25	22
	max		33	
qR	min		6.5	

As regards their physical meaning, both the flange thickness fT and the flange height fH describe the size of the flange: variations of the first quota are due to the action of the wear which progressively reduces the thickness of the flange and its structural resistance, while the rise of the flange height is a measure of the wear on the tread. Conversely, the qR dimension is a shape parameter which quantifies the local conicity on the flange. Although the performance in terms of dynamic behaviour depend on the coupling between the wheel and rail profiles rather than just the wheel profile, the check of the reference quotas aims to guarantee an acceptable running behaviour; in particular, the safety against the hunting in straight track at high speed and the derailment is of fundamental importance. The first phenomenon is enhanced by high values of equivalent conicity at the wheel-rail contact interface, while the second one can occur in case of worn wheel profile characterized by a low flange angle, which reduces, all other things being equal, the maximum allowable lateral force on wheel.

5.4.1 Treatment of the experimental data

The experimental data used in the model validation are the evolutions of the reference dimensions measured on three different ALn 501 "Minuetto" during the service on the Aosta-Pre Saint Didier line, which were conventionally named MD061, MD068, MD082. The Figs. 5.6, 5.7 and 5.8 show respectively the dimension progresses for all the wheels of each vehicle as a function of the travelled mileage (equal to 2500 km for the MD061 and MD068 and equal to 3500 km for the MD082). The overall mileage of the three vehicles is quite low but sufficient to produce appreciable variations in the wheel dimensions.

In the numerical simulations, the distance of 3500 km (km_{tot}) has been divided in $N_{step} = 10$ steps, with a resulting km_{step} equal to 350 km, corresponding to a km_{runs} equal to 400 m. These number are also summarized in Tab. 5.9.

During the model validation with the experimental data, both the strategies (the constant and the variable step) were tested before choosing the constant step. In fact, in this context, characterized by a low overall mileage, the constant step provides comparable

km	flange dimensions	1 r	1 l	2 r	2 l	3 r	3 l	4 r	4 l	5 r	5 l	6 r	6 l	7 r	7 l	8 r	8 l
		wheel diameter 816 mm		wheel diameter 815 mm		wheel diameter 824 mm		wheel diameter 823 mm		wheel diameter 823 mm		wheel diameter 823 mm		wheel diameter 819 mm		wheel diameter 820 mm	
0	FT	30.953	30.944	30.983	30.784	31.099	30.957	30.938	31.076	30.401	30.367	30.830	30.987	30.437	30.717	30.852	30.933
	FH	27.970	27.894	28.141	28.043	27.969	28.187	28.030	28.271	28.245	27.918	28.141	27.982	28.013	27.937	28.333	27.883
	QR	10.208	10.140	10.424	10.457	10.220	10.306	10.279	10.833	10.332	10.445	10.364	10.219	10.421	10.500	10.338	10.396
1426	FT	29.855	28.977	30.283	29.317	30.118	29.383	30.152	29.450	29.796	29.799	30.288	29.483	29.802	29.085	30.267	29.316
	FH	28.010	27.923	28.104	28.108	28.000	28.249	28.095	28.278	28.248	28.284	28.247	28.030	28.997	28.003	30.383	27.919
	QR	9.297	8.226	9.822	8.956	9.344	8.749	9.511	9.072	9.635	9.767	9.773	8.763	9.593	8.883	9.675	8.762
2001	FT	29.056	28.498	29.722	28.878	29.441	28.667	29.629	28.717	29.153	28.101	29.739	28.841	29.066	28.447	29.625	28.777
	FH	27.990	27.880	28.161	28,0,80	29.998	28.248	28.128	28.283	28.290	27.994	28.273	28.022	28.027	28.014	28.362	27.957
	QR	8.404	7.558	9.233	8.637	8.702	7.950	8.873	8.436	9.144	8.141	9.236	8.086	9.038	8.152	9.248	8.373
2575	FT	28.259	27.096	29.333	28.045	28.972	28.385	29.029	28.124	29.053	27.600	29.095	28.505	28.553	27.866	29.205	28.473
	FH	28.009	27.089	28.173	28.020	28.063	28.243	28.090	28.241	28.285	27.963	28.244	28.085	28.030	28.018	28.352	27.968
	QR	7.198	7.024	8.853	8.163	8.123	7.598	8.438	7.791	8.868	7.395	8.559	7.840	8.372	7.340	8.777	7.900

Figure 5.6. Experimental data of the ALn 501 "Minuetto" MD061.

km	flange dimensions	1 r	1 l	2 r	2 l	3 r	3 l	4 r	4 l	5 r	5 l	6 r	6 l	7 r	7 l	8 r	8 l
		wheel diameter 846 mm		wheel diameter 846 mm		wheel diameter 846 mm		wheel diameter 846 mm		wheel diameter 846 mm		wheel diameter 846 mm		wheel diameter 846 mm		wheel diameter 846 mm	
0	FT	30.919	31.320	30.754	30.825	30.934	30.549	31.083	30.626	31.066	31.038	31.002	30.758	30.687	30.957	30.895	30.709
	FH	28.270	27.826	28.329	27.968	28.137	28.084	28.091	28.084	28.257	27.995	28.295	27.811	28.390	27.651	28.221	27.518
	QR	10.613	10.083	10.716	10.273	10.430	10.006	10.024	10.006	10.511	10.364	10.509	10.408	10.700	10.338	10.335	10.080
1050	FT	30.428	29.918	30.259	29.803	30.390	29.358	30.333	29.513	30.582	29.723	30.367	29.488	30.191	30.580	30.415	29.004
	FH	28.228	27.876	28.325	27.922	28.148	28.006	28.091	28.112	28.262	28.092	28.307	27.884	28.383	27.710	28.245	27.552
	QR	10.134	8.684	10.377	9.267	9.973	8.740	9.615	8.834	9.980	9.083	10.130	8.998	10.202	8.965	9.895	8.370
2253	FT	28.753	28.218	29.117	29.014	28.776	27.530	28.970	28.218	28.687	27.722	29.022	27.512	28.809	27.845	29.141	27.306
	FH	28.304	27.911	28.344	28.054	28.202	28.104	28.085	28.216	28.295	28.099	28.320	27.926	28.382	27.698	28.318	27.632
	QR	8.604	7.209	9.130	8.382	8.294	7.326	8.238	7.343	8.395	7.444	8.793	7.274	8.862	7.065	8.662	7.034
2576	FT	28.142	27.978	29.128	28.867	28.690	27.570	29.122	28.008	28.465	27.621	28.888	27.448	28.482	27.882	28.829	26.971
	FH	28.278	27.883	28.335	28.037	28.213	28.102	28.113	28.171	28.236	28.172	28.341	27.889	28.406	27.792	28.180	27.581
	QR	8.142	7.111	9.032	8.237	8.064	7.246	8.213	7.422	8.058	7.319	8.692	7.284	8.470	7.070	8.181	6.940

Figure 5.7. Experimental data of the ALn 501 "Minuetto" MD068.

km	flange dimensions	1 r	1 l	2 r	2 l	3 r	3 l	4 r	4 l	5 r	5 l	6 r	6 l	7 r	7 l	8 r	8 l
		wheel diameter 846 mm		wheel diameter 846 mm		wheel diameter 846 mm		wheel diameter 846 mm		wheel diameter 846 mm		wheel diameter 846 mm		wheel diameter 846 mm		wheel diameter 846 mm	
0	FT	30.973	30.778	31.045	30.737	30.894	30.923	30.882	30.809	30.904	30.564	30.899	31.164	30.616	30.976	30.867	30.838
	FH	28.239	27.916	28.032	27.851	28.294	27.947	28.260	27.910	28.196	27.918	28.100	27.931	28.064	28.071	27.958	28.143
	QR	10.447	10.108	10.518	10.274	10.728	10.229	10.782	10.178	10.474	10.483	10.559	10.283	10.441	10.202	10.313	10.321
852	FT	30.917	30.360	30.836	30.311	30.563	30.429	30.824	30.276	30.910	30.092	30.666	30.536	30.317	30.564	30.530	30.141
	FH	28.189	28.043	28.040	27.917	28.332	28.050	28.331	28.008	28.237	27.914	28.170	28.002	28.213	28.126	27.866	28.130
	QR	10.141	9.800	10.256	9.912	10.405	9.865	10.466	9.951	10.284	10.015	10.220	9.812	10.496	9.721	10.147	9.835
1800	FT	29.732	29.221	30.039	29.238	29.880	29.304	30.039	29.273	29.861	28.849	30.221	29.317	29.644	29.682	29.969	28.716
	FH	28.209	28.001	28.009	27.908	28.374	27.995	28.240	28.061	28.285	27.923	28.165	28.014	28.110	28.126	27.975	28.179
	QR	9.206	8.619	9.503	8.765	9.672	8.644	9.831	8.792	9.372	8.856	9.609	8.650	9.334	8.992	9.321	8.341
2802	FT	28.439	28.114	29.278	28.364	28.854	28.568	29.557	27.885	28.527	27.958	29.497	28.178	28.552	28.907	29.100	27.727
	FH	28.165	28.044	28.088	27.897	28.287	28.024	28.293	28.045	28.233	27.883	28.128	27.931	28.072	28.126	27.562	28.201
	QR	7.844	7.348	8.733	7.885	8.762	7.871	9.065	7.486	8.385	7.885	9.009	7.321	8.172	8.224	8.390	7.431
3537	FT	28.160	27.821	29.012	28.121	28.523	28.306	28.998	27.566	28.260	27.643	28.538	27.804	28.054	28.658	28.524	27.244
	FH	28.196	28.021	28.062	27.928	28.320	28.056	28.298	27.996	28.314	28.002	28.229	27.956	28.067	28.130	28.075	28.202
	QR	7.106	7.234	8.460	7.553	8.383	7.608	8.707	7.111	7.809	7.455	8.229	7.176	7.920	7.917	7.851	7.273

Figure 5.8. Experimental data of the ALn 501 "Minuetto" MD082.

results in terms of accuracy and better performance from a numerical point of view. Conversely, the variable step has been chosen for most part of the simulations performed in this

Table 5.9. Values of km_{tot}, km_{step} and km_{runs}.

km_{tot} (km)	km_{step} (km)	km_{runs} (km)
3500	350	0.4

work; it has been set according to the absolute maximum of the removed material function (Fig. 4.7), as described in the relative section (Sec. 4.3). To make possible a comparison with the profile arising from the simulations, a single wheel profile progress for each vehicle has been evaluated taking the average of values of the quotas on the sixteen wheels (the mean results are given in Tab. 5.10). The data processing consisted of the following steps:

- scaling of the dimensions to eliminate the initial offsets, by imposing the nominal values at the beginning of the mileage;
- average of each dimensions on the sixteen wheels of a vehicle, in order to establish a single wheel profile progress to compare with the numerical results.

Table 5.10. Averaging and scaling of experimental data.

Vehicle	**Distance** km	qR (mm)		fH (mm)		fT (mm)	
		Mean	St. dev.	Mean	St. dev.	Mean	St. dev.
MD061	0	10.8	0.16	28.0	0.14	32.5	0.23
	1426	9.8	0.48	28.2	0.61	31.5	0.43
	2001	9.1	0.52	28.1	0.51	30.8	0.50
	2575	8.6	0.60	28.0	0.28	30.2	0.63
MD068	0	10.8	0.24	28.0	0.25	32.5	0.20
	1050	10.0	0.65	28.0	0.23	31.8	0.49
	2253	8.5	0.73	28.0	0.23	30.2	0.64
	2576	8.4	0.64	28.0	0.22	32.5	0.65
MD082	0	10.8	0.19	28.0	0.14	32.5	0.15
	852	10.6	0.25	28.0	0.14	32.3	0.26
	1800	9.6	0.44	28.0	0.13	31.3	0.44
	2802	8.7	0.58	28.8	0.18	30.3	0.56
	3537	8.3	0.51	28.1	0.13	30.0	0.50

The two steps have been performed on each "Minuetto" (MD061, MD068, MD082) without further averages on the three vehicles, preserving the mean behaviour of each of them and guaranteeing a tolerance zone for a better and more significant experimental data fitting.

5.4.2 Progress of the reference dimensions

This section presents the first results of the validation, showing the comparison between the numerically evaluated progresses of the three dimensions (flange thickness fT, flange

height fH and qR dimension) and the treated experimental data. A certain difference between numerical results and experimental data is present, probably due to the presence of other wear mechanisms; on average, the wear rate is slightly underestimated.

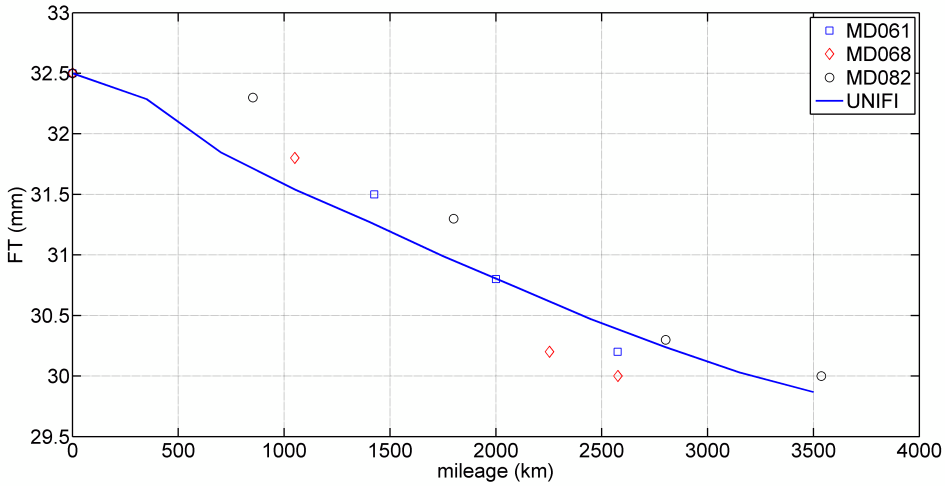

Figure 5.9. FT dimension progress.

The progress of the fT dimension is shown in Fig. 5.9; as it can be seen, the decrease of the quota is almost linear with the travelled mileage except in the first phases, where the profiles of wheel and rail are not conformal enough. The fH curve progress is presented instead in Fig. 5.10, which shows that, due to the presence of many sharp curves in the track and the low covered mileage, the wear is localized mainly on the flange rather than on the tread; thus the flange height remains nearly constant.

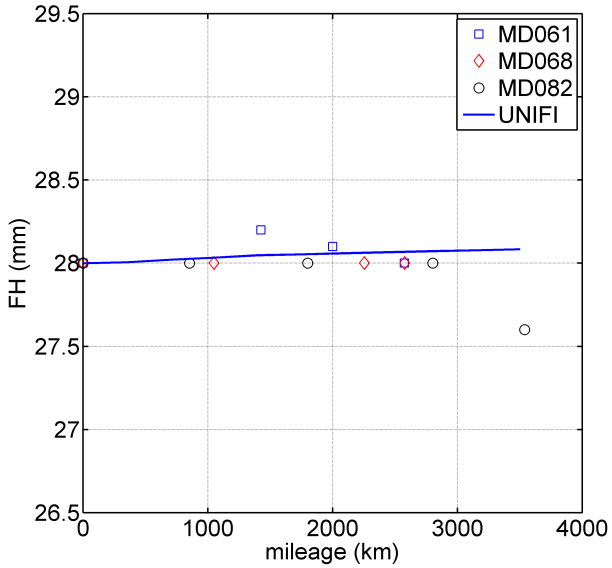

Figure 5.10. fH dimension progress.

The comparison between the real and simulated qR is finally shown in Fig. 5.11: the dimension decreases almost linearly too, leading to an augmentation of the conicity on

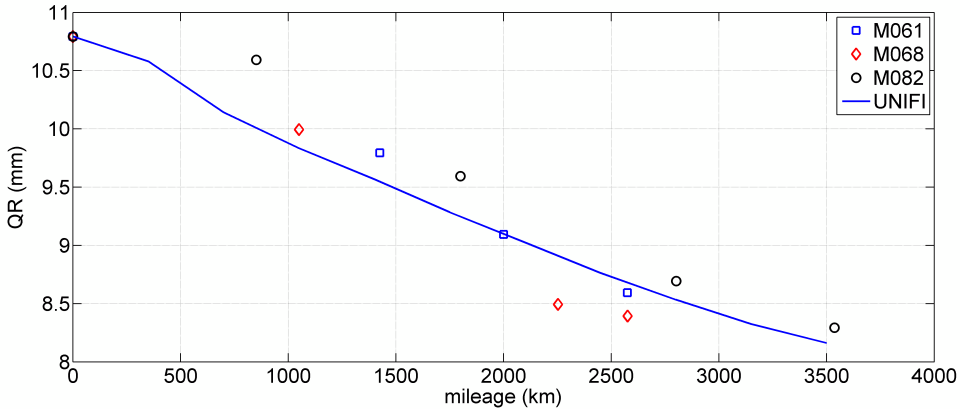

Figure 5.11. qR dimension progress.

the flange. Although the simulated mileage is quite short considering the mean covered distance between two turning of the wheels in a normal scenery, the variations of the fH and qR dimensions are remarkable and evidence difficulties in terms of wear in travelling this railway line with this vehicle.

As a conclusion, the comparisons show that the outputs of the wear model are very consistent with the experimental data, both for the flange dimensions (fT, fH) and the qR; therefore the validation of the model can be considered satisfactory.

5.4.3 Progress of the wheel profile

The numerical evolution of the wheel profile is presented in Fig. 5.12. Due to the low covered mileage and to the sharpness of the track, the wear is mainly localized on the flange rather than on the tread, where it is quite low and implies a slight reduction of the rolling radius.

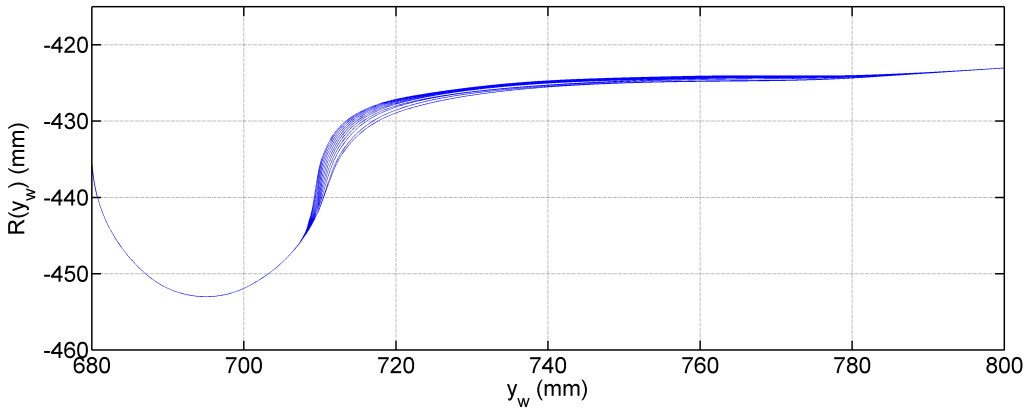

Figure 5.12. Evolution of the wheel profile.

However, in regard to the flange zone, the wear rate is higher during the first steps because of the non-conformal contact due to the coupling between the ORE S1002 wheel profile and the UIC60 rail with a inclination of 1/20 rad; then it decreases becoming more

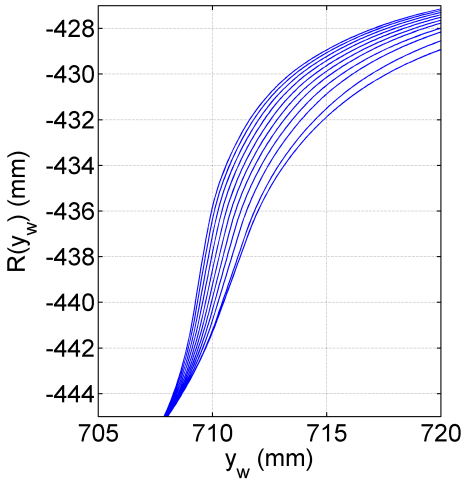

Figure 5.13. Evolution of the profile in the flange zone.

regular and constant in the last phases, when the contact is more and more conformal. The situation is clarified with the zoom on the flange zone, shown in Fig. 5.13: the distance between two consecutive profiles decreases as the wear increases.

CHAPTER 6

Formulation of the new wheel profiles

The following chapter is focused on the methodology which has been used in the development of the new wheel profiles to be tested by means of multibody simulations. The performance in terms of wear of the new profiles presented in this work have been compared with that provided by the current ORE S1002 wheel profile, adopted on the most part of the vehicles in service in the Italian railways.

6.1 Normative prescriptions for wheel profiles

For what regards the wheel profile, the European Standard EN 13715 [38] defines the tread profiles of wheels having a diameter greater than or equal to 330 mm used on vehicles running on European standard gauge tracks, to fulfil interoperability requirements in accordance with the International Union of Railways.

The above-mentioned standard describes the rules, the parameters and the construction methods of the wheel tread profile and also defines the geometry of the flange and the reverse slope, while thickness and height of the flange are determined by the railway undertaking or its representative in compliance with the normative documents in force.

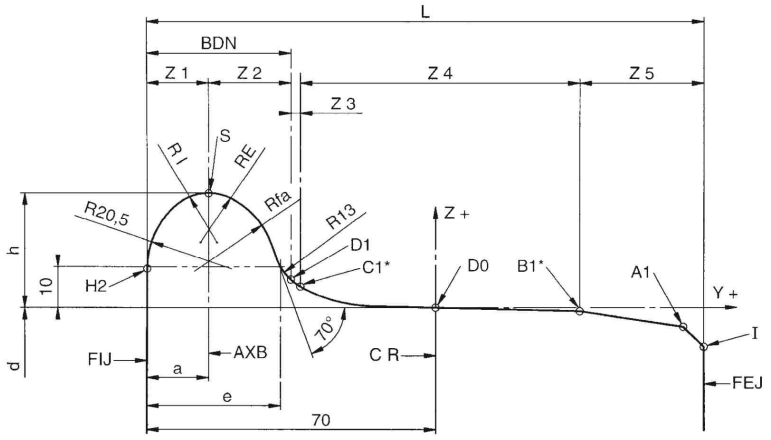

Figure 6.1. Wheel profile nomenclature [38].

In particular, the EN 13715 defines the geometry of the following three reference tread profiles for wheels and their reverse slopes:

- $1/40^{th}$ (reverse slope 15 %);
- S1002 (reverse slope 6.7 % or as an alternative 15 %) in conformity with UIC Leaflet 510-2;
- EPS (reverse slope 10 %).

These profiles apply to new wheels, both in the case of free-standing wheels or wheelsets, as well as to wheels that require re-profiling during maintenance. Any profile that does not conform to this standard shall only be used following agreement between the train operator and the infrastructure manager.

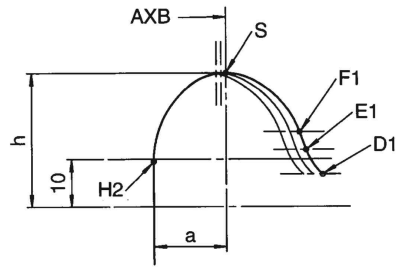

Figure 6.2. Changing in flange thickness by shifting of the D1-C1 zone.

The boundary conditions to be respected in building a new profile can be found rather constricting, both in the tread and the flange. Basically, the profile, of which the nomenclature is indicated in Fig. 6.1, comprises four zones:

- two zones H2-S and S-D1 having fixed geometry;
- a connection zone D1-C1, unique to each of the three profiles, to make a tangential connection at point C1;
- a zone C1-B1 (either B1a, or B1b, depending on the considered profile) unique to each profile;
- a zone B1-A1-I (either B1a or B1b), comprising the reverse slope and chamfer, unique to each reference profile; the reverse slope must be in the range 6.7 to 15 %.

The base profile is that obtained with a flange 32.5 mm thick and 28 mm high. Any other profile must be developed starting from this fundamental profile. The flange thickness can be lower than the standard value, but for structural resistance reasons the minimum allowable value is 28.5 mm. Nevertheless, the geometry of the flange is clearly almost fixed; for flange thicknesses greater than 28.5 mm, but less than 32.5 mm, the profiles are obtained by translating (Fig. 6.2) the zones D1-C1 (connection zone) and C1-T1 along the Y axis

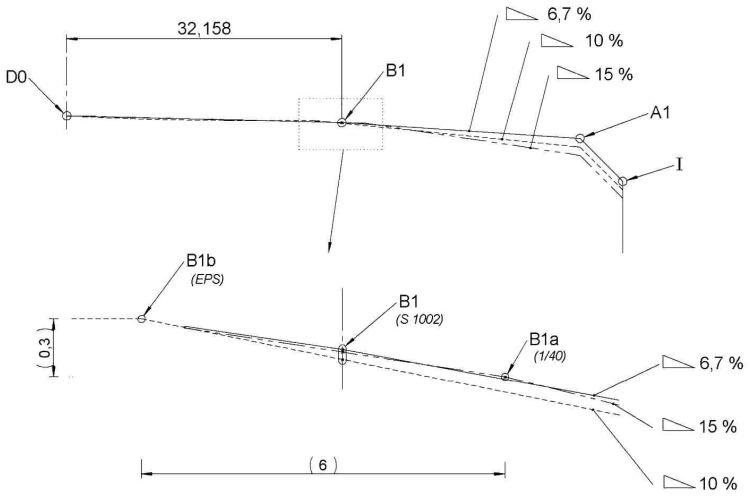

Figure 6.3. Reverse slope for the three profiles treated in the EN 13715 standard.

towards the internal face of the wheel by an amount equal to the reduction in thickness of the flange with respect to the standard value of 32.5 mm.

The reverse slope B1-A1 (Fig. 6.3) of the wheel profile is the external part which is connected to the tread in the B1 point (more precisely B1 for the S1002, B1a for the $1/40^{th}$ and B1b for the EPS), which, as previously stated, must have a slope between 6.7 and 15 %.

6.2 CD1 wheel profile

The CD1 wheel profile (*Contact Distribution* 1) is the first proposed proposed profile to replace the ORE S1002 without changing the rail cant. The basic idea behind this first new proposal is the attempt to achieve a wider and better distribution of the contact points both on the rail and the wheel surface as the wheelset moves laterally, thus avoiding the remarkable concentration in a few locations previously highlighted for the standard combination S1002-UIC60-1/20 (Fig. 1.15). In this sense the profile is conceived from a wear viewpoint for a better exploitation of the contact surfaces, especially the transition zone between the flange and the tread, where usually no contact occurs with the new profiles when the 1/20 rail cant is adopted.

The first step in building the CD1 profile was the assessment of the available clearance between wheelset and track for the 1/20 inclination, equal to about 6 mm as specified in Fig. 6.4; the other condition to be respected is the value of the contact angle γ, due to the inclination of the flange in the contact point when the wheelset is displaced laterally and flange contact occurs.

The profile has been built with the method schematically presented in Fig. 6.5. The basic idea is to express the lateral position of the contact point on the wheel as a function of the available flangeway clearance for each lateral position of the wheelset. By doing that, it is clear that there is no direct control on the consequent kinematic characteristics of the wheel-rail interaction (such as the RRD and the gravitational stiffness), thus an assessment

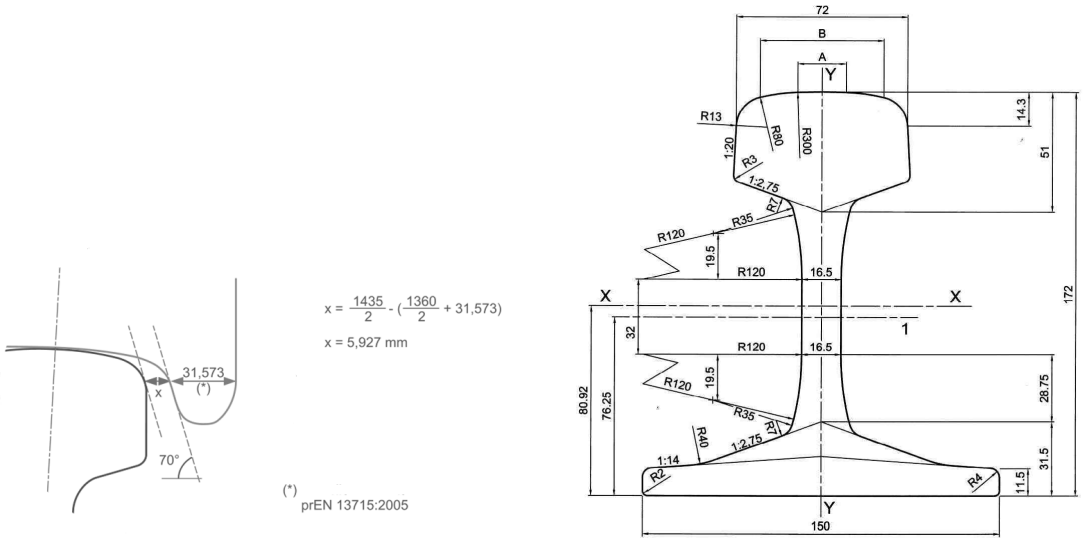

(a) (b)

Figure 6.4. Clearance between the wheel and rail profile measured 14 mm below the top of rail (a); detail of the UIC60 rail [39] (b).

of the contact geometry has to be carried out straight afterwards to verify whether the theoretical requirements of guidance and stability are satisfied.

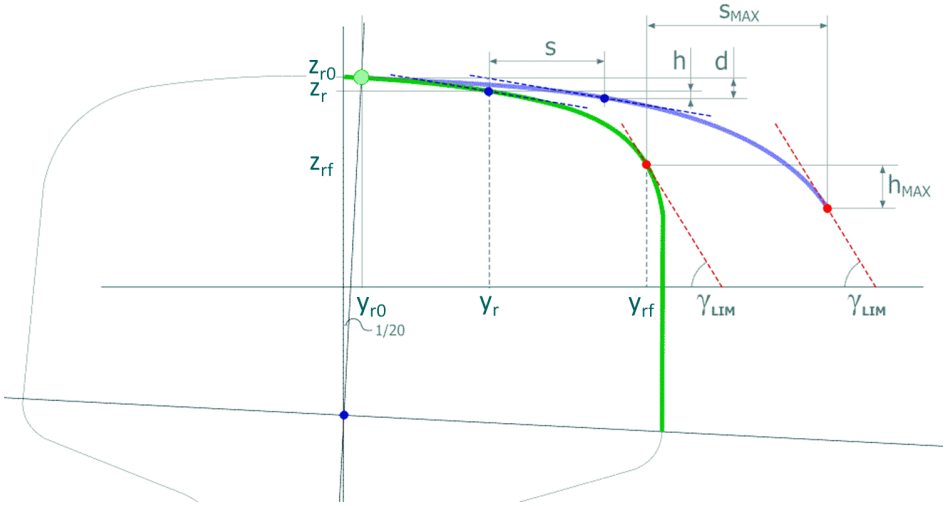

Figure 6.5. Nomenclature adopted in building the CD1 wheel profile.

With reference to the nomenclature presented in Fig. 6.5, for each point of the track (y_r, z_r) with $y_{r0} \leq y_r \leq y_{rf}$ corresponds a point of the wheel profile defined as follows:

$$y_w = y_r(s) + s\,, \tag{6.1a}$$

$$z_w = z_r(y_r) - h(s)\,. \tag{6.1b}$$

in which $0 \leq s \leq s_{max}$ and $h(s)$ can be evaluated by integration of the quantity h:

$$h(s) = -\int_0^s tan(\gamma(y_r(s')))ds' \,; \tag{6.2}$$

the boundary conditions for the integration are the following:

$$h(0) = 0 \quad h(s_{max}) = h_{max} \,; \tag{6.3a}$$
$$y_{r0} = y_r(0) \quad z_{r0} = z_r(0) \,; \tag{6.3b}$$
$$y_{rf} = y_r(s_{max}) \quad z_{rf} = z_r(s_{max}) \,; \tag{6.3c}$$
$$\gamma_0 = \gamma(y_{r0}) \quad \gamma_{lim} = \gamma(y_{rf}) \,. \tag{6.3d}$$

The relation $y_r(s)$ is arbitrary and can be chosen in different ways provided it satisfies the boundary conditions listed in (6.3). In regard to the present problem, as a first attempt, a simple polynomial function such as the following has been exploited:

$$y_r = \frac{y_{rf} - y_{r0}}{s_{max}^k} s^k + y_{r0} \quad k = 1, 2, \ldots . \tag{6.4}$$

Nevertheless, after a few attempts, the function described in Fig. 6.6 has been chosen in place of the previous one in order to:

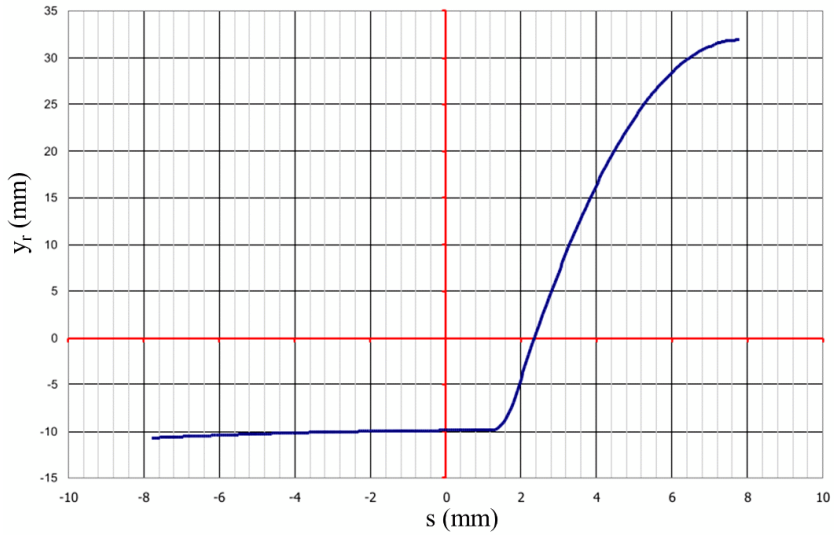

Figure 6.6. Graphical representation of the $y_r(s)$ function in building the CD1 profile.

- have a constant and low value of the equivalent conicity in the neighbourhood of the central position in the track;
- distribute the flange contact points on an higher area, to ease the effect of wear especially during the first thousands of kilometres.

The CD1 wheel profile has been proposed in three different versions which basically differ from each other in the flange thickness: 28.5, 30.5 and 32.5 mm. The wheel profiles

are shown respectively in Figs. 6.7, 6.11 and 6.14. The profiles are expressed by using a reference system with the origin in the point to which corresponds the nominal rolling radius (+750 mm with respect the wheelset centre) and consequently the coordinates do not depend on the nominal wheel rolling radius.

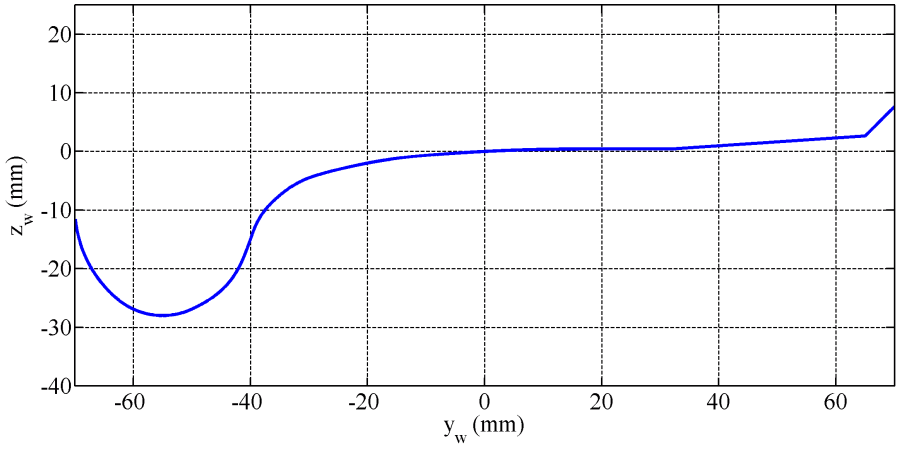

Figure 6.7. CD1 wheel profile with a flange thickness of 32.5 mm.

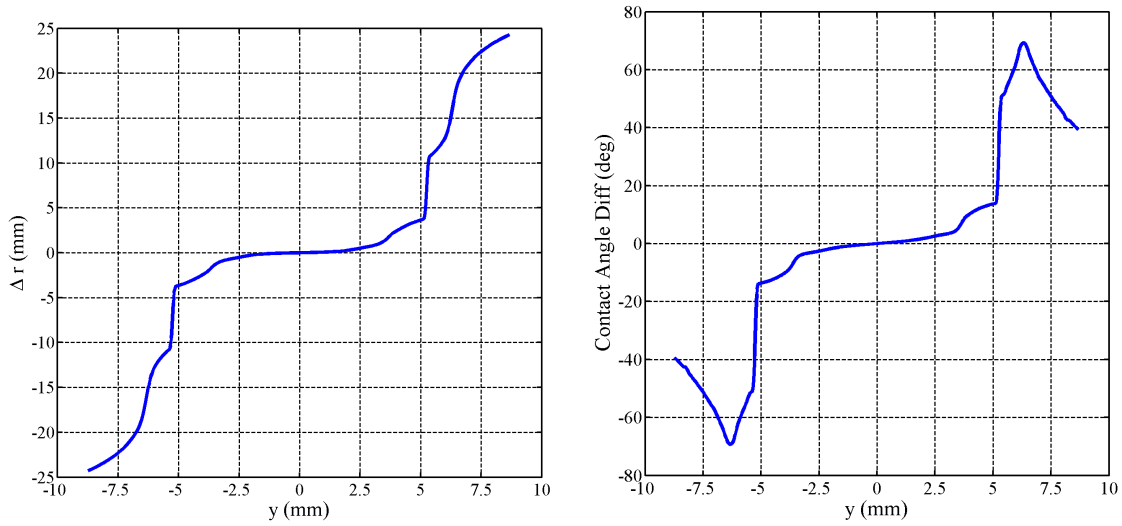

(a) (b)

Figure 6.8. Contact geometry characteristics of the CD1-32.5 mm profile (UIC60, 1/20 rad): Δr function (a), contact angle difference function (b).

For the standard profile with a flange thickness of 32.5 mm, the most interesting contact geometry characteristics are calculated for the matching characterized by UIC60, inclination of 1/20 rad, gauge of 1435 mm and reported in Figs. 6.8, 6.9 and 6.10. The RRD function and the contact angle difference are shown in the first one, while the lateral positions of the contact positions on wheel and rail are depicted in the second figure. The reference system of the rail is located on the top of the rail with the y_r axes pointing outward from the track. Regarding these functions, since the profiles of rail and wheel are symmetrical,

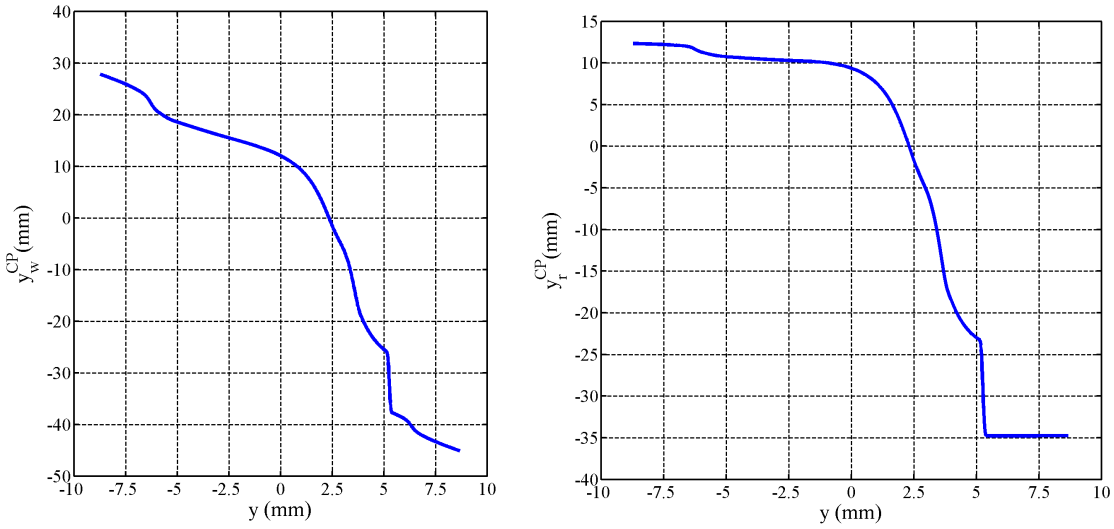

(a) (b)

Figure 6.9. Contact point positions for the CD1-32.5 mm profile on the right side of the track (UIC60, 1/20 rad): on wheel (a), on rail (b).

the graphs can be simply shown for only one side of the track, as it has been done for the contact point positions. Obviously, when the geometries are not exactly symmetrical, both the sides of the track must be included in the analysis.

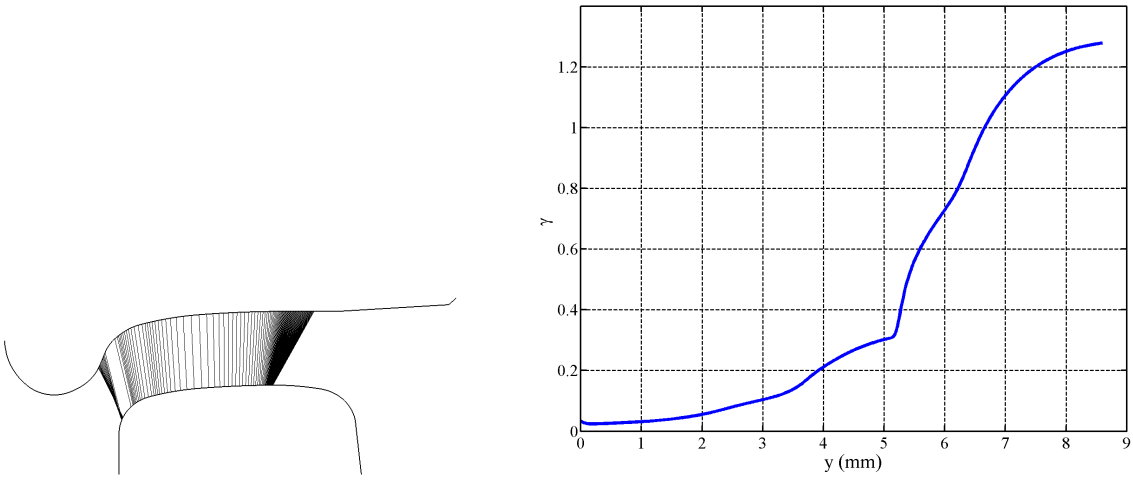

(a) (b)

Figure 6.10. CD1-32.5/UIC60 matching: Correspondence between wheel and rail contact point for a lateral displacement of $y = \pm 10$mm (a); equivalent conicity (b).

The equivalent conicity is calculated via harmonic linearisation and reported in Fig. 6.10, which shows that the value for small displacement is low enough to meet the stability requirements, whereas for $y = 4$ mm it is already greater than 0.2. The progress of conicity is clearly different from the one provided by the S1002 in the same conditions (see Fig. 1.15), which is characterized by a wide range (0-5 mm) where the conicity is almost constant.

Even for large amplitude the two profiles have their own behaviour, since the mean slope of the CD1 is greater than that given by the S1002.

The most important geometrical characteristics of the CD1 profile having a thinner flange are summarized from Fig. 6.11 to Fig. 6.16. The comparison of the three profiles CD1 in terms of conicity reveals that the functions are very similar and the two variants having a smaller flange seem to differ from the first one basically for a scaling factor in the wheelset lateral displacement.

6.3 DR2 wheel profile

In the following section the development and the characteristics of the second wheel profile proposed in the present research project will be analysed. For the sake of brevity, in the following this profile will be referred to as "DR2" profile (*Delta R*, second version).

The DR2 profile proposed in this work has been conceived by means of an approach totally different from the one exploited in building the CD1 profile. In place of a criterion based on the distribution of the contact points aimed at reducing the concentration of wear in a few locations, the strategy adopted in formulating the DR2 profile starts from kinematic considerations instead. The basic idea is to reproduce the kinematic behaviour of the S1002-UIC60-1/40 matching since it can be reckoned a good compromise among guidance, stability and resistance to wear. Clearly, for each railway application with its own track and vehicles, will exist an optimal solution once an objective function has been chosen, but in this work a better and general solution for more applications is being searched to resolve the main issues in the wheel-rail interaction on Italian Railways.

First of all, the nomenclature adopted for the profile formulation, consistent with the coordinate systems previously introduced, is shown in Fig. 6.17 where as usual the apexes r and w respectively refer to auxiliary and local reference systems. The position of the local reference system origin expressed in the auxiliary reference system is denoted by:

$$\mathbf{O}_w^r = [\ y \quad z(y)\ ]^T. \tag{6.5}$$

After introducing the apexes 1 and 2 to denote respectively the right and left wheel, the coordinates of the contact points in the auxiliary reference system can be written as follows:

$$\mathbf{P}_c^{r1} = [\ y^{r1}(y) \quad z^{r1}(y^{r1}(y))\ ]^T \tag{6.6a}$$

$$\mathbf{P}_c^{r2} = [\ y^{r2}(y) \quad z^{r2}(y^{r2}(y))\ ]^T. \tag{6.6b}$$

Similarly, the positions of the contact points in the local reference system are defined as

$$\mathbf{P}_c^{w1} = [\ y^{w1}(y) \quad z^{w1}(y^{w1}(y))\ ]^T \tag{6.7a}$$

$$\mathbf{P}_c^{w2} = [\ y^{w2}(y) \quad z^{w2}(y^{w2}(y))\ ]^T. \tag{6.7b}$$

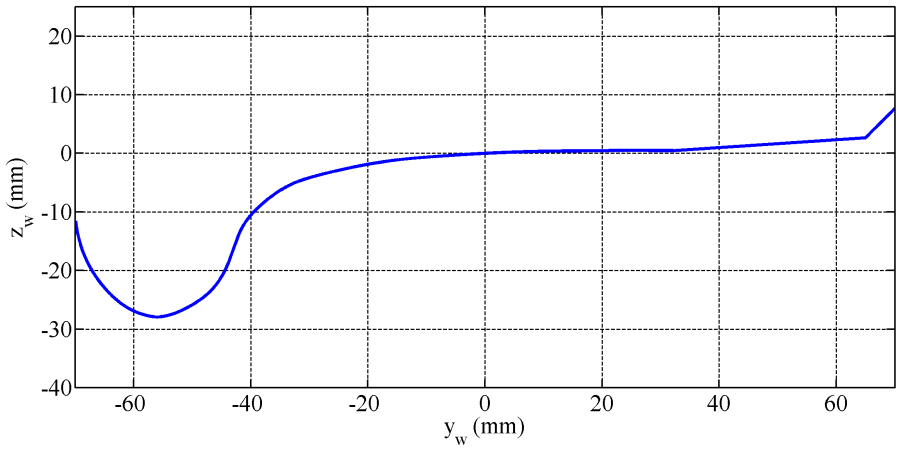

Figure 6.11. CD1 wheel profile with a flange thickness of 30.5 mm.

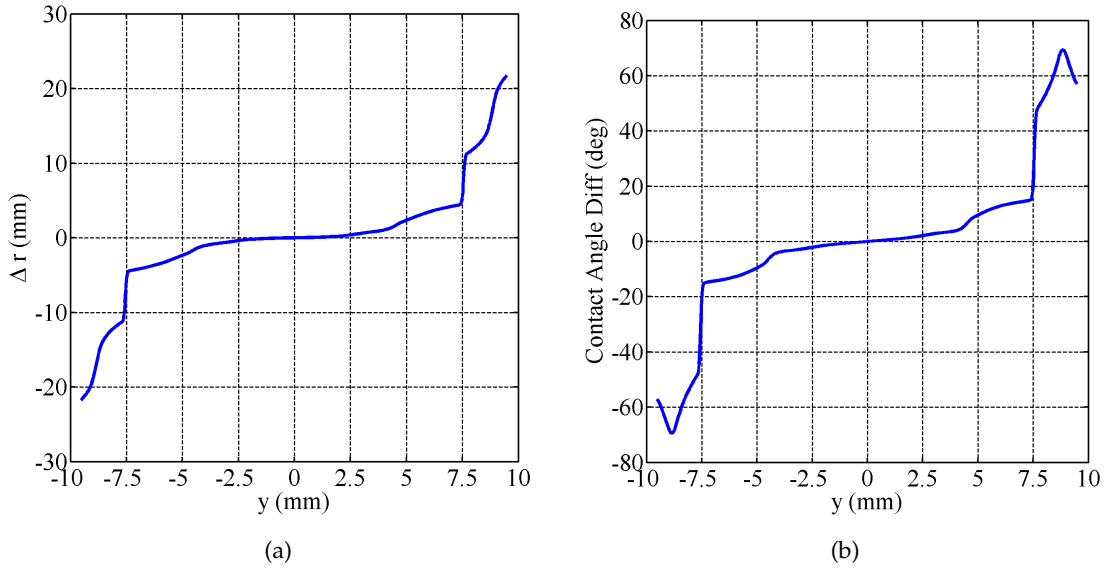

Figure 6.12. CD1-30.5 mm profile matched with UIC60 at 1/20 rad: RRD function (a); contact angle difference function (b).

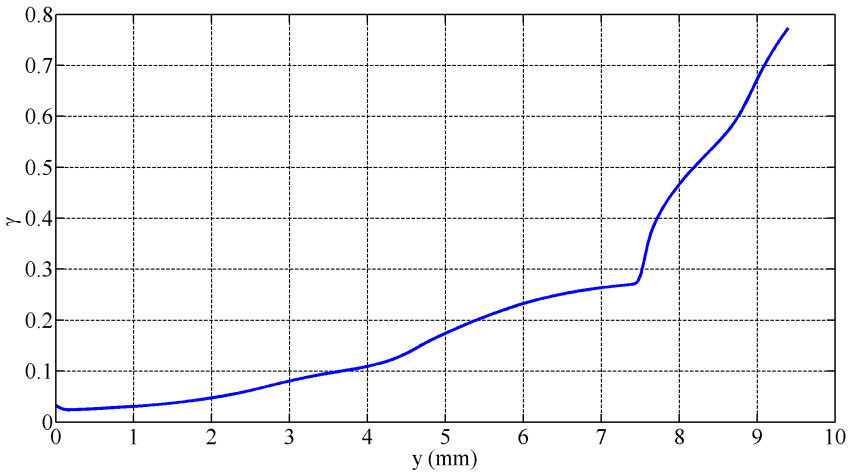

Figure 6.13. Conicity of the CD1-30.5 mm wheel profile matched with the UIC60 rail.

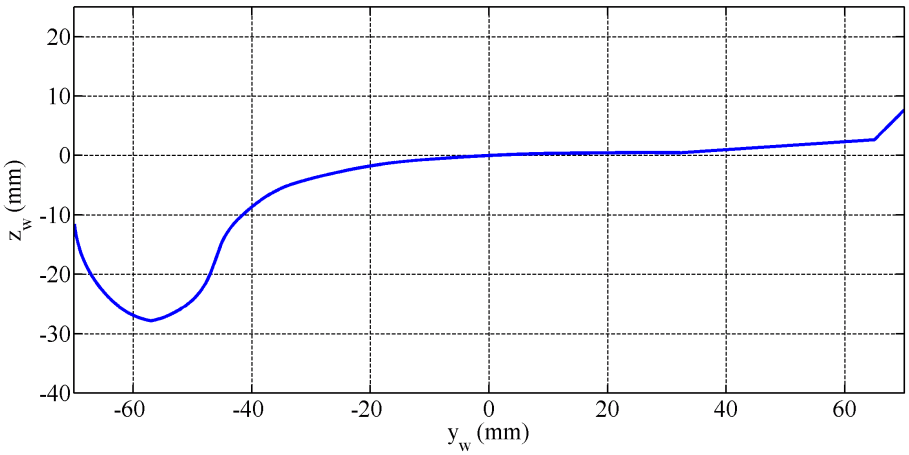

Figure 6.14. CD1 wheel profile with a flange thickness of 28.5 mm.

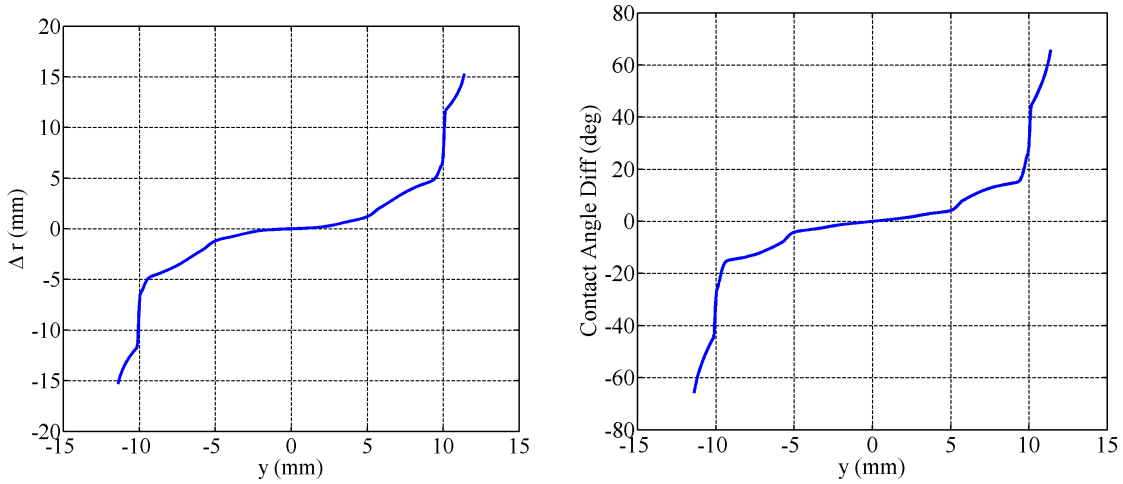

Figure 6.15. CD1-28.5 mm profile matched with UIC60 at 1/20 rad: a) RRD function, b) contact angle difference function.

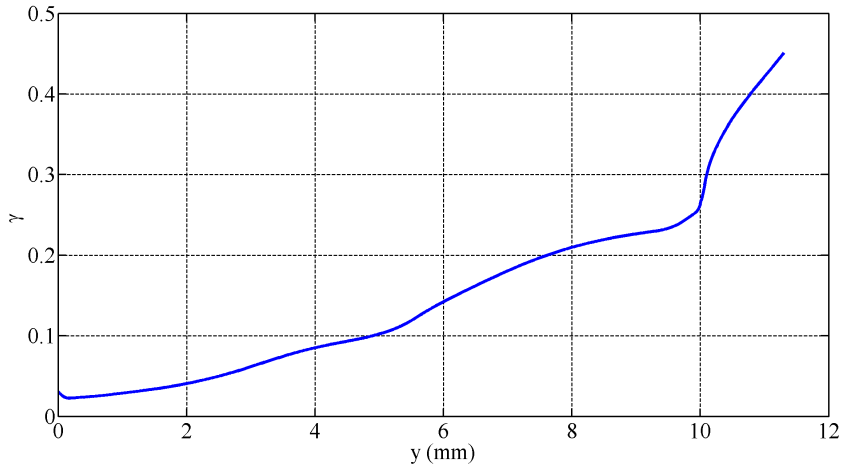

Figure 6.16. Conicity of the CD1-28.5 mm wheel profile matched with the UIC60 rail.

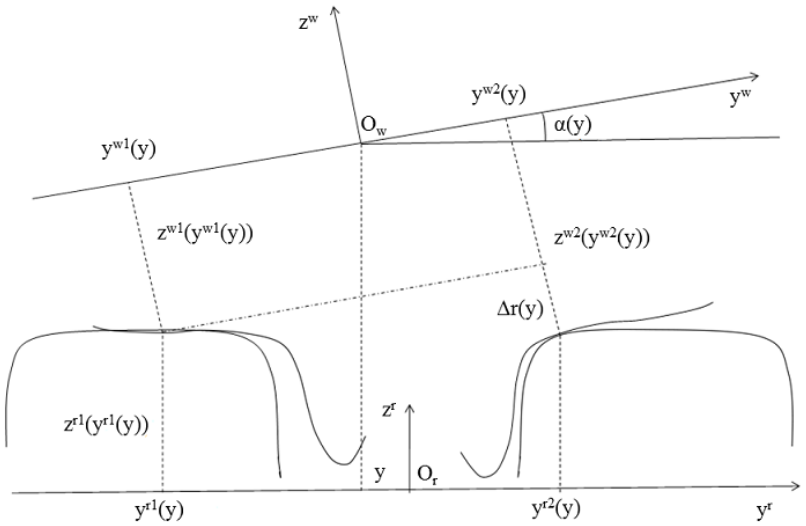

Figure 6.17. Nomenclature in building the DR2 wheel profile.

In the present research activity, the maintaining of the kinematic properties of the 1002-UIC60 canted at 1/40 rad reference matching is achieved by imposing that a few functions of the new wheel-rail combination (DR2 wheel profile-UIC60 canted at 1/20 rad) remain the same of the original ones. More specifically, these function, all depending on the wheelset lateral displacement y, are:

- the lateral coordinates y_{r1}, y_{r2} of the contact points expressed in the auxiliary reference system;
- the rail functions $z_{40}^{r1}(\bullet)$, $z_{40}^{r2}(\bullet)$;
- the vertical coordinate $z(y)$;
- the wheelset roll angle $\alpha(y)$.

For the sake of clarity, in the following the variables characterising the original matching and those referring to the new coupling will be respectively denoted with the subscripts 40 and 20 respectively.

Taking into account what has been pointed out so far, the design procedure requires six inputs from the old matching $y_{40}^{r1}(y)$, $y_{40}^{r2}(y)$, $\alpha_{40}(y)$, z_{40}^{r}, $z_{40}^{r1}(\bullet)$, $z_{40}^{r2}(\bullet)$ and two further inputs from the new matching $z_{20}^{r1}(\bullet)$, $z_{20}^{r2}(\bullet)$. Starting from these inputs, the equations describing the coordinate transformation of the contact points from the local to the auxiliary reference system can be consequently written both for the original matching as

$$\begin{pmatrix} y_{40}^{r1}(y) \\ z_{40}^{r1}(y_{40}^{r1}(y)) \end{pmatrix} = \begin{pmatrix} y \\ z_{40}(y) \end{pmatrix} + R(\alpha_{40}(y)) \begin{pmatrix} y_{40}^{w1}(y) \\ z_{40}^{w1}(y_{40}^{w1}(y)) \end{pmatrix} \tag{6.8a}$$

$$\begin{pmatrix} y_{40}^{r2}(y) \\ z_{40}^{r2}(y_{40}^{r2}(y)) \end{pmatrix} = \begin{pmatrix} y \\ z_{40}(y) \end{pmatrix} + R(\alpha_{40}(y)) \begin{pmatrix} y_{40}^{w2}(y) \\ z_{40}^{w2}(y_{40}^{w2}(y)) \end{pmatrix} \tag{6.8b}$$

and for the new matching as

$$\begin{pmatrix} y_{40}^{r1}(y) \\ z_{20}^{r1}(y_{40}^{r1}(y)) \end{pmatrix} = \begin{pmatrix} y \\ z_{40}(y) \end{pmatrix} + R(\alpha_{40}(y)) \begin{pmatrix} y_{20}^{w1}(y) \\ z_{20}^{w1}(y_{20}^{w1}(y)) \end{pmatrix} \tag{6.9a}$$

$$\begin{pmatrix} y_{40}^{r2}(y) \\ z_{20}^{r2}(y_{40}^{r2}(y)) \end{pmatrix} = \begin{pmatrix} y \\ z_{40}(y) \end{pmatrix} + R(\alpha_{40}(y)) \begin{pmatrix} y_{20}^{w2}(y) \\ z_{20}^{w2}(y_{20}^{w2}(y)) \end{pmatrix}, \tag{6.9b}$$

where the wheelset lateral displacement value y is bounded in the range $[-y_M, y_M]$. The outputs of the design procedure that characterise the new wheel profile are the lateral $y_{20}^{w1}(y)$, $y_{20}^{w2}(y)$ and vertical $z_{20}^{w1}(y_{20}^{w1}(y))$, $z_{20}^{w2}(y_{20}^{w2}(y))$ coordinates of the contact points of the new wheel profile in the local reference system. The design procedure is carried out in a discrete way for every y value of the discretised range $[-y_M, y_M]$.

It should be noticed that the resulting profile is so far from being continuous since it exhibits a few holes (see Fig. 6.18), that are the regions where there is not any computed contact point. In the present method, as a first attempt these regions have been filled by fitting the computed points with spline functions and the resulting wheel profile, named DR1 (first version of the DR), is illustrated in Fig. 6.19.

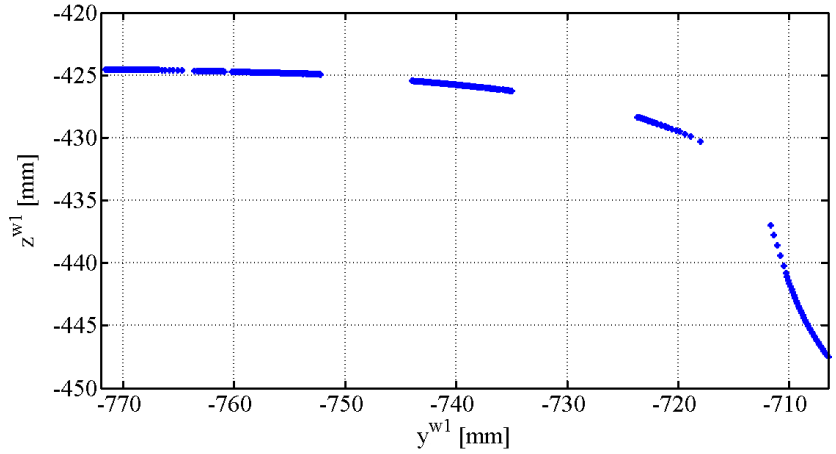

Figure 6.18. Incomplete DR1 profile: distribution of the calculated contact points on wheel.

Given that the geometrical wheel-rail contact characteristics are effectively summed up through the rolling radius difference function, the following expression have been used in the building procedure respectively for the original (ORE S1002 wheel profile and UIC60 canted at 1/40 rad) and the target matching:

$$\Delta r_{40} = z_{40}^{w2}(y_{40}^{w2}(y)) - z_{40}^{w1}(y_{40}^{w1}(y)) \tag{6.10a}$$

$$\Delta r_{20} = z_{20}^{w2}(y_{20}^{w2}(y)) - z_{20}^{w1}(y_{20}^{w1}(y)). \tag{6.10b}$$

The adopted design procedure implies that the RRD of the output matching must be equal to the one of the original coupling, disregarding a small estimable gap $e = \Delta r_{20} - \Delta r_{40}$ (see

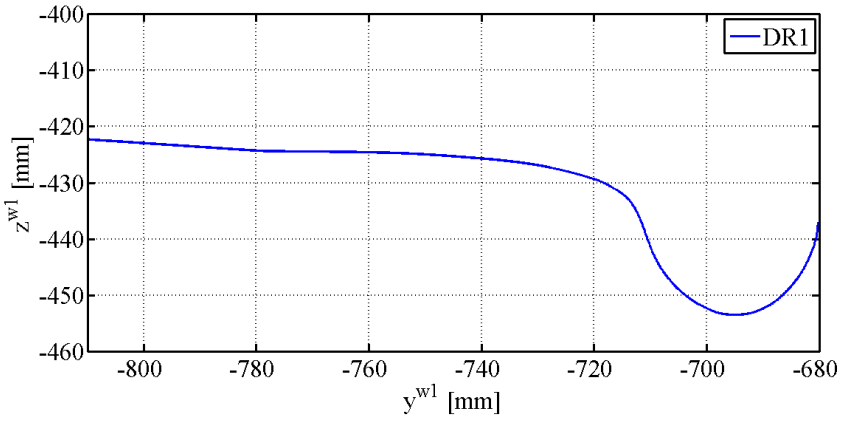

Figure 6.19. Complete DR1 wheel profile after applying the spline functions.

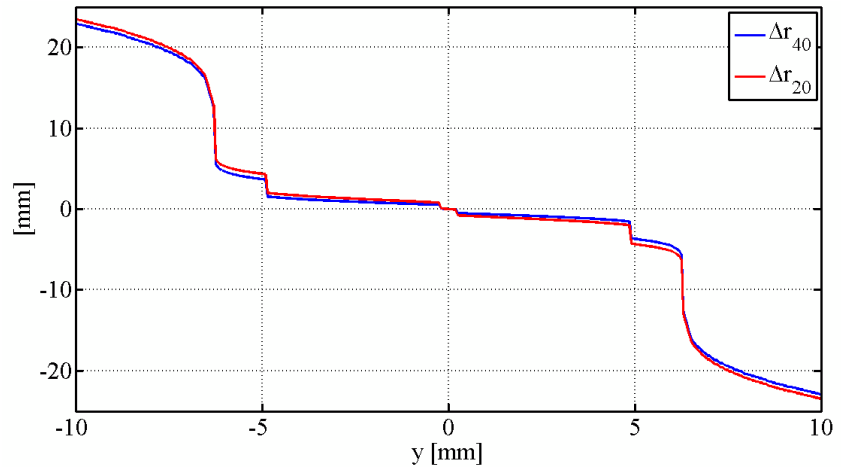

Figure 6.20. Rolling radius difference for the DR1-UIC60 canted at 1/20 rad matching, compared to the 1/40 cant.

Fig. 6.21). In order estimate this error (which is a function of the lateral displacement y even it), after subtracting the Eq. 6.8a from the Eq. 6.8b and the Eq. 6.9a from the Eq. 6.9b, the following expressions hold:

$$\begin{pmatrix} y_{40}^{r2}(y) - y_{40}^{r1}(y) \\ z_{40}^{r2}(y_{40}^{r2}(y)) - z_{40}^{r1}(y_{40}^{r1}(y)) \end{pmatrix} = R(\alpha_{40}) \begin{pmatrix} y_{40}^{w2}(y) - y_{40}^{w1}(y) \\ \Delta r_{40} \end{pmatrix} \tag{6.11a}$$

$$\begin{pmatrix} y_{40}^{r2}(y) - y_{40}^{r1}(y) \\ z_{20}^{r2}(y_{40}^{r2}(y)) - z_{20}^{r1}(y_{40}^{r1}(y)) \end{pmatrix} = R(\alpha_{40}) \begin{pmatrix} y_{20}^{w2}(y) - y_{20}^{w1}(y) \\ \Delta r_{20} \end{pmatrix}. \tag{6.11b}$$

By subtracting on turn the Eq. 6.11a from the Eq. 6.11b, the expression (6.12) holds:

$$R_{(\alpha_{40})}^{T} \begin{pmatrix} 0 \\ \Delta z_{20}^{r} - \Delta z_{40}^{r} \end{pmatrix} = \begin{pmatrix} \Delta y_{20}^{r} - \Delta y_{40}^{r} \\ \Delta r_{20} - \Delta r_{40} \end{pmatrix}. \tag{6.12}$$

The second component of the (6.12) leads to the expression of the rolling radius functions

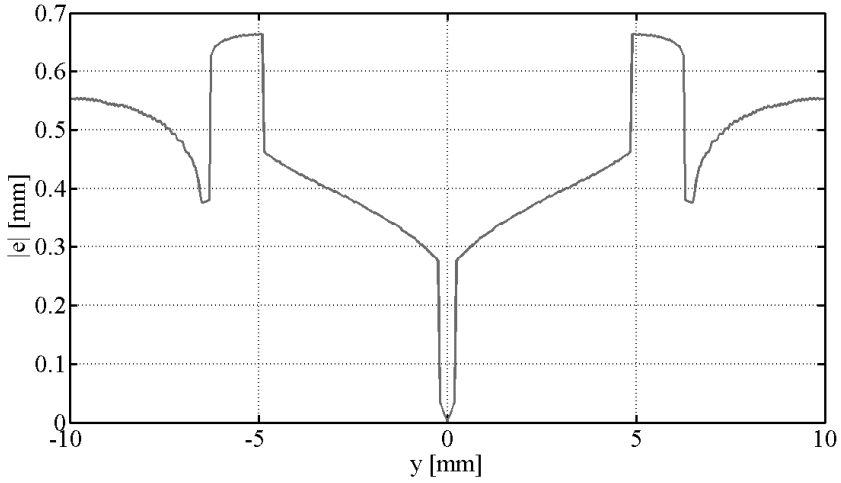

Figure 6.21. Error in the RRD function for the DR1-UIC60 canted at 1/20 rad matching as a function of y.

variation between the new and the original matching (6.13):

$$(\Delta z^r_{20} - \Delta z^r_{40}) \cos \alpha_{20} = \Delta r_{20} - \Delta r_{40} = e(y) \tag{6.13}$$

as a function of the wheelset lateral displacement, where $\Delta z^r_{20} = z^{r2}_{20}(y^{r2}_{40}(y)) - z^{r1}_{20}(y^{r1}_{40}(y))$ and Δz^r_{40} and $\Delta z^r_{40} = z^{r2}_{40}(y^{r2}_{40}(y)) - z^{r1}_{40}(y^{r1}_{40}(y))$. The error depicted in Fig.6.12 means that the DR1 profile would provide a higher conicity if applied on 1/20 lying angle rails than the S1002 does. The profile might work fine anyway but such an error cannot be accept if the aim is to have exactly the same RRD function.

In order to minimise the rolling radius difference error between the original matching and the DR1 wheel profile-UIC60 canted at 1/20 rad combination, an optimisation algorithm has been developed. The basic idea of this algorithm consists in translating the lateral input coordinates $y^{r1}_{40}(y)$, $y^{r2}_{40}(y)$ of a certain quantity $k(y)$, evaluated through a minimisation process of the rolling radius error for each possible lateral wheelset displacement y. The lateral coordinates of the contact points in the auxiliary reference system can be then re-defined as:

$$y^{r1^k}_{40} = y^{r1}_{40} + k \tag{6.14a}$$

$$y^{r2^k}_{40} = y^{r2}_{40} + k\,, \tag{6.14b}$$

where the k value is bounded in the range $[-\bar{k}, +\bar{k}] = I_k$. Therefore the expression of the rolling radius error becomes a function of both the y and k values:

$$E(y,k) = \cos \alpha_{20}(z^{r2}_{20}(y^{r2}_{40} + k) - z^{r1}_{20}(y^{r1}_{40} + k) - z^{r2}_{40}(y^{r2}_{40}) + z^{r1}_{40}(y^{r1}_{40})). \tag{6.15}$$

The Eq. 6.15 is exploited as the objective function to find the optimal value k_{opt} of the translation quantity, which is hence defined for each value of the wheelset lateral displacement y

in the following manner:

$$k_{opt}(y) = \arg\min_{k \in I_k} |E(y,k)| \tag{6.16}$$

The optimisation process has been performed in a discrete way; the Fig. 6.22 illustrates the graphical representation of the k_{opt} value for a given lateral displacement y.

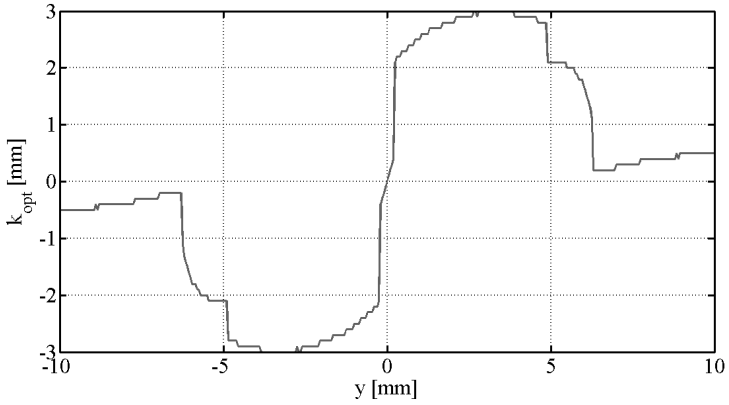

Figure 6.22. Optimal value of the translation parameter k as the lateral displacement y changes.

It should be noticed that the resulting values are small if compared to the characteristic length of the problem. The arising lateral coordinates of the contact points in the auxiliary reference system are evaluated as:

$$y^{r1}_{opt} = y^{r1}_{40} + k_{opt} \tag{6.17a}$$

$$y^{r2}_{opt} = y^{r2}_{40} + k_{opt}. \tag{6.17b}$$

Through the introduction of these coordinates into Eqs. 6.9a and 6.9b, the outputs $y^{w1}_{20}(y)$, $z^{w1}_{20}(y^{w1}_{20}(y))$, $y^{w2}_{20}(y)$, $z^{w2}_{20}(y^{w2}_{20}(y))$ of the optimised wheel profile-UIC60 at 1/40 rad matching are obtained according to the following expressions:

$$\begin{pmatrix} y^{r1}_{opt}(y) \\ z^{r1}_{20}(y^{r1}_{opt}(y)) \end{pmatrix} = \begin{pmatrix} y \\ z_{40}(y) \end{pmatrix} + R(\alpha_{40}(y)) \begin{pmatrix} y^{w1}_{20}(y) \\ z^{w1}_{20}(y^{w1}_{20}(y)) \end{pmatrix} \tag{6.18a}$$

$$\begin{pmatrix} y^{r2}_{opt}(y) \\ z^{r2}_{20}(y^{r2}_{opt}(y)) \end{pmatrix} = \begin{pmatrix} y \\ z_{40}(y) \end{pmatrix} + R(\alpha_{40}(y)) \begin{pmatrix} y^{w2}_{20}(y) \\ z^{w2}_{20}(y^{w2}_{20}(y)) \end{pmatrix}. \tag{6.18b}$$

The optimised wheel profile, achieved after the hole fitting procedure, has been named "DR2" and is depicted in Fig. 6.23. In regarding to the final result, the new RRD function is compared with the original one in Fig. 6.24; the comparison shows that the two plots overlap since the error, depending on the discretisation precision of the range I_k, has been greatly reduced with respect to the initial configuration (see Fig. 6.25).

The design procedure adopted to define the DR2 wheel profile may be affected by numerical errors coming from different sources, such as:

- use of splines to fill the holes and of fictitious points at the edges of the wheel profile,

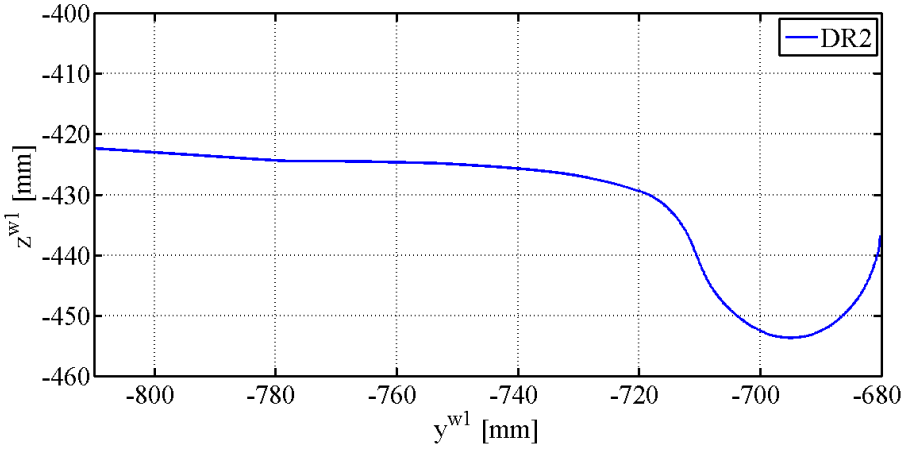

Figure 6.23. DR2 wheel profile.

where there is not a contact point distribution and parts of the S1002 have been exploited in the rebuilding process;

- subsequent re-interpolations and smooth processes of profiles and derivatives of the wheel and the rail geometries;
- numerical stiffness due to the typical conformal contact proper to the original matching, since the DR2 wheel profile and the UIC60 rail at 1/20 rad is an attempt to reproduce the same features.

At the same time, one of the numerical advantage of the procedure lies in the fact that the new DR2 wheel profile is designed without any condition on the profile derivatives; this aspect implies less requirements in terms of smoothness and does not further increase the ill-conditioning intrinsic characteristic of the design problem.

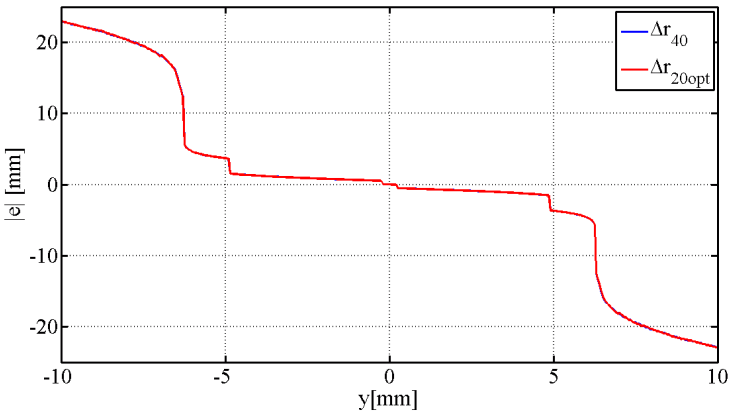

Figure 6.24. Rolling radius difference distribution for the optimised DR2-UIC60 canted at 1/20 rad.

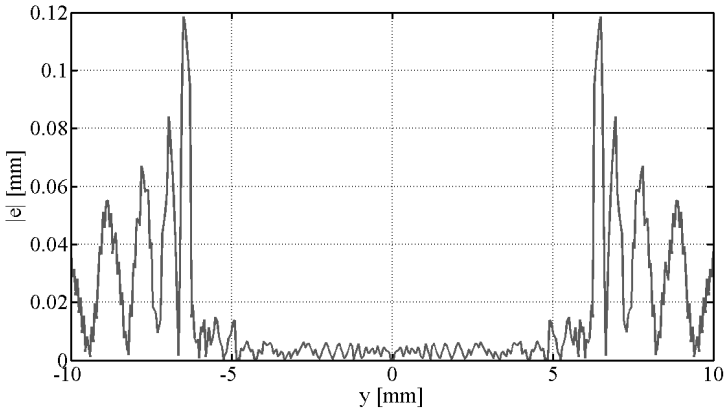

Figure 6.25. Error in rolling radii difference distribution for the optimised DR2-UIC60 canted at 1/20 rad matching.

6.4 Comparison of the resulting wheel profiles

As already underlined time and time again, all the resulting profiles have been designed in order to achieve suitable kinematic and wear performance when matched with the UIC60 rail canted at 1/20 rad. This section deals with the comparison of the CD1, DR1 and DR2 characteristics with those relative to the standard ORE S1002 (optimised to match the UIC60 rail canted at 1/40 rad). In that regard, Fig. 6.26 and 6.27 show the comparison of the resulting CD1, DR1 and DR2 wheel profiles as well as the original ORE S1002, while in Fig. 6.28 their relative differences along the vertical coordinates are plotted.

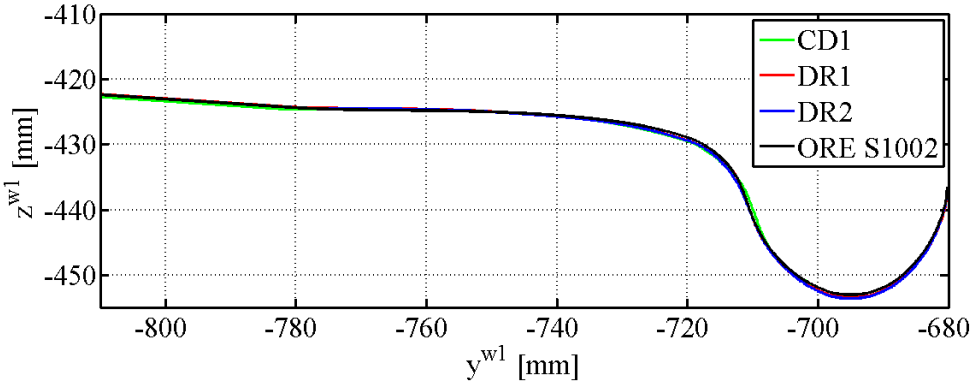

Figure 6.26. CD1, DR1, DR2 and ORE S1002 wheel profiles.

The derivatives of the resulting CD1, DR1 and DR2 wheel profile compared with the derivative of the standard S1002 are illustrated in Figs. 6.29 and 6.30.

Differences in CD1 and DR2 wheel profiles properties coherently reproduce the fact that they have been conceived with two different strategies and procedures. The DR1 and DR2 wheel profiles are instead almost coincident each other, representing that the DR2 optimisation algorithm may improve the DR1 designing procedure which nevertheless, produces itself a wheel profile with suitable kinematic and wear characteristics. It can be also noticed that the new DR1 and DR2-UIC60 canted at 1/20 combination seem to

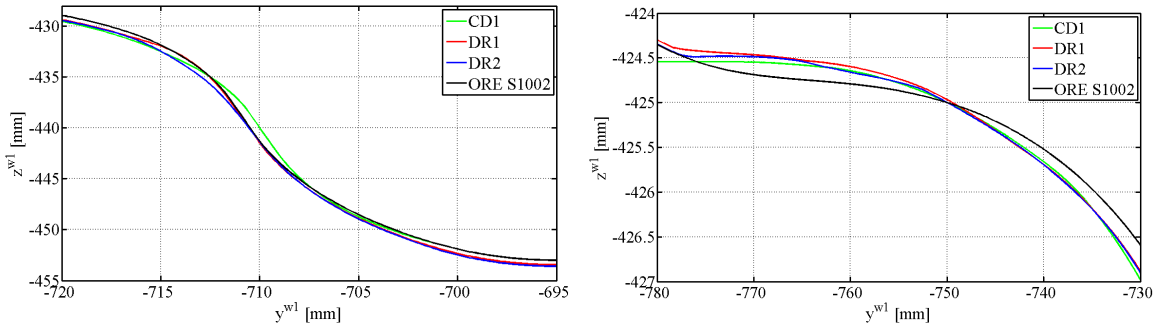

Figure 6.27. Detailed comparison of the four wheel profiles: flange zone (a); tread zone (b).

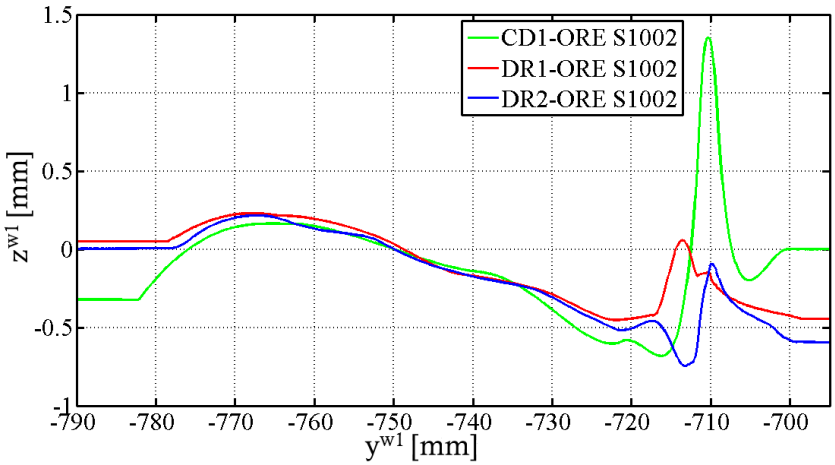

Figure 6.28. Differences along the vertical between the CD1, DR1 and DR2 wheel profiles and the standard ORE S1002 wheel profile.

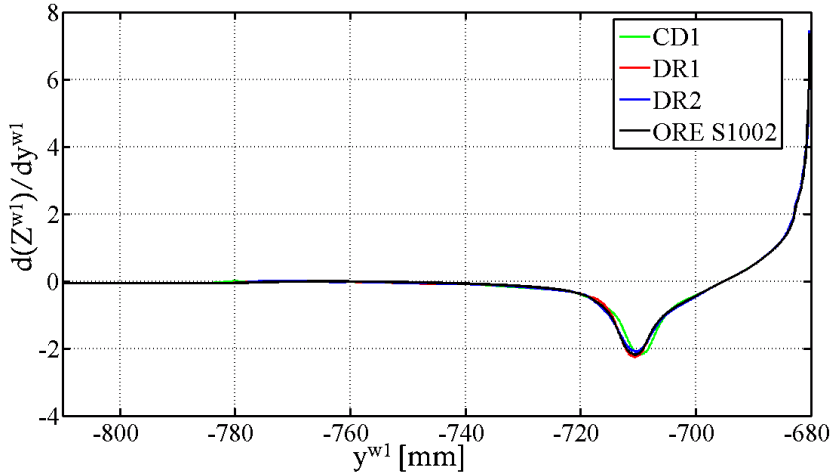

Figure 6.29. CD1, DR1, DR2 and ORE S1002 wheel profile derivatives.

reproduce the conformal contact proper to the original ORE S1002-UIC60 canted at 1/40 with coherent vertical translations of the tread and flange zone.

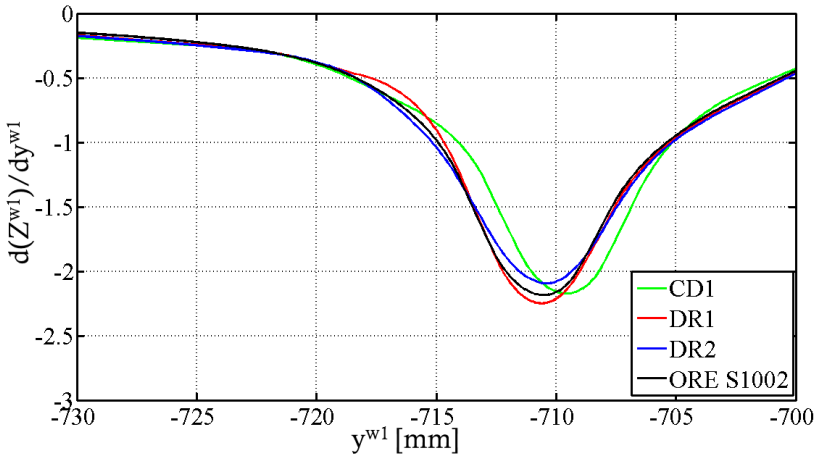

Figure 6.30. CD1, DR1, DR2 and ORE S1002 wheel profile: detail of the first derivatives in the flange zone.

Among the profiles with a flange thickness of 32.5 mm, the DR1 will not be taken into consideration in the wear analysis presented in the next chapter (7); in fact only the improved version DR2 have been tested and compared with the other wheel geometries involved in this study.

CHAPTER 7

Wear Analysis

In the present section the results of the wear analyses will be presented in order to compare the performance of the wheel profiles involved in the study. For each vehicle-profile combination the evolution of the wheel shape and the progress of the three reference dimensions (fH, fT, qR; see Sec. 5.4) as a function of the total covered distance will be shown. The initial values of the quotas for the profiles having an initial flange thickness of 32 mm are reported in Tab. 7.1.

Table 7.1. Initial values (in mm) of the reference dimensions of the profiles having a nominal flange thickness of 32 mm.

	ORE S1002	**CD1 32.5 mm**	**DR2**
$\boldsymbol{fT}$	28.00	27.90	28.48
$\boldsymbol{fH}$	32.50	32.73	32.54
$\boldsymbol{qR}$	10.79	11.01	10.90

The total distance simulated for each train-wheel profile combination is summarized in Tab. 7.2.

Table 7.2. Overall distance covered by each train-wheel profile combination.

	ORE S1002	**CD1 32.5 mm**	**CD1 30.5 mm**	**CD1 28.5 mm**	**DR2**
Minuetto (km)	80 000	130 000	94 000	68 000	71 000
Vivalto-E464 (km)	320 000	275 000	175 000	175 000	240 000

With regard to the covered distances and the corresponding results, they have been obtained by setting a variable step procedure with the maximum height $\hat{d}$ of the function of material to be removed $\hat{d}$ equal to 0.1 mm (see Sec. 4.3). Furthermore, in order to investigate dry conditions of medium severity at the wheel-rail interface, a friction coefficient of 0.3 has been chosen for all the analysed cases.

To draw a comparison among the quotas of the considered profiles, for convenience the reference value of 24.0 mm for the flange thickness fT and 7.5 mm for the qR have been utilized instead of the acceptable limits suggested by the regulations (Tab. 5.8) which

are 22.0 mm and 6.5 mm respectively and which would have required higher mileages. However, it is important to highlight that for a particular vehicle-profile combination, the two mentioned reference limits are usually reached at different mileages and moreover this difference may be remarkable, depending on the service condition of the vehicle. Therefore, as the reference dimension having the slowest mean progress reaches its limit (or comparison) value, the quota having the fastest evolution might assume a value far from the threshold limit.

Generally, the maximum allowable mileage for a wheel is due to the reaching of the limit value in flange thickness or in qR, while seldom does the height of the flange go beyond the maximum value (36.0 mm, Tab. 5.8). For this to happen, the wear on the tread must be appreciably higher than the detriment on the flange, as can occur in railway line characterized by only large radius curve and straight sections.

7.1 Results of the Minuetto

7.1.1 Minuetto: S1002 profile

The results for the first case analysed, the Minuetto-S1002 matching, are shown in the Figs. 7.1, 7.2, 7.3 and 7.4. The first figure depicts the volume and the distribution along the profile of the material totally removed by wear. The flange height in the second figure shows a slight reduction at half mileage, but this behaviour, of poor extent, is imputable to the filter action used in smoothing the wheel profile at each step, when applied several times in situations in which the wear rate on the tread is quite low; as a consequence, the reduction in the mean rolling radius is extremely low too.

The covered distance involved in the comparison are the following:

- fT (24.0 mm): 70 000 km;
- qR (7.5 mm): 79 000 km,

thus the maximum mileage is limited by the rate of the flange thickness reduction.

7.1.2 Minuetto: CD1 32.5 mm profile

When the Minuetto is equipped with the CD1 profile having an initial flange thickness of 32.5 mm, it exhibits a higher and more uniform wear on the tread (Fig. 7.5) with respect to the previous case, as proven by the increase in the fH, visible in Fig. 7.6. The first comparison value is reached by the qR quota; more precisely the corresponding covered distances before reaching the limits are:

- fT (24.0 mm): 100 000 km;
- qR (7.5 mm): 84 000 km.

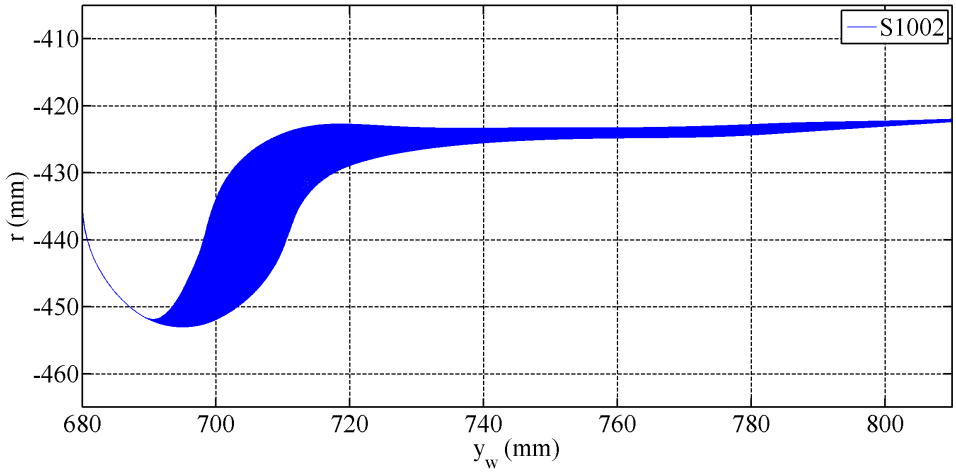

Figure 7.1. Evolution of the wheel shape (Minuetto).

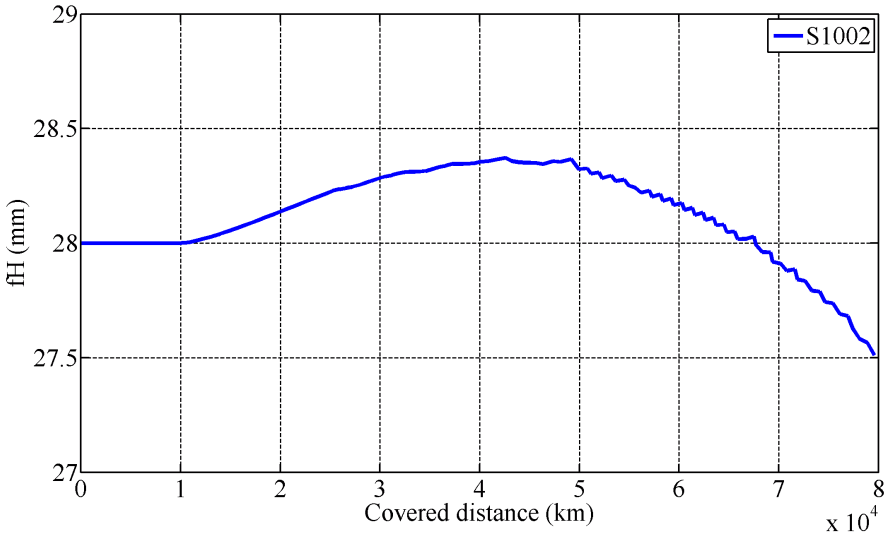

Figure 7.2. Progress of the fH dimension (Minuetto).

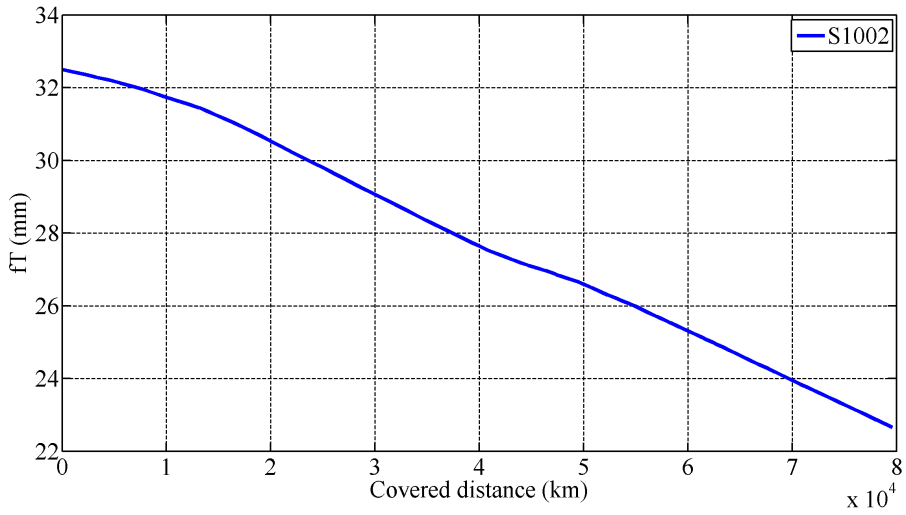

Figure 7.3. Progress of the fT dimension (Minuetto).

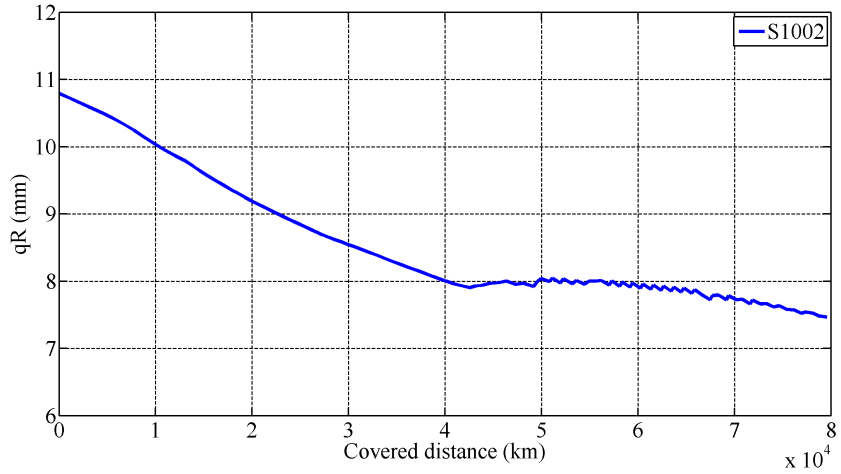

Figure 7.4. Progress of the qR dimension (Minuetto).

7.1.3 Minuetto: CD1 30.5 mm profile

For the intermediate CD1 profile of the Minuetto the following total distances have been found:

- fT (24.0 mm): 89 000 km;
- qR (7.5 mm): 79 000 km;

the total mileage is hence limited by the progress of the qR dimension. A graphical representation of the results in given in Figs. 7.8 (wheel shape evolution) and 7.9 (qR).

The distance for which each quota reaches its own limit is slightly lower than those calculated when the CD1-32.5 is applied. This behaviour is reasonable because the shorter life of the wheel in terms of the flange thickness was to be expected, even if the two profiles have detectable kinematic and dynamic differences. On the contrary, the rate of change of the qR can be whatever and a wider flange not necessarily assures a longer life before re-turning.

However, even with a minor flange thickness, the performance of this CD1 profile are slightly better than those provided by the S1002 as regards both the two most important dimensions.

7.1.4 Minuetto: CD1 28.5 mm profile

The version of the CD1 profile with the thinnest flange has provided the following results:

- fT (24.0 mm): 67 000 km;
- qR (7.5 mm): 45 000 km,

with a further reduction in the wheel life from a point of view of both reference dimensions. Particularly, the qR quota goes down quickly in the first steps and the reduction rate

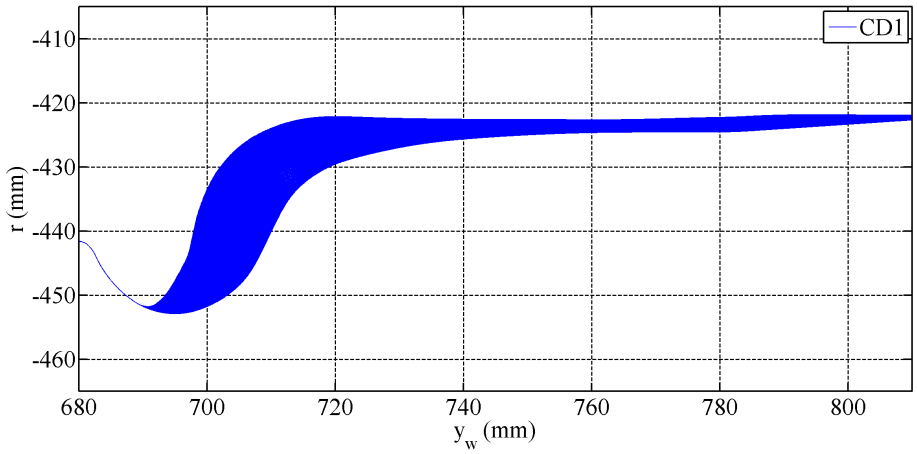

Figure 7.5. Evolution of the wheel shape (Minuetto).

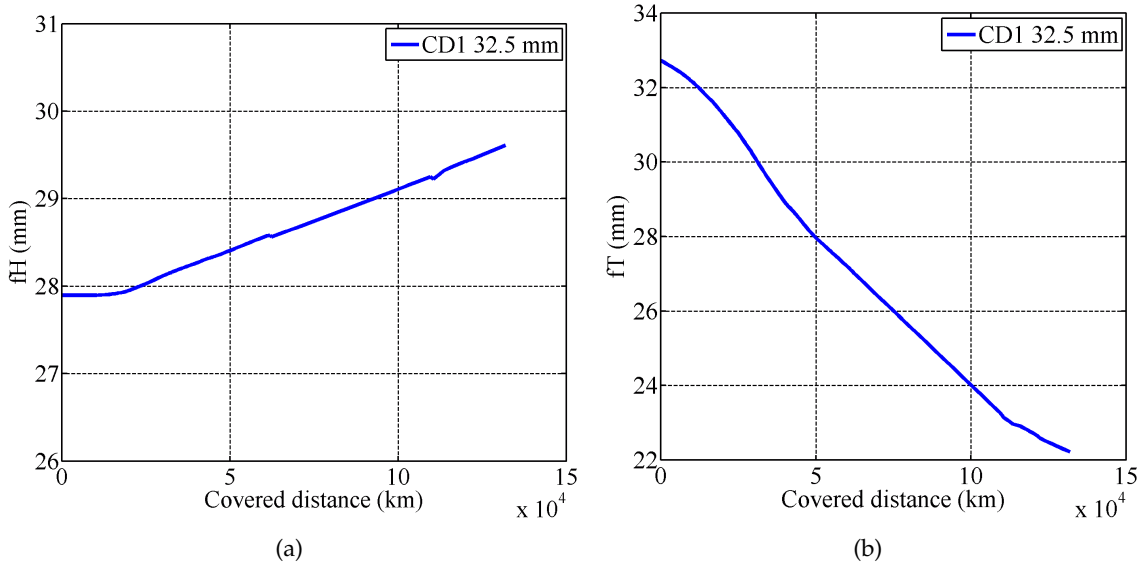

Figure 7.6. Progress of the flange height (a) and thickness (b) (Minuetto).

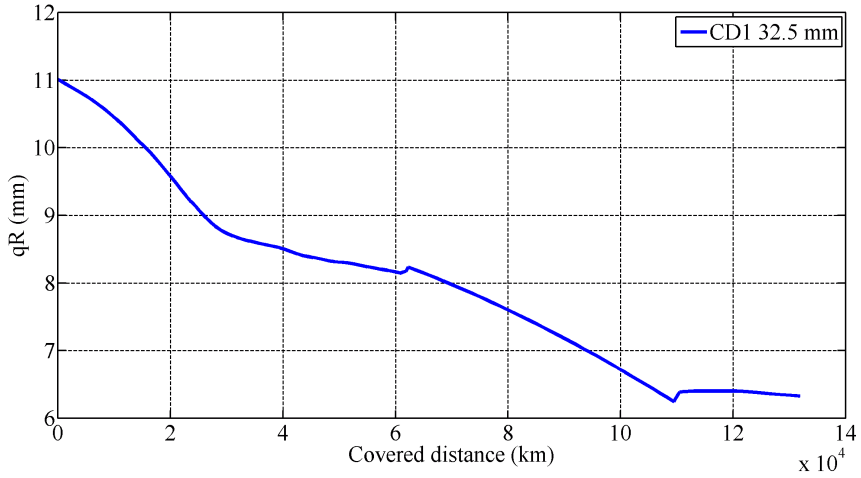

Figure 7.7. Progress of the qR dimension (Minuetto).

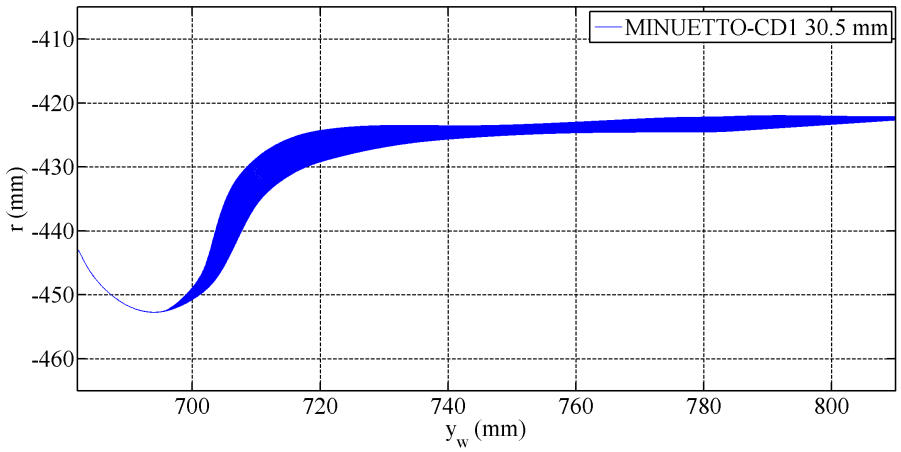

Figure 7.8. Evolution of the wheel shape (Minuetto).

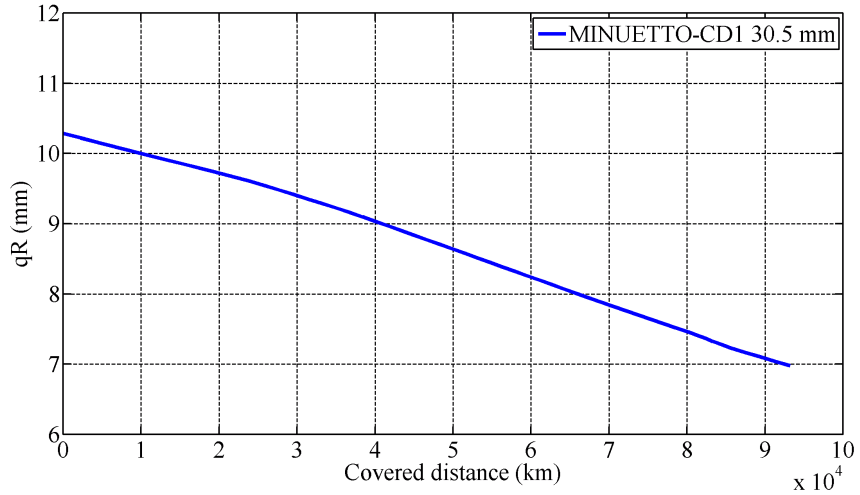

Figure 7.9. Progress of the qR dimension (Minuetto).

starts to drop shortly after 45 000 km, when the prearranged limit has already been reached. However, apart from the performance comparison, the life in terms of qR might be considerably higher than 45 000 km and globally not excessively worse than that of CD1-30.5 shape.

7.1.5 Minuetto: DR2 profile

On the whole, by adopting the DR2 profile the results for the Minuetto are slightly better than those provided by the CD1 having the same flange thickness; in fact, the distances after reaching the comparison limits turn out to be respectively:

- fT (24.0 mm): 90 000 km;
- qR (7.5 mm): 100 000 km.

The main difference to be highlighted is that the behaviour of the model when the Minuetto is equipped with the DR2 profile involves a slower reduction of qR and the comparison

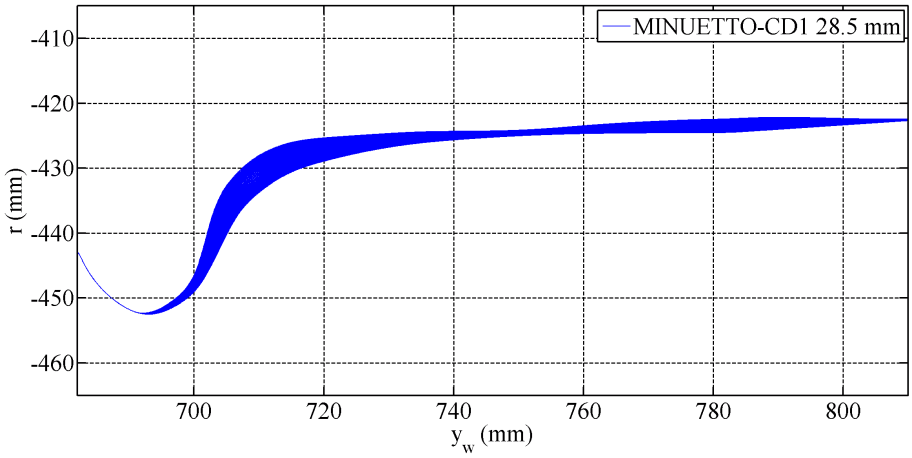

Figure 7.10. Evolution of the wheel shape (Minuetto).

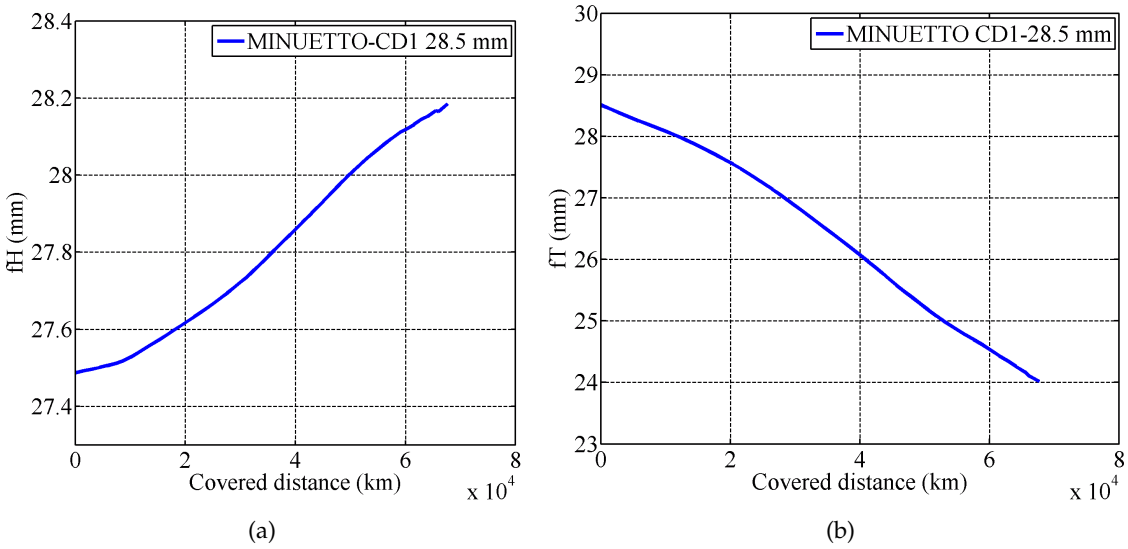

Figure 7.11. Progress of the flange height (a) and thickness (b) (Minuetto).

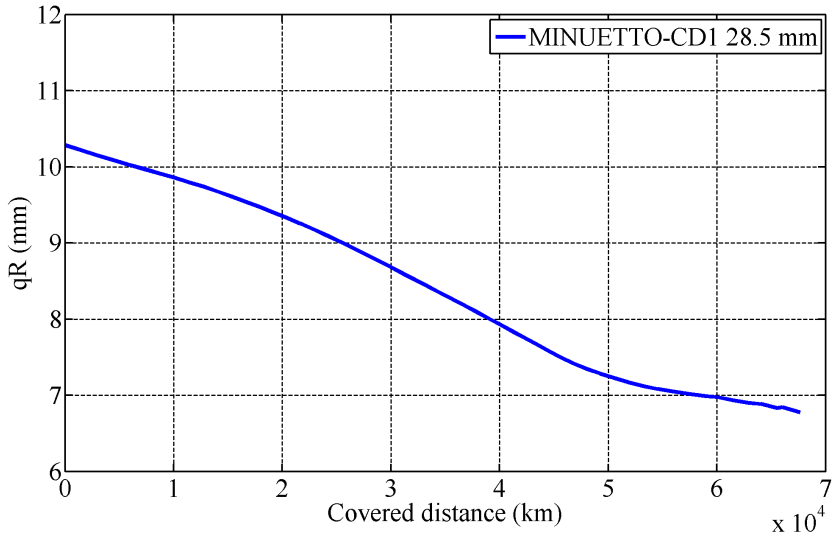

Figure 7.12. Progress of the qR dimension (Minuetto).

threshold is reached by the flange thickness first.

7.1.6 Minuetto: summing up

The comparison of the performances obtained with the considered wheel profiles are finally summarized in Tab. 7.3, where the reported distances of each train-profile combination are to be considered as the lowest between the two caused by the concurrent reduction in the qR and fT quotas.

It can be surely stated that the adoption of either the CD1-32.5 and the DR2 profile in place of the S1002 leads to a general improvement in the progress of the reference dimension and in the total distance, considering the comparison limits of 24.0 mm for the flange thickness and of 7.5 mm for the qR. In detail, the CD1 having the widest flange increases the distance by about 20 % with respect to the S1002 (70 000 km), while the total distance rises of about 28 % by selecting the DR2 shape. The performance of the two other versions of the CD1 are instead less interesting: the 30.5 mm version provide a slight improvement while the 28.5 mm seems not be promising, since the covered distance is notably lower than 70 000 km.

Table 7.3. Summary of the Minuetto results.

Wheel profile	ORE S1002	CD1 32.5 mm	CD1 30.5 mm	CD1 28.5 mm	DR2
Total distance (km)	70 000	84 000	79 000	45 000	90 000

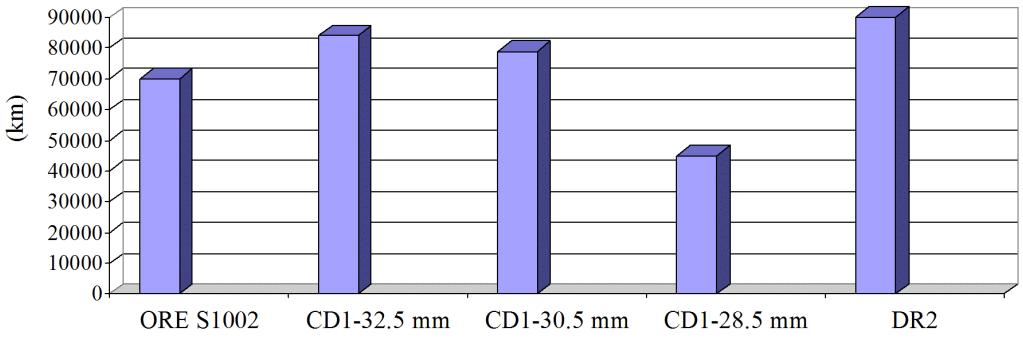

Figure 7.13. Graphical representation of the results summarized in Tab. 7.3.

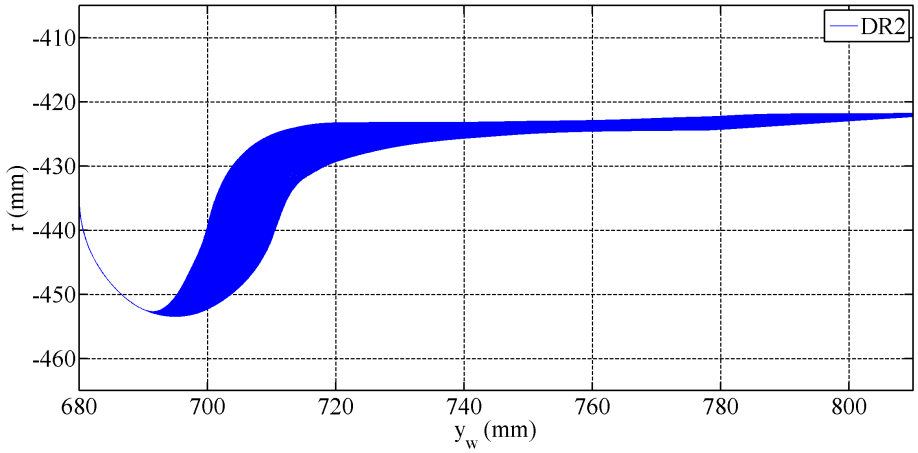

Figure 7.14. Evolution of the wheel shape (Minuetto).

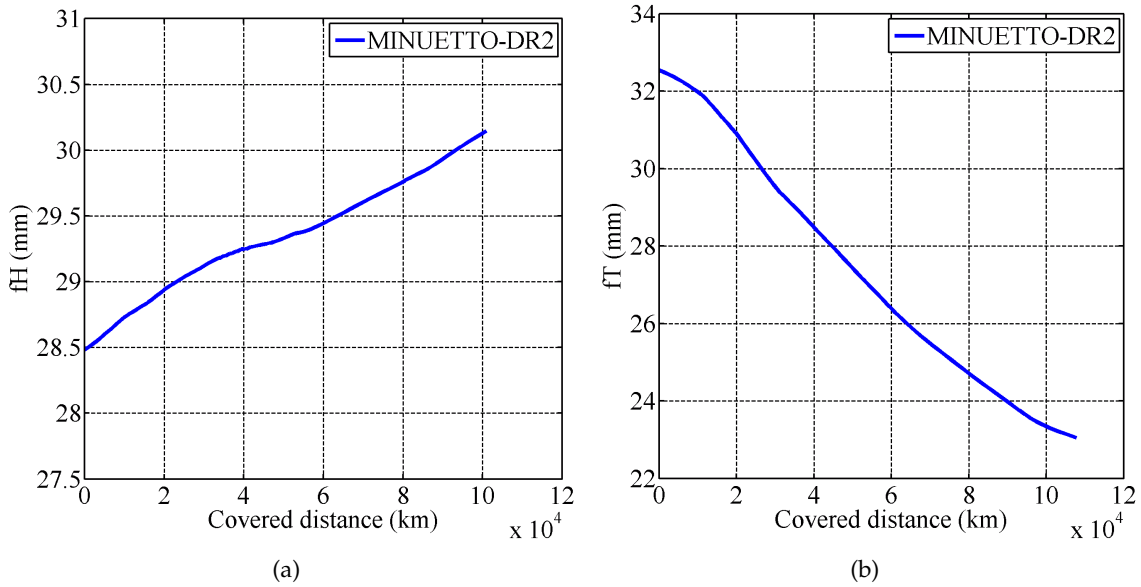

Figure 7.15. Progress of the flange height (a) and thickness (b) (Minuetto).

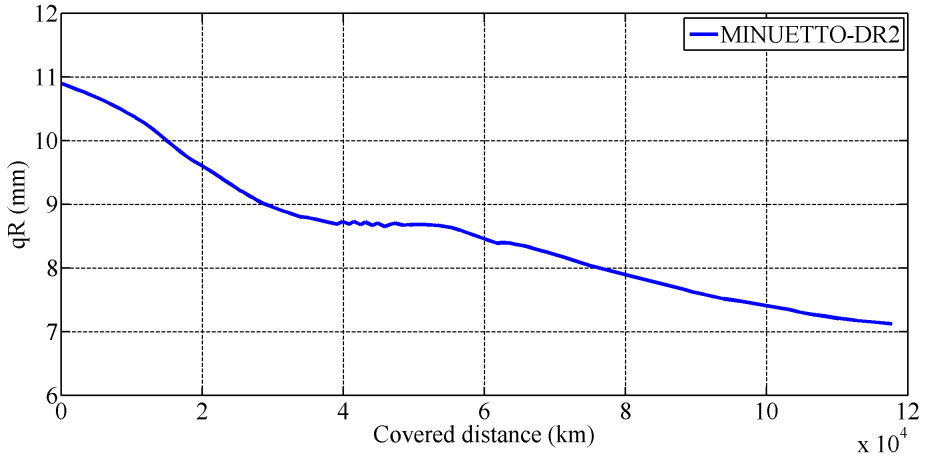

Figure 7.16. Progress of the qR dimension (Minuetto).

7.2 Results of the Vivalto-E464 train

In this section the results of the wear analysis carried out on the Vivalto-E464 train will be shown and discussed in detail. Unlike the Minuetto, where the four bogies resemble to each other even though two are motorized and two are trailed, being this composition made up of two vehicles having substantial differences, the evolution of the mean profile is monitored on the Vivalto and on the E464 separately, hence the two vehicle share only the initial unworn profile. For each train-profile combination taken under consideration, the progress of reference dimensions and wheel shape of both the vehicles will be presented. As has been done for the Minuetto, the threshold values chosen in order to compare the wheel profiles are the same: 24.0 mm for the flange thickness and 7.5 mm for the qR quota.

7.2.1 Vivalto-E464: S1002 profile

The performance concerning the Vivalto coach matched with the S1002 are depicted in the Figs. 7.17, 7.18 and 7.19 whereas the wear evolution of the E464 is summed up in the Figs. 7.20, 7.21 and 7.22. Since the statistical influence of curves is noticeably lower in the virtual track of the Vivalto, the resultant travelled distances before reaching the thresholds are conspicuously longer than those resulting from the simulation of the Minuetto mean line. The difference in wear severity between the two virtual tracks can be also confirmed by analysing the typical progress of the variable km_{step}: in the simulations of the Vivalto the average length of a step is about three times as much the length of a step in the Minuetto mean line. Clearly the maximum height in the function of removed material is even in this case equal to 0.1 mm in order to assure the same accuracy in the two distinct contexts in terms of evolution of the wheel geometry.

The overall distance covered in this scenery are visible in Tab. 7.4.

Table 7.4. Distance covered before reaching the limit values (Vivalto-E464, S1002).

	$qR(7.5\,\text{mm})$	$fT(24.0\,\text{mm})$
Vivalto (km)	120 000	276 000
E464 (km)	166 000	$> 300\,000$

With respect to what has been presented, the kilometrage of both the vehicles is bounded by the progress of the qR dimension. Comparing the global trends, the reference quota of the E464 exhibits a slower rate reduction as the simulated distance increases: this tendency has been occurred even when the other wheel profile were being exploited, as it will be further discussed in the following. Besides the remarkable intrinsic differences owing to the diverse purposes for which the two vehicles were designed, the further reason which can surely justify a different resistance to wear is the presence of a significant difference in the rolling radius. In fact, the E464 have a mean rolling radius of 1100 mm, that is about 20 % higher than the radius of wheels of the Vivalto. As a matter of fact, the presence of a larger wheel radius implies a generally global slower wear rate since the circumference

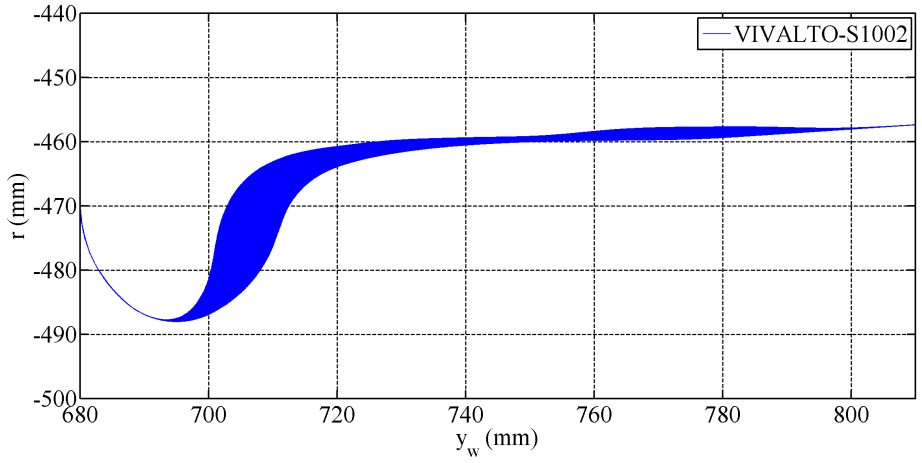

Figure 7.17. Evolution of the wheel shape (Vivalto).

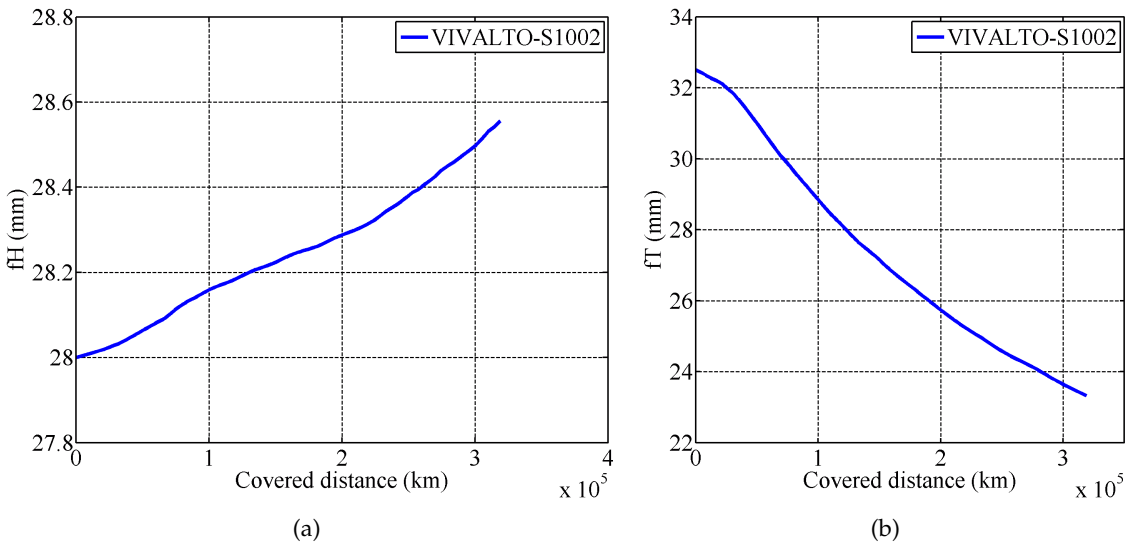

Figure 7.18. Progress of the flange height (a) and thickness (b) (Vivalto).

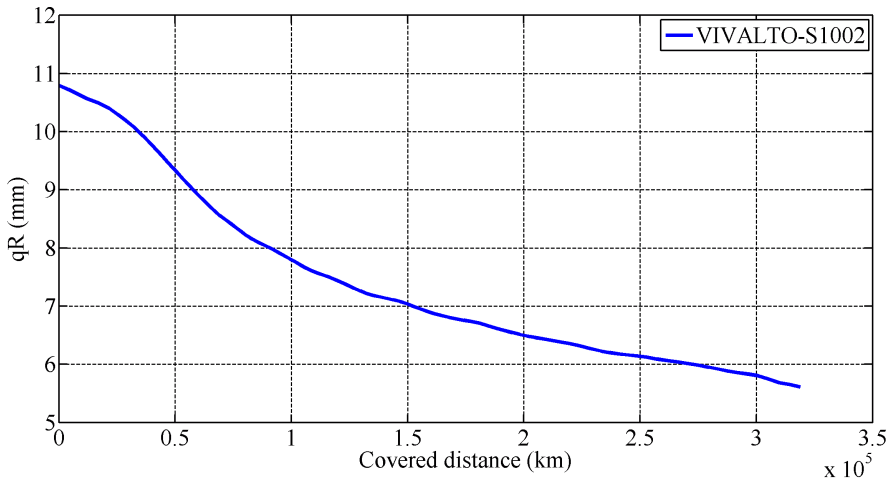

Figure 7.19. Progress of the qR dimension (Vivalto).

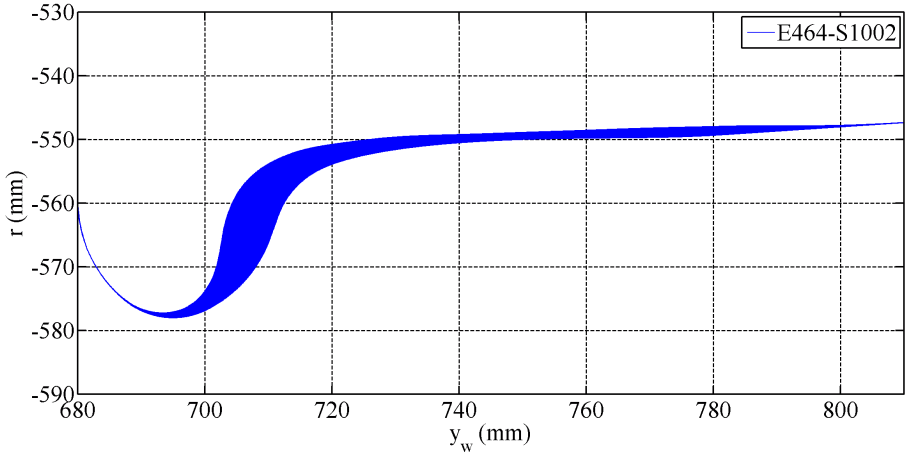

Figure 7.20. Evolution of the wheel shape (E464).

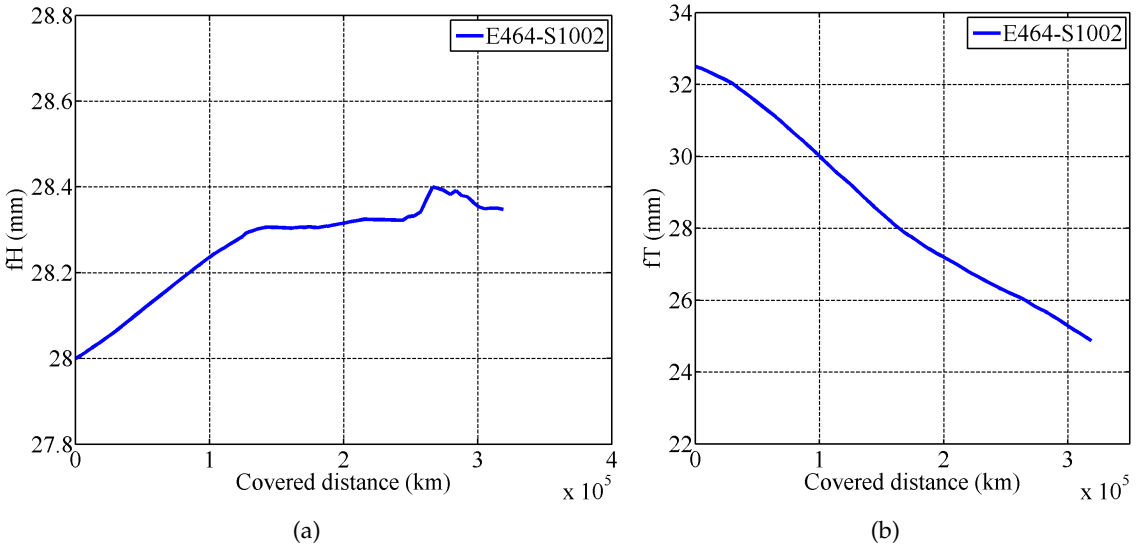

Figure 7.21. Progress of the flange height (a) and thickness (b) (E464).

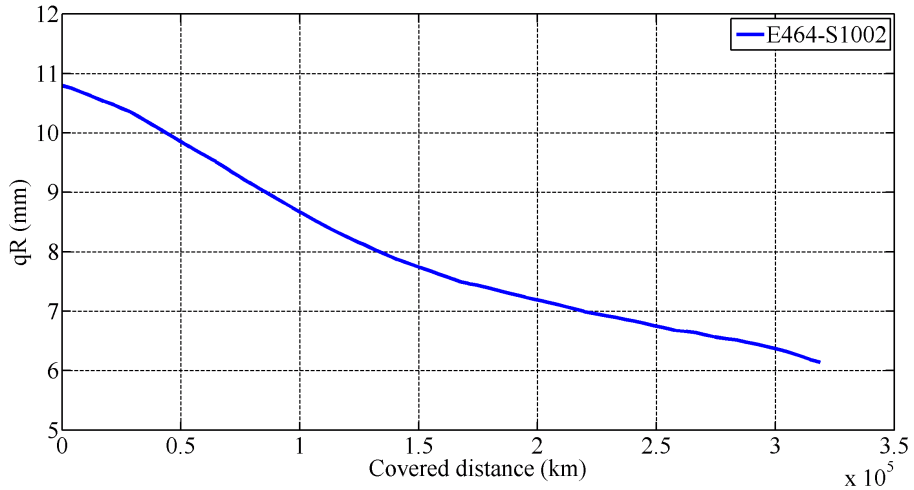

Figure 7.22. Progress of the qR dimension (E464).

of the wheel is longer; besides this intuitive observation, other differences arise from the results of Hertz's theory in the normal contact problem since the distribution of the normal pressure depends on both the curvatures of the wheel and the rail. In that regard, even though it is not easy to draw general conclusions, it must be remembered anyway that the maximum stress in the contact patch tends to be higher as the wheel radius is reduced. However, at the same time it has to be taken into account that the wheel radius has a strong influence on the longitudinal position of the contact points on the flange (and consequently on its lateral position) and hence on the components of the resultant contact force. Thus the rebounds on wear cannot be simply inferred.

In regarding to other important influential parameters, the total mass of the Vivalto coach in full load conditions is about 10 t lower than the mass of the locomotive, while the two bogie wheelbases are rather similar (Vivalto: 2500 mm, E464: 2650 mm) tough the influence of this parameter is usually very considerable especially as regards the wear due to sharp curves.

7.2.2 Vivalto-E464: CD1-32.5 mm profile

Like the Minuetto, by substituting the 1002 profile with the CD1-32.5 in both the vehicles, a considerable benefit has been proven, as clearly demonstrated by the comparison between Tab. 7.5 and Tab. 7.4. While the gain in travelled distance from a flange thickness point of view is not appreciable, rather the S1002 seems to be more resistant, the increase in covered kilometrage from a qR dimensions viewpoint, which is the real constrictive evolution in this case, is of great importance. In fact, the simulation results state that the travelled distance is being increased of about 20 % for both the vehicles. A graphical representation of the results is given in the Figs. 7.23, 7.24 and 7.25 (Vivalto) and Figs. 7.26, 7.27 and 7.28 (E464).

Table 7.5. Distance covered before reaching the limit values (E464-Vivalto, CD1-32.5 mm).

	$qR(7.5\,\text{mm})$	$fT(24.0\,\text{mm})$
Vivalto (km)	144 000	252 000
E464 (km)	197 000	$>$ 280 000

7.2.3 Vivalto-E464: CD1-30.5 mm profile

The response of the multibody models when the intermediate version of the CD1 profile is adopted on the Vivalto composition is conceptually similar to the behaviour of the standard version witha a flange 32.5 mm, except for the overall mileage, which is strongly reduced. For the coach and the traction unit the reaching of a situation in which a re-turning is indispensable is again owing to the faster rate of decrease in the qR rather than in the flange thickness. The results are summed up in Tab. 7.6; globally the maximum distances are on average the 30 % less than those of CD1-32.5 mm.

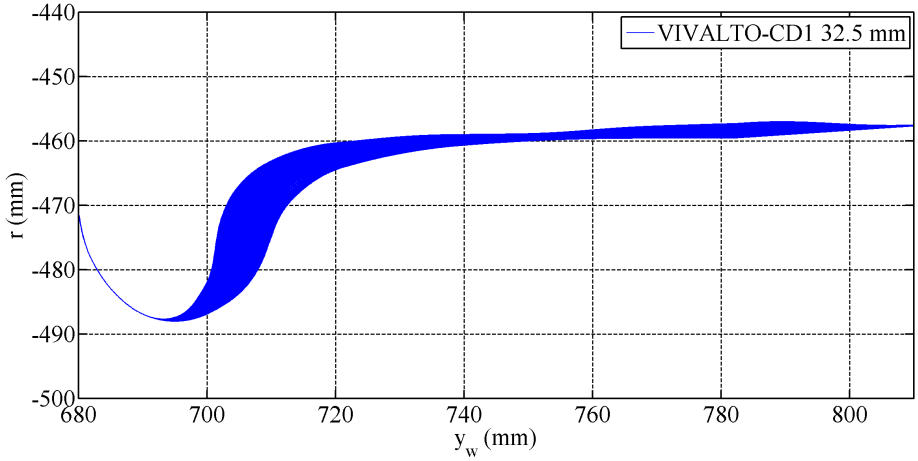

Figure 7.23. Evolution of the wheel shape (Vivalto).

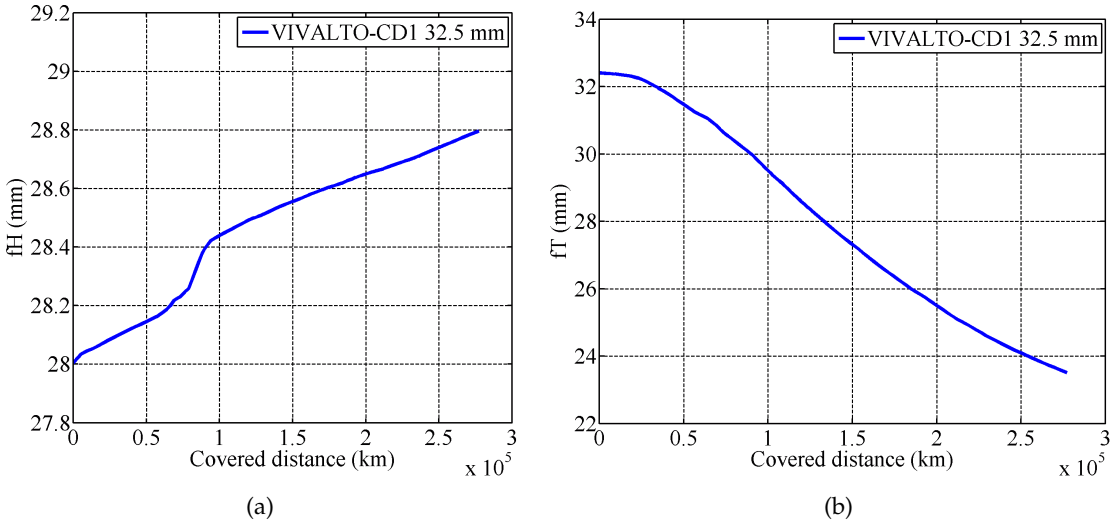

Figure 7.24. Progress of the flange height (a) and thickness (b) (Vivalto).

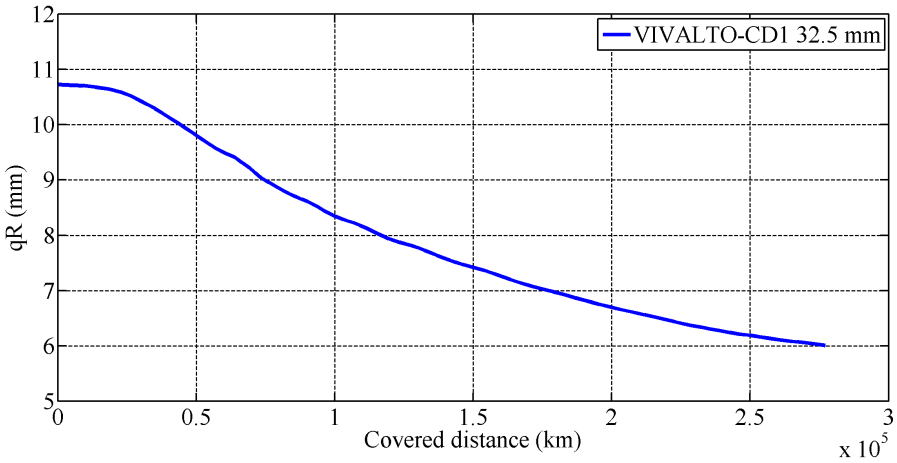

Figure 7.25. Progress of the qR dimension (Vivalto).

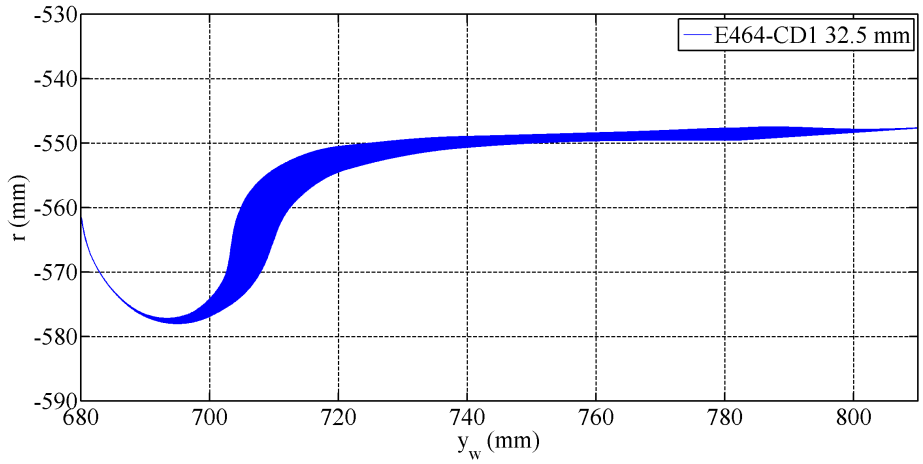

Figure 7.26. Evolution of the wheel shape (E464).

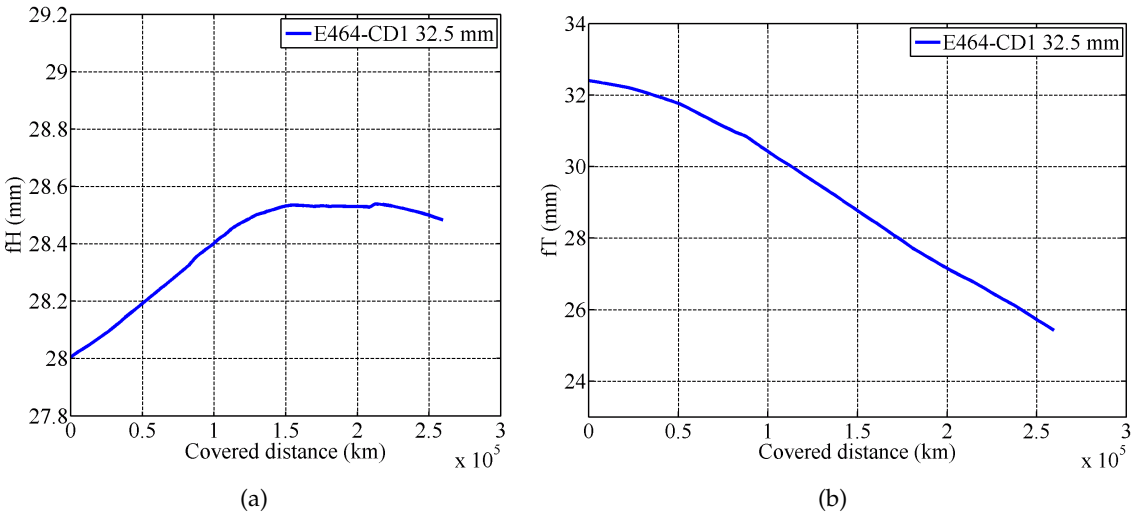

Figure 7.27. Progress of the flange height (a) and thickness (b) (E464).

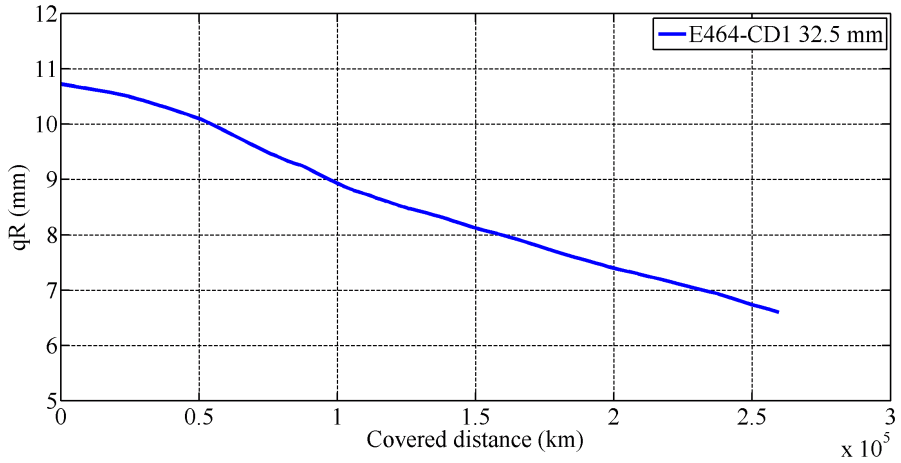

Figure 7.28. Progress of the qR dimension (E464).

Table 7.6. Distance covered before reaching the limit values (E464-Vivalto, CD1-30.5 mm).

	qR(7.5 mm)	fT(24.0 mm)
Vivalto (km)	92 000	131 000
E464 (km)	146 000	159 000

The progress of the three dimensions is depicted in detail in Figs. 7.29, 7.30 and 7.31 for the Vivalto, whereas the corresponding graphs of the traction unit are shown in Figs. 7.32, 7.33 and 7.34. The trend of the flange thickness and the flange height is almost linearly related to the distance, while the qR progress is nonlinear instead, as has been seen even in the previous case. The qR evolution is characterized by range of kilometrage during which the variation in the flange shape is quicker if compared to the last phases: the presence of a long steep slope in the first steps can reduce considerably the maximum mileage before going over the threshold limits.

7.2.4 Vivalto-E464: CD1-28.5 mm profile

To complete the close examination on the CD1 profile and its variants, the results for the flange thickness of 28.5 mm are illustrated from Fig. 7.35 to Fig. 7.40. Making a comparison with the other CD1 profiles, a higher wear on the tread is more pronounced when the thinnest flange is adopted on the train. This is due to the mean position on the tread of the contact point on the internal wheel in curves, so that it can be stated that this sort of profile induces a larger utilisation of the tread from the start to end because the wheelsets have a wider lateral clearance available in the track, especially at the beginning of the whole procedure. This is particularly important for those trailer axles which, depending on the bogie characteristics and the curve radius, may run in flange contact by using a certain wheel profile and conversely may run without any flange contact if equipped with thinner flange profile. It must also be remembered that, due to the choice to sum up the wear contributions in a global average on the vehicle, the contribution to wear on the flange of the internal wheels and the trailer wheelset of a the bogies is generally lower with respect to the first external wheel of each bogie, but as regards the wear on the tread, the contribution of each wheel is significant, because first of the longitudinal and tangential forces due to the creepage on the two sides of the wheelset have similar magnitude and even in trailer axes the longitudinal force arising from the creepages can have a remarkable magnitude.

Table 7.7. Distance covered before reaching the limit values (E464-Vivalto, CD1-28.5 mm).

	qR(7.5 mm)	fT(24.0 mm)
Vivalto (km)	78 000	106 000
E464 (km)	103 000	112 000

The summary on the results of this matching are summed up in Tab. 7.7: a further decrease in the overall performance was to be expected; the reduction is anyway apprecia-

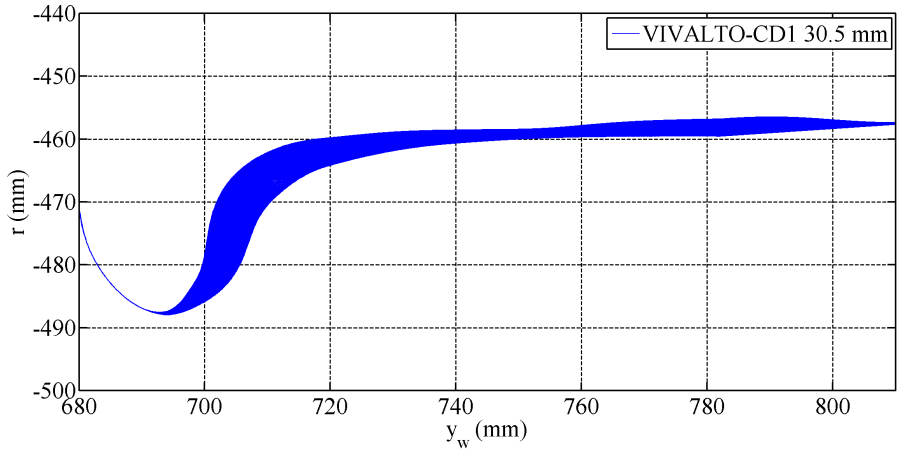

Figure 7.29. Evolution of the wheel shape (Vivalto).

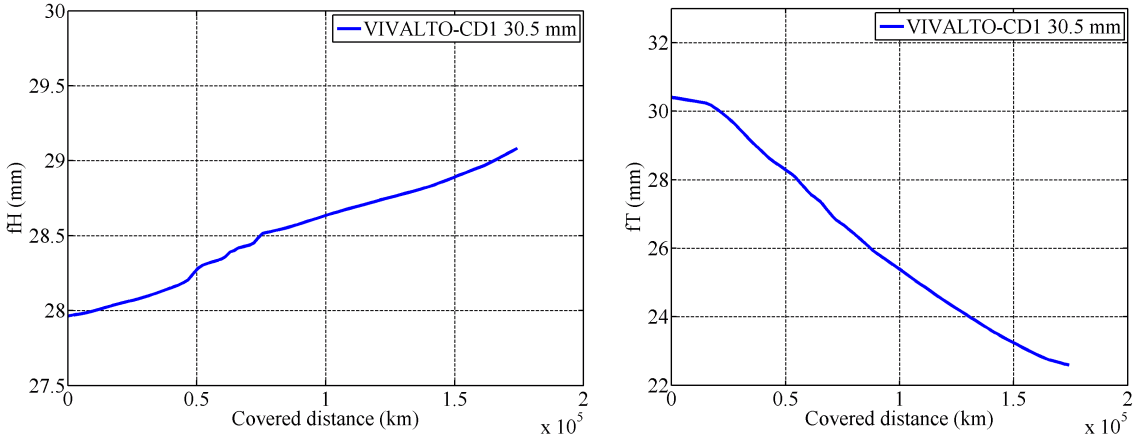

Figure 7.30. Progress of the flange height (a) and thickness (b) (Vivalto).

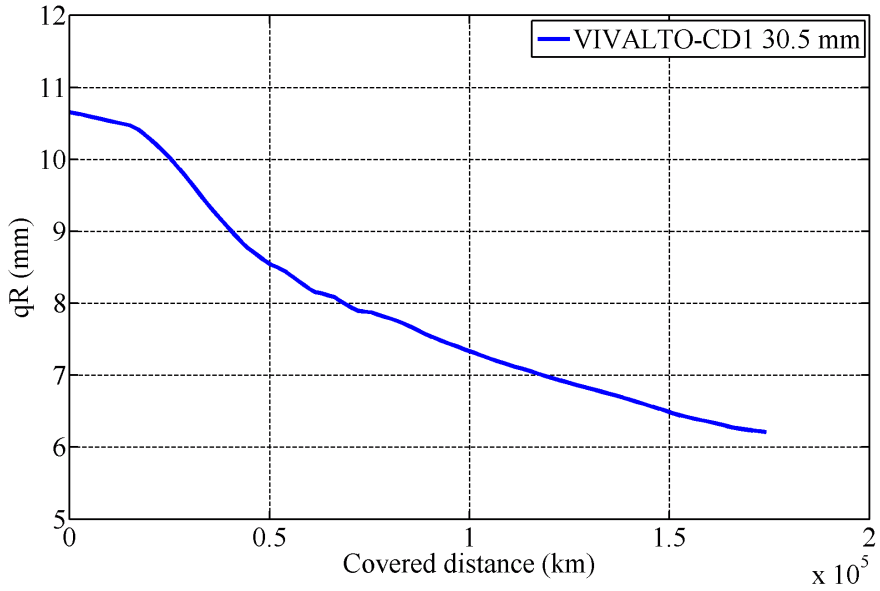

Figure 7.31. Progress of the qR dimension (Vivalto).

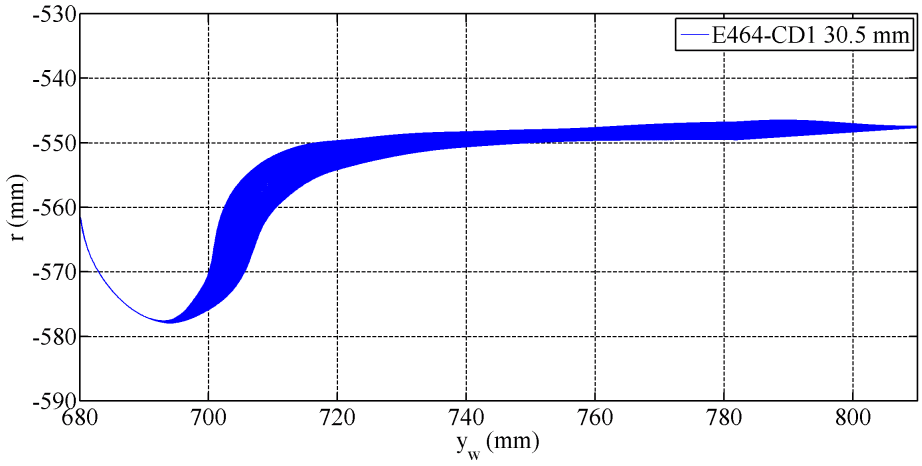

Figure 7.32. Evolution of the wheel shape (E464).

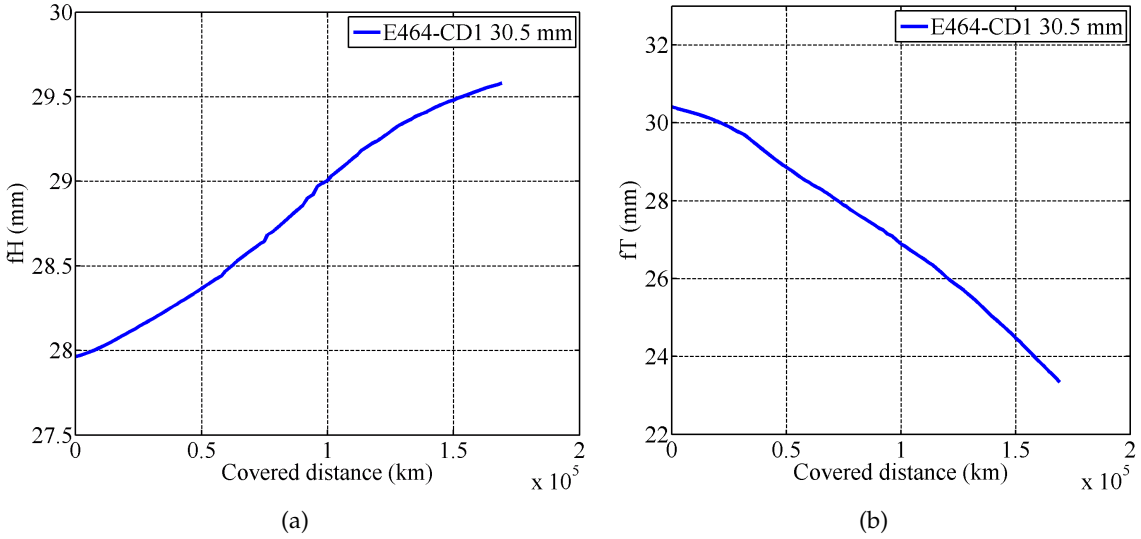

Figure 7.33. Progress of the flange height (a) and thickness (b) (E464).

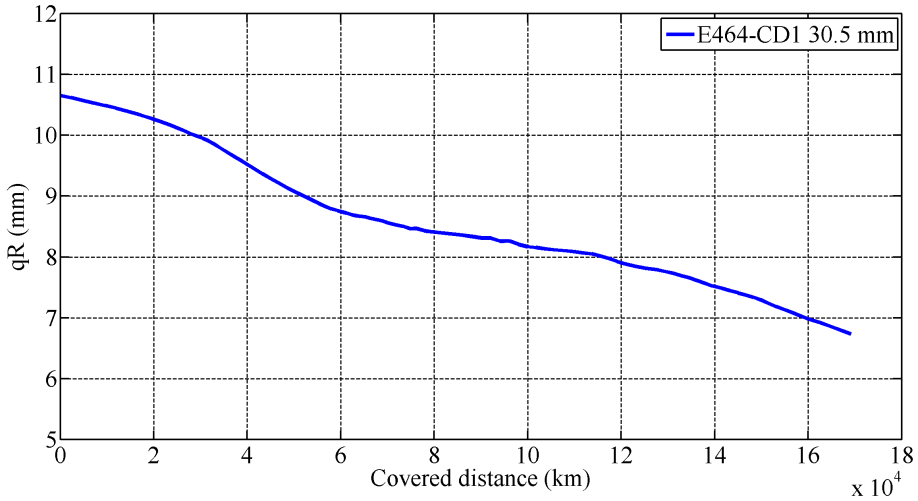

Figure 7.34. Progress of the qR dimension (E464).

ble if compared with the performance provided by the intermediate CD1 version (flange of 30.5 mm, see Tab. 7.6). The resistance to wear of the traction unit is again better than that of the Vivalto.

7.2.5 Vivalto-E464: DR2 profile

The last train-profile matching to be examined in order to conclude the review on the resistance against wear is the combination Vivalto composition-DR2 profile. Even for this train composition, the DR2 profile has proven to be the best one in terms of wear among all the combinations which have been investigated. As shown in Tab. 7.8, the covered distances as long as the reference dimensions remain within the prearranged limits, are greater than 150 000 km (200 000 km as regards the E464). With respect to the S1002, the distances are increased of about 27 % by choosing this wheel profile for the two vehicles: the improvement concerns the progress of the qR quota while the flange thickness reduction can be considered on average the same (see from Fig. 7.41 to Fig. 7.46).

Table 7.8. Distance covered before reaching the limit values (E464-Vivalto, DR2).

	$qR(7.5\,\text{mm})$	$fT(24.0\,\text{mm})$
Vivalto (km)	153 000	252 000
E464 (km)	211 000	$>$ 270 000

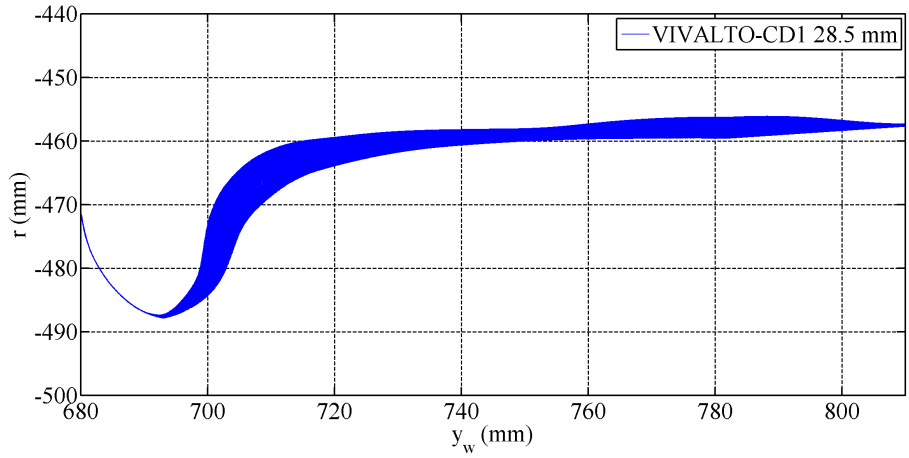

Figure 7.35. Evolution of the wheel shape (Vivalto).

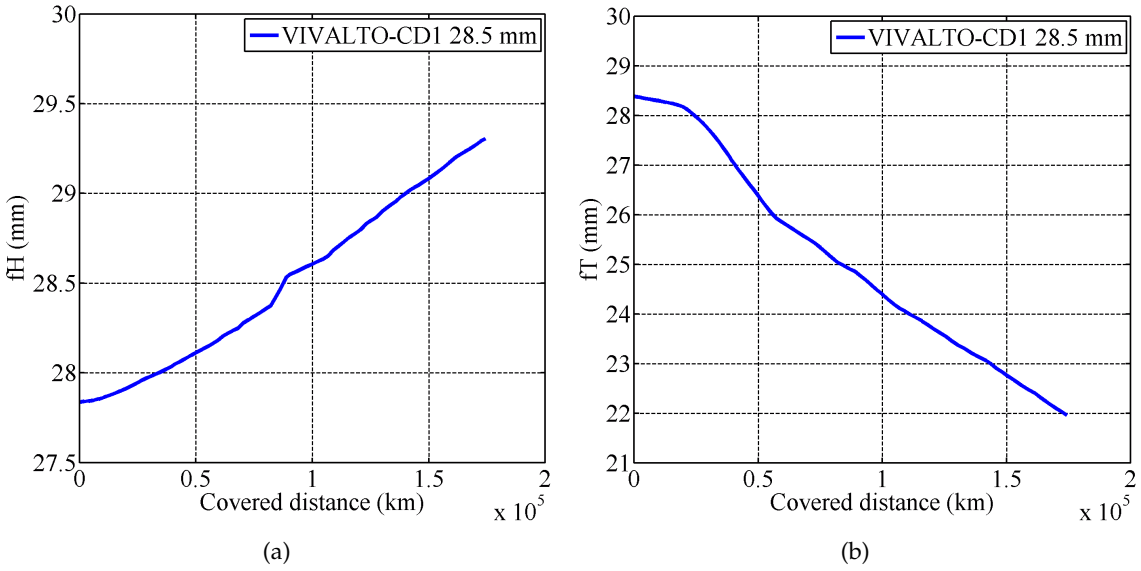

Figure 7.36. Progress of the flange height (a) and thickness (b) (Vivalto).

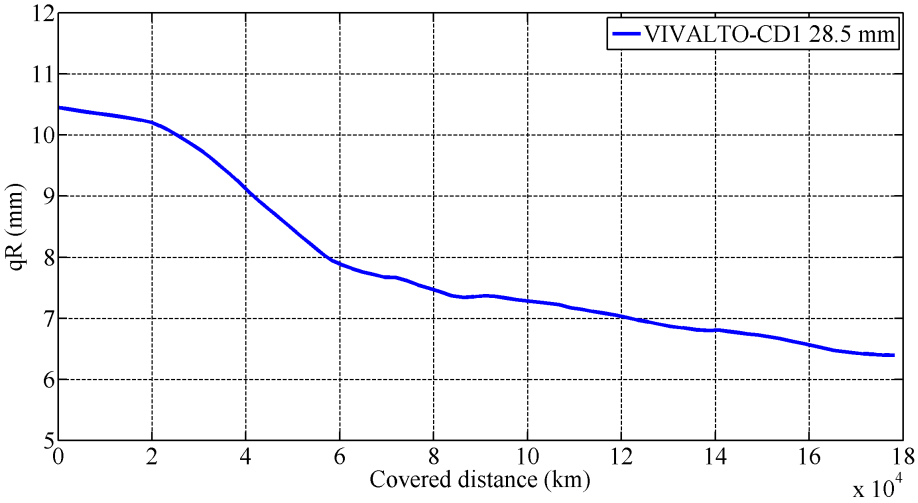

Figure 7.37. Progress of the qR dimension (Vivalto).

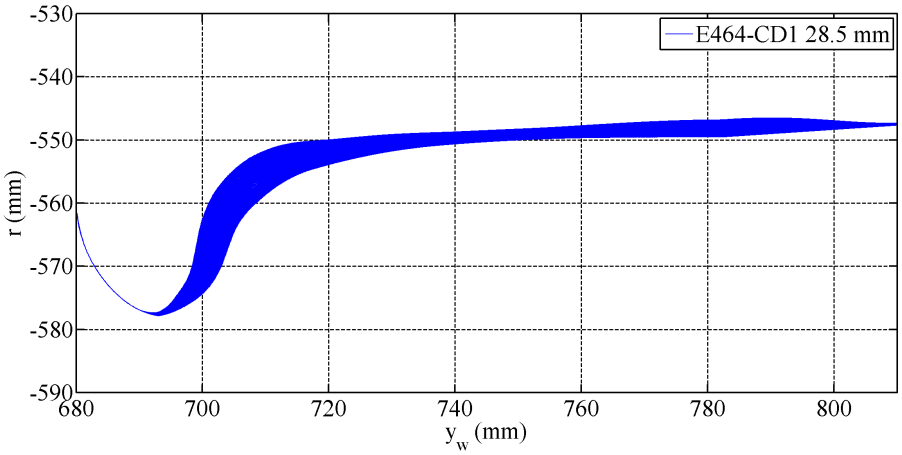

Figure 7.38. Evolution of the wheel shape (E464).

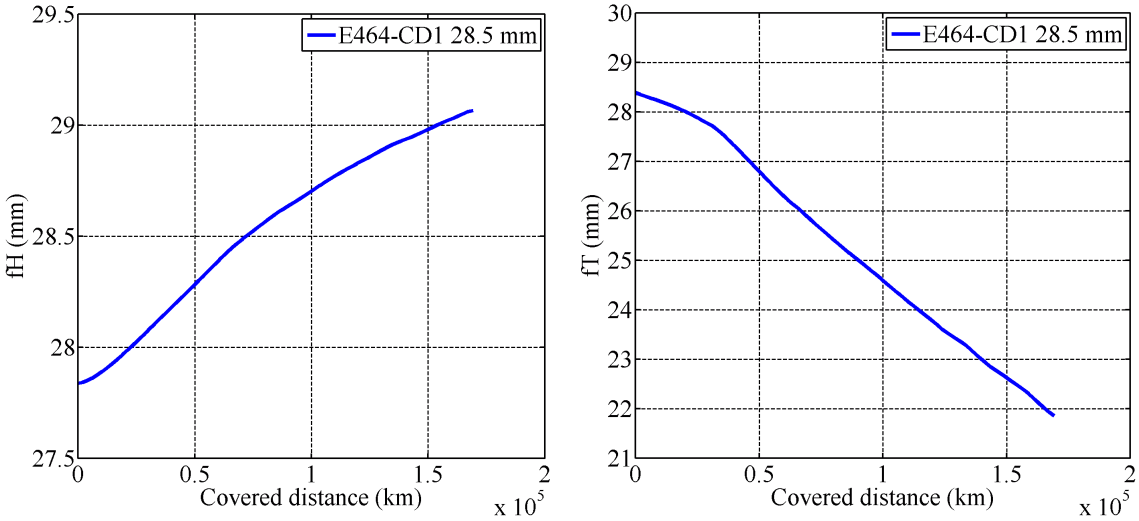

Figure 7.39. Progress of the flange height (a) and thickness (b) (E464).

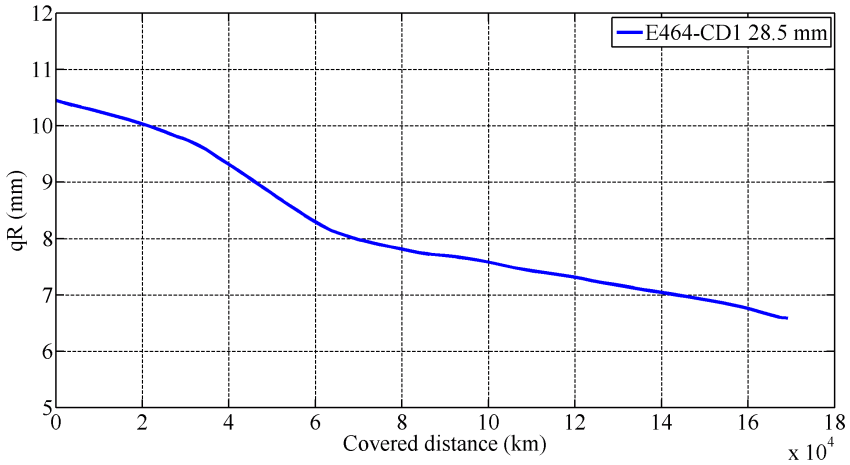

Figure 7.40. Progress of the qR dimension (E464).

7.2.6 Vivalto-E464: summing up

A brief summary of results for the Vivalto composition is reported in Tab. 7.9 and its graphical representation in Fig. 7.47. As hinted in previous subsections the best performance is provided by the DR2 profile which guarantees, according to the response of the model, a total mileage beyond 150 000 km, by far exceeding the S1002 result. However, even the results of the CD1-32.5 are surely to be considered interesting (144 000 km), while the other two variants of this profile lead to overall distance comparable with the S1002. In regard to the new wheel geometries, in this context the difference between the DR2 and the CD1 is of slight extent ($6 \div 7$ %).

Table 7.9. Summary of the Vivalto-E464 results.

Wheel profile	ORE S1002	CD1 32.5 mm	CD1 30.5 mm	CD1 28.5 mm	DR2
Total distance (km)	120 000	144 000	92 000	78 000	153 000

7.3 Further considerations on the results

The review on the wear assessment just presented has shown that, as it was expected, a correct choice of the wheel profile without any change in the rail profile (or profiles, such as in this work) can positively affect not only the dynamic behaviour of the vehicle but also the resistance against wear, leading to a significant improvement of the performance from this point of view. Even under condition of severe wear, such as those experimented by the Minuetto model on its mean line, the results may be encouraging: the CD1 profile and the DR2 have proven to work fine and better than the S1002, which is clearly inadequate for the rail inclination of 1/20 as regards both the kinematic characteristics and the resistance against wear.

The best performance has been shown by the DR2 profile either the scenery was the Minuetto mean line or the Vivalto virtual track; the increase in the total distance is very interesting in both the cases, taking also into consideration that the initial value of the reference dimensions are practically the same.

Considering what has been seen up to this point, the wear tends to remove material especially on the flange of the profile rather than on the tread and as a consequence the reduction in rolling radius of the wheel profiles is quite low. For this reason, the flange height during the wear simulation increases of a modest amount and the evolution of the dimension itself is of poor interest even if it has been reported for the sake of completeness. This behaviour of the wear model arises from the validation on the Aosta Pre-Saint Didier track by means of a wear model mainly based on an experimental wear law deduced in roller rig test and mainly based on the adhesive wear. The presence of other wear mechanisms is hence implicitly and partially included, but could be made more explicit as previously discussed; nevertheless, the introduction of other mechanisms such as the rolling contact fatigue or the plastic wear would require further detailed and experimental data related to

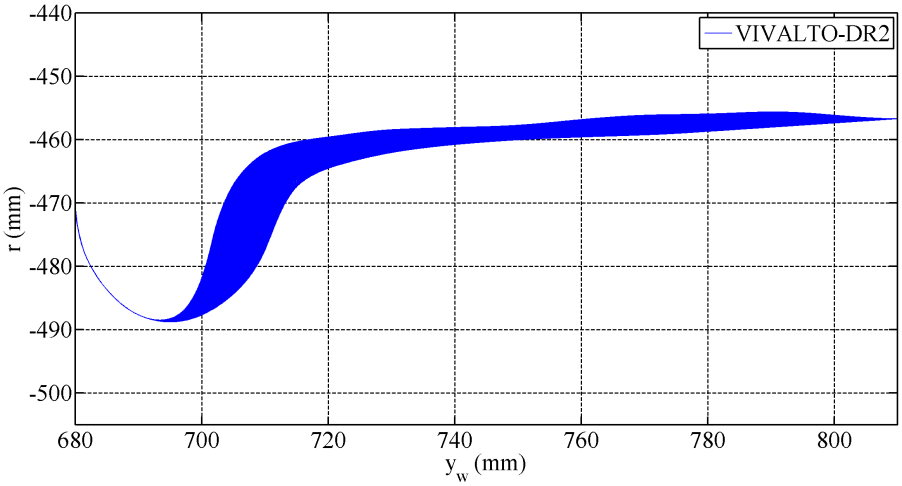

Figure 7.41. Evolution of the wheel shape (Vivalto).

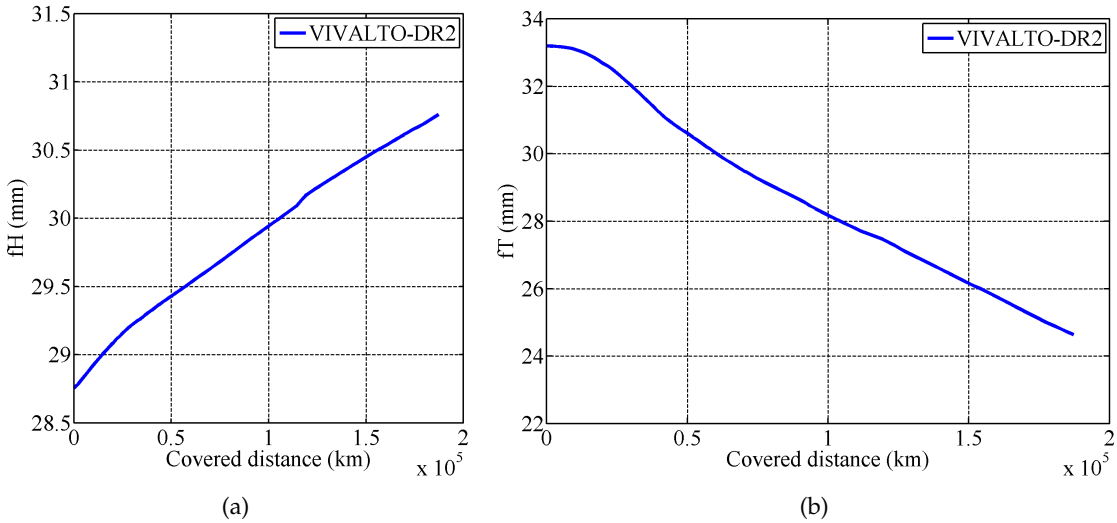

Figure 7.42. Progress of the flange height (a) and thickness (b) (Vivalto).

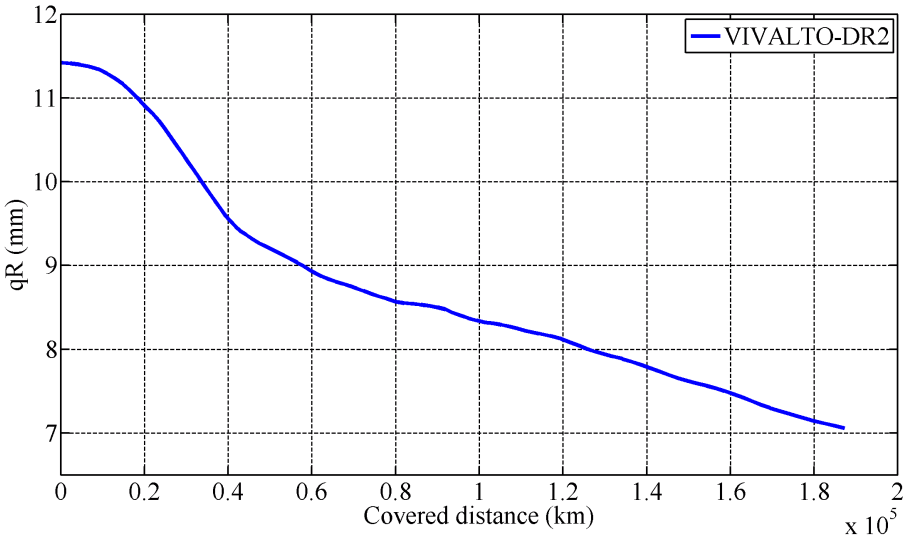

Figure 7.43. Progress of the qR dimension (Vivalto).

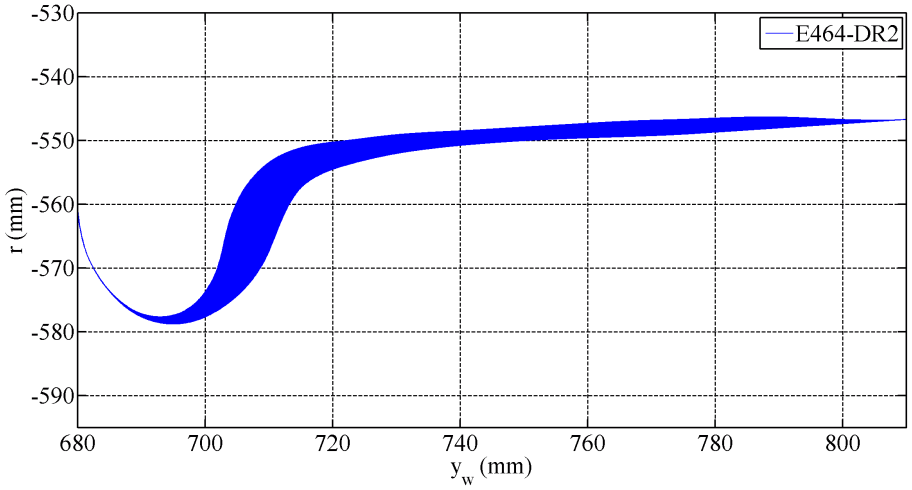

Figure 7.44. Evolution of the wheel shape (E464).

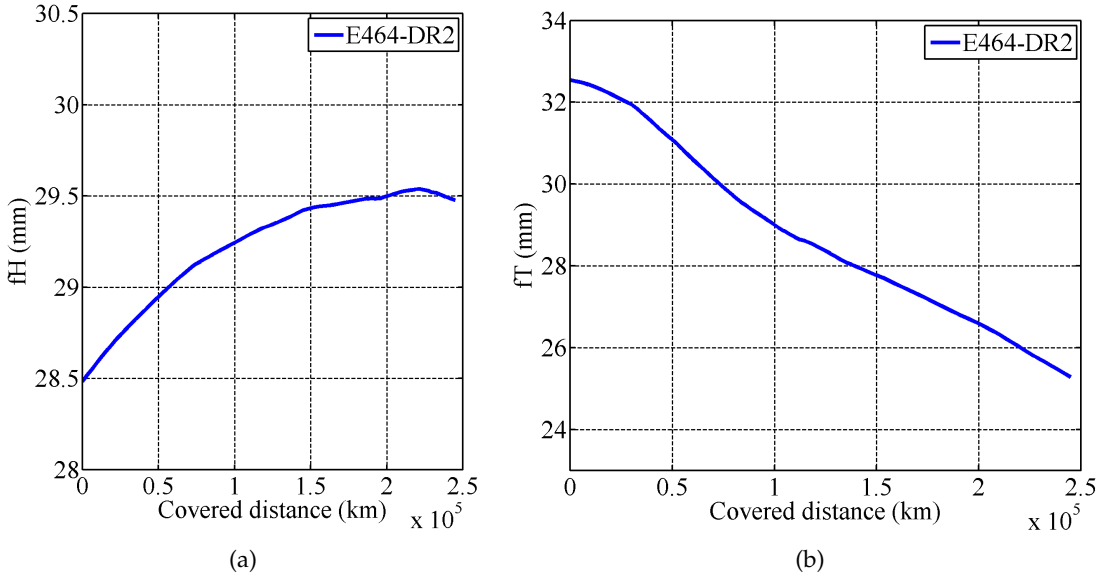

Figure 7.45. Progress of the flange height (a) and thickness (b) (E464).

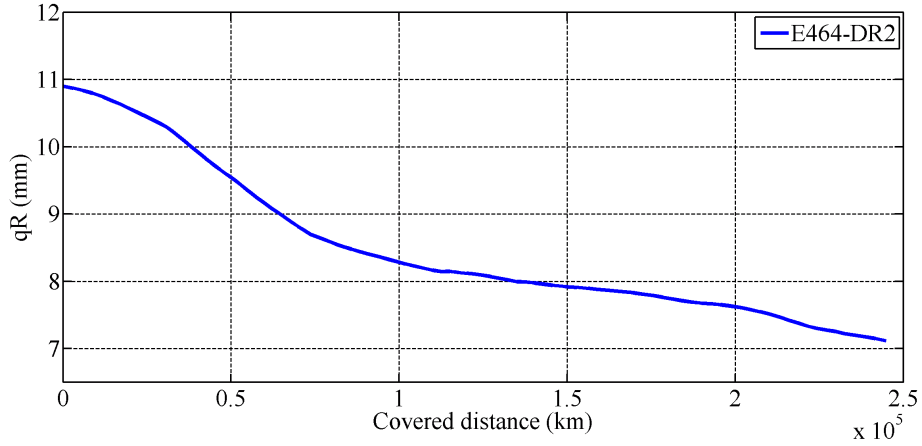

Figure 7.46. Progress of the qR dimension (E464).

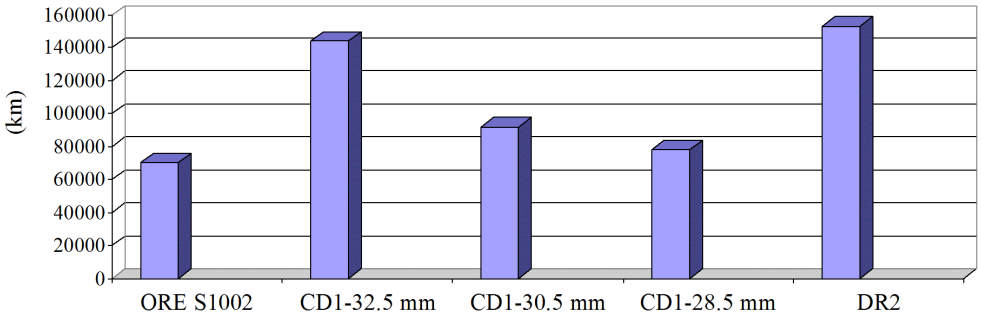

Figure 7.47. Graphical representation of the results summarized in Tab. 7.9.

tests conveniently organised in order to isolate the phenomenon, not to mention the need to overcome the statistical dispersion of the results.

However, the aim of the comparison was to establish and quantify the relative difference in behaviour by varying the wheel profile, in order to find a new wheel profile to be tested on real vehicles. It follows that a slight difference in the absolute value of the presented travelled distances due to the underestimation (or overestimation) of the real wear rate does not alter significantly the results. This is even more true when the simulation context comprises a set of different running situation (straight track, sharp curves and large curves) instead of a certain condition, where a particular wear mechanism might predominate on the others.

The analysis of the final wheel shapes show that the resultant wheel profiles often turn out to be quite similar to each other, according to the fact that, when a significant distance has been covered, the influence of the initial wheel profile become to be less evident and the final wheel shape is more and more strictly linked to characteristics of the rail profile and the rail inclination (or of the set of rails, as in this research), which are the same for all the vehicle-wheel profile combination.

CHAPTER 8

Stability Assessment

The following chapter presents a series of results pertaining to the stability assessment of the vehicles equipped with the innovative wheel profiles taken into account in this work. The aim of the analysis is to verify the stability condition at high speed of the three vehicles under consideration (Minuetto, Vivalto, E464) for different levels of wear, by using the wheel profiles evaluated via wear analysis and shown in Ch. 6.

Owing to its influence both in running safety and in track preservation, the assessment of stability for a railway vehicle is surely one of the most important analysis to be carried during the vehicle design. The definition of vehicle stability is tightly linked to the motion of its wheelsets as was hinted in Sec. 1.3. If a wheelset, due to the presence of track irregularities is displaced laterally with respect to the centre of the track or yawed by a certain angle, the consequent oscillatory motion will be damped or undamped, depending on the speed, the characteristic of the vehicle and the wheel-rail contact geometry and conditions. Supposing that the speed is constant and the lateral displacement or the yaw angle are small, if the resultant motion is damped the vehicle is considered stable, otherwise, if growing amplitude oscillations take place and the motion (hunting) is finally restricted only by flange contact, the vehicle has to be considered unstable for that value of speed. The lowest speed at which the hunting occurs is the *critical speed* of the vehicle; clearly the maximum speed of the vehicle in service should be enough lower than the critical speed.

Going into detail, a railway vehicle running at a certain speed is a complex mechanical system which can be thought in terms of its modal representation. Assuming that the linearised form is suitable to represent the vehicle behaviour for small displacements with respect the linearised state, the presence of the wheel-rail contact forces, which are dependent on the travelling speed, is the reason why, while some natural frequencies are constant as the speed changes, other mode shapes are dependent on speed instead. These mode shapes are referred to as “hunting movements”. In addition, as can be seen for example in [13], in the linearised model of a restrained wheelset, the positional part of the contact force is not conservative while the damping is inversely proportional to speed. With the change in speed, the frequency of the hunting movements increase while the damping tends to become lower. As a consequence, up to a certain speed all the mode shapes of the

vehicle are regularly damped, but above this speed, one ore more damping factors become negative and the system must be considered unstable. In the linear approach, this dividing line between stable and unstable behaviour is the critical speed for the vehicle: for this particular value of speed, the vehicle could be theoretically subjected to hunting of whatever amplitude without showing neither increase nor reduction in oscillation amplitude over time.

The linear model of the vehicle can represent a good approximation to investigate the real behaviour for small displacements, except for those vehicle which are strongly nonlinear. The linear solution for small displacements is also independent of the oscillation amplitude. Conversely, the behaviour of the system for displacement which can not be considered small depends on the amplitude and it is influenced by two major nonlinearities: flange contact and creep force saturation due to friction. When the nonlinear behaviour has to be investigated, the solution must be found via numerical solution of equations of motion by simulating the dynamic response to a disturbance.

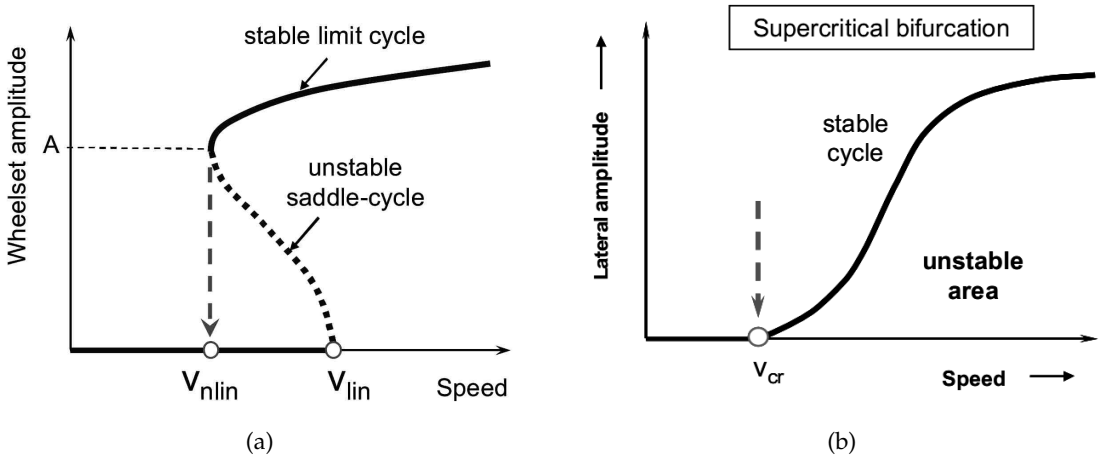

Figure 8.1. Example of limit cycle diagram for a nonlinear system: subcritical bifurcation (a); supercritical bifurcation (b) [40].

As it can be seen in Fig. 8.1a, as the travelling speed is increased, the dynamic response to a disturbance for small amplitude is practically the same of the linear model up to V_{lin}. As the amplitude increases, the locus of the equilibrium point (the dash line) moves back to lower speeds since the rolling radius difference, with its destabilizing effect, increases. By contrast, for amplitudes even higher, creep saturation progressively takes places, with a double stabilizing effect: the first one is the saturation of the contact forces itself due to friction and the second one is the reduction of the lateral force due to spin. In fact, this lateral force, acts in the opposite direction with respect to the force due to the gravitational stiffness and therefore tends to ease the stabilizing effect of this latter, especially for small displacement of wheelset, while for large amplitude these stabilizing effect is no longer reduced. The combination of these phenomena justifies the curve progress shown in Fig. 8.1a; the stability boundary moves to higher speed, on the stable limit cycle, which is the limit

cycle that is referred to as "hunting". The real critical speed of practical interest is V_{nlin}, which is often lower than the linear critical speed. The unstable saddle cycle represents the locus of points in which the solution given by the nonlinear equations is unstable. More precisely, for $V_{nlin} \leq V \leq V_{lin}$, three steady motions are possible; two of these three motions are stable (the two solid lines) while the solution on the dotted boundary is unstable because if the amplitude become slightly greater than that corresponding to the boundary, the oscillation will rise and the new equilibrium point will be on the upper stable limit cycle, while conversely, if the amplitude become slightly lower than the boundary unstable value, the oscillation will decay until the lower solid line is reached. Furthermore, if the vehicle is speed is greater than V_{lin}, whatever the amplitude is, the oscillation amplitude will converse to the upper stable limit cycle and the motion is anyway unstable.

Sometimes the behaviour of the vehicle may be differ from the one of Fig. 8.1a just discussed; it may be simpler, as depicted in Fig. 8.1b, where the linear and nonlinear critical speeds are the same (indicated with V_{cr} in the figure); it may even more complicated due to the presence of more than one unstable saddle cycle.

Typically, the instability occurs as bogie hunting, that is a movement in which the two wheelset are parallel during the sinusoidal motion. Car body hunting can also appear if the wheel-rail contact geometry causes low frequency oscillation and the car body moves together with the bogies.

8.1 Linear stability

Considering what has been seen up to this point, a stability assessment of the vehicle can be performed by checking the position of the eigenvalues in the complex plane as the constant travelling speed increases. Nevertheless, this kind of analysis is used in vehicle design mainly for optimisation purposes or as a complementary tool, since it provides indicative results which cannot take into account the important nonlinearities (bumpstop clearance, flange contact, contact force saturation, contact geometry). If the vehicle model is highly nonlinear, the equivalent linear model could be meaningless even for small displacement.

However, the linear approach is usually being exploited by introducing harmonic linearisation of the wheel-rail contact [18]. The analyses are usually carried out by varying the equivalent conicity and the creep coefficients of the contact forces: in fact, even tough the saturation of the contact force due to friction cannot be taken into consideration, the variation in creep coefficients allows the simulations of different contact conditions (dry or wet). However, the main issues in the linear approach stability were widely investigated by Polach and a few results can be found in [41, 40].

8.2 Nonlinear stability

An alternative and most reliable method in calculating via software the critical speed is the nonlinear time integration, by using an accurate multibody model of the vehicle. All other parameters being equal, the result of a nonlinear stability analysis is strongly influenced by the following factors:

- contact geometry characteristics;
- friction coefficient between wheel and rail;
- method and criteria applied.

The influence of the contact geometry has already been discussed in the previous sections; it plays a fundamental role in terms of equivalent conicity and gravitational stiffness. The influence of the coefficient of friction in the wheel-rail contact is remarkable likewise: if the coefficient of friction is low, the modulus of the tangential force vector is low too; high creepages take places in the contact patch and the resultant motion of the wheelset is far enough to the equivalent kinematic Klingel's solution for the same amplitude of oscillation. Vice versa, an high coefficient of friction makes the solution of the equation of motion very near to the kinematic motion, with lower creepages and a strong wheel-rail interaction since the tangential force can reach high values. To sum up the phenomenon, a reduction in coefficient of friction leads to a minor effect of the conicity on the vehicle dynamics and hence to a an higher critical speed; by contrast the critical speed decreases significantly as the friction increases up to 0.5. Nevertheless, by increasing the friction above 0.5, the reduction in the critical speed become slighter.

The other important advantage above-mentioned in calculating the critical speed via nonlinear time integration is the possibility to investigate the effect of the gravitational stiffness for large displacement up to the flange takes place. Since the gravitational stiffness provides a restoring force which might be even destabilizing in certain case, the phenomena should always be taken into consideration in evaluating the stability.

A certain influence on the results of the stability assessment is also given by the method and the criteria adopted in the analysis. In fact, at least three different methods are commonly used and depending on the strategy chosen, the physical quantities involved can be:

- sum of guiding (lateral) forces between wheelset and track;
- lateral accelerations on the bogie frame (RMS value over 100 m of track);
- wheelset displacement (RMS value over 100 m of track);

A further classification could also be done on the basis of the type of excitation excitation (singular or stochastic) as well as on the amplitude of the latter.

The first two methods are suggested by [17, 42] respectively in the normal and simplified measuring method are conceived to be applied on vehicles during experimental measurements for approval. The third method is instead suitable especially in computer simulations and it is even more interesting from a theoretical point of view, thus it has been used in this work to investigate the stability performance of the considered vehicles. The approach consists in observing the behaviour of the wheelset oscillation after a disturbance has applied; to decide whether the vehicle is stable or not at a certain travelling speed, by observing the amount of available damping. The vehicle can be considered stable if no growing oscillations take place and if at the same time the system have sufficient damping to converse at the unperturbed state.

In addition, unlike the other two criteria, since the physical quantity under examination is a displacement and not a force or an acceleration, the results do not need any filter treatment and the difference between the stable and unstable motion of the vehicle is usually easier to be detected without any data processing. Nevertheless, if applied in dynamic simulation, the three criteria generally lead to comparable results as regards the critical speed of engineering interest.

8.3 Results of stability assessment

The results of the stability analyses on all the three vehicles will be presented in the following sections. For each vehicle, the critical speed has been calculated via time integration in SIMPACK by applying three different wheel profile: the S1002, the CD1-32.5 and the DR2. For each combination of vehicle and profile, three different levels of wear are taken into account: the unworn profile, the profile when about half of steps have been completed and the final geometry, after the whole mileage of that combination has been reached. The three levels of wear will be referred to as new or unworn, 50 % worn or 50 % of wear, and fully worn or worn respectively. Being the km_{step} variable, the profile at 50 % of wear does not corresponds to the half simulated kilometrage, but generally to a longer distance, since the km_{step} usually decreases as the wear proceeds. According to the aim of the project, the rail inclination has always been set to $1/20$ rad, to analyse the dynamic response in the same scenery for which the wear evaluation have been carried out; whatever exception has been highlighted to avoid misunderstandings.

The analysis have been carried out by introducing a sudden lateral shift of the track as a ramp having longitudinal width equal to 0.15 m and height equal to 5 mm. In order to calculate exactly the nonlinear critical speed even in those cases where one or more unstable limit cycles exist, the simulation has been performed by starting from the limit cycle at high speed and then reducing gradually the speed until the oscillation vanishes. In this way the lowest critical speed can be easily found even in those cases in which the amplitude-speed diagram is quite complicated and presents small amplitude limit cycles besides to the large amplitude cycle. The speed profile applied to the vehicle consists of a linear reduction as a function of the travelled distance, of which an example of time

progress is reported in Fig. 8.2.

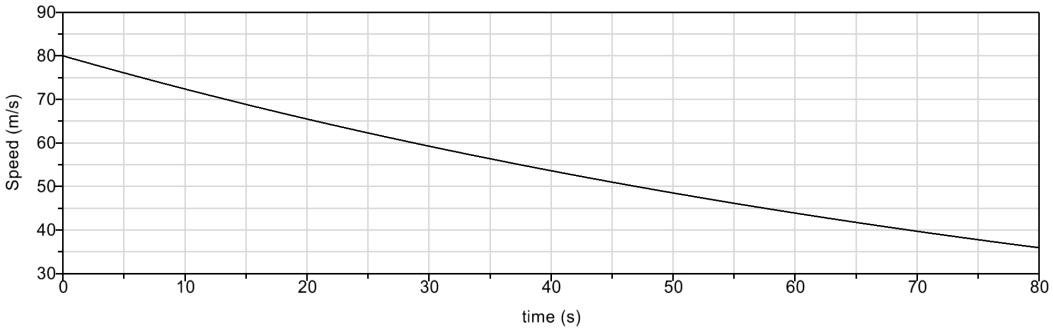

Figure 8.2. Example of speed profile adopted in evaluating the critical speed.

For the purpose of analysing the worst running conditions, a high friction coefficient, equal to 0.4, has been selected for all the simulations which will be presented in the following. In all the investigated cases, the lateral displacement with respect to the centre of the track of the most critical wheelset of the vehicle and the critical speed will be shown.

8.4 Stability analysis of the Minuetto

8.4.1 S1002 wheel profile

The behaviour of the ALn 501 Minuetto equipped with the ORE S1002 profile is summarized by Figs. 8.3, 8.4 and 8.5.

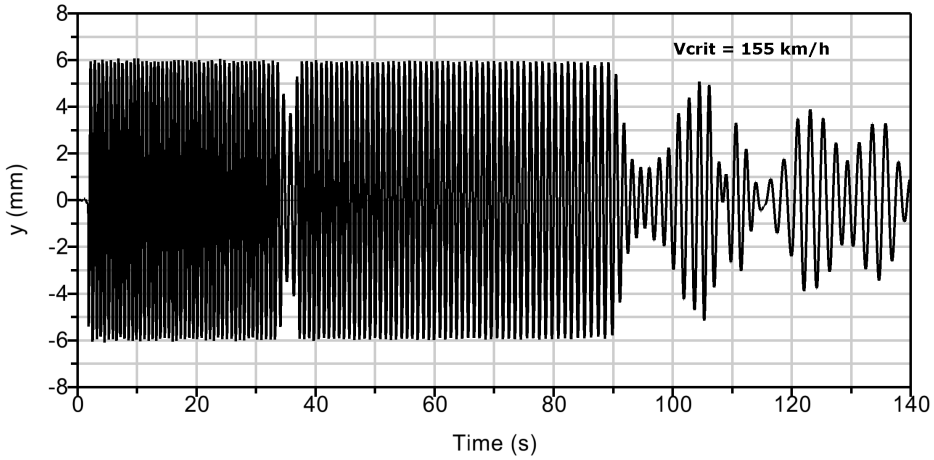

Figure 8.3. Lateral displacement of the most critical wheelset; Minuetto, unworn S1002 profile.

The Minuetto exhibits a low critical speed even when equipped with unworn wheel profile if the rail inclination is 1/20 rad, equal to about 155 km/h. In the other two cases the low conicity leads to low frequency oscillations and low steering forces: the system seems to be strongly underdamped especially in the intermediate condition of worn where the system has to be classified as unstable. In the third case (fully worn profile), the amplitude of the limit cycle reduces only at 125 km/h, without a significant decay rate.

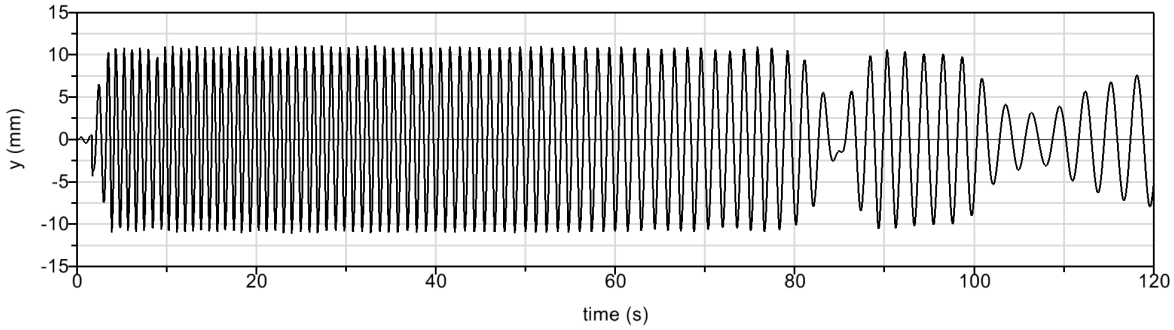

Figure 8.4. Lateral displacement of the most critical wheelset; Minuetto, 50 % worn S1002 profile.

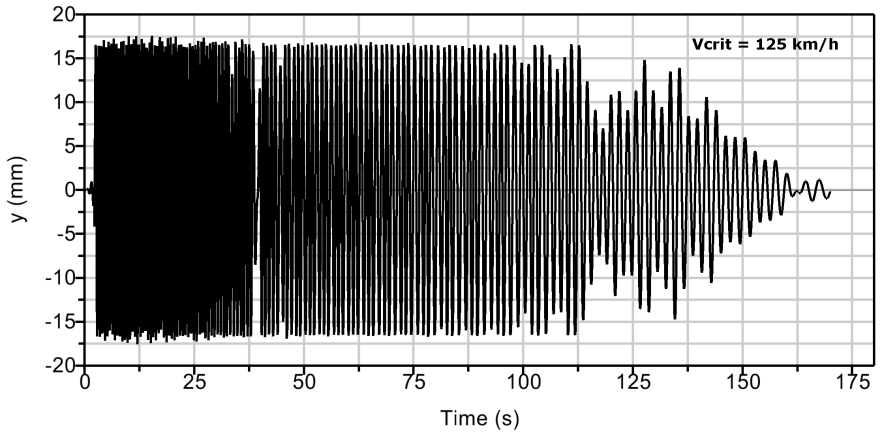

Figure 8.5. Lateral displacement of the most critical wheelset; Minuetto, fully worn S1002 profile.

For comparison, the response of the model with a rail inclination of 1/40 is shown in Fig. 8.6: although the conicity of this matching is higher with respect to the previous case, the behaviour is totally different and can be surely considered better. In fact, the critical speed (230 km/h) is resolutely higher and the residual oscillation converge quickly to zero. The restoring force due to the conicity are stabilizing below 230 km/h.

8.4.2 CD1-32.5 wheel profile

By equipping the Minuetto with the CD1-32.5 wheel profile, the stability analyses give the results shown in Figs. 8.7, 8.8 and 8.9.

The response with the unworn profile is very to close to the behaviour of the S1002-1/40 even if the conicity for small displacements in the neighbour of the track centre are a little different. Probably a linear analysis, strongly influnced by the linearisation of the contact geometry parameters, would produce a wider difference in the critical speeds.

The critical speed with the worn profiles, depicted in the other two figures, is lower of about 80-90 km/h and the response is more complicated. When the 50 % worn profile is used, a significant reduction in the amplitude of the limit is reached at about 150 km/h; in addition, a small amplitude limit cycle is also present as it can be seen by observing

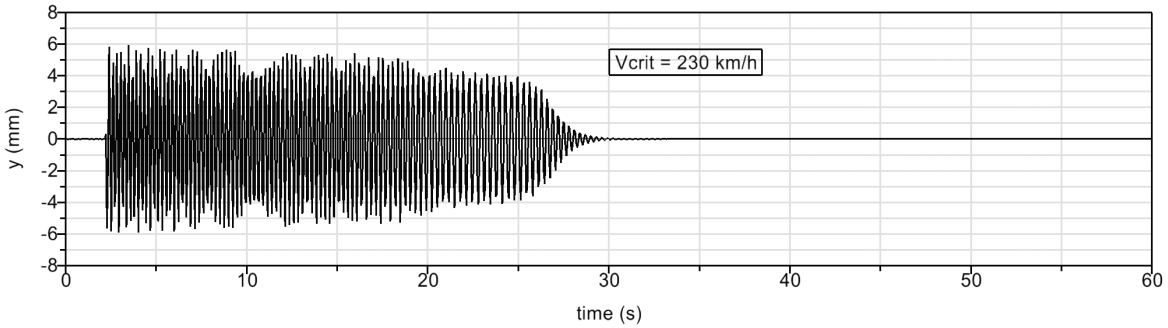

Figure 8.6. Lateral displacement of the most critical wheelset; Minuetto, unworn S1002 profile 1/40 rad.

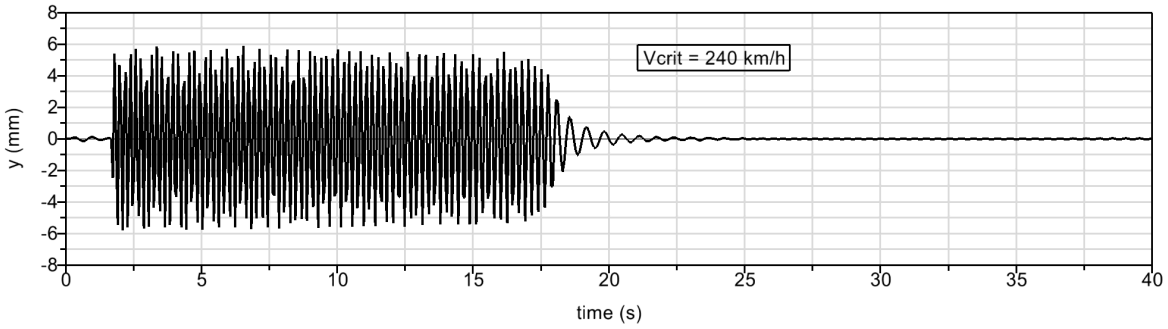

Figure 8.7. Lateral displacement of the most critical wheelset; Minuetto, unworn CD1-32.5.

the slow decay in the oscillation as the speed increases. It is interesting to note that at high speed the oscillation are even lower than the amplitude of the displacement applied through the irregularity. For the lower speed range, the fully worn profile provide a similar behaviour to the intermediate worn shape; the response of the model in these two cases is strongly influenced by a low conicity and a gravitational stiffness effect which besides not providing a significant restoring force, it tends to destabilize the vehicle in a certain speed range.

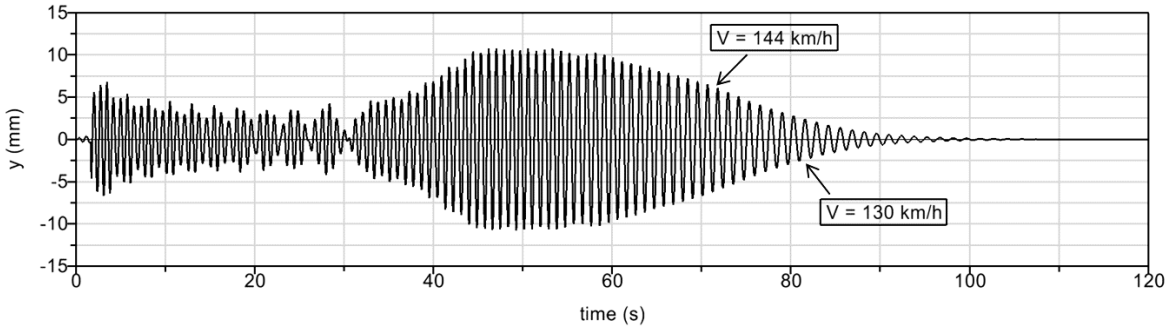

Figure 8.8. Lateral displacement of the most critical wheelset; Minuetto, 50 % worn CD1-32.5 profile.

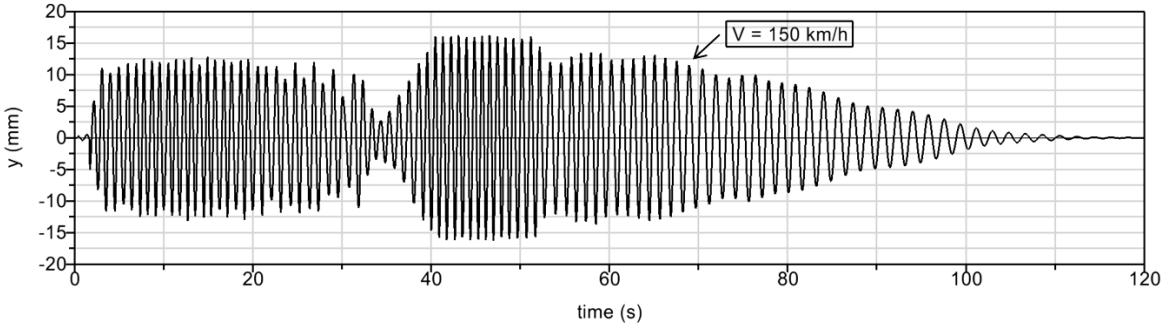

Figure 8.9. Lateral displacement of the most critical wheelset; Minuetto, fully worn CD1-32.5 profile.

8.4.3 DR2 wheel profile

As regards the stability assessment of the Minuetto equipped with the DR2 profile, the critical speed value (225 km/h, Fig. 8.10) is consistent with the results of the unworn CD1-32.5 and S1002 when this latter is used on rails having a lying angle of 1/40 rad.

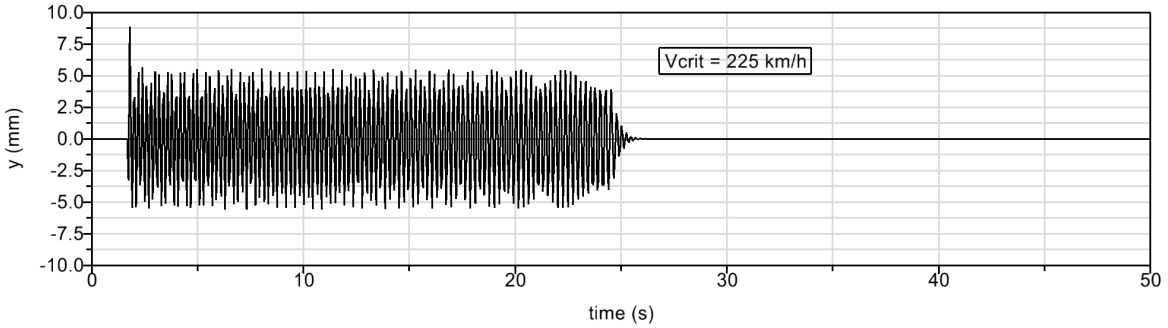

Figure 8.10. Lateral displacement of the most critical wheelset; Minuetto, unworn DR2 profile.

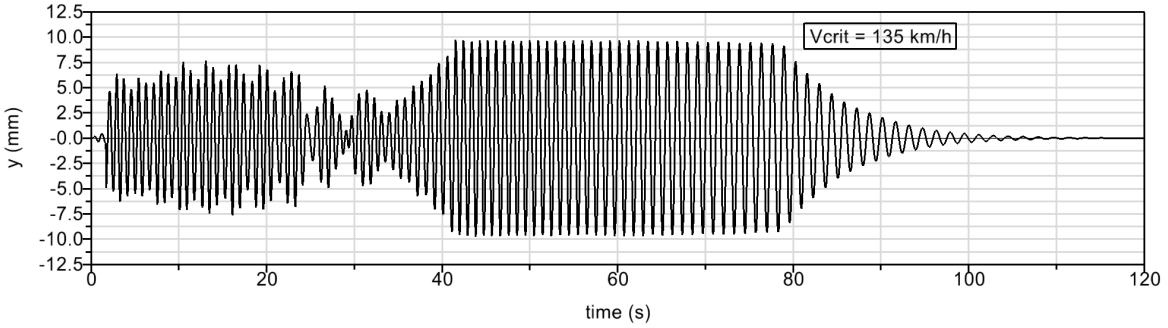

Figure 8.11. Lateral displacement of the most critical wheelset; Minuetto, 50 % worn DR2 profile.

Like in the case of the CD1-32.5 wheel profile, the response at the 50% of wear (Fig. 8.11) shows that the vehicle has a limit cycle with an amplitude which is lower than the flangeway clearance; by reducing the speed the amplitude grows and flange contact occurs. The oscillation begin to decay at significantly at about (140 km/h). At the speed of (135 km/h)

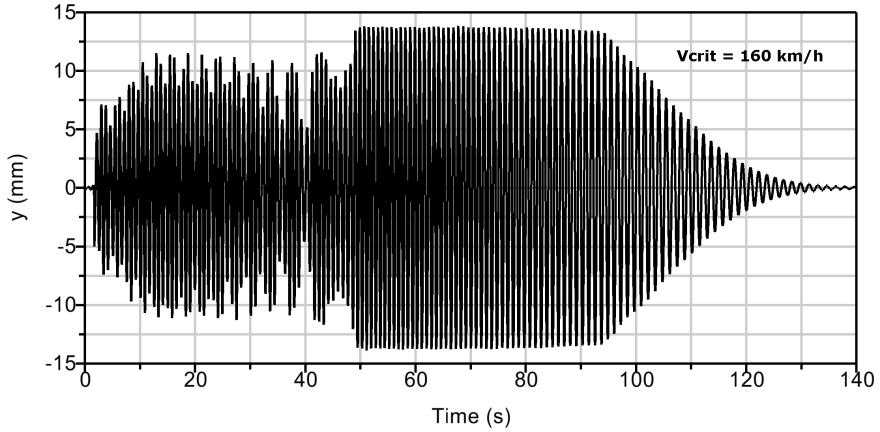

Figure 8.12. Lateral displacement of the most critical wheelset; Minuetto, fully worn DR2 profile.

can be considered stable from a practical point of view.

When the fully worn profile is applied to the vehicle (Fig. 8.12), the critical speed of interest is similar to the previous one; the oscillation start to vanish at about 160 km/h, while at high speed the limit cycle has an amplitude almost equal to the flangeway clearance. The slowness of the decay rate of the residual oscillations may be attributed to the low value equivalent conicity of the worn profile coupled with a destabilizing gravitational stiffness, which have a slight negative slop in the neighbour of zero lateral displacement.

8.5 Stability analysis of the Vivalto

8.5.1 S1002 wheel profile

In regarding to the behaviour of the Vivalto with the S1002 profile, the vehicle is completely stable in all the three configurations without any limit cycle: the resultant critical speeds (Figs 8.13, 8.14 and 8.15) are greater than 270 km/h even with the fully worn condition.

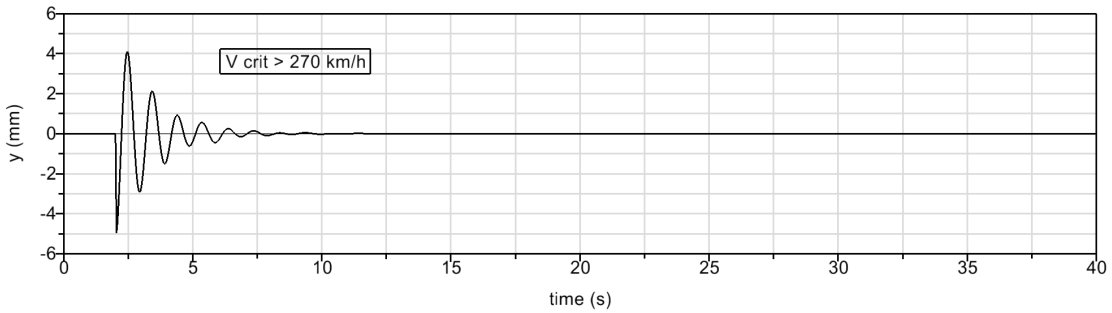

Figure 8.13. Lateral displacement of the most critical wheelset; Vivalto, unworn S1002 profile.

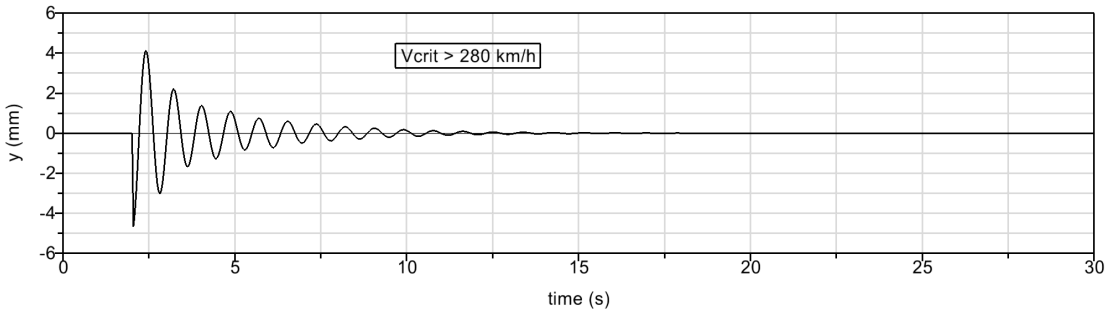

Figure 8.14. Lateral displacement of the most critical wheelset; Vivalto, 50 % worn S1002 profile.

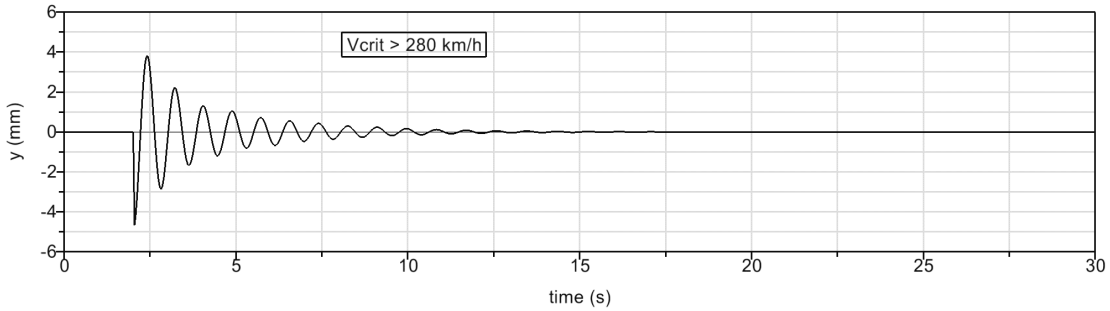

Figure 8.15. Lateral displacement of the most critical wheelset; Vivalto, fully worn S1002 profile.

8.5.2 CD1-32.5 wheel profile

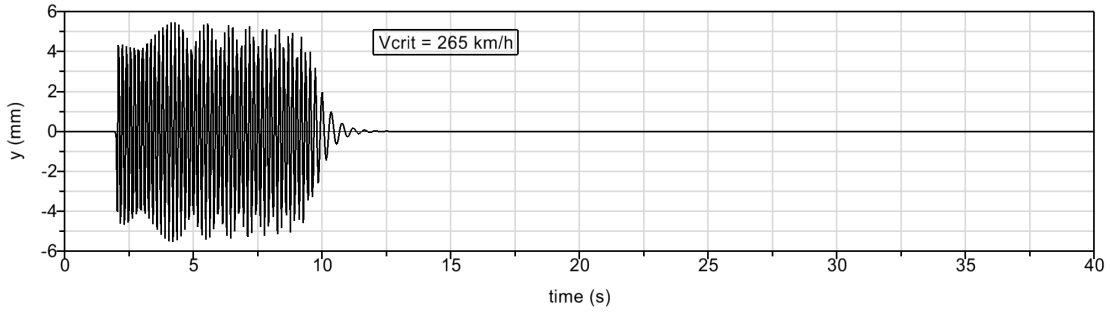

Figure 8.16. Lateral displacement of the most critical wheelset; Vivalto, unworn CD1-32.5 profile.

The matching between the CD1-32.5 and the Vivalto coach demonstrates an unusual behaviour: the critical speed using the unworn profile is lower than those evaluated when the wheel shape is modified by wear. The critical speed in first case is consistent with the value arising from the adoption of the S1002 (Fig. 8.16), while in the two other cases (depicted respectively in Figs. 8.17 and 8.18) it is higher.

This result must not surprise because the worn profile are characterized by a considerable enlargement of the available of flangeway clearance while at the same time the reduction in rolling radius is slight, hence the conditions for a low equivalent conicity, even for profile near to the re-turning exists.

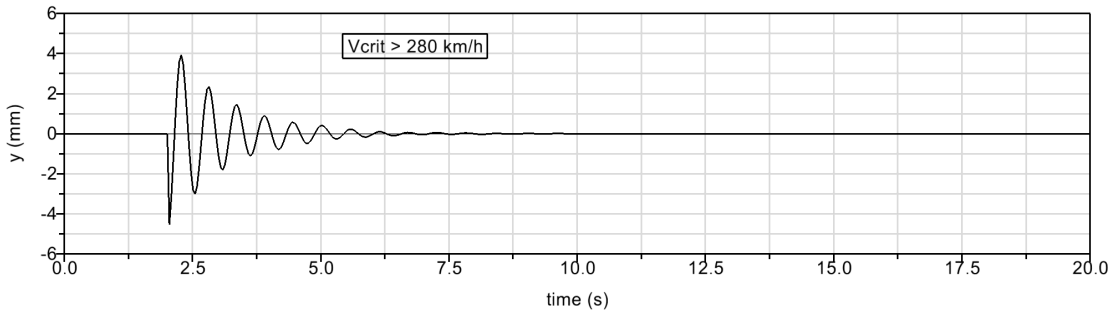

Figure 8.17. Lateral displacement of the most critical wheelset; Vivalto, 50 % worn CD1-32.5 profile.

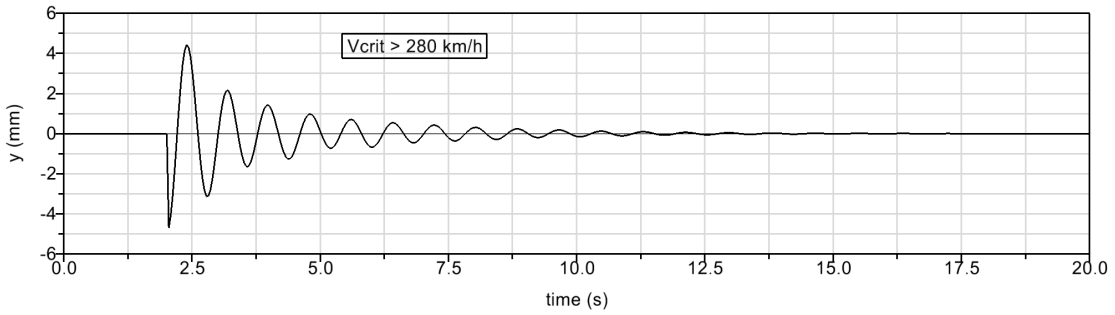

Figure 8.18. Lateral displacement of the most critical wheelset; Vivalto, fully worn CD1-32.5 profile.

8.5.3 DR2 wheel profile

Even when equipped with the DR2 profile (Figs. 8.19, 8.20 and 8.21), the Vivalto exhibits a higher critical speed in the worn conditions. The stability limit with the unworn profile is about 250 km/h, once again much greater than the maximum service speed.

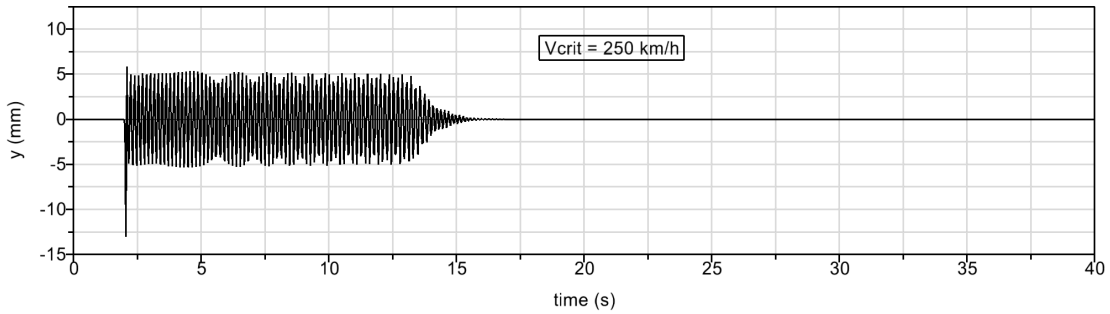

Figure 8.19. Lateral displacement of the most critical wheelset; Vivalto, unworn DR2 profile.

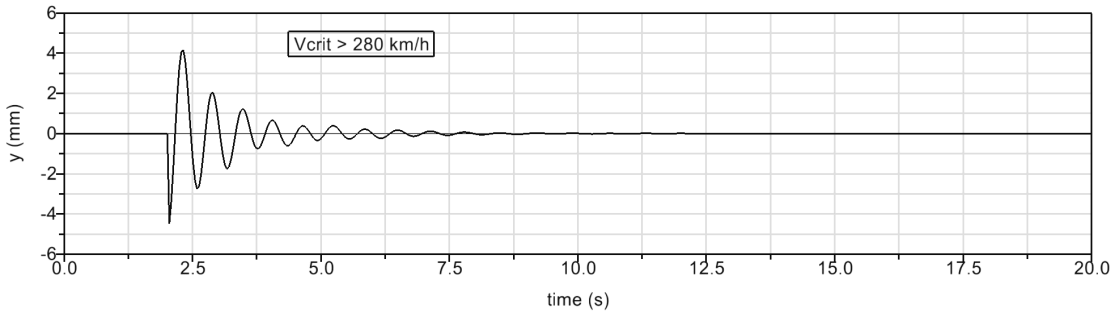

Figure 8.20. Lateral displacement of the most critical wheelset; Vivalto, 50 % worn DR2 profile.

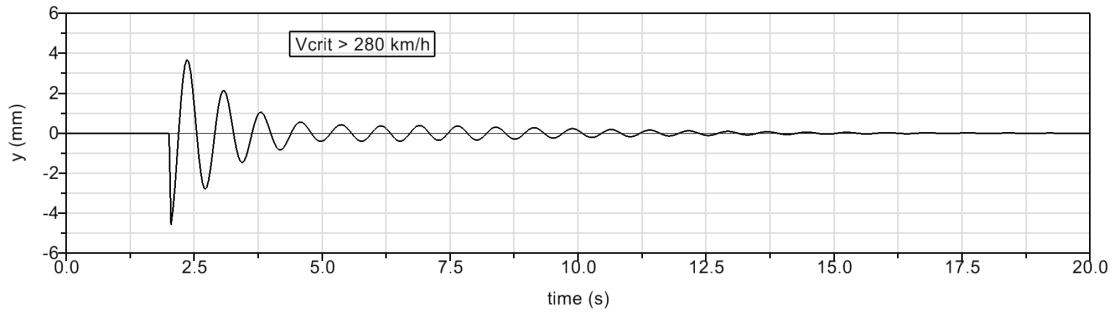

Figure 8.21. Lateral displacement of the most critical wheelset; Vivalto, fully worn DR2 profile.

8.6 Stability analysis of the E464

8.6.1 S1002 wheel profile

The results of the stability evaluation for the E464-S1002 combination are illustrated from Fig. 8.22 to Fig. 8.24: the comparison between the unworn and the unworn conditions shows that the reduction in critical speed is of little importance. The top allowable speed when the new profiles is applied is quite lower with respect to the other two vehicles and moreover it is not as affected by the level of wear as in the previous cases which have been discussed.

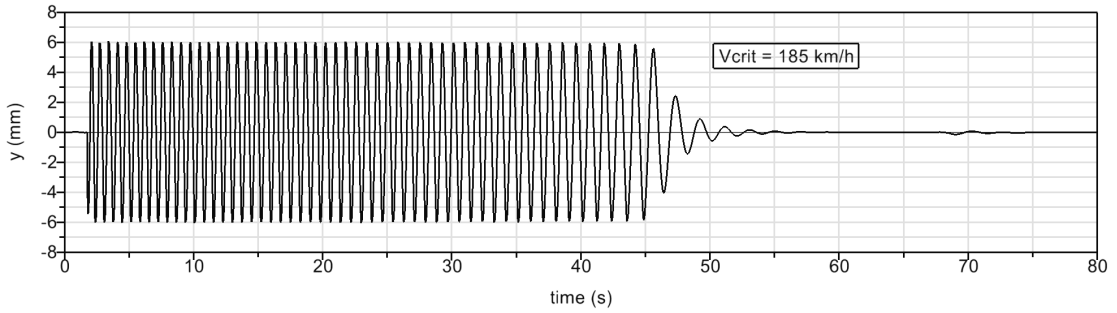

Figure 8.22. Lateral displacement of the most critical wheelset; E464, unworn S1002 profile.

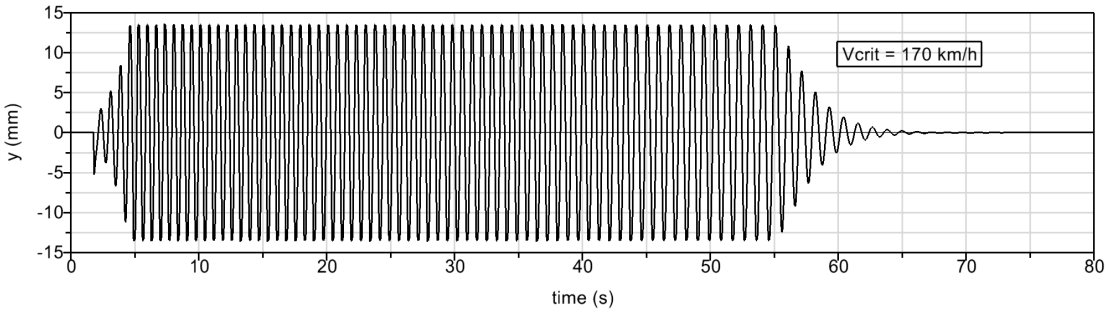

Figure 8.23. Lateral displacement of the most critical wheelset; E464, 50 % worn S1002 profile.

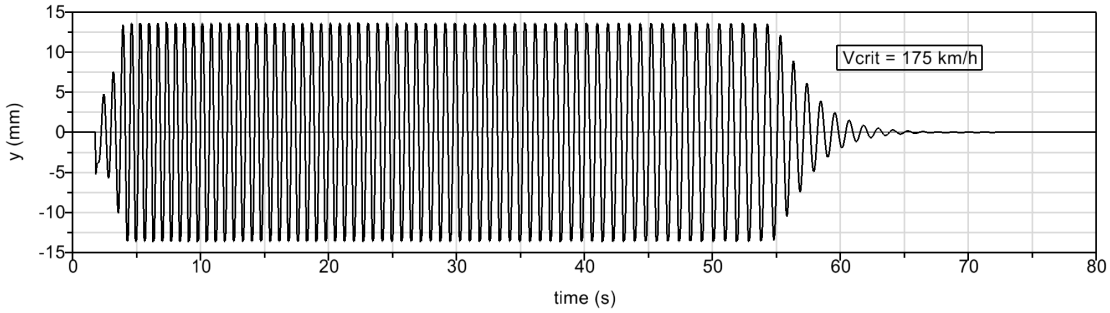

Figure 8.24. Lateral displacement of the most critical wheelset; E464, fully worn S1002 profile.

8.6.2 CD1-32.5 wheel profile

For what concerns the matching between the traction unit and the CD1-32.5 profile, the results are depicted from Fig. 8.25 to Fig. 8.27. The critical speed in unworn condition is the highest among the combinations involving the E464, whereas the performance with worn profiles are the same of those obtainable with the S1002.

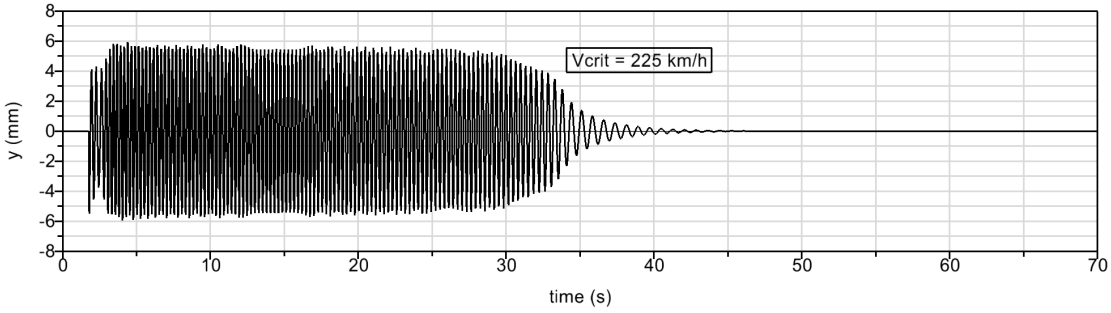

Figure 8.25. Lateral displacement of the most critical wheelset; E464, unworn CD1-32.5 profile.

8.6.3 DR2 wheel profile

For the last scenery investigated during the stability assessment the results, visible from Fig. 8.28 to Fig. 8.30 are qualitatively similar to those provided by the S1002. The critical speed for the unworn condition is equal to 185 km/h, which is being reduced to about 165 km/h when instead unworn profiles are used.

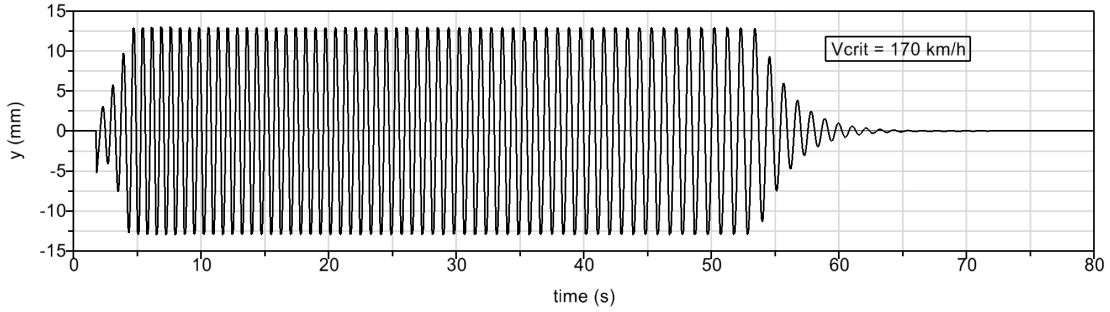

Figure 8.26. Lateral displacement of the most critical wheelset; E464, 50 % worn CD1-32.5 profile.

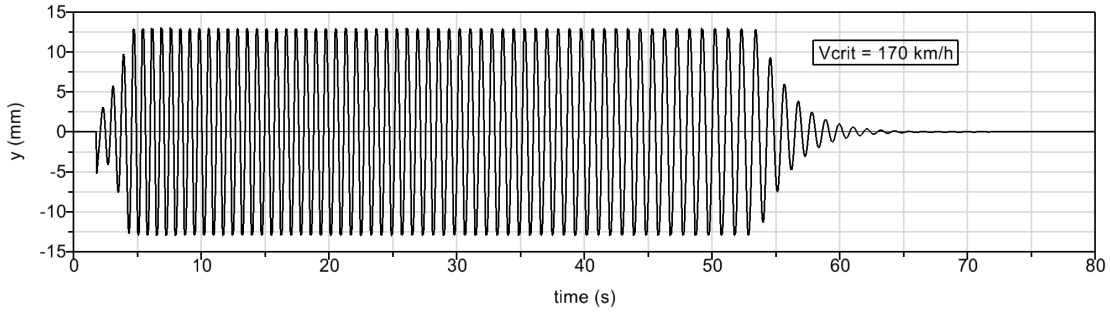

Figure 8.27. Lateral displacement of the most critical wheelset; E464, fully worn CD1-32.5 profile.

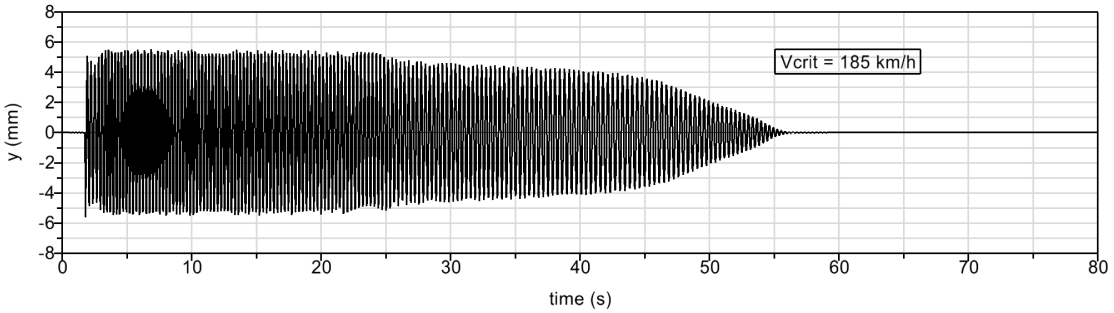

Figure 8.28. Lateral displacement of the most critical wheelset; E464, unworn DR2 profile.

8.7 Discussion of the results

With respect to what has been presented in the review on the stability of the three vehicles, first of all it can be stated that the new profiles (CD1-32.5, DR2) under unworn conditions lead to a critical velocities comparable with the S1002 or even higher in a few cases. For all the profiles which have been tested, the reduction due to wear is appreciable for the Minuetto, unimportant for what concerns the Vivalto coach and finally of moderate entity for the E464.

The three models also exhibit different responses to the stability analysis both for their intrinsic characteristics and also because each vehicle has its own worn profiles. In detail, the Minuetto show the presence of unstable limit cycles at high speeds; the Vivalto coach

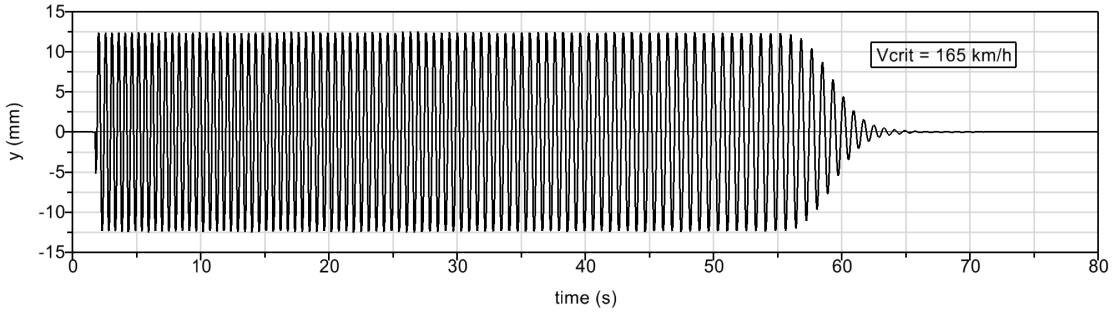

Figure 8.29. Lateral displacement of the most critical wheelset; E464, 50 % worn DR2 profile.

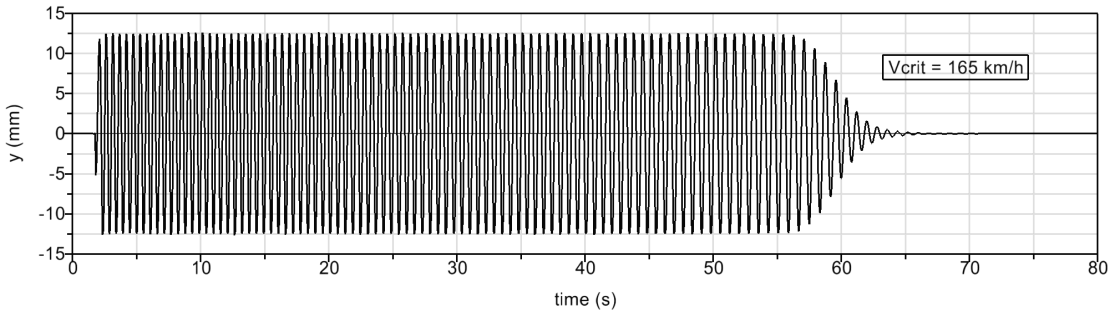

Figure 8.30. Lateral displacement of the most critical wheelset; E464, fully worn DR2 profile.

has the best behaviour and critical speeds much greater than its maximum service speed while the E464 seems to be the most unstable vehicle in terms of maximum allowable speed having the top critical speed lower than 200 km/h.

The unworn profiles used as inputs in the assessment are typically characterized by low equivalent conicities due to the localisation of the wear on the flange rather than on the tread. The remarkable wear rate on the flange causes a notable and quick increase in the flangeway clearance and, as a consequence, the wear on the tread begin to occur on the external part of the wheel due to the wide displacement of wheelsets in curves. The arising profiles does not present a pronounced hollow form, which would imply a high equivalent conicity. Conversely, the final shapes due to wear present a reduction of the mean slope of the Δr function but they also present, in a few cases, a negative gravitational stiffness for small displacement, which might make the vehicles unstable.

As it was expected, the results are also then highly depending on the vehicle characteristics, (especially on the global damping) since similar wheel profiles lead to significant differences in the final results. Nevertheless, anomalous behaviour of the vehicles equipped with unworn wheel profiles have not been detected and the critical speed are consistent with the maximum speeds on service. An higher critical velocity may be preferable in a pair of cases; however, it must be considered that the critical speeds evaluated via numerical simulation are very pessimistic since a high value of the friction coefficient in the wheel-rail contact has been used in all the analyses.

Conclusions and Future Work

In this thesis a research work aimed at wear assessment and wheel profile optimisation in the railway field has been presented. The research activity has been carried out within the Section of Applied Mechanics of the University of Florence in collaboration with Trenitalia S.p.A (the main Italian society for the passenger transport) and Rete Ferroviaria Italiana (RFI, the administrator of the railway infrastructure), the partners of the project issued by Trenitalia itself and titled "Ottimizzazione dei profili delle ruote su binario con posa 1/20". The main purpose of this collaboration was the formulation of alternative wheel profiles in place of the commonly used ORE S1002 in order to improve the performance in terms of both resistance to wear (with advantages on the maintenance costs) and kinematic behaviour of the wheel-rail interaction (with advantages in terms of vehicle running dynamic). The research activity had to be performed via numerical simulations of the vehicle dynamics taking into consideration real situations of practical interest and by using the experimental and technical data provided by the project partners, concerning the involved vehicles and tracks.

To this end, a general architecture made up of a group of software tools has been specifically developed for this work. This general model, which can anyway used in different contexts of the railway field, basically enclose a mathematical model capable of estimating the wheel wear, which has been developed in the activity. The wear model is exploited in combination with a multibody model of the railway vehicle under investigation, by adopting a discrete approach for the evaluation of the evolution in wheel wear. A special attention is given to the wheel-rail contact model, by using a model, the development of which began during previous works within the Section of Applied Mechanics; this innovative contact model permits an accurate evaluation of the position of the contact points during multibody simulations, avoiding some typical simplifications usually adopted by tools provided by the commercial multibody software, often optimised to reduce the overall required computational time with a few compromise on the accuracy.

The whole architecture has been validated thanks to the experimental data relative to the Aosta-Pre Saint Didier track before being used to perform wear evaluations required in the project. The main part of the work have been focused on two real train compositions: the Aln 501 Minuetto and the E464-Vivalto train, both widely used for the regional

passenger transport in Italy. An interesting aspect of the activity lies in the fact that the main numerical simulations have been carried out on "virtual tracks", that are statistical representations, made up of several basic tracks, of the whole railway nets on which the vehicles are operated daily. This statistical approach, made possible by the large amount of data provided by RFI, is conceptually simple and at the same time strictly linked to the real context, being based on detailed analyses of track databases. It was introduced considering that for each railway application exists an optimal profile (or probably more than one, depending on the constraint and the final goals) and the study should be strongly connected to the real railway net on which the vehicle operate. Although it permits to overcome the difficulty in formulating an alternative strategy, the weak point which must be underlined is the lack of the contribution of the longitudinal traction efforts (due to braking and tractive manoeuvres) which cannot be conceptually included in this kind of analysis. Nevertheless the effect might be appreciable only when simulating the wear on tracks having long straight sections and large curves, especially if the vehicle have to exert continuously relevant longitudinal efforts.

During the work different wheel profiles have been tested and compared with each other to evaluate in detail the performance in terms of resistance to wear, while ensuring at the same time acceptable kinematic characteristics of the wheel-rail coupling. With regard to the adopted strategy and the results, there are several points that turn out to be discussed. First of all, even though the two innovative profiles are conceived choosing different approaches, they have both demonstrated better performance in terms of total kilometrage covered before reaching the thresholds selected for the comparison with the standard S1002. The results in terms of resistance to wear are interesting and encouraging: the second proposed profile, the DR2, guarantees numerically an increase in the travelled distance up to 28 % in the Minuetto virtual track and up to 19 % in the Vivalto composition one; the performance of the CD1 profile (the first proposed alternative geometry) having the same flange thickness are in both the cases of about 20 % and deserve to be taken into serious consideration. The variants of the CD1 profile having a reduced flange thickness are instead less interesting, though the intermediate version (30.5 mm of thickness) has shown performance even better than those provided by the S1002. A nonlinear stability assessment have also been performed in order to verify that the the two vehicle equipped with the unworn and worn wheel geometries previously calculated do not exhibit unstable behaviour at low speeds.

The review on the wear assessment has shown that, as it was expected, a correct choice of the wheel profile without any change in the rail profile (or profiles, like in this case) can positively affect not only the dynamic behaviour of the vehicle but also the wear, leading to a significant improvement of the performance from this point of view. The effects of a proper profile, having suitable contact geometry characteristics has a great importance especially at the beginning of the wheel life, when the wear rate can be considerably reduced. After completing a long kilometrage, the effect of the initial shape decrease and whatever the original shape was, the final profile shapes are affected not only by the characteristic of

the vehicle but also, in a relevant manner, by the conditions of the rails on which the train runs.

For what concerns the prosecution of the activity, experimental dynamic tests, aimed at verifying the behaviour of vehicles equipped with these unconventional wheel profile will be soon carried out. Probably the first test will be performed on a Minuetto with the CD1-32.5 wheel profile after completing, by means of multibody simulations, further dynamic investigations on running safety according to the EN 14363. In fact, every new wheel profile not included in the relative regulation in force must be approved by carrying out progressive experimental tests before applying the new profile on all the wheelsets of a vehicle in service to verify the performance in an experimental wear assessment.

As regards other theoretical aspects of the presented study, there are some ideas to extend the research. The first point is the type of average to be employed in summarizing and in the comparison the results: from a conceptual point of view, it might be interesting in certain contexts to take the average on each wheelset instead of the average on all the wheels; in this research, according to the working hypotheses agreed with the partners, the output of the wear model had to be a single mean profile to sum up the results effectively. This choice obviously tends to hide the own response of each wheel but it is very useful when applied in combination with the statistical approach to reproduce the average evolution of a wheel which for instance, half of the times runs on the external side of the track being part of a leading wheelset and the other half of the times runs on the internal side, being part of a trailer wheelset.

Further experimental data, by exploiting the programmed and above-mentioned tests can be of great help for a further validation of the model, especially for what concerns the introduction of other wear mechanisms such as the plastic wear and the rolling contact fatigue.

Currently, with regard to the response of the model, considering what has been seen in the evolution of wheel profiles, the wear tends to remove material especially on the flange of the profile rather that on the tread and consequently the decreasing in rolling radius of the profiles is quite low. For this reason, the flange height during the wear simulation increases of a modest quantity and the evolution of the dimension itself is of poor interest even if it has been reported for the sake of completeness. This behaviour of the wear model arises from the validation on the Aosta Pre-Saint Didier track where severe wear on the flanges were detected.

However, the aim of the comparison, the real purpose of the research activity, was to establish and quantify the relative difference in behaviour by varying the wheel profile, in order to develop a new wheel profile to be tested on real vehicles. It follows that a slight difference in the absolute value of the presented kilometrage due to the underestimation of the real wear rate would not alter significantly the conclusions of the work. This is even more true if the simulations comprise a set of different running situations (straight track, sharp curves and large curves) instead of a particular condition, where a wear mechanism might predominate on the others.

List of Figures

List of Tables

References

[1] C. Esveld. *Modern Railway Track*. Delft University of Technology, Delft, Netherlands, 2001.

[2] F. Braghin, R. Lewis, R. S. Dwyer-Joyce, and S. Bruni. A mathematical model to predict railway wheel profile evolution due to wear. *Wear*, 261: 1253–1264, 2006.

[3] T. Telliskivi and U. Olofsson. Wheel-rail wear simulation. *Wear*, 257: 1145–1153, 2004.

[4] J. Pombo, J. Ambrosio, M. Pereira, R. Lewis, R. Dwyer-Joyce, C. Ariaudo, and N. Kuka. A study on wear evaluation of railway wheels based on multibody dynamics and wear computation. *Multibody System Dynamics*, 24:347–366, 2010.

[5] J. Kalousek. Wheel/rail damage and its relationship to track curvature. *Wear*, 258: 1330–1335, 2005.

[6] H. Wu K. Sawley. The formation of hollow-worn wheels and their effect on wheel/rail interaction. *Wear*, 258: 1179–1186, 2005.

[7] C. Esveld I. Y. Shevtsov, V. L. Markine. Optimal design of wheel profile for railway vehicles. *Wear*, 258: 1022–1030, 2004.

[8] C. Esveld I. Y. Shevtsov, V. L. Markine. Shape optimisation of railway wheel profile. In *Mechanics of the 21st Century*, Warsaw, Poland, August 2004. Proceedings of the 21st International Congress of Theoretical and Applied Mechanics (ICTAM).

[9] C. Esveld I. Y. Shevtsov, V. L. Markine. Design of railway wheel profile taking into account rolling contact fatigue and wear. *Wear*, 265: 1273–1285, 2008.

[10] I. Y. Shevtsov. *Wheel/Rail Interface Optimisation*. PhD thesis, Delft University of Technology, The Netherlands, 2008.

[11] S. Iwnicki I. Persson. Optimisation of railway wheel profiles using a genetic algorithm. *Vehicle System Dynamics*, 41: 517–527, 2004.

[12] A. Orro M. Novales and M. R. Bugarì. Use of a genetic algorithm to optimize wheel profile geometry. *Journal of Rail and Rapid Transit*, 221: 467–476, 2007.

[13] A. H. Wickens. *Fundamentals of Rail Vehicle Dynamics*. Swets & Zeitlinger Publishers, Lisse, The Netherlands, 2003.

[14] S. Iwnicki. *Handbook of Railway Vehicle Dynamics*. CRC Press, Taylor & Francis Group, 2006.

[15] J. J. Kalker. *Three-dimensional Elastic Bodies in Rolling Contact*. Kluwer Academic Publishers, Dordrecht, Netherlands, 1990.

[16] EN 15302:2011. Railway applications - Method for determining the equivalent conicity.

[17] EN 14363:2005. Railway applications - Testing for the acceptance of running characteristics of railway vehicles - Testing of running behaviour and stationary tests, June 2005.

[18] SIMPACK®. SIMPACK AG, Gilching, Germany. Official Web Site: www.simpack.com.

[19] R. V. Dukkipati and J. R. Amyot. *Computer Aided Simulation in Railway Dynamics*. Dekker, New York, 1988.

[20] R. Enblom and M. Berg. Simulation of railway wheel profile development due to wear: influence of disk braking and contact environment. *Wear*, 258: 1055–1063, 2005.

[21] E. Meli, S. Falomi, M. Malvezzi, and A. Rindi. Determination of wheel-rail contact points with semianalytic methods. *Multibody System Dynamics*, 20(4): 327–358, 2008.

[22] M. Malvezzi, E. Meli, J. Auciello, and S. Falomi. Dynamic simulation of railway vehicles: wheel - rail contact analysis. *Vehicle System Dynamics*, 47(7): 867–899, 2009.

[23] E. Meli, S. Falomi, M. Malvezzi, and M. Rinchi. Multibody modelling of railway vehicles: innovative algorithms for the detection of wheel - rail contact points. In *Multibody Dynamics 2009* (ECCOMAS), Varsavia, Polonia, 2009.

[24] F. Cheli and E. Pennestrì. *Cinematica e dinamica dei sistemi multibody*. CEA, 2006.

[25] J. Auciello. WP3: Modellazione dei rotabili. Progetto di Ricerca *Ottimizzazione dei profili delle ruote su binario con posa 1/20*, 2010.

[26] S. Iwnicki. *The Manchester Benchmarks for Rail Vehicle Simulators*. Swets & Zeitlinger, Lisse, Netherlands, 1999.

[27] A. A. Shabana and J. R. Sany. An augmented formulation for mechanical systems with non-generalized coordinates: application to rigid body contact problems. *Nonlinear Dynamics*, 24: 183–204, 2001.

[28] A. A. Shabana and J. R. Sany. A survey of rail vehicle track simulations and flexible multibody dynamics. *Nonlinear Dynamics*, 26: 179–210, 2001.

[29] A. A. Shabana, M. Berzeri, and J. R. Sany. Numerical procedure for the simulation of wheel/rail contact dynamics. *Trans. Am. Soc. Mech. Eng.*, 123: 168–178, 2001.

[30] J. Pombo and J. Ambrosio. Dynamic analysis of a railway vehicle in real operation conditions using a new wheel-rail contact detection model. *International Journal of Vehicle Systems Modelling and Testing*, 1: 79–105, 2005.

[31] A. A. Shabana, M. Tobaa, H. Sugiyama, and K. E. Zaazaa. On the computer formulations of the wheel/rail contact problem. *Nonlinear Dyn*, 40: 169–193, 2005.

[32] A. A. Shabana and K. E. Zaazaa. Modeling two-point wheel/rail contacts using constraint and elastic-force approaches. In *Proc. IMECE'02: 2002 ASME International Mechanical Engineering Congress and Exposition*, New Orleans, 2002.

[33] W. Kik and D. Moelle. Implementation of the wheel-rail element in ADAMS/Rail version 10.1. In *5th ADAMS/Rail Users' Conference*, Haarleem, 2000.

[34] M. Bozzone, E. Pennestrì, and P. Salvini. A lookup table-based method for wheel-rail contact analysis. *Proceedings of the Institution of Mechanical Engineers, Part K: Journal of Multibody Dynamics*, 225:127–138, 2010.

[35] M. Do Carmo. *Differential Geometry of Curves and Surfaces*. Prentice Hall, Upper Saddle River, New Jersey, 1976.

[36] MATLAB®. Mathworks Inc., Natick, USA. Official Web Site: www.mathworks.com.

[37] EN 15313:2010. Railway applications - In service wheelset operation requirements - In service and off-vehicle wheelset maintenance.

[38] EN 13715:2006+A1. Railway applications - Wheelsets and bogies - Wheels - Tread profile.

[39] EN 13674-1:2011. Railway applications - Track - Rail - Vignole railway rails 46 kg/m and above.

[40] O. Polach. Influence of wheel/rail contact geometry on the behaviour of a railway vehicle at stability limit. In *Proc. 5th EUROMECH Nonlinear Dynamics Conference ENOC-2005*, Netherlands, 2005. Eindhoven University of Technology.

[41] O. Polach. Comparability of the non-linear and linearized stability assessment during railway vehicle design. *Vehicle System Dynamics*, 44, Supplement: 129–138, 2006.

[42] UIC 518. Testing and approval of railway vehicles from the point of view of their dynamic behaviour - Safety - Track fatigue - Ride quality. Second edition, 2003.